

**FERROMAGNETIC AND MULTIFERROIC THIN FILMS AIMED  
TOWARDS OPTOELECTRONIC AND SPINTRONIC APPLICATIONS**

A Dissertation  
Presented to  
The Academic Faculty

By

Syed Muhammad Tahir Zaidi

In Partial Fulfillment  
Of the Requirements for the Degree  
Doctor of Philosophy in the  
School of Electrical and Computer Engineering

Georgia Institute of Technology

August 2010

**FERROMAGNETIC AND MULTIFERROIC THIN FILMS AIMED  
TOWARDS OPTOELECTRONIC AND SPINTRONIC APPLICATIONS**

Approved by:

Dr. Ian Ferguson, Advisor  
School of Electrical and Computer  
Engineering  
*Georgia Institute of Technology*

Dr. Thomas Michaels  
School of Electrical and Computer  
Engineering  
*Georgia Institute of Technology*

Dr. David Citrin  
School of Electrical and Computer  
Engineering  
*Georgia Institute of Technology*

Dr. Alan Doolittle  
School of Electrical and Computer  
Engineering  
*Georgia Institute of Technology*

Dr. Nazanin Bassiri-Gharb  
School of Materials Science and  
Engineering  
*Georgia Institute of Technology*

Date Approved: May 13, 2010

Scientific principles and laws do not lie on the surface of nature. They are hidden, and must be wrested from nature by an active and elaborate technique of inquiry.

- John Dewey

(“Reconstruction in Philosophy” June 11, 2004)

*Dedicated to my wife  
For her unconditional love and support*

## ACKNOWLEDGEMENTS

I would like to take this opportunity to sincerely thank my advisor Professor Ian Ferguson for his wonderful guidance, support and encouragement in making this thesis possible. I am also thankful to the current and past members of my research group for their help and support namely Vincent Woods, Will Fenwick, Olivier Hamard, Shalini Gupta, Balakrishnam Jampana, Omkar Jani, Hun Kang, Nola Li, Enno Malguth, Andrew Melton, David Nicol, Eun-Hyun Park, Petkov Petko, Zaili Fang, Peter Speirs, Shenjie Wang, Tianming Xu, Hongbo Yu, and Muhammad Jamil. I would especially like to thank Andrew, Jamil and Tim, the last remaining members, who provided me with help and support to finish this work.

I am also thankful to Eric Burgett of Department of Nuclear Engineering for carrying out complex experiments to support my research and for explaining the corresponding theory and techniques, which were completely alien to me.

My special thanks to Elisa Hurwitz for putting in long hours with me while helping me out with the experiments and the dissertation.

I am grateful to Professor Thomas Micheals, Professor David Citrin, Professor Alan Doolittle and Professor Nazanin Bassiri-Gharb for agreeing to be my defense committee members and for being extremely understanding and helpful.

My heartfelt gratitude goes to my wife Malika and father-in-law Syed Javed Raza. Without their enduring love and support I would not have come this far.

I thank the Higher Education Commission Pakistan, Pakistan Army and the United States Air Force Office of Scientific Research for providing me with this opportunity and for funding this research.

# TABLE OF CONTENTS

<b>ACKNOWLEDGEMENTS .....</b>	<b>v</b>
<b>LIST OF TABLES .....</b>	<b>xii</b>
<b>LIST OF FIGURES .....</b>	<b>xiii</b>
<b>LIST OF SYMBOLS AND ABBREVIATIONS .....</b>	<b>xviii</b>
<b>SUMMARY .....</b>	<b>xxi</b>
<b>CHAPTER 1: INTRODUCTION.....</b>	<b>1</b>
1.1 Spintronics .....	3
1.2 Ferromagnetic Metals in Spintronics .....	5
1.3 Dilute Magnetic Semiconductor .....	6
1.4 History of Semiconductor Materials for Spintronics Applications.....	7
1.5 Transition Metal Doped Dilute Magnetic Semiconductors .....	9
1.6 Rare Earth Doped Dilute Magnetic Semiconductors.....	11
1.7 Light Emitting Diode .....	13
1.8 Spin Polarized Light Emitting Diode.....	14
1.9 Summary.....	14
<b>CHAPTER 2: MAGNETISM IN DILUTE MAGNETIC SEMICONDUCTORS ...</b>	<b>16</b>
2.1 Introduction.....	16
2.2 Origin of Magnetism.....	16
2.3 Types of Magnetism .....	19
2.3.1 <i>Diamagnetism</i> .....	19
2.3.2 <i>Paramagnetism</i> .....	21
2.3.3 <i>Ferromagnetism</i> .....	21
2.3.4 <i>Antiferromagnetism</i> .....	22
2.3.5 <i>Ferrimagnetism</i> .....	23
2.3.6 <i>Superparamagnetism</i> .....	23
2.4 Dilute Magnetic Semiconductor Exchange Mechanisms .....	24
2.4.1 <i>Direct Exchange</i> .....	24
2.4.2 <i>Indirect Exchange</i> .....	25

2.4.2.1 Carrier Mediated Exchange (RKKY).....	25
2.4.2.2 Double Exchange .....	27
2.4.2.3 Super Exchange .....	27
2.5 Summary .....	27
<b>CHAPTER 3: BACKGROUND: GADOLINIUM DOPED GaN.....</b>	<b>29</b>
3.1 Introduction.....	29
3.2 Properties of Wurtzite GaN .....	30
3.3 Band Structure and Allowed Optical Transitions in GaN .....	31
3.4 Properties of Gadolinium .....	33
3.5 Literature Review: Gd Doped GaN .....	36
3.6 Proposed Models for Magnetic Moment in $\text{Ga}_{1-x}\text{Gd}_x\text{N}$ .....	39
3.6.1 Long-Range Spin Polarization.....	39
3.6.2 Impurity States .....	39
3.6.3 Ga vacancies.....	40
3.6.4 Interstitial N.....	44
3.6.5 Interstitial O.....	45
3.7 Challenges for a $\text{Ga}_{1-x}\text{Gd}_x\text{N}$ DMS .....	47
3.8 Summary .....	47
<b>CHAPTER 4: EXPERIMENTAL EQUIPMENT AND TECHNIQUES .....</b>	<b>49</b>
4.1 Introduction.....	49
4.2 MOCVD Growth Technique.....	49
4.2.1 Thermodynamics .....	50
4.2.2 Kinetics .....	52
4.2.3 Fluid Dynamics and Mass Transport .....	53
4.3 Growth Rate Regimes .....	57
4.4 Modes of Thin Film Growth.....	58
4.5 MOCVD Gas Delivery System.....	59
4.6 MOCVD Reaction Chamber.....	62
4.7 Exhaust Handling System .....	63
4.8 Precursors for MOCVD Growth of GaN .....	63
4.9 Substrates for GaN Growth.....	65

4.10	MOCVD GaN Growth.....	66
4.11	Doping GaN Thin Films .....	68
4.11.1	<i>n-GaN Thin Films</i> .....	69
4.11.2	<i>p-type GaN Thin Films</i> .....	69
4.12	Characterizations.....	70
4.13	Summary .....	70
<b>CHAPTER 5: MOCVD GROWTH OF Ga<sub>1-x</sub>Gd<sub>x</sub>N .....</b>		<b>71</b>
5.1	Introduction.....	71
5.2	MOCVD Growth Tool.....	71
5.3	Gd Precursors.....	73
5.4	Modified Precursor Delivery System.....	74
5.5	Experimental Method.....	76
5.6	Structural Characterization .....	76
5.7	Optical Characterization .....	79
5.8	Magnetic Characterization .....	81
5.9	Electrical Characterization.....	86
5.10	Alpha Stopping Power of Ga <sub>1-x</sub> Gd <sub>x</sub> N thin Films .....	89
5.11	Neutron Scintillation Property of Ga <sub>1-x</sub> Gd <sub>x</sub> N Thin Films.....	90
5.12	EDS Data for Ga <sub>1-x</sub> Gd <sub>x</sub> N Thin Film Composition.....	92
5.13	Analysis and Conclusions .....	94
5.14	Summary .....	96
<b>CHAPTER 6: SPIN-POLARIZED LIGHT EMITTING DIODE .....</b>		<b>98</b>
6.1	Introduction.....	98
6.2	Light Emitting Diode - Historical Background .....	98
6.3	Spin-Polarized Light Emitting Diode .....	100
6.3.1	<i>Spin-injection</i> .....	101
6.3.2	<i>Spin transport</i> .....	103
6.3.3	<i>Spin Injection Detection</i> .....	106
6.3.4	<i>Spin-polarized LED in Literature</i> .....	107
6.4	Ga <sub>1-x</sub> Gd <sub>x</sub> N LED by MOCVD.....	109
6.4.1	<i>Structural Characterization of Ga<sub>1-x</sub>Gd<sub>x</sub>N LED</i> .....	113

6.4.2	<i>Electrical Characterization</i> .....	115
6.4.3	<i>Magnetic and Spin Characterization</i> .....	115
6.5	Summary .....	122
<b>CHAPTER 7: CONCLUSION AND FUTURE WORK .....</b>		<b>123</b>
7.1	Introduction.....	123
7.2	Conclusions.....	123
7.3	Achievements.....	126
7.4	Future Work .....	127
7.5	Summary .....	128
<b>CHAPTER 8: ADDITIONAL WORK.....</b>		<b>129</b>
8.1	Introduction.....	129
8.2	N-Doped ZnO .....	131
8.2.1	<i>Pulsed MOCVD growth of N-Doped ZnO</i> .....	136
8.3	Multiferroic Bismuth Ferrite.....	136
8.3.1	<i>BFO MOCVD Growth</i> .....	140
8.3.2	<i>BFO Spintronics Applications</i> .....	141
8.3.3	<i>Growth and Characterization of BFO</i> .....	143
8.3.4	<i>MOCVD Growth of BFO</i> .....	145
8.4	Summary .....	148
<b>APPENDIX A: CHARACTERIZATION .....</b>		<b>149</b>
A.1	Introduction.....	149
A.2	In-situ Characterization.....	149
A.2.1	<i>Optical reflectometry</i> .....	150
A.3	Structural Characterization .....	153
A.3.1	<i>X-ray Diffraction (XRD)</i> .....	153
A.4	Magnetic Characterization .....	155
A.4.1	<i>Vibrating Sample Magnetometry</i> .....	155
A.4.2	<i>SQUID</i> .....	156
A.5	Optical Characterization .....	158
A.5.1	<i>Photoluminescence Spectroscopy (PL)</i> .....	159
A.6	Electrical Characterization.....	159

A.6.1	<i>Hall Effect Measurement</i> .....	160
A.7	Device Characterization.....	161
A.7.1	<i>Current-Voltage (I-V) Measurement</i> .....	162
A.7.2	<i>Electroluminescence (EL)</i> .....	163
A.7.3	<i>Optical Power Measurements</i> .....	164
<b>APPENDIX B: DEVICE FABRICATION</b> .....		<b>165</b>
B.1	Introduction.....	165
B.2	Annealing .....	166
B.3	Photolithography.....	166
B.4	Wafer Cleaning .....	166
B.5	Metal Deposition – Current Spreading Contact.....	166
B.6	Current Spreading Contact Annealing .....	167
B.7	Mesa Pattern Transfer .....	167
B.8	Mesa Etch.....	168
B.9	n-GaN Contact .....	168
B.10	p-GaN Contact .....	169
B.11	Packaging.....	169
<b>REFERENCES</b> .....		<b>170</b>
<b>PUBLICATIONS</b> .....		<b>187</b>
<b>CONFERENCE PRESENTATIONS</b> .....		<b>189</b>

## LIST OF TABLES

Table 3.1: Material properties of wurtzite GaN	30
Table 3.2: Electronic Configuration of rare earth elements	33
Table 3.3: Material properties of wurtzite GaN	34
Table 3.4: Composition of naturally occurring Gd [90]	34
Table 3.5: Covalent radii of common impurities in GaN	41
Table 4.1: MO precursors used in MOCVD of GaN	63
Table 4.2: Lattice constants and thermal expansion coefficients for GaN and sapphire	65
Table 5.1: Hall Data for $\text{Ga}_{1-x}\text{Gd}_x\text{N}$ films	88
Table 5.2: EDS for $\text{Ga}_{1-x}\text{Gd}_x\text{N}$ films	93
Table 6.1: Spin polarization percentages reported in emissions from spin LEDs	108
Table 6.2: Design structure of the baseline GaN LED	112
Table 6.3: $P_{\text{spin}}$ for $\text{Ga}_{1-x}\text{Gd}_x\text{N}$ LED Vs Magnetic field	120
Table 8.1: Hall effect data for samples annealed in $\text{N}_2$ ambient at $800^\circ\text{C}$ for 60 min	134
Table 8.2: Reports of MOCVD growth of BFO thin films.	141

## LIST OF FIGURES

Figure 1.1 :	(a) GMR-based spin valve. (b) TMR-based spin valve. (c) GMR-based spin valve for read head [3]	4
Figure 1.2 :	Spin injection across ferromagnetic semiconductor junction [5]	6
Figure 1.3 :	Dilute magnetic semiconductor synthesis	7
Figure 1.4 :	Timeline of spintronic material developments.	8
Figure 1.5 :	Calculated $T_c$ for p-type 5 % Mn doped semiconductors with $3.5 \times 10^{20} \text{ cm}^{-3}$ holes [23]	9
Figure 2.1 :	An electron in an orbit traveling around the nucleus	16
Figure 2.2 :	Types of magnetism (a) Diamagnetism (b) Paramagnetism (c) Ferromagnetism (d) Antiferromagnetism (e) ferrimagnetism	19
Figure 2.3 :	Typical hysteresis curve for a FM	20
Figure 2.4 :	Indirect exchange mechanisms: (a) carrier mediated, (b) double exchange, (c) superexchange	25
Figure 3.1:	Schematic of the different polarities of wurtzite GaN [87]	30
Figure 3.2:	(a) Schematic of wurtzite band structure, (b) allowed optical transition in GaN [86, 88].	32
Figure 3.3 :	A single Gd atom and one $V_{\text{Ga}}$ (a) GaN lattice (b) Density of states	40
Figure 3.4 :	Relation between $V_{\text{Ga}}$ and magnetic moment	41
Figure 3.5 :	Total energies of various spin configurations of GaN:Gd with ten Ga vacancies	43

Figure 3.6 :	Density of states of $N_i$ atoms in wurtzite GaN	44
Figure 3.7 :	Density of states of $O_i$ atoms in wurtzite GaN	45
Figure 3.8 :	Difference in ferromagnetic and antiferromagnetic interactions with $N_i$ and $O_i$ in wurtzite GaN	45
Figure 4.1 :	MOCVD process showing adsorption, diffusion of reactants across the surface, attachment to a surface site, and desorption.	52
Figure 4.2 :	Gas flows inside an MOCVD chamber	55
Figure 4.3 :	MOCVD growth regimes	56
Figure 4.4 :	Epitaxial growth modes	58
Figure 4.5 :	Bubblers in a (a) direct connection (b) double dilution configuration	60
Figure 4.6 :	A vertical flow MOCVD growth chamber	61
Figure 4.7 :	GaN growth process (a) Temperature (b) reflectivity curve	67
Figure 5.1 :	Nitride MOCVD-growth tool with dual injection block	72
Figure 5.2 :	Clausius-Clapeyron plot for $Gd(thd)_3$	73
Figure 5.3:	(a) & (b) Heater Jacket with thermocouple fabricated for the Gd source (c) Schematic of delivery system modification on delivery pipes	75
Figure 5.4 :	X-Ray Diffraction of (XRD) $Ga_{1-x}Gd_xN$ films with $Gd(thd)_3$	77
Figure 5.5 :	X-Ray Diffraction of (XRD) $Ga_{1-x}Gd_xN$ with $(Cp)_3Gd$	78
Figure 5.6 :	X-Ray Diffraction of (XRD) $Ga_{1-x}Gd_xN$ co-doped films	79
Figure 5.7 :	Photoluminescence (PL) of $Ga_{1-x}Gd_xN$ films (a) from 340 to 450nm, (b) from 450nm to 750nm	81

Figure 5.8 :	Vibrating Sample Magnetometry (VSM) of Ga <sub>1-x</sub> Gd <sub>x</sub> N films	82
Figure 5.9 :	SQUID results for Ga <sub>1-x</sub> Gd <sub>x</sub> N films	83
Figure 5.10 :	Vibrating Sample Magnetometry (VSM) Ga <sub>1-x</sub> Gd <sub>x</sub> N co-doped films	84
Figure 5.11:	Electron Paramagnetic Resonance (EPR) results of Ga <sub>1-x</sub> Gd <sub>x</sub> N films	85
Figure 5.12:	Resistivity results for Ga <sub>1-x</sub> Gd <sub>x</sub> N films grown with (a) 10Sccm (Cp) <sub>3</sub> Gd flow, (b) 160Sccm (Cp) <sub>3</sub> Gd flow, (c) 10Sccm (Cp) <sub>3</sub> Gd flow co-doped with Si 1x10 <sup>18</sup> cm <sup>-3</sup> , (d) 10Sccm (Cp) <sub>3</sub> Gd flow co-doped with Mg 1x10 <sup>20</sup> cm <sup>-3</sup>	87
Figure 5.13:	Alpha stopping power of Ga <sub>1-x</sub> Gd <sub>x</sub> N compared to GaN	90
Figure 5.14:	Neutron cross section of Gd	91
Figure 5.15:	Neutron scintillation signature of Ga <sub>1-x</sub> Gd <sub>x</sub> N compared to GaN	92
Figure 6.1 :	Typical GaN LED structure	99
Figure 6.2 :	Typical spin LED structure	100
Figure 6.3 :	Density of occupied states for spin-up and spin-down electrons	101
Figure 6.4 :	Calculated spin mean free path in GaN	106
Figure 6.5 :	Spin life time vs temperature for GaN and GaAS	106
Figure 6.6 :	The LED structure fabricated (a) GaN LED (b) Ga <sub>1-x</sub> Gd <sub>x</sub> N spin LED	110
Figure 6.7 :	(a) XRD of Ga <sub>1-x</sub> Gd <sub>x</sub> N LED (b) XRD of standard GaN LED	113
Figure 6.8 :	I-V curves for a standard GaN LED and Ga <sub>1-x</sub> Gd <sub>x</sub> N spin LED	114
Figure 6.9 :	Setup used for functional testing of Ga <sub>1-x</sub> Gd <sub>x</sub> N spin LED	115

Figure 6.10:	Circularly polarized light measurements for Ga <sub>1-x</sub> Gd <sub>x</sub> N spin LED	116
Figure 6.11:	Circularly polarized light measurements for baseline GaN LED	117
Figure 6.12:	Circularly polarized light measurements for Ga <sub>1-x</sub> Gd <sub>x</sub> N spin LED under external magnetic field	118
Figure 6.13:	Spin polarization values at different magnetic fields for Ga <sub>1-x</sub> Gd <sub>x</sub> N spin LED	119
Figure 6.14:	Spin polarization behavior of Ga <sub>1-x</sub> Gd <sub>x</sub> N spin LED under external magnetic field	120
Figure 8.1 :	Updated liquid delivery MOCVD system	130
Figure 8.2 :	Room temperature VSM results for ZnO:N	131
Figure 8.3 :	(a) ZnO:N XRD plot (b) ZnO (002) XRD peak position of plotted against NH <sub>3</sub> flow rate	132
Figure 8.4 :	SEM images of ZnO:N films grown with (a) 0.2% NH <sub>3</sub> flow, (b) 1.0% NH <sub>3</sub> flow, and (c) 4.0% NH <sub>3</sub> flow	133
Figure 8.5 :	Raman Spectroscopy for ZnO:N films grown with different NH <sub>3</sub> flow rates.	134
Figure 8.6 :	Low temperature PL spectra of ZnO:N	135
Figure 8.7 :	Couplings in multiferroic materials	136
Figure 8.8 :	BiFeO <sub>3</sub> structure showing the ferroelectric polarization (bold arrows) and AFM plane (shaded planes). (a) Polarization before electrical polling. (b) 180° (c)109° (d) 71° polarization switching by an external electrical field	137
Figure 8.9 :	FO XMCD from different angles	139
Figure 8.10:	Recipe for spin coating BFO thin films	144
Figure 8.11:	Room temperature ferromagnetism observed in BiFeO <sub>3</sub> films	144

Figure 8.12: BiFeO <sub>3</sub> layer on GaN substrate	145
Figure 8.13: XRD for MOCVD grown BFO	146
Figure 8.14: BFO transmission data (a) As grown (b) Annealed at 800°C	147
Figure A.1 : In-situ reflectrometry principle	150
Figure A.2 : X-ray Diffraction principle	153
Figure A.3 : Layout of a VSM measurement system	156
Figure A.4 : Schematic of a SQUID measurement system	157
Figure A.5 : Hall Effect measurement setup with an electric field applied in the x direction and the magnetic field applied perpendicular to it	160
Figure B.1 : A GaN LED (a) after fabrication (b) being tested on a probe station	169

## LIST OF SYMBOLS AND ABBREVIATIONS

$\sigma^-$	Left-polarized light
$\sigma^+$	Right-polarized light
AFM	Atomic Force Microscopy
AlN	Aluminum Nitride
CB	Conduction Band
CBM	Conduction Band Minimum
Cr	Chromium
DMS	Dilute Magnetic Semiconductors
EDS	Energy Dispersive X-ray Spectroscopy
EPR	Electron Paramagnetic Resonance
Eu	Europium
Fe	Iron
FM	Ferromagnetism
FWHM	Full Width Half Maximum
GaAs	Gallium Arsenide
GaN	Gallium Nitride
Gd	Gadolinium
HH	Heavy Hole
LDA	Local Density Approximation
LEDs	Light Emitting Diodes
LH	Light Hole
LT	Low Temperature

MBE	Molecular Beam Epitaxy
Mg	Magnesium
Mn	Manganese
MOCVD	Metal Organic Chemical Vapor Deposition
$n\uparrow$	Spin up states
$n\downarrow$	Spin down states
NN	Nearest Neighbor
NNN	Next Nearest Neighbor
PL	Photoluminescence
PLD	Pulsed Layer Deposition
$P_{\text{spin}}$	Spin polarization
QD	Quantum Dot
QW	Quantum Well
RE	Rare Earth
RKKY	Ruderman, Kittel, Kasuya, and Yoshida
RT	Room Temperature
SEM	Scanning Electron Microscope
Si	Silicon
SIMS	Secondary Ion Mass Spectrometer
SO	Spin Orbit
SQUID	Superconducting Quantum Interference Device
$T_c$	Curie Temperature
TM	Transition Metal
VB	Valence Band
VBM	Valence Band Maximum

VP	Vapor Pressure
VSM	Vibrating Sample Magnetometer
V-W	Volmer Weber
ZnO	Zinc Oxide
ZnSe	Zinc Selenide

## SUMMARY

This work targeted the growth of gadolinium (Gd)-doped gallium nitride (GaN) thin films ( $\text{Ga}_{1-x}\text{Gd}_x\text{N}$ ) by metal organic chemical vapor deposition (MOCVD). Characterization and evaluation of these  $\text{Ga}_{1-x}\text{Gd}_x\text{N}$  thin films for application in spintronics/optoelectronics devices also formed part of this work.

This work presents: (1) the first report of stable, reproducible n- and p-type  $\text{Ga}_{1-x}\text{Gd}_x\text{N}$  thin films by MOCVD; (2) the first  $\text{Ga}_{1-x}\text{Gd}_x\text{N}$  p-n diode structure; and (3) the first report of a room temperature spin-polarized LED using a  $\text{Ga}_{1-x}\text{Gd}_x\text{N}$  spin injection layer.

The  $\text{Ga}_{1-x}\text{Gd}_x\text{N}$  thin films grown in this work were electrically conductive, and co-doping them with Silicon (Si) or Magnesium (Mg) resulted in n-type and p-type materials, respectively. All the materials and structures grown in this work, including the  $\text{Ga}_{1-x}\text{Gd}_x\text{N}$ -based p-n diode and spin polarized LED, were characterized for their structural, optical, electrical and magnetic properties. The spin-polarized LED gave spin polarization ratio of 22% and systematic variation of this ratio at room temperature with external magnetic field was observed.

## CHAPTER 1: INTRODUCTION

The discovery of semiconductors has revolutionized the electronics industry, and currently semiconductor devices are pervasive in all walks of life. The miniaturization of devices with growing speed and functionality has been made possible by the ability to manipulate the electron charge in semiconductors with ever increasing precision. In 1965 Gordon E. Moore predicted with remarkable accuracy the doubling of transistor density every 18 months, resulting from the miniaturization of semiconductor technology. However, this miniaturization is also pushing currently used materials to their physical limits, threatening to violate and end the validity of Moore's Law.

The desire to build smaller, faster, cheaper electronics has prompted researchers to explore the use of the electron's "spin" - in addition to its charge - as a carrier of information, yielding a new field of study called "spintronics". The addition of the spin as a degree of freedom in charge-based electronic devices or the use of spin alone promises potential advantages to spintronic devices over conventional semiconductor devices, including non-volatility, increased data processing speed, decreased electric power consumption, and increased integration densities. Moreover, spintronic optoelectronic applications - for example, lasers and light-emitting diodes that take advantage of the spin of electrons for light polarization manipulation - could increase the data-carrying capacity of light.

Although spintronic devices such as magnetic random access memories (MRAM) and high-capacity hard drives are already commercially available, the full potential of

spintronics has yet to be realized. The major challenge has resulted from a lack of understanding of the relationship between the crystal structure and the material properties of the numerous new materials under investigation. The ability to successfully produce ferromagnetic semiconductors - i.e. semiconductors that experience a change in polarization/spin upon exposure to a magnetic field while below their Curie temperature - with Curie temperatures above room temperature remains a priority. Furthermore, it must be possible to manufacture economically viable materials using standard techniques that are scalable to industrial levels, such as metal organic chemical vapor deposition (MOCVD).

Gadolinium doped GaN thin films have been extensively grown by molecular beam epitaxy (MBE) and pulsed laser deposition (PLD). Room temperature ferromagnetism of varying magnitude in these films has been reported by a number of research groups. The report of a colossal magnetic moment in these films by Dhar in 2005 focused the research community's attention on the magnetic behavior of these films. However, no published report exists of use of these films in a practical device structure because of their high resistivity and the inability to form p-type material. Furthermore, there is still neither a consensus on the existence nor on the mechanism behind the observed colossal magnetism.

This research focuses on MOCVD growth of room temperature ferromagnetic gadolinium-doped gallium nitride ( $\text{Ga}_{1-x}\text{Gd}_x\text{N}$ ) thin films. The suitability of these thin films for spintronic and optoelectronic applications is demonstrated by integrating them into device structures and evaluating their performance as a function of their material properties. The achievements of this research include successful MOCVD growth of (1)

device-quality  $\text{Ga}_{1-x}\text{Gd}_x\text{N}$  conducting thin films on gallium nitride (GaN) templates, (2) n-type  $\text{Ga}_{1-x}\text{Gd}_x\text{N}$  films with Si co-doping, (3) p-type  $\text{Ga}_{1-x}\text{Gd}_x\text{N}$  films with Mg co-doping, (4) a p-n diode structure comprised of n-type Si co-doped  $\text{Ga}_{1-x}\text{Gd}_x\text{N}$  and p-type Mg co-doped  $\text{Ga}_{1-x}\text{Gd}_x\text{N}$ , (5) a spin-polarized GaN-based LED using  $\text{Ga}_{1-x}\text{Gd}_x\text{N}$  for spin injection, and (6) successful manipulation of spin polarized light emission by external magnetic field application.

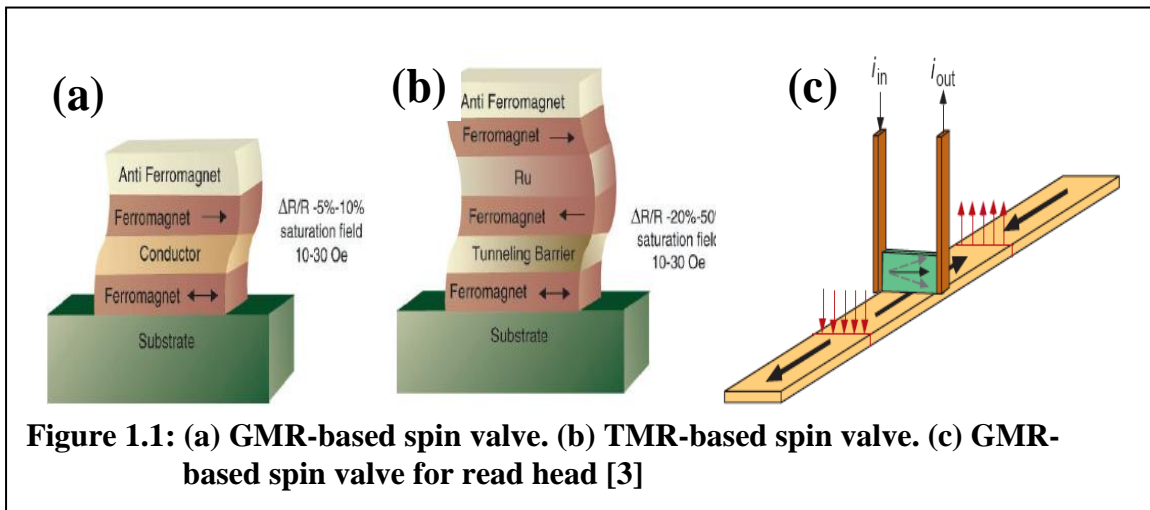
The first chapter of this dissertation introduces the field of spintronics and the possible candidate materials for application in this field. Chapter 2 give an overview of magnetism and dilute magnetic semiconductors. Chapter 3 describes the experiments conducted and the intricacies of the experimental setup used in this research. Chapter 4 presents the results of the experiments and a discussion of these results. Chapter 5 examines the magnetic behavior of  $\text{Ga}_{1-x}\text{Gd}_x\text{N}$  thin films. Chapter 6 discusses the spin-polarized LED fabricated in this research. Chapter 7 generates conclusions based on the performed research, lists the achievements, and suggests future direction for research in this material system. Chapter 8 reviews additional work performed during the course of this research, which includes: the construction of a new gas panel for the oxide MOCVD tool; the growth and characterization of zinc oxide (ZnO) thin films; and MOCVD growth and characterization of multiferroic bismuth ferrite thin films.

## **1.1 Spintronics**

Spintronics (spin transport electronics) exploits both the spin and the charge of electrons to generate devices with new functionality and increased performance. This offers opportunities for a new generation of devices combining standard microelectronics with spin-dependent effects that arise from the interaction between the spin of charge

carriers and the magnetic properties of the material. The potential advantages of these spintronic devices over current non-spintronic devices are new functionality, enhanced non-volatility, increased data processing speed, decreased electric power consumption, and decreased size [1-3].

Spintronics has already found successful application in magnetic read-heads, non-volatile memories, and sensors that take advantage of giant magneto-resistance (GMR) and tunnel magneto-resistance (TMR) effects (Figure 1.1). Nearly all modern hard disk drives incorporate a GMR-based read head, which has significantly increased their storage capacity [1]. The GMR technology has been introduced to other devices such as nonvolatile magnetic random access memory (MRAM) devices, which are now commercially available [2,3].



New functionalities for electronics and photonics can be derived if the injection, transfer, and detection of carrier spin can be controlled in materials above room temperature. This new class of devices includes spin transistors, spin LEDs, fast non-volatile semiconductor memory, and integrated magnetic/electronic/photonics devices.

Optoelectronic applications of spintronic materials exist in lasers and LEDs. The spin of electrons can affect the photons emitted from these devices: an electron with a certain spin can create a photon with a corresponding spin, resulting in polarized light. Polarization, the electric field orientation of light waves, could be exploited to add another layer of data to light used in telecommunications. Currently, information is encoded by adjusting the frequency and phase of light; polarization encoding could therefore increase the information capacity of optical lines.

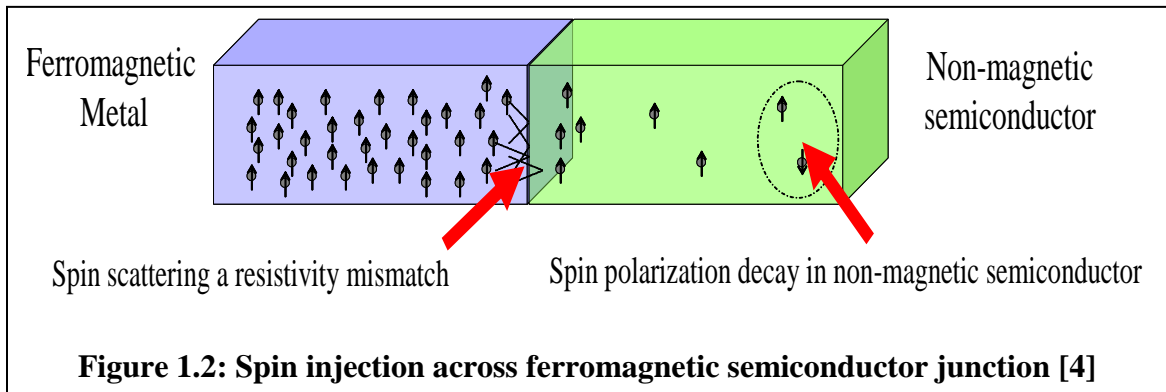
For all the reasons listed above, a growing effort is underway among researchers to find a way to make spintronics, the manipulation of electrons' "spin", practical. The major challenge is to find the right material to build practical devices and to be able to successfully grow the material using industry standard techniques.

## **1.2 Ferromagnetic Metals in Spintronics**

Most of the devices in spintronics made so far are based on metallic thin films. An example of such a device is the GMR-based disk drive read-head that uses ferromagnetic metallic films with metallic spacer layers. Another example is the TMR-based non-volatile random access memory that uses ferromagnetic metallic films with an insulating spacer layer for tunneling magneto-resistance. Ferromagnetic metals have several advantageous characteristics for device applications:

- The transition temperatures are above room temperature
- The magnetic anisotropy can be tuned by alloying

- The fabrication techniques are well established



However, the key challenge in this emerging field is the notorious incompatibility between magnetic and semiconductor materials necessary to fabricate spintronic devices. The very large resistance mismatch makes spin-injection difficult. When electrons travel across the barrier between the metal and the semiconductor, a large percentage of these electrons lose their original spin (Figure 1.2) [4]. Another problem is the spin decay in a non-magnetic semiconductor. The following sections provide a detailed examination of spin transport and the spin relaxation mechanism.

### 1.3 Dilute Magnetic Semiconductor

The most common approach to achieve ferromagnetic semiconductors is to introduce magnetic ions into otherwise non-magnetic semiconductors (Figure 1.3), forming a dilute magnetic semiconductor (DMS) [5, 6].

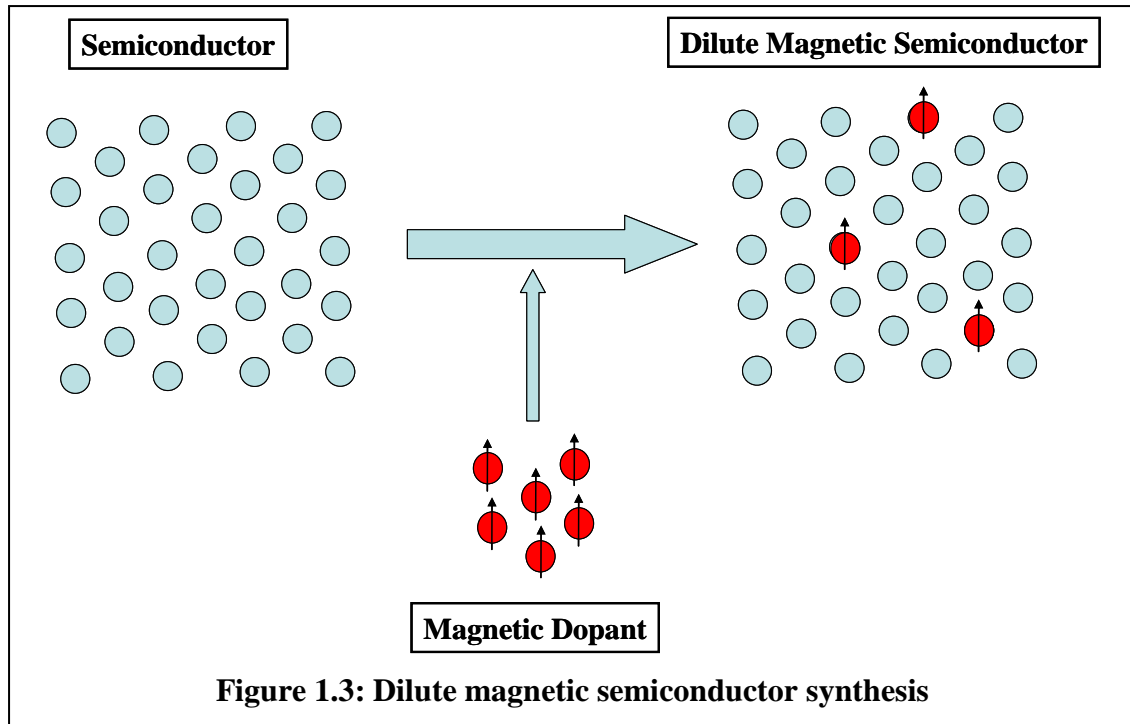


**Figure 1.3: Dilute magnetic semiconductor synthesis**

The study of DMS has mostly been focused on compound III-V and II-VI semiconductors. The magnetic dopants used in these DMS include transition metals (Mn, Fe, Ni, Co, etc.) and rare earth elements (Gd, Eu, Er, etc.).

When semiconductors are doped with magnetic ions, exchange mechanisms exist between the magnetic ion and the host semiconductor. These exchange interactions eventually determine the overall magnetic properties of the material. A detailed discussion of exchange mechanisms in a DMS is presented in Chapter 2

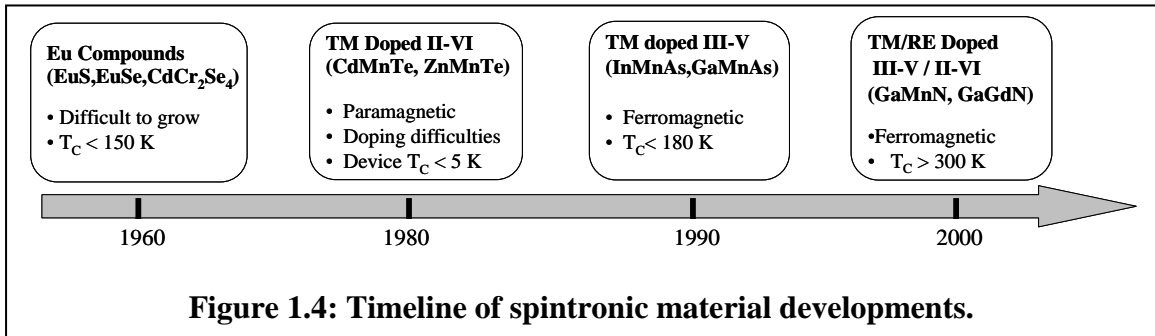
#### **1.4 History of Semiconductor Materials for Spintronics Applications**

Efforts to grow materials for spintronic applications began in the 1960's with europium-based (Eu) compounds. The concept of spin filtering was demonstrated by studying the spin polarization of the field emission from EuS-coated W tips. Exchange interactions cause energy splitting of the conduction band, resulting in the creation of different barrier heights for "spin up" and "spin down" electrons. However, due to the

low Curie temperature ( $T_c$ ) of 130°K -150°K and the difficulty in growing high quality thin films and heterostructures, these materials did not result in commercially viable devices [4, 7, 8].

In the 1980's, significant research was directed towards developing II-VI dilute magnetic semiconductors (DMS) such as CdMnTe and ZnMnS, but these films were found to be paramagnetic, antiferromagnetic, or exhibit spin-glass behavior [9, 10].

In the 1990's the research efforts shifted towards transition metal (TM) doping of III-V semiconductors, for example, InAs or GaAs, with GaMnAs emerging as the most studied DMS [5, 11]. Significant progress was made with the Arsenides, and spin-LEDs were fabricated. However this material system had a maximum  $T_c$  of 173K, making it impractical for commercial applications.



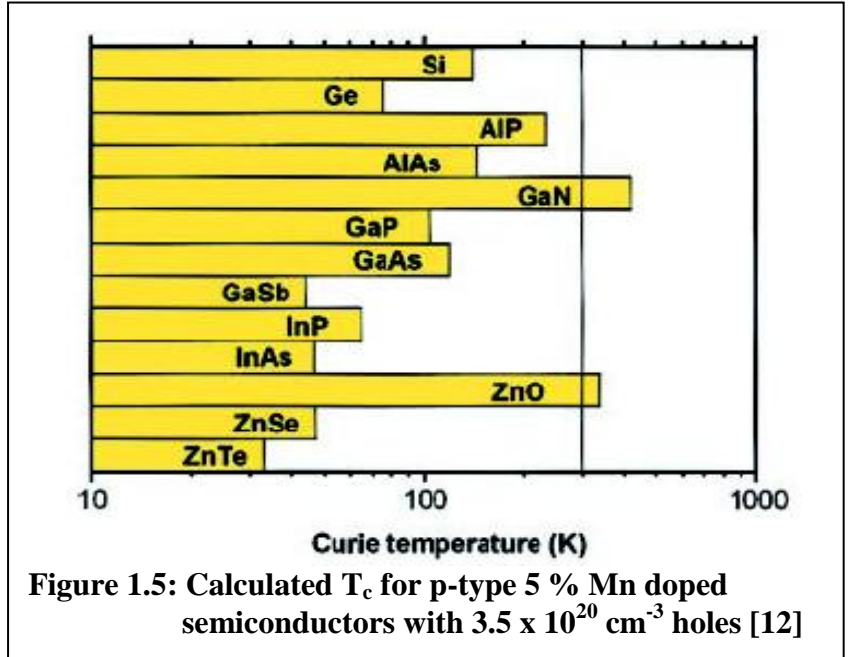
Recent research efforts are aimed towards the synthesis of DMS using the family of transition metals (TM), such as, Sc, Ti, V, Cr, Mn, Fe, Co, Ni and Cu, and rare earth metals (RE), for example, Sm, Eu, Gd, Tb, Dy, and Er, as the magnetic dopant in III-V and II-VI semiconductors. The TM and RE metals are incorporated so that they substitute an atom in the semiconductor's lattice [6, 12]. The unpaired spins of TM/RE metals interact with the host semiconductor through exchange mechanisms and make the

semiconductor magnetic [5, 6]. Figure 1.4 displays the progress of spintronic material development over the last 50 years [13].

In DMS materials, when TM (or RE) ions are substituted for the cations of the host, the resulting electronic structure is affected by the hybridization of the d(or f) orbital of the magnetic ion and the p(or s) orbital of the neighboring atoms.

### 1.5 Transition Metal Doped Dilute Magnetic Semiconductors

In 2000, theoretical studies by Dietl simulated the  $T_c$  for various p-type semiconductors doped with 5% Mn and a hole concentration of  $3.5 \times 10^{20} \text{ cm}^{-3}$  (Figure 1.5) [12]. His studies predicted that wide-bandgap semiconductors, such as GaN and ZnO, should have a  $T_c$  greater than room temperature (RT) due to their smaller lattice constants, allowing for greater p-d hybridization and reduced spin-orbit coupling.



Although ZnO was a promising candidate for spintronic devices, its integration into these devices has been stymied by difficulties in fabrication of high quality ZnO and p-

doping of ZnO [14]. GaN, on the other hand, has progressed at a phenomenal pace. Presently, a well-established technology base is in place for optoelectronic - primarily UV/blue LEDs and lasers - and electronic devices - such as high power FETs - into which the GaN-based DMS can be incorporated. First-principles calculations [15] indicate that Mn-, Cr-, and V-doped GaN can be ferromagnetic, though this behavior may be potentially attributed to precipitates and clusters observed within the crystal structure [16, 17].

Growth of (Ga,Mn)N thin films has been successfully performed by a variety of techniques including ion implantation [18], epitaxial growth [19–23] and diffusion of Mn ions into GaN templates [24]. Along with extensive studies of (Ga,Mn)N [25-28], multiple reports on doping with other transition metal ions in III-nitride materials exist. These include Mn-doped AlN [29], Cr-doped GaN [30, 31], Cr-doped AlN [30, 32], Co-doped GaN [33], Fe-doped GaN [34–39], Cu-implanted GaN [40], and V-doped GaN [33].

The electronic and magnetic properties of these films, however, are still hotly debated [41–44]. Generally, many of the reports indicated ferromagnetic behavior above RT, and this observation was attributed to the double exchange interaction, which involves hopping of electrons within the d-impurity-like band. However, there are studies [35–37, 45], which identify the likely presence of some other phases - due to the low solubility of magnetic ions - as being responsible for the observation of ferromagnetism.

In addition to the ambiguity of the underlying ferromagnetic mechanism(s), there are several practical limitations, which afflict TM-doped DMS. The most problematic of these is the highly resistive nature of TM-doped thin films [46, 47]. Other limitations

include the low solubility limit of TMs in III-V and II-VI materials and the formation of secondary phases. These problems have prevented major breakthroughs in optoelectronic and spintronic devices with the TM-doping approach.

GaN is of great interest as the basis for DMS due to the long spin lifetime caused by weak spin-orbit coupling. However, to date no unambiguous demonstration of spin-injection in a nitride-based spin-LED has surfaced in GaN [5]. Experiments conducted on wurtzite GaMnN/InGaN/AlGaIn spin-LEDs failed to detect spin polarization within the active region [48]. Similar results were found for wurtzite ZnMnO/ZnMgO/ZnO/AlGaIn/GaN spin-LEDs where the n-type ferromagnetic ZnMnO spin-aligner layer was grown by pulsed-laser deposition [49]. Furthermore, all the TM-doped films obtained, show that TM levels lie deep in the GaN bandgap and are insulating. These findings contradict the original model put forward by Dietl [50, 51].

Thus, the hunt for a ferromagnetic semiconductor that could be integrated with standard semiconductor technology still continues. Development of spin injectors with perpendicular magnetic anisotropy, low coercivities, and large spin-injection efficiencies is necessary for the commercial success of spintronic devices. There exists a need for a new class of materials that is easy to fabricate, is compatible with existing material growth and device technology, and, above all, is ferromagnetic at room temperature.

## **1.6 Rare Earth Doped Dilute Magnetic Semiconductors**

Rare earth (RE) elements have one or more half-filled 4f electron levels, which gives them larger magnetic moments compared to the magnetic moment given by 3d electrons in TMs. The 4f orbitals are localized, and direct coupling between the 4f ions is weak [52]. In order to create a DMS using RE elements, gadolinium (Gd:  $4f^7, 5d^1 6s^2$ ) is most

attractive, as it is the only RE ion that has both unfilled d and f orbitals, which can participate in magnetic coupling through intra-ion 4f-5d exchange interaction followed by inter-ion 5d-5d coupling mediated by charge carriers.

Teraguchi et al. [53] first reported MBE growth of  $\text{Ga}_{1-x}\text{Gd}_x\text{N}$  layers, and the material system drew a great deal of attention when Dhar et al. reported a very large ferromagnetic moment ( $\sim 4000 \mu_{\text{B}}/\text{atom}$  compared to the Gd atomic moment of  $8 \mu_{\text{B}}/\text{atom}$ ) [54]. Dhar attributed the giant magnetic moment to the long-range spin-polarization of the GaN matrix. The latter effect has been attributed to the strain field induced by the Gd atom, due to its much larger size compared to Ga [54].

Recently, RE-doping of GaN has attracted much attention, not only in the search for a RT ferromagnetic semiconductor, but also in the search for light-emitter applications, since emission extending from the infrared (IR) to the blue arising from sharp intra-f-shell optical transitions has been observed in RE-doped semiconductors [55]. Among the investigated systems are Gd-doped GaN and AlN [56–60], Eu-doped GaN [31, 61], Dy-doped GaN [62], Er-doped GaN [63, 64] and Er-implanted GaN [33].

Several theoretical analyses have been performed to determine the validity of the long-range polarization of the GaN lattice by the Gd atoms [65, 66]. These calculations show that the net spin exchange splitting in the valence band or conduction band for RE-doped GaN is smaller than that of TM-doped, as the f-s, f-p, and f-d couplings in GaN are weaker than those of the d-s, d-d, and d-p hybridization in  $\text{Ga}_{1-x}\text{TM}_x\text{N}$ . Thus, more Gd atoms enhance the magnetic coupling through the N atoms, and these N atoms are visibly polarized in the presence of Gd atoms, but this polarization is too small to result in the large magnetic moment of  $4000 \mu_{\text{B}}/\text{Gd atoms}$ .

Hite et. al. reported  $\text{Ga}_{1-x}\text{Gd}_x\text{N}$  films with Gd concentration of  $10^{17}$  atoms/cm<sup>3</sup> which showed RT ferromagnetism but were highly resistive. It was also shown that Si doping improved the film conductivity without affecting the magnetization [67]. Gd concentrations as high as 12.5 % have been obtained using MBE, which exhibited a magnetic moment of  $6.4 \mu_B/\text{Gd}$  atom. The saturation magnetization in  $\text{Ga}_{1-x}\text{Gd}_x\text{N}$  films were enhanced by Si doping, increasing from  $137 \text{ emu/cm}^3$  to  $1046 \text{ emu/cm}^3$  (for 8.9% Gd incorporation) [68].

After Dhar's publication [54] many groups reported room temperature ferromagnetism in Gd-doped GaN films. However none were able to reach the ferromagnetic moment of  $4000 \mu_B/\text{Gd}$  atom [69-73]. Furthermore, there is still no consensus regarding the underlying mechanism. Some of the proposed mechanisms by different groups include:

- Ruderman-Kittel-Kasuya-Yoshida (RKKY)-type interaction via the spin-polarized valence band of GaN [69]
- Long range spin-polarization of the GaN matrix by Gd atoms [70]
- Electron coupling between Gd f and host s states provided by Si doping or defects (nitrogen vacancies) [71].

## **1.7 Light Emitting Diode**

The semiconductor light-emitting diode (LED) has penetrated a large segment of the lighting market. Today's households have numerous LEDs that are used in television back-lighting, for transmitting signals to electronic equipment from remote controls, and as indicators in a multitude of devices. White LEDs are beginning to be used for general-

purpose illumination. Increasingly, cars are equipped with LED turn indicators and brake lights. But perhaps the most crucial contribution of LED technology is the birth of high-speed digital communication across greater distances via modulated optical signals in fiber optic cables, serving the ever-growing demand for broadband telecommunication and the internet.

### **1.8 Spin Polarized Light Emitting Diode**

In a spin-polarized LED spin-polarized electrons (or holes) are injected into an active region where they recombine radiatively with unpolarized holes (or electrons) to emit preferentially right- or left-circularly polarized light. If control over the optical polarization of LED emission is achieved under reasonable operating conditions, it will translate into optical communication systems with enhanced bandwidth and security. The application areas of such devices include: cryptography, reconfigurable optical interconnects, and advanced optical switches / modulators [74]. Chapter 6 is dedicated to the discussion of a spin-polarized LED.

### **1.9 Summary**

The most promising candidates for the development of future spintronic devices are dilute magnetic semiconductors (DMS). The most studied materials for fabrication of a DMS are semiconductors doped with partially filled 3d transition metals (TMs). However, the formation of precipitates or compensation by n-type carriers intrinsic to these wide band-gap semiconductors impedes utilization of the high  $T_c$  property of the 3d TM-doped nitrides and oxides. GaN doped with rare-earth (RE) gadolinium ions ( $\text{Ga}_{1-x}\text{Gd}_x\text{N}$ ) with

partially filled 4f is an alternative DMS material. Ferromagnetism has already been observed in  $\text{Ga}_{1-x}\text{Gd}_x\text{N}$  with a Curie temperature larger than 400 K [54].

## CHAPTER 2: MAGNETISM IN DILUTE MAGNETIC SEMICONDUCTORS

### 2.1 Introduction

This chapter illuminates the basic concepts of magnetism, including the origin of magnetism, its various types, and the mechanisms contributing to it. A brief discussion of magnetic exchange mechanisms that may exist in a DMS is also presented here.

### 2.2 Origin of Magnetism

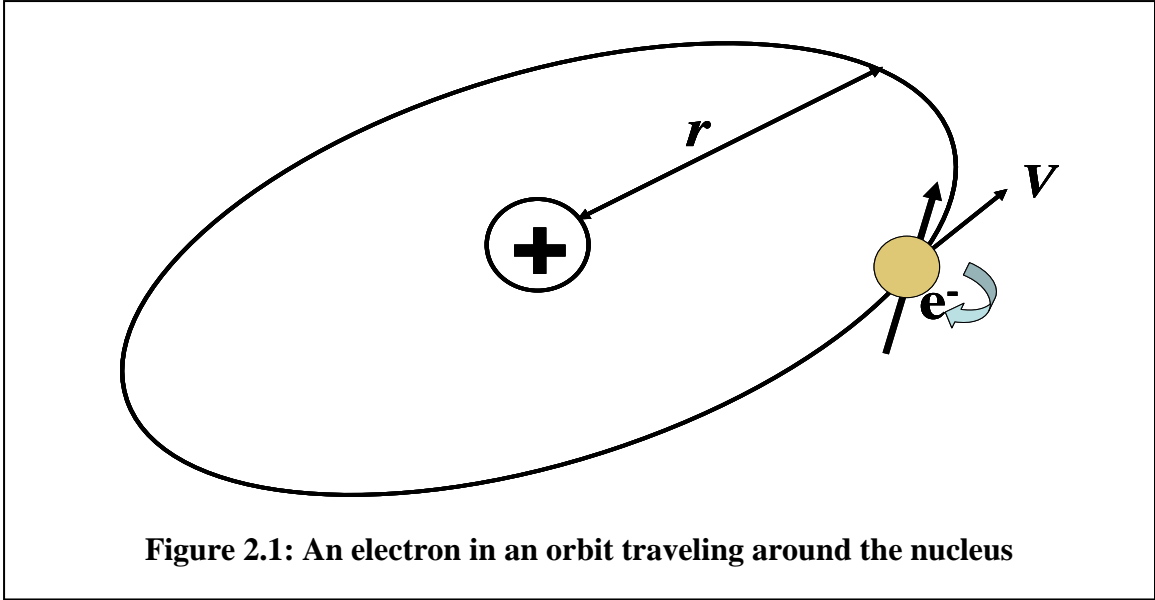
The magnetic fields in atoms are produced by the movement of electrons (Figure 2.1). Magnetic moments primarily result from three sources: the spin of electrons; the orbital angular momentum of electrons about the nucleus; and the change in the orbital moment induced by an applied magnetic field. The current due to motion of an electron is given by

$$\mathbf{I} = e/\tau , \quad \text{Equation (2.1)}$$

where  $e$  is the charge of an electron (  $1.6 \times 10^{-19} \text{C}$  ), and  $\tau$  is the travel time of electron around the nucleus is given by

$$\tau = 2\pi r/V \quad \text{Equation (2.2)}$$

where  $r$  is the radius and  $V$  is the velocity.



The strength of the generated magnetic field is known as magnetic moment  $\mu$ . Magnetic moments are associated with both the spin  $s$  and orbital angular momentum of electrons  $\mathbf{I}$ . The magnetic moment of an electron is given by:

$$\mu = \pi \times r^2 I = \frac{-e\hbar}{2m_e} = \mu_B \quad \text{Equation (2.3)}$$

In the equation above  $\mu_B$  is the magnetic moment of an individual electron and is known as the Bohr Magneton given by Equation 2.4.

$$\mu_B = \frac{eh}{2\pi m_e} \quad \text{Equation (2.4)}$$

where  $e$ : is the charge of the electron;

$h$ : Planck constant;

$m_e$ : mass of an electron.

Magnetism is a quantum mechanical phenomenon that depends on the spin and charge of the electrons. Thus the quantum numbers of the involved electrons play a central role. According to Pauli's exclusion principle no two electrons in an atom can have the same set of quantum numbers. The manner in which the electrons fill an orbital is given by Hund's rule. It states that before any two electrons occupy an orbital in a subshell, other orbitals in the same subshell must first each contain one electron. So when electrons start filling a subshell they will initially have parallel spins before it fills up with the opposite spin electrons. So the net magnetic moment of a completely filled electron shell will be zero, and that of partially filled orbitals will not be zero.

In solids the electron orbitals are fixed in the crystal lattice, and cannot change orientation when a magnetic field is applied. This phenomenon is called the quenching of the orbital moment. So practically the entire magnetic moment in solids is due to the spin of electrons. In the case of rare earth elements, the outer electrons effectively shield the electrons in the partially filled 4f orbital, and therefore the orbital moment is not quenched. [75]

An external magnetic field induces lines of magnetic flux inside a material. The number of flux lines per unit area is called the flux density or inductance  $B$ .

$$\mathbf{B} = \mu_0 \mathbf{H} [\text{Tesla (wb/m}^2) = 10^4 \text{ Gauss (Volts sec/ cm}^2) ] \quad \text{Equation (2.5)}$$

When a material is placed in a magnetic field ( $\mathbf{H}$ ), the net magnetic moment per unit volume of the material is defined as the magnetization ( $\mathbf{M}$ ). Inside a magnetic material, the relationship between  $\mathbf{B}$  and  $\mathbf{H}$  due to the magnetization is given by the following equation:

$$\mathbf{B} = \mu_0 (\mathbf{H} + \mathbf{M}) \quad \text{Equation (2.6)}$$

The magnetic susceptibility ( $\chi$ ) is the ratio between the magnetization and the applied magnetic field, which is the degree of magnetization induced in a material per unit of applied magnetic field.

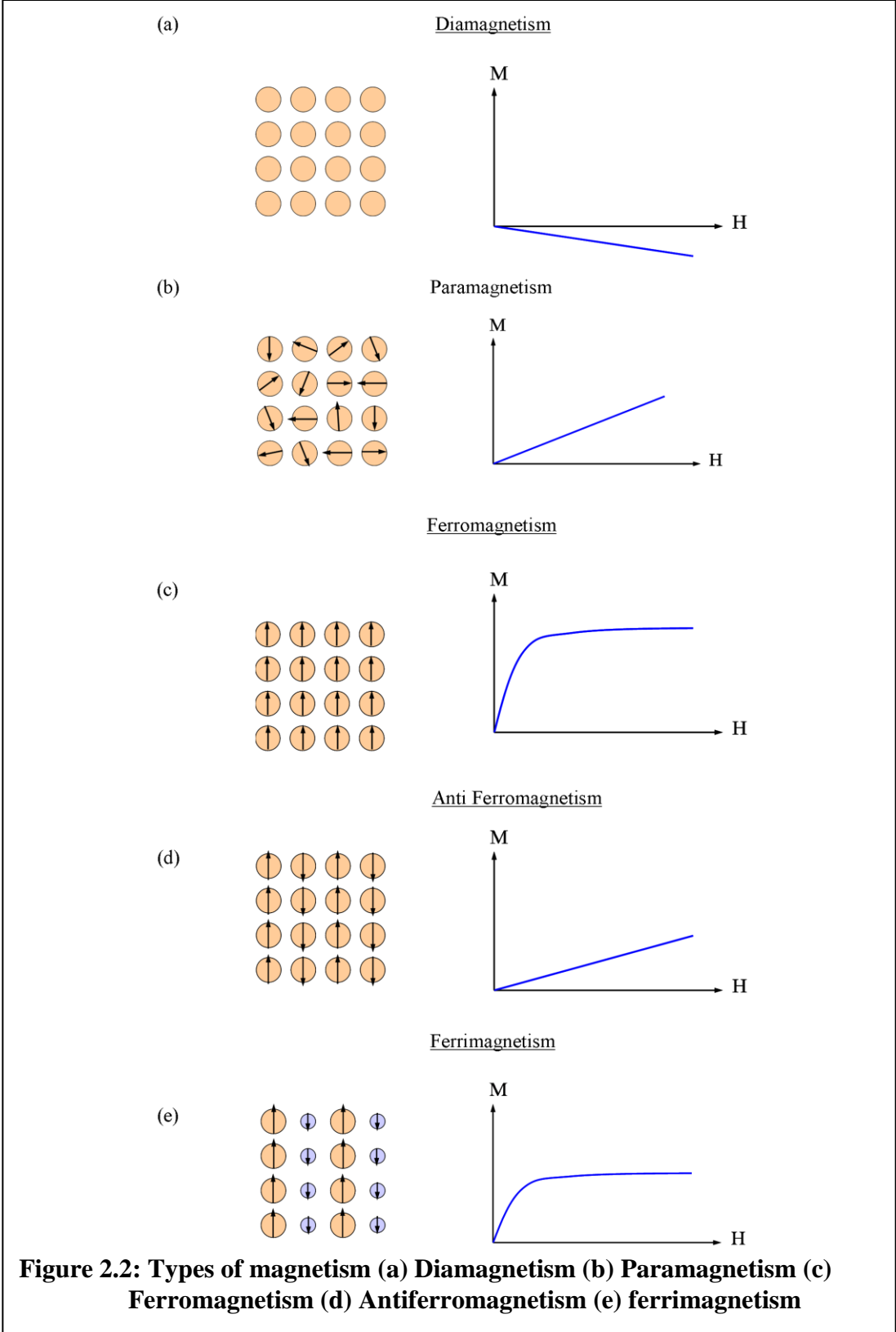
$$\chi = \frac{M}{H} \quad \text{Equation (2.7)}$$

### 2.3 Types of Magnetism

Materials are divided into different classes of magnetism depending on how the atoms interact collectively [75]. These classes are depicted schematically in Figure 2.2 and their explanation is given in the following subsections.

#### 2.3.1 *Diamagnetism*

In this class of materials the magnetic response is in the opposite direction to the applied magnetic field. Such materials have a negative magnetic susceptibility, no unpaired electrons, and therefore no net internal magnetic moment. The diamagnetic signal is independent of temperature and is seen as a line with a negative slope in magnetization (M) vs. magnetic field (H) plots (Figure 2.2a).



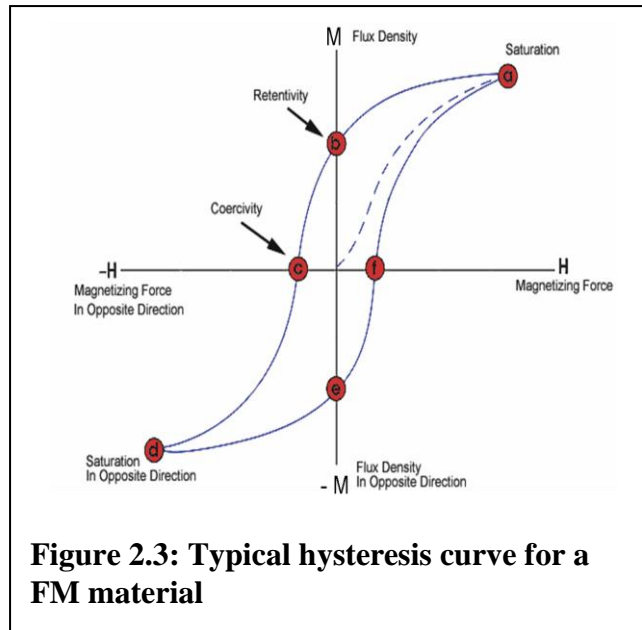
### **2.3.2 Paramagnetism**

Paramagnetism generally occurs in atoms or molecules with an odd number of electrons, giving rise to a net spin in the electrons. In isolation all the spins are randomly aligned giving zero net magnetization. However, in the presence of an external magnetic field the spins align with the direction of the magnetic field, resulting in a net magnetic moment in the direction of the applied field. The  $M$  vs.  $H$  plot is a straight line with a positive slope (Figure 2.2b). Increased temperature increases thermal agitations, prevents domain alignment, and thus decreases the magnetization.

### **2.3.3 Ferromagnetism**

Ferromagnetic materials have unpaired electrons and therefore have a net magnetic moment. When an external field is applied, the electron spins align themselves to the applied magnetic field with the same polarity. These spins remain aligned even after the magnetic field is removed (Figure 2.2c). The alignment is retained - despite the effect of  $kT$  - by the electron spins interacting with one another through an energetically favorable exchange mechanism.

Most ferromagnetic materials contain magnetic domains comprising atoms aligned in the same direction. The magnetic moment lies along a specific crystalline zone axis, referred to as the easy axis, which is the result of coupling between the electron spin and the angular momentum of the orbit. When the direction of the applied magnetic field is not along the easy axis, the applied magnetic field has to overcome the energy barrier known as magneto-crystalline anisotropy ( $E_A$ ). Figure 2.3 shows a typical hysteresis curve for a ferromagnetic material.



Ferromagnetism is strongly temperature dependent, and the magnetization of a ferromagnetic material is inversely related to temperature. The maximum temperature at which a ferromagnetic material retains its magnetization is known as the Curie temperature ( $T_c$ ). At temperatures greater than  $T_c$ , the spins become random due to thermal energy and the material becomes paramagnetic.

#### 2.3.4 Antiferromagnetism

The materials in this class have mixed parallel and antiparallel magnetic moments that cancel each other out, resulting in a zero net magnetization (Figure 2.2d). Antiferromagnetism (AFM) is normally seen in transition metal oxides such as NiO and CoO. The temperature above which antiferromagnetic order ceases to exist is called the Néel temperature ( $T_N$ ). Above  $T_N$ , antiferromagnetic materials behave like ferromagnets and their susceptibility exhibits Curie-Weiss behavior but with a negative intercept during negative exchange interactions.

### ***2.3.5 Ferrimagnetism***

This type of magnetism is similar to ferromagnetism and is seen in ferrites and garnets. In this type of magnetism the interaction between nearest neighbors is antiferromagnetic. However these materials have unequal magnetic moments, and, hence, a resultant net magnetic signal is obtained (Figure 2.2e). Such materials generally consist of two different elements or ions (such as  $\text{Fe}^{2+}$  and  $\text{Fe}^{3+}$ ) and their ferromagnetic sublattices have unequal magnetic moment. This type of magnetism is usually mediated by superexchange or indirect exchange interactions (described later). Ferrimagnetism is therefore similar to ferromagnetism and exhibits all the characteristics of ferromagnetic behavior: spontaneous magnetization, Curie temperatures, hysteresis, and remanence.

### ***2.3.6 Superparamagnetism***

Superparamagnetism occurs in materials that are composed of small crystallites, analogous to nanoparticles ranging from 1-10 nm in size, that are so small that they can randomly flip direction due to thermal fluctuations. As a result the material typically is not magnetic, except under the influence of an externally applied magnetic field, and thus behaves similarly to a paramagnetic material. In these materials the magnetic moment of the entire crystallite tends to align itself with the magnetic field. The temperature at which the magnetic anisotropy of small particles is overcome by the thermal activation energy is known as the blocking temperature ( $T_B$ ). At  $T < T_B$ , the moments of some of the particles are blocked: they do not possess sufficient magnetic energy to overcome the energy barriers in the timescale of the experiment. For  $T > T_B$ , the thermal energy is high enough to overcome the coupling forces and randomizes the spins, and, hence, the

magnetic signal wanes. Since there is no longer any magnetic order, the internal magnetic field no longer exists, and the material exhibits paramagnetic behavior.

## **2.4 Dilute Magnetic Semiconductor Exchange Mechanisms**

When semiconductors are doped with magnetic ions, exchange mechanisms exist between the magnetic ion and the host semiconductor. These exchange interactions eventually determine the overall magnetic properties of the material. Exchange mechanisms can be divided into two main categories, direct and indirect. These interactions are described in the following subsection.

### ***2.4.1 Direct Exchange***

Direct exchange interaction occurs between neighboring magnetic atoms that have overlapping wave functions. The exchange interaction ( $J$ ) between these atoms arises from the Coulombic interaction between electrons. Electrons with parallel spins are kept apart due to Pauli's exclusion principle, which leads to a decrease in Coulombic repulsion. Thus, there is a difference in the exchange energy between parallel and antiparallel couplings of the exchange energy. If  $J$  is positive, the spins are parallel and point in the same direction. However, if the exchange interaction is negative, the spins are antiparallel. Except in the case of magnetic atom clustering in the material, the magnetic orbitals of the atoms do not possess sufficient overlap to develop ferromagnetism through direct exchange. In a typical homogeneously-doped dilute magnetic semiconductor material, indirect exchange mechanisms play a major role in shaping the magnetic properties.

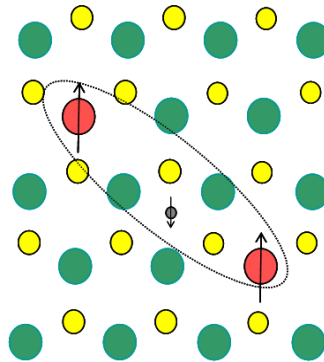
## 2.4.2 Indirect Exchange

Several indirect exchange mechanisms have been proposed to explain magnetism in TM- and RE-doped semiconductors. The three classical indirect exchange mechanisms are RKKY, Double exchange, and Superexchange. In recent years, based on the observations of ferromagnetism in II-VI and III-V DMS, several other indirect exchange mechanisms have been proposed. The following sections discuss the classical indirect exchange models.

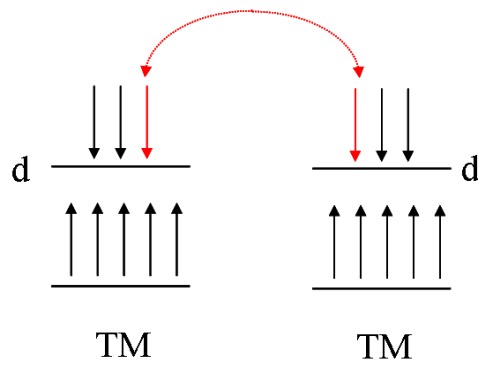
### 2.4.2.1 Carrier Mediated Exchange (RKKY)

This type of exchange mechanism is also known as RKKY after its discoverers: Ruderman, Kittel, Kasuya, and Yoshida [76-78]. This mechanism permits the coupling of magnetic moments through Coulomb exchanges via band electrons over relatively large distances. This theory was originally formulated to explain ferromagnetism in metals and is an efficient mechanism when a high concentration of free carriers are present (Figure 2.4a). The original RKKY studies showed that the spin polarization sign of the conduction electrons oscillates (Friedel oscillations) as a function of the distance from localized moments. The coupling may be ferromagnetic or antiferromagnetic depending on the separation of the interacting atoms. This mechanism has been used to explain the ferromagnetic mechanism for 4f electrons which are localized. In 4f metals, there is an indirect exchange mechanism between the outer 5d electrons, which partially overlap the 4f shell. This exchange mechanism was found to be responsible for ferromagnetism in  $\text{Ga}_x\text{Mn}_{1-x}\text{As}$  [79, 80].

(a) RKKY- Carrier-Mediated Exchange



(b) Double Exchange



(c) Superexchange

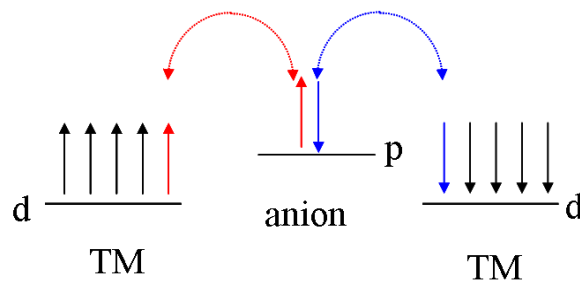


**Figure 2.4: Indirect exchange mechanisms: (a) carrier mediated, (b) double exchange, (c) superexchange**

#### 2.4.2.2 *Double Exchange*

This mechanism involves the coupling of magnetic ions in different charge states as a result of electron hopping between ions through interaction with the p-orbital (Figure 2.4b) [81]. Spin flips are forbidden in this model, and, if both the ions have a similar magnetic structure, the double exchange mechanism is energetically favorable. This model explains magnetism in spinel magnetite, manganites, and Mn-perovskites. It has also been used to describe the ferromagnetism in  $\text{In}_{1-x}\text{Mn}_x\text{As}$  [82].

#### 2.4.2.3 *Super Exchange*

Superexchange is the coupling of nearest neighbor transition metals through a shared anion (Figure 2.4c). This mechanism was first propounded by Kramers in 1934 and then developed in detail by Anderson in 1950 [83, 84]. It results from the virtual hopping of carriers between the completely filled p-orbitals of anions and the d orbitals of the magnetic cations. Pauli's exclusion principle dictates that electrons from two adjacent cations must possess opposite spin to occupy the same p-orbital of a sandwiched anion. This leads to antiferromagnetic coupling of nearest-neighbor cations through a shared anion. In nitrides the superexchange mechanism is an order of magnitude less effective than in the oxide-based materials [85].

### 2.5 **Summary**

An overview of the magnetism in materials was presented in this chapter. The focus of the discussion was the origin and various types of magnetism that are present in solids. Since this dissertation targets semiconductor magnetic thin films, a discussion of various exchange mechanisms that can exist therein was also included. The concepts laid down in

this chapter will form an essential part of the experimental work and analysis performed in this dissertation.

## CHAPTER 3: BACKGROUND: GADOLINIUM DOPED GaN

### 3.1 Introduction

GaN, with its wide direct bandgap, strong bonding, chemical stability, radiation hardness, high thermal conductivity, mature growth techniques, and, application in optoelectronic devices including LEDs and LDs, is regarded as one of the most promising semiconductors. The dilute magnetic semiconductor (DMS) based on GaN has been the focus of extensive research because of its potential applications in spintronic devices.

The existence of local magnetic moments in solids has traditionally been associated with elements containing partially filled 3d or 4f subshells. This is a result of the strongly localized nature of the 3d and 4f states that when coupled with their high degree of degeneracy that favors spin-polarized electron configurations, leads to the formation of local moments. The collective coupling of these local moments renders the material magnetic and defines type of magnetism.

Semiconductors doped with TMs with partially filled 3d shells have been the most widely studied candidate material for the development of a room temperature DMS. Their hole-mediated ferromagnetic feature at room temperature [12] and high  $T_c$  are well recognized. However, formation of precipitates [70] or compensation by intrinsic n-type carriers makes them unsuitable for device applications.

GaN-doped by RE atoms with a partially filled 4f orbital has been proposed as a material free from the limitations of the TM-doped GaN and exhibits a high  $T_c$ . Ferromagnetism has already been reported in  $Ga_{1-x}Gd_xN$ , with  $T_c$  above 400 K by a

number of research groups [54-58]. The electronic and magnetic structures in the  $\text{Ga}_{1-x}\text{Gd}_x\text{N}$  material system are intriguing and are still not well understood.

Several studies have been performed with the goal of developing ferromagnetic  $\text{Ga}_{1-x}\text{Gd}_x\text{N}$  using ion implantation, molecular beam epitaxy (MBE), and pulsed laser deposition (PLD). This chapter summarizes the state of the art in  $\text{Ga}_{1-x}\text{Gd}_x\text{N}$  growth and characterization.

### **3.2 Properties of Wurtzite GaN**

The MOCVD grown GaN in this work has a wurtzite crystal structure. This structure is tetrahedrally coordinated with each atomic site having four nearest neighbors. The wurtzite structure has a  $P6_3mc$  space group. The Bravais lattice of the wurtzite structure is hexagonal and the axis perpendicular to the hexagons is the c-axis [86]. The epitaxial growth direction for GaN in MOCVD is (0001). The resulting wurtzite structure consists of alternating Ga and N pairs stacked in an ABABAB sequence [87]. GaN like other III-Nitrides lack an inversion plane perpendicular to the c-axis, and hence the crystals surfaces have either a Ga polarity (0001) or a N-polarity (000-1) (Figure 3.1). The non-centrosymmetry of GaN causes it to be piezoelectric and undergo spontaneous polarization. This results in band bending of the quantum well (QW) structures grown in this material system. The material properties of GaN are summarized in Table 3.1.

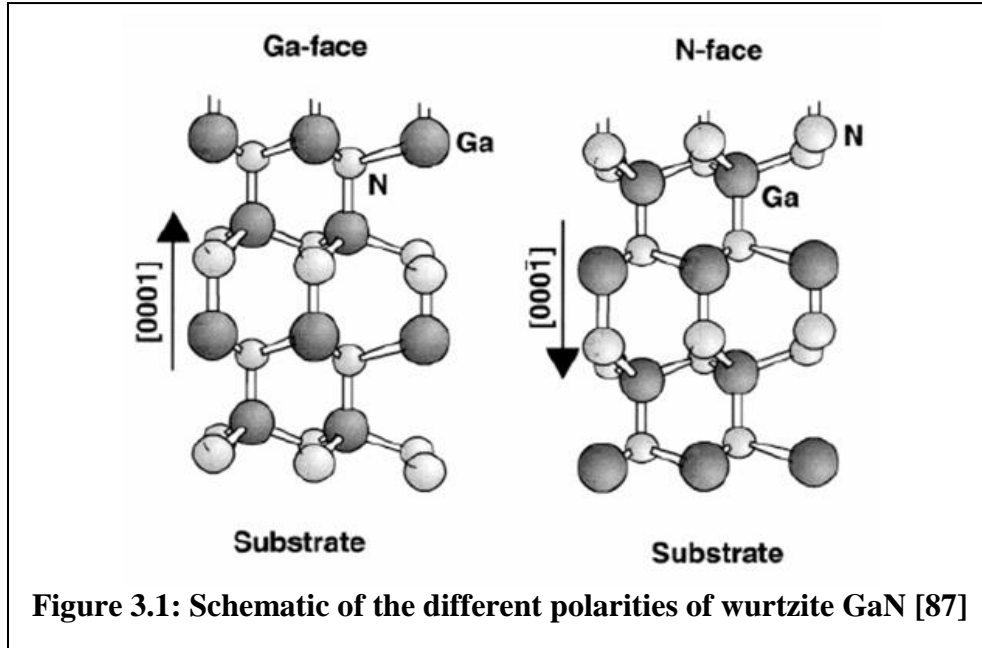


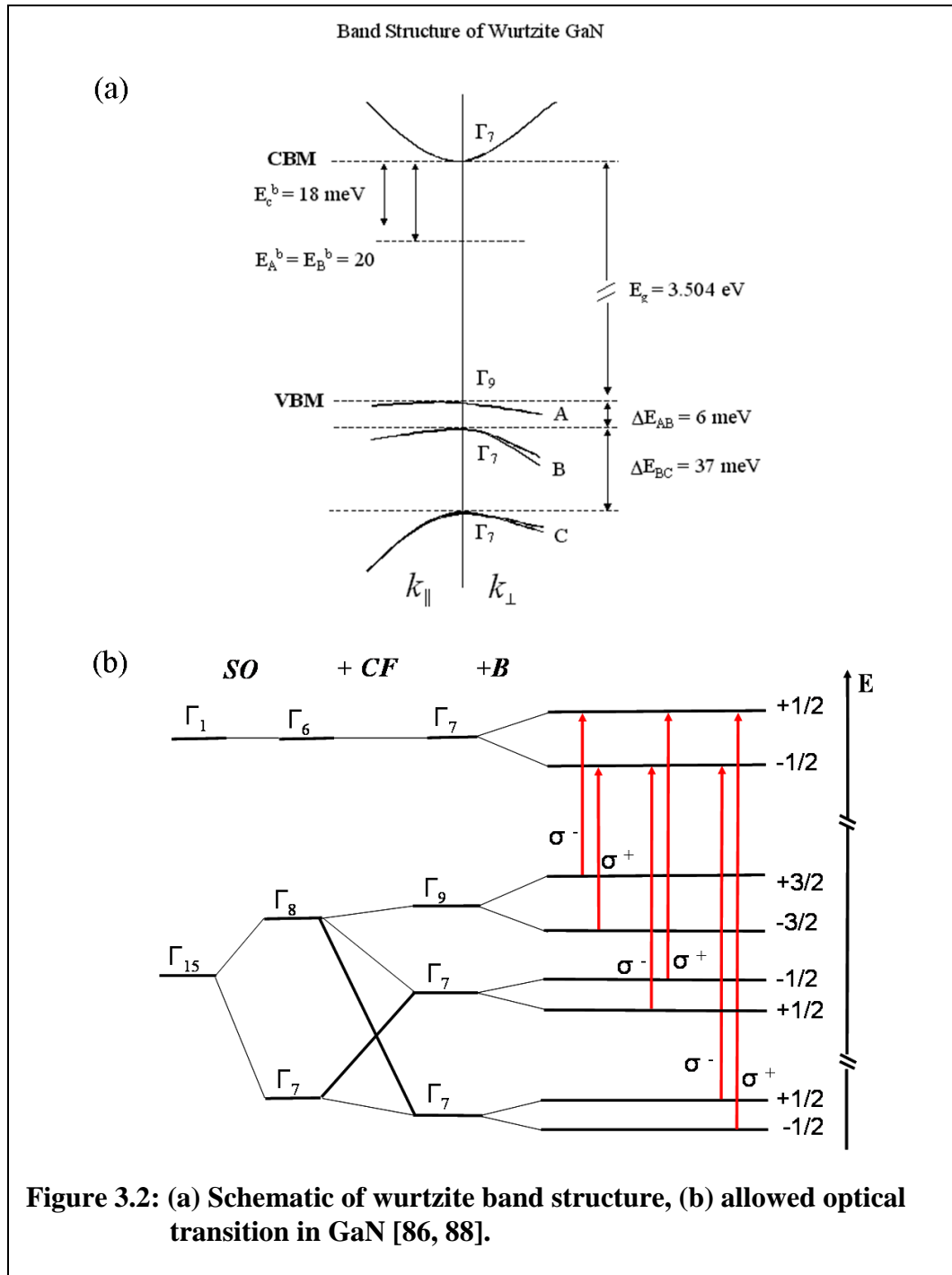
**Table 3.1: Material properties of wurtzite GaN [86]**

Property	Value
Band-gap energy (300K)	3.39 eV
Lattice constant, $a$	3.189 Å
Lattice constant, $c$	5.185 Å
Thermal expansion ( $\Delta a/a$ )	$5.59 \cdot 10^{-6}/\text{K}$
Thermal expansion ( $\Delta c/c$ )	$3.17 \cdot 10^{-6}/\text{K}$
Thermal conductivity ( $\kappa$ )	1.3 W/cm.K
Index of refraction ( $n$ )	2.33
Static dielectric constant ( $\epsilon_0$ )	8.9
High- $\omega$ dielectric constant ( $\epsilon_\infty$ )	5.35
Density ( $\rho$ )	6.15 g/cm
Electron effective mass ( $m_e$ )	$0.20m_0$
Melting temperature	$>2000 \text{ }^\circ\text{C}$

### 3.3 Band Structure and Allowed Optical Transitions in GaN

Wurtzite GaN is a direct bandgap semiconductor with its conduction band minima and valence band maxima centered at  $\Gamma$  point  $K = 0$  as shown in Figure 3.2a. The

conduction band at  $\Gamma_7$  has an s-character, while the valence band split into three by the crystal field and spin orbital coupling has a p-character. The holes and excitons in split valence band are denoted as A ( $\Gamma_9$ ), B ( $\Gamma_7$ ), and C ( $\Gamma_7$ ) [86]. The A, B and C are designated as heavy hole, light hole, and crystal field splitting respectively. The allowed optical transitions in GaN are shown in Figure 3.2b. The influence of spin-orbit (SO), crystal-field (CF), and the magnetic-field (B) are shown in the Figure 3.2b from left to right [88]. The six degenerate valence band and two degenerate conduction band states in GaN can clearly be seen.



### 3.4 Properties of Gadolinium

Gadolinium is a rare earth (RE) element belonging to the lanthanide series in group III-A of the periodic table. The 14 lanthanide elements, from lanthanum (La) to lutetium

(Lu), all have outer  $6s^2$  electrons while the electronic configurations of their 4f and 5d shells differ as shown in Table 3.2. The properties of the lanthanides vary only slightly with the atomic number because the outer shells do not change within the group. RE metals have a high electrical conductivity, high melting and boiling points and share many common properties. With increasing atomic number the effective nuclear charge experienced by each 4f electron increases, causing a shrinking of the RE radii from Ce to Yb known as lanthanide contraction.

**Table 3.2: Electronic Configuration of rare earth elements [89]**

Z	Symbol	Name	4f	5d
57	La	Lanthanum	0	1
58	Ce	Cerium	2	2
59	Pr	Praseodymium	3	0
60	Nd	Neodymium	4	0
61	Pm	Promethium	5	0
62	Sm	Samarium	6	0
63	Eu	Europium	7	0
64	Gd	Gadolinium	7	1
65	Tb	Terbium	9	0
66	Dy	Dysprosium	10	0
67	Ho	Holmium	11	0
68	Er	Erbium	12	0
69	Tm	Thulium	13	0
70	Yb	Ytterbium	14	0
71	Lu	Lutetium	14	1

Gadolinium is a silvery-white malleable and ductile rare-earth metal. It crystallizes in hexagonal, close-packed  $\alpha$ - form at room temperature, but, when heated to temperatures above 1235 °C, it transforms into its  $\beta$ - form, which has a body-centered cubic structure. Properties of Gd are given in Table 3.3.

**Table 3.3: Material properties of wurtzite GaN [89]**

Property	Value
Density:	7.900 g/cm <sup>3</sup>
Melting Point :	1586K
Boiling Point :	3539K
Atomic Radius :	1.79 Å
Covalent Radius :	1.61 Å
Ionic Radius:	0.938 Å (+3e)
Specific Heat (@20°C):	0.230 J/g mol
Evaporation Heat :	398 kJ/mol
Pauling Negativity Number:	1.2
First Ionizing Energy:	594.2 kJ/mol
Electronic Configuration:	4f7 5d1 6s2
Lattice Structure:	Hexagonal
Lattice Constant :	3.640 Å
Lattice c/a Ratio:	1.588

Naturally occurring gadolinium is a mixture of 7 isotopes <sup>152</sup>Gd, <sup>154</sup>Gd, <sup>155</sup>Gd, <sup>156</sup>Gd, <sup>157</sup>Gd, <sup>158</sup>Gd and <sup>160</sup>Gd. The percentages of these isotopes are given in Table 3.4. <sup>157</sup>Gd has the highest thermal neutron capture cross-section among any stable nuclides at 259,000 barns [90].

**Table 3.4 Composition of naturally occurring Gd [90]**

Isotope	Percentage
<sup>152</sup> Gd	0.20%
<sup>154</sup> Gd	2.18%
<sup>155</sup> Gd	14.80%
<sup>156</sup> Gd	20.47%
<sup>157</sup> Gd	15.65%
<sup>158</sup> Gd	24.84%
<sup>160</sup> Gd	21.86%

### 3.5 Literature Review: Gd Doped GaN

Ferromagnetism in Gd-doped GaN was first reported by Teraguchi et. al. in 2002 [53]. Later Dhar et al. [54] reported a colossal magnetic moment ( $\sim 4000 \mu_B/\text{atom}$  compared to Gd atomic moment of  $8\mu_B/\text{atom}$ ) in a very lightly Gd-doped GaN system ( $10^{15} \text{ Gd}/\text{cm}^3$ ). Dhar attributed the giant magnetic moment reported to the long range spin-polarization of the GaN matrix caused by the strain field induced by the Gd atom, which is much larger than the Ga atom. Dhar et al.'s finding of colossal magnetic moment [54] still remains controversial with no conclusive explanation available. Later [58], they showed that the Gd-implanted GaN samples show even stronger magnetic effects. However, a post-implantation anneal was shown to reduce the effect [58]. This strongly links the magnetic behavior to a defect-related mechanism.

Theoretical analysis of the proposed long-range polarization of the GaN lattice model does show net spin exchange splitting in the valence band or conduction band for RE-doped GaN. However this splitting is even smaller than that of TM-doped GaN (coupling of 4f orbital is weaker than coupling of 3d orbital). N atoms are visibly polarized in the presence of Gd atoms, but this polarization is too small to result in the large magnetic moment of  $4000 \mu_B/\text{Gd atoms}$  [65, 66].

X-ray magnetic circular dichroism XMCD and EXAFS recently performed by Ney et. al. on Gd-doped GaN samples show that Gd on a Ga site contributes very little to the overall magnetization [91, 92]. Gd was seen not to follow the hysteresis curves of the overall magnetism measured by SQUID but instead behave paramagnetically. These tests point towards a defect induced magnetism model.

Dalpian et al. [93] by analyzing a ZB Gd-doped GaN argued that impurity states lying within the spin split conduction band would account for the extra magnetic moments in the system. They also found that Gd atoms interacted anti-ferromagnetically in their ZB Gd-doped GaN samples

Hite et. al. reported  $\text{Ga}_{1-x}\text{Gd}_x\text{N}$  films with Gd concentration of  $10^{17}$  atoms/cm<sup>3</sup> which showed RT ferromagnetism but were highly resistive. It was also shown that Si doping improved the film conductivity without affecting the magnetization [67]. They also showed that defects in the material caused by proton irradiation reduced the magnetism, however this effect was found to be reversible by annealing [67].

Hejtmanek et al. [58] confirmed weak ferromagnetism up to about 700K in Gd-implanted GaN samples but also found evidence for multiphase behavior at higher Gd concentrations to co-exist with paramagnetic behavior. Recently a paramagnetic and ferromagnetic resonance study was reported for Gd-doped during growth and Gd implanted GaN [60].

The research group of the Institute of Scientific and Industrial Research, in Osaka, Japan has been consistently publishing reports of Gd-doped GaN by MBE and PLD. They have recently reported Gd concentrations as high as 12.5 % in the Gd-doped GaN films. These films exhibited a magnetic moment of  $6.4 \mu_{\text{B}}/\text{Gd}$  atom. Si doping enhanced the saturation magnetization in  $\text{Ga}_{1-x}\text{Gd}_x\text{N}$  films and increased it from  $137\text{emu}/\text{cm}^3$  to  $1046\text{emu}/\text{cm}^3$  (for 8.9% Gd incorporation) [68]. The same group also reported Gd incorporation in InGaN films and successful growth of GaN/  $\text{Ga}_{1-x}\text{Gd}_x\text{N}$  heterostructures by plasma-enhanced PLD. The group, however, neither showed any magnetic data of the grown films, nor did they report fabrication of any device.

Chandrima et al. [94] concluded from their research that both N and oxygen octahedral interstitials are more likely to be responsible for defect-induced magnetism in Gd-doped GaN than are Ga vacancies. The argument they presented was that these interstitials form defect states in the bandgap similar to Ga vacancies, which support a magnetic moment of  $2-3\mu_B$ , and have sufficiently extended tails to experience relatively long-range ferromagnetic coupling with each other and as well as with Gd. Unlike Ga vacancies, however, they can support a neutral charge and magnetic state for mid-gap Fermi levels consistent with semi-insulating conditions because their defect levels occur at higher energies in the bandgap. They also have significantly lower energy of formation. Chandrima et al. also showed that it is favorable for Ni and oxygen to migrate toward Gd. However, their work fails to explain the colossal moments in the ultra-dilute limit since this would require a large number of such defects to form per Gd atom.

After Dhar's publication [54] many groups reported room temperature ferromagnetism in Gd-doped GaN films; however none were able to reach the ferromagnetic moment of  $4000 \mu_B/\text{Gd atom}$  [69-73]. Furthermore, there is still no consensus regarding the underlying mechanism.

The most recent theoretical models [95, 96] that have been proposed to explain ferromagnetism in Gd-doped GaN suggest that the magnetism arises from the presence of Ga vacancies. Liu et al. further found that introducing N vacancies, on the other hand, actually enhanced the anti-ferromagnetic interactions between the Gd atoms. This suggested that ferromagnetic interactions were more likely to occur in p-type GaN, whereas anti-ferromagnetism was more likely to occur in n-type GaN. Supporting this model Dev et al. [97] further showed that these Ga vacancies also helped in creating a

long-range ferromagnetic interaction between the Gd atoms. They described models with a large number of Ga vacancies and showed that they keep adding magnetic moment parallel to the Gd moment.

### **3.6 Proposed Models for Magnetic Moment in $\text{Ga}_{1-x}\text{Gd}_x\text{N}$**

A number of theoretical models have been proposed to explain the magnetic moment in a  $\text{Ga}_{1-x}\text{Gd}_x\text{N}$  material system. The most prominent of these are discussed in the subsequent sections.

#### ***3.6.1 Long-Range Spin Polarization***

Dhar et al's proposed long-range spin polarization of the GaN matrix by the Gd atom to explain the colossal magnetic moment observed in the  $\text{Ga}_{1-x}\text{Gd}_x\text{N}$  material system. The model suggests that the long range spin polarization of the GaN matrix is caused by the strain field induced by the Gd atom due to its larger atomic size [54]. Due to the large piezoelectric coefficient of GaN along the c axis, a strain field generates a potential dip around each Gd atom. These potential minima trap the carriers locally, and if there is spin spin splitting in the band structure, the localized carriers become spin polarized [60].

However recently, it has been shown that the magnetic moment rapidly attenuates with increasing distance from the Gd atom [94], and the magnetic moments are too small to explain a colossal value. Thus the 'long range spin polarization' model due to Gd seems questionable.

#### ***3.6.2 Impurity States***

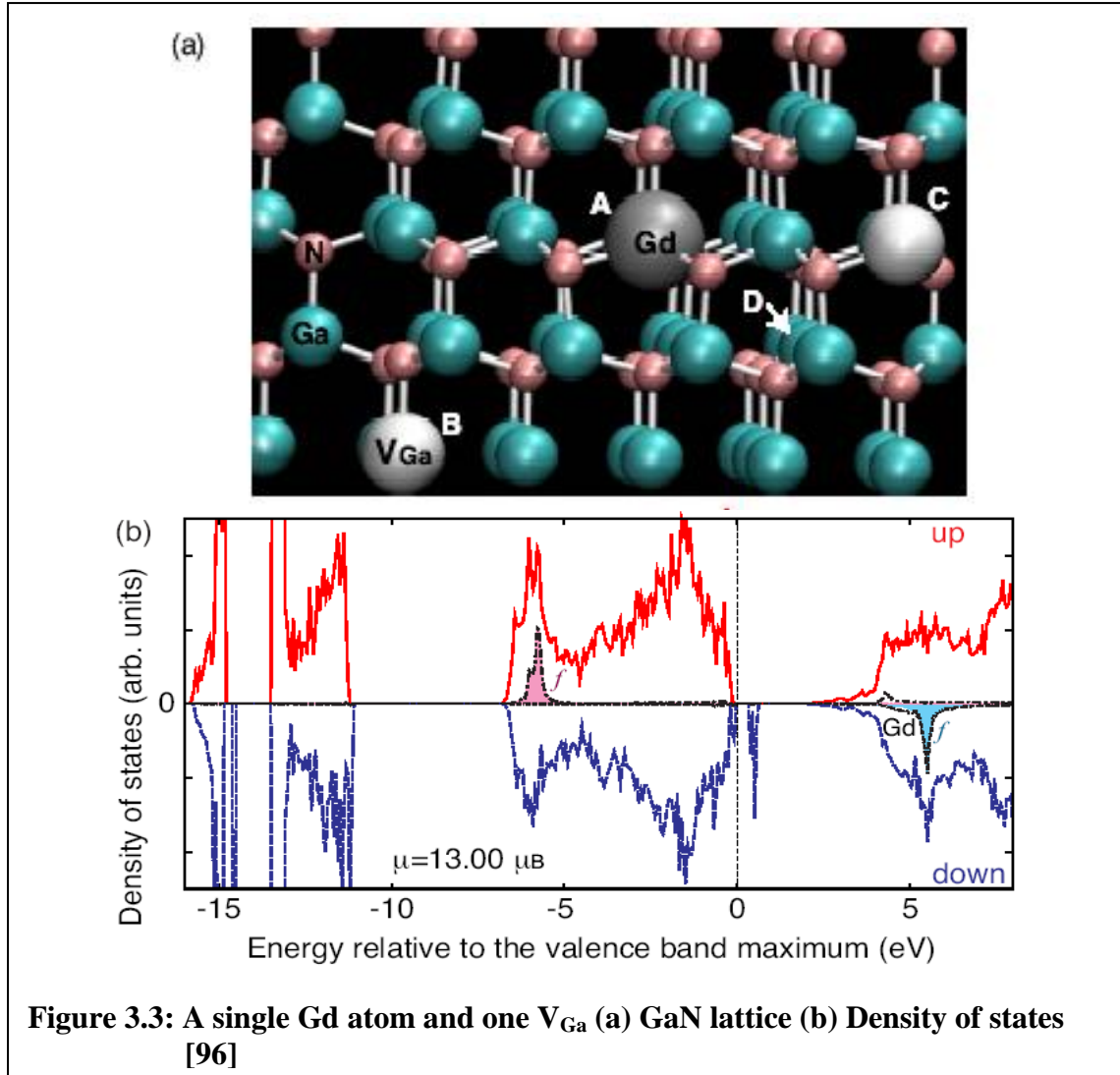
Dalpian et al. [98], Larson, and Lambrecht [99] proposed a model based on impurity states within the spin-split conduction band. This model is based on the spin-splitting of

conduction band minima calculated by Dalpian et al. Larson and Lambrecht [99] made an generate a colossal magnetic moment per Gd atom. The magnetic moments on the order of  $1000\mu_B$  were claimed to occur for Gd concentrations of  $10^{15}/\text{cm}^3$ .

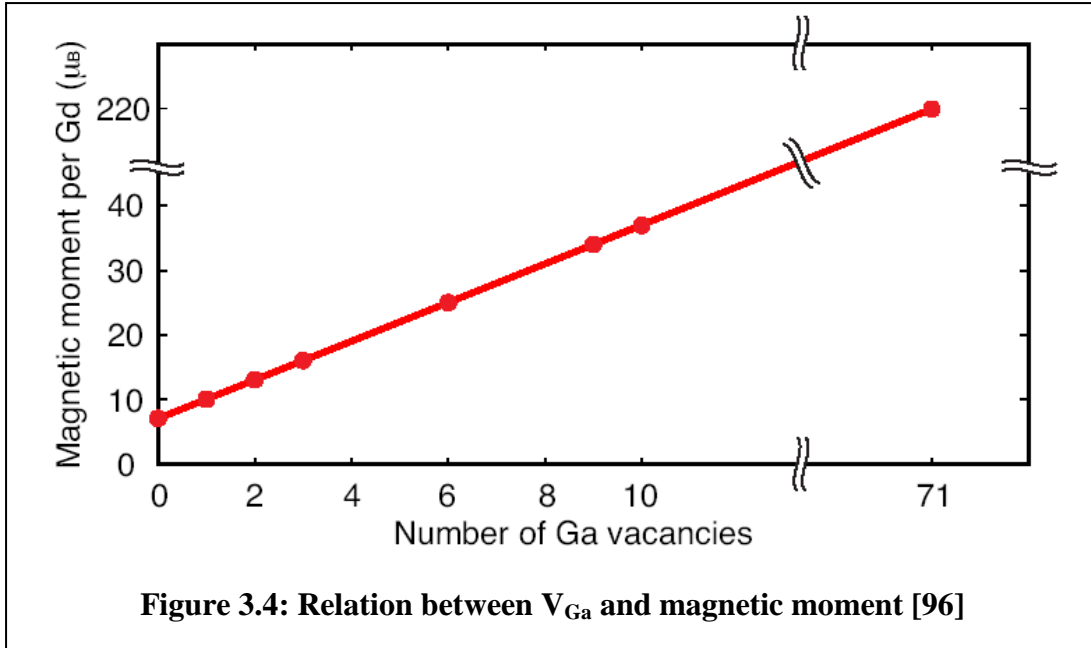
If this dilute concentration of Gd were capable of producing a spin splitting of 50 meV, it would be possible to quantitatively account for the colossal magnetic moments. However, Chandrima et al [94] argued that a spin-splitting on the order of 50 meV is obtained for Gd concentrations around 6 %, not  $10^{15}/\text{cm}^3$  which would correspond to 0.01 ppm.

### **3.6.3 Ga vacancies**

Gohda et. al. performed first-principles calculations on the spin polarization of Ga vacancies in Gd-doped GaN focusing on the interaction among Ga vacancies and the Gd atom (Figure 3.3). They found that the ferromagnetic configuration of the spins of Ga vacancies and the Gd atom is most energetically stable, and that the magnetic moment increases monotonically with increasing number of Ga vacancies. Their results also indicate the possibility of intrinsic ferromagnetism due to Ga vacancies in GaN. [96]



In the neutral charged state, Ga vacancies add an additional magnetic moment of  $3\mu_B$ . Gohda et al. showed that, if the number of  $V_{Ga}$  around the Gd atom is increased, the magnetic moment increases linearly by  $3\mu_B$  per  $V_{Ga}$  due to the three holes arising from the vacancy with the minority spin. The magnetic moment reaches  $220\mu_B$  per Gd atom with 71  $V_{Ga}$  (Figure 3.4).



These vacancy states are still relatively more delocalized over various atoms compared to the Gd f states. They have a tail extending over several atoms. This has led to the hypothesis that these states are the origin of both the formation of additional magnetic moments and rather strong and long-range interactions and explain the high Curie temperatures of  $Ga_{1-x}Gd_xN$ .

**Table 3.5: Covalent radii of common impurities in GaN [89]**

Symbol	Name	Covalent Radius
H	Hydrogen	0.32 Å
O	Oxygen	0.73 Å
N	Nitrogen	0.75 Å
C	Carbon	0.77 Å
Si	Silicon	1.11 Å
Ga	Gallium	1.26 Å
Mg	Magnesium	1.36 Å
In	Indium	1.44 Å
Gd	Gadolinium	1.61 Å

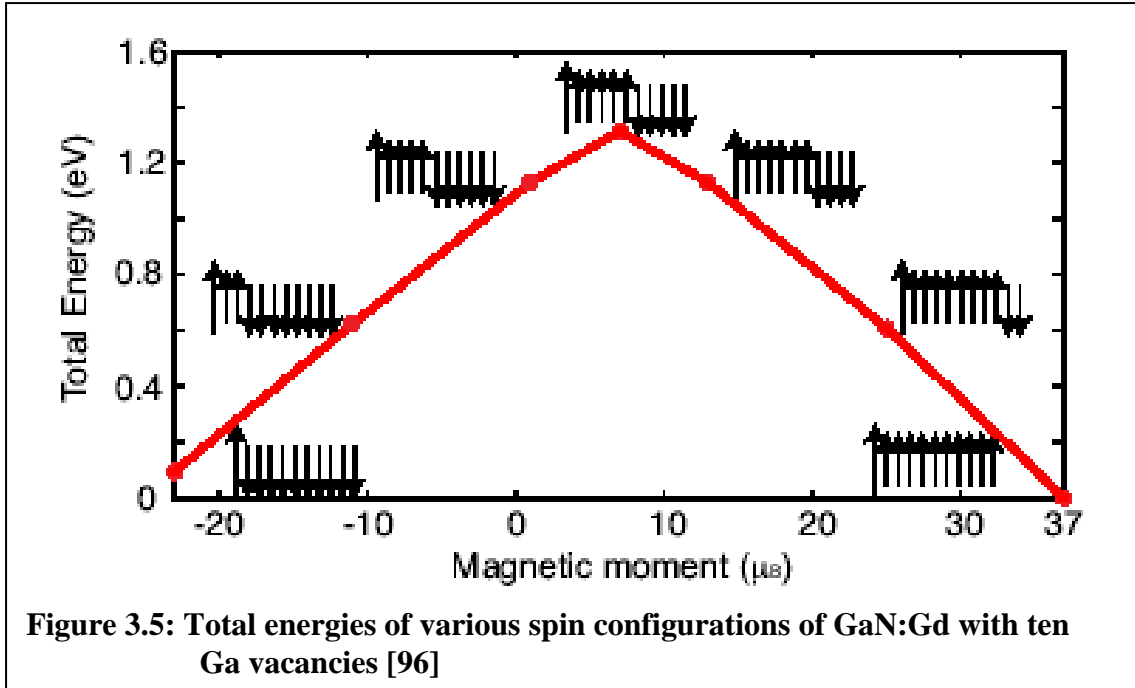
Chandrima et. al. explained the formation of large number of Ga vacancies in the  $Ga_{1-x}Gd_xN$  material system as a result of the need for relief of stress induced by the large size

mismatch of Gd and Ga atoms. Table 3.5 lists the ionic radii of Ga, Gd and other atoms likely to be present in a  $\text{Ga}_{1-x}\text{Gd}_x\text{N}$  material system.

According to Chandrima, because the Gd atom is significantly larger in size than Ga, a large number of Ga vacancies are needed to relieve the tensile stress [94]. By plotting the two different total energy curves, one with the vacancies and one without them, vs. the lattice constant, Chandrima et. al. [94] estimated that for the lattice expansion due to each Gd atom, 22 Ga vacancies are required to relieve the stress and match the lattice constant of pure GaN. They, however, could not explain how such a large number of vacancies would continue to form as their energy of formation would continue to rise.

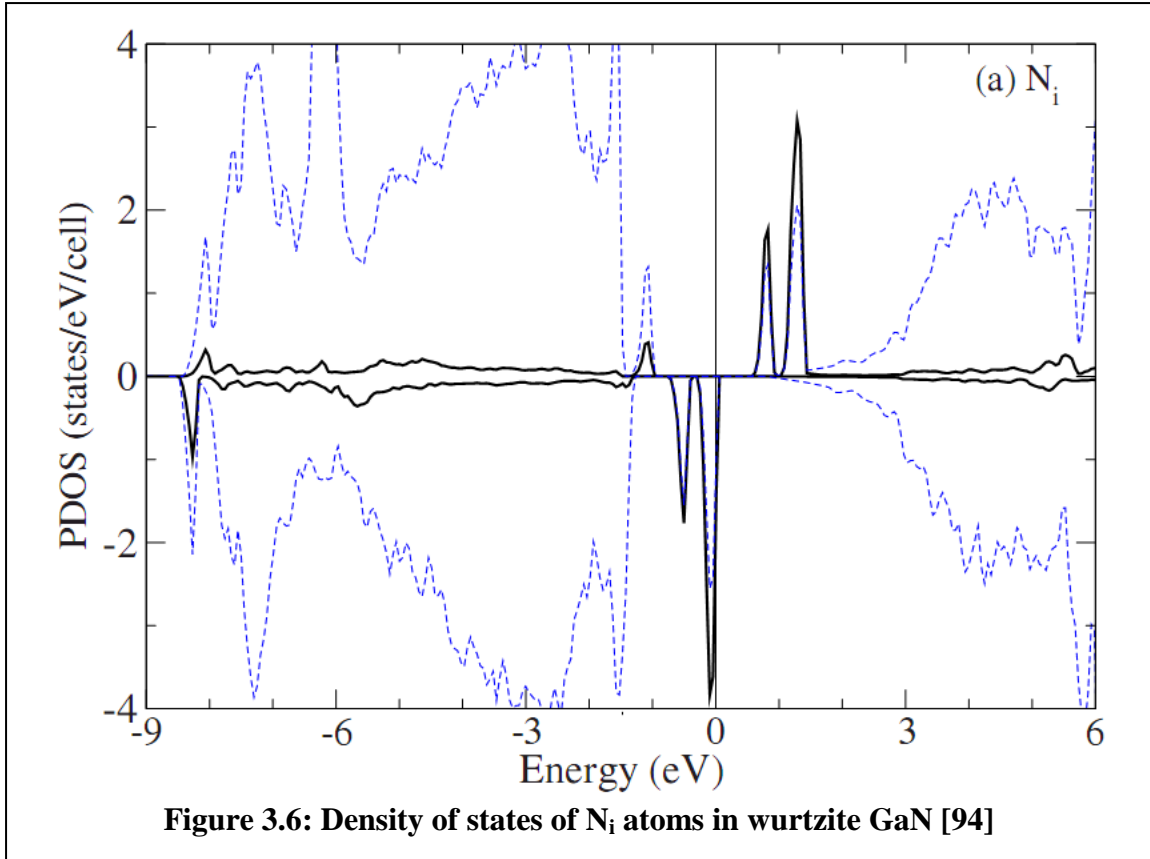
Thus the model proposed by Liu et al. [95] and Dev. et al. [97] based on Ga vacancies does appear to be untenable. It can also be argued that  $V_{\text{Ga}}$  has magnetic moment of  $3\mu_{\text{B}}$  in the neutral charge state that can occur in a p-type material.  $\text{Ga}_{1-x}\text{Gd}_x\text{N}$  materials have been reported n-type or semi-insulating. A p-type state is not in agreement with experimental data on these samples.

Gohda et. al. compared total energies of various spin configurations of GaN:Gd with ten Ga vacancies. Figure 3.5 shows their energy calculations for seven spin configurations, each of which has a particular magnetic moment. Whereas the ferromagnetic configuration with a magnetic moment of  $37\mu_{\text{B}}$  is most stable, an antiferromagnetic configuration among ten Ga vacancies with a magnetic moment of  $7\mu_{\text{B}}$  is the least stable. This is again indicative of intrinsic ferromagnetism due to  $V_{\text{Ga}}$ .



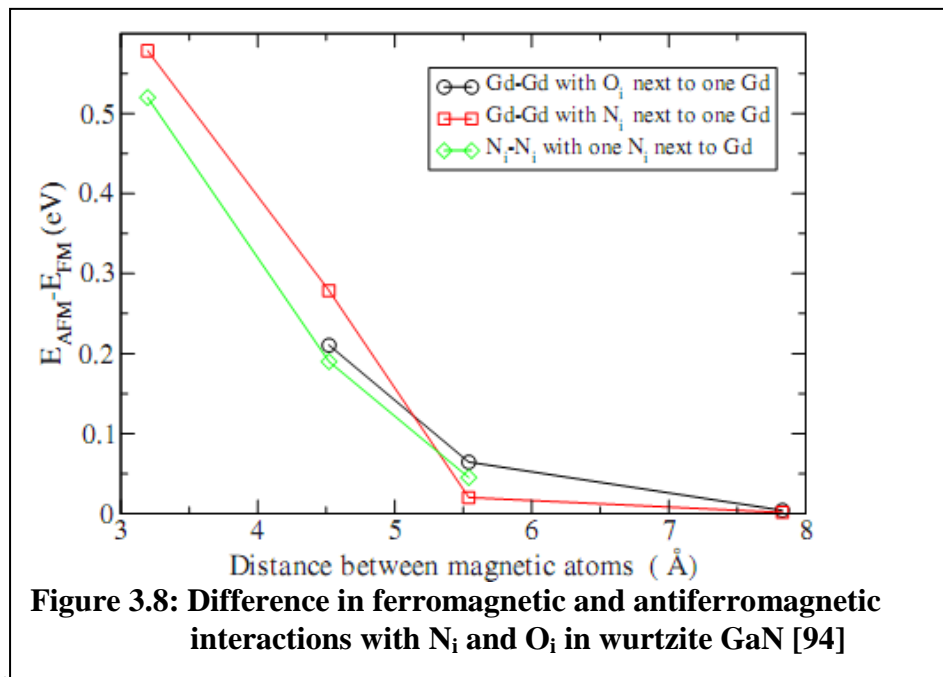
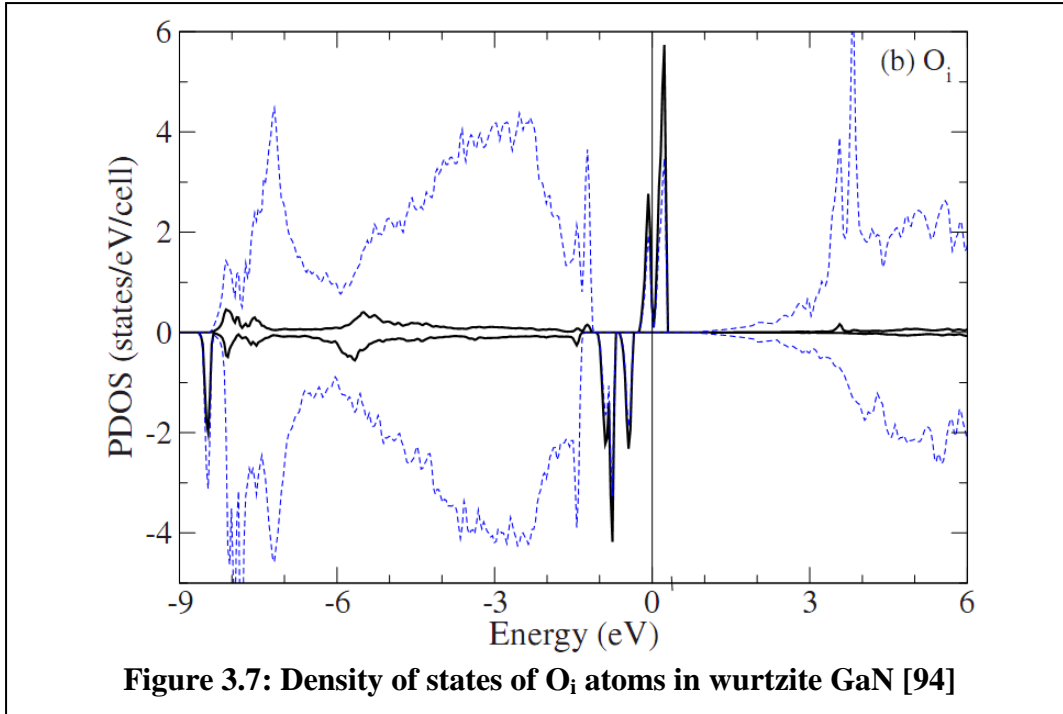
#### 3.6.4 Interstitial N

N interstitials ( $N_i$ ) could naturally form in conjunction with N vacancies ( $V_N$ ) as Frenkel pairs when Gd is introduced in GaN. It is more likely in case of Gd-implanted samples. Simulation of the implantation process by Dhar et al. [54] suggests formation of  $N_i$  in large numbers. This is quite possible, since Limpijumngong et. al [100] showed that the  $N_i$  formation energy is the defect with the second-lowest energy of formation for near mid-gap Fermi levels. Analysis of the density of states of  $N_i$  atoms (Figure 3.6) showed that they have a net spin polarization, and, if present in GaN layers, they would contribute a magnetic moment of 2  $\mu_B$  to the system. It may, however, be highlighted that the entire discussion of  $N_i$  is based on the Gd-implanted GaN model. The same may not hold completely true for MOCVD-grown samples.



### 3.6.5 Interstitial O

The chemical affinity of Gd for oxygen is well known. This means that any oxygen present in the material system during growth or implantation is likely to have a tendency to migrate close to the Gd atoms and occupy octahedral interstitial sites. In a pure GaN, oxygen atoms are more favorable to occupy a nitrogen site, the presence of another defect atom like Gd which has a strong affinity for oxygen, may act as a driving force for the substitutional oxygen atoms to occupy an interstitial site near a Gd atom. The formation energy for  $O_i$  was shown to be negative by Chandrima et. al. in  $Ga_{1-x}Gd_xN$ . This means that oxygen will move to an interstitial site near Gd if the latter is present in GaN. Figure 3.7 shows the density of states of the  $O_i$  atoms. They are clearly found to have a net spin polarization and thus add a net magnetic moment of  $3\mu_B$  to the system.



Chandrima et. al. showed that even for the fourth nearest neighbor the Gd atoms favor ferromagnetic interactions over the anti-ferromagnetic interactions, if at least one of the atoms has a  $N_i$  or an  $O_i$  atom as its nearest neighbor (Figure 3.8).

### 3.7 Challenges for a $\text{Ga}_{1-x}\text{Gd}_x\text{N}$ DMS

While the  $\text{Ga}_{1-x}\text{Gd}_x\text{N}$  material system promises to be a better alternative to TM-doped GaN, it also has a number of challenges of its own that need to be addressed. Some of the challenges that have surfaced for  $\text{Ga}_{1-x}\text{Gd}_x\text{N}$  thin films so far are listed below:

- Lack of availability of MO precursor with reasonable vapor pressure for MOCVD
- No established growth technique
- Resistive nature of the films reported by MBE and PLD growth techniques
- No report of p-type  $\text{Ga}_{1-x}\text{Gd}_x\text{N}$  material in literature
- Inconsistencies in the magnetic behavior (reports of ferromagnetic, paramagnetic, and non-magnetic behavior)
- Colossal magnetic moment reported only in very dilute doping levels
- Origin of the magnetic moment controversial – unexplained
- Still no practical device based on  $\text{Ga}_{1-x}\text{Gd}_x\text{N}$  thin films

### 3.8 Summary

The two unresolved (controversial) issues in a  $\text{Ga}_{1-x}\text{Gd}_x\text{N}$  material system are the colossal magnetic moment and the ferromagnetism. The colossal magnetic moment on the order of magnitude reported is highly unlikely even if defects contribute to the net magnetic moment of the system, especially at such a dilute limit of Gd concentration. The magnetic behavior of  $\text{Ga}_{1-x}\text{Gd}_x\text{N}$  also remains controversial as different groups report a wide range of ferromagnetic, paramagnetic, and even non-magnetic behaviors of the films.  $V_{\text{Ga}}$ ,  $N_i$ , and  $O_i$  are all shown to contribute to the magnetic moment, while the contribution from Gd itself remains controversial since more recent papers do not assign any magnetic contributions from it.

Many research groups have successfully obtained  $\text{Ga}_{1-x}\text{Gd}_x\text{N}$  samples either by Gd implantation in GaN or epitaxial growth using MBE or PLD. No reports of MOCVD growth of  $\text{Ga}_{1-x}\text{Gd}_x\text{N}$  exists except for those of our research group. No report of any functioning device exists based on  $\text{Ga}_{1-x}\text{Gd}_x\text{N}$  thin films.

Work toward MOCVD growth of  $\text{Ga}_{1-x}\text{Gd}_x\text{N}$  thin films focuses on many different issues, but the ultimate goal is to achieve reproducible, device-quality material useful for spintronic and optoelectronic devices and applications.

## **CHAPTER 4: EXPERIMENTAL EQUIPMENT AND TECHNIQUES**

### **4.1 Introduction**

The research presented in this dissertation is composed of several aspects, including materials growth, characterization, and processing. This chapter is dedicated to the description of the techniques used and the specific equipment employed for this research.

Semiconductor thin film research is driven by a number of epitaxial growth techniques which include pulsed laser deposition (PLD), molecular beam epitaxy (MBE), and chemical vapor deposition (CVD). Metal organic chemical vapor deposition (MOCVD) is a special case CVD, where one or more of the precursors supplied are a metal-organic (metal with an organic ligand attached to it). MOCVD is a method for depositing films of various materials, and involves the thermally induced reaction of a molecule on a heated surface. This technology is now an essential factor in the manufacture of semiconductors. This technique offers a number of advantages such as good film uniformity, compatibility, conformal growth with very good step coverage, high deposition rates, and scalability from laboratory to production systems. MOCVD has matured over the past decade into the the state-of-the-art technique used for high-volume production of high-quality optoelectronic devices like LEDs.

### **4.2 MOCVD Growth Technique**

The MOCVD growth technique uses metal-organic precursors comprising a metallic atom attached to an organic ligand e.g. trimethylgallium where three methyl molecules are attached to gallium. The metal-organic precursors have adequate vapor pressure at or

near room temperature that permits their transport in the vapor phase through the delivery system to the growth chamber. Precursors of the desired constituents are delivered through separate lines and undergo many chemical and physical processes, resulting in the epitaxial growth of thin films on the substrate inside the growth chamber. The growth process itself can be described in terms of thermodynamics and kinetics, where thermodynamics is the driving force and kinetics control the rate at which these reactions occur.

#### **4.2.1 Thermodynamics**

The chemical reactions which dictate how dopants are incorporated depend upon the free energy of the system. The chemical reaction at constant temperature is associated with a change in energy of the system given by the Gibbs free energy equation:

$$\Delta G = \Delta H - T\Delta S \quad \text{Equation (4.1)}$$

where  $\Delta G$  is the Gibbs free energy;

$\Delta H$  is the enthalpy (formation energy) that depends on the internal system energy;

$\Delta S$  is the change in entropy (disorder, randomization);

and  $T$  is the temperature.

The internal energy of a system is the combined of the total kinetic and potential energy. The kinetic energy comprises the vibrational, translational, and rotational energies of atoms in a given state, whereas the potential energy stems from bonding and the interactions between atoms.

For a simple two-phase system moving a small amount of component  $i$  from phase  $\alpha$  to phase  $\beta$  in equilibrium causes no change in  $G$ . The following equation describes this as:

$$\left(\frac{\partial G}{\partial n_i}\right)_{T,P,n_j}^{\alpha} - \left(\frac{\partial G}{\partial n_j}\right)_{T,P,n_i}^{\beta} = 0 \quad \text{Equation (4.2)}$$

where  $n_i$  is the molar concentration of component  $i$ ;

$P$  is the pressure,

and  $T$  is the temperature.

The partial derivative of  $G$  with respect to  $n_i$  is known as the chemical potential ( $\mu_i$ ), and is expressed as:

$$\mu_i = \mu_i^0 + RT \ln(a_i) \quad \text{Equation (4.3)}$$

where  $\mu_i$  is the chemical potential;

$\mu_i^0$  is the chemical potential at some arbitrary standard state;

$R$  is the gas constant;

and  $a_i$  is known as the activity coefficient.

In a non-equilibrium state, the difference in chemical potential ( $\Delta\mu$ ) is non-zero and is expressed as:

$$\Delta\mu = \mu_A - \mu_B \quad \text{Equation (4.4)}$$

In the MOCVD growth chamber a non-equilibrium gas phase is intentionally created to drive the reaction at the surface. The formation of the solid phase decreases the difference in chemical potential, pushing the system back towards equilibrium. The growth rate of the films is determined by the amount of material that would return the

system to complete equilibrium. The maximum growth rate is also dependent on reactor geometry and total precursor flow rates.

Mass transport and surface reaction rates also have an effect on the growth rate, which is determined by the flux of atoms reaching the film surface from the gas phase. It is possible for near-equilibrium conditions to exist near the film surface, even when a large difference in chemical potential exists in the gas phase. This occurs when the surface reactions proceed more rapidly than the mass transport and is referred to as mass transport-limited growth.

#### 4.2.2 Kinetics

Kinetics in the MOCVD growth process describes the steps involved as well as the rates at which those steps proceed. A major part of kinetics in MOCVD growth is describing the chemical reactions that occur both in the gas phase and at the solid surface.

For a given chemical reaction, the rate of the forward and reverse reactions is given by the product of the concentration and the rate constant ( $k$ ), which is often expressed using the Arrhenius equation:

$$k = A e^{-E_a/RT} \quad \text{Equation (4.5)}$$

where  $E_a$  is the activation energy;

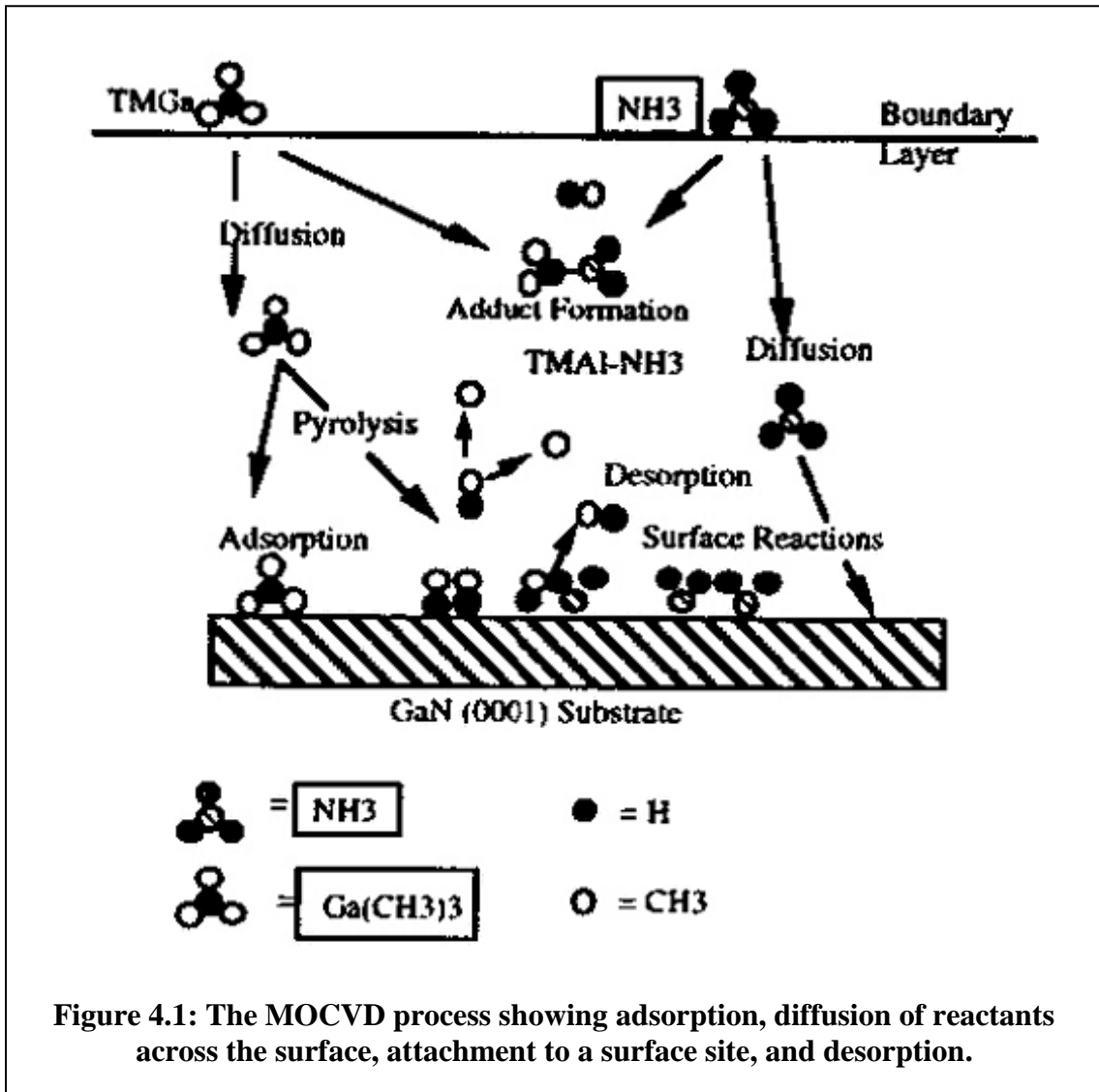
$A$  is a pre-exponential factor;

$R$  is the gas constant;

and  $T$  is the temperature.

Typical growth of high-quality thin films proceeds with adsorption, diffusion of reactants across the surface, attachment to a surface site, and desorption of the products.

This process often proceeds by the formation of steps on the surface, with the diffusion of adsorbed atoms across the surface and attachment to a step (Figure 4.1).



#### 4.2.3 Fluid Dynamics and Mass Transport

Fluid dynamics like thermodynamics and kinetics is an important aspect of MOCVD growth. It depends on the reactor geometry and experimental equipment more than any other aspect of MOCVD growth. Gas flow through an MOCVD reactor occurs through forced convection, i.e. gas flows because of an intentional pressure gradient across the

reactor. The velocity vectors of the gas flow are both parallel to each other and parallel to the walls of the reactor. This type of flow is called laminar flow. In the laminar flow regime, both convection effects, created by rapid heating of injected gases, and mass diffusion of the precursors to the substrate, caused by a gradient in chemical potential, play a significant role in determining the growth rate. Because temperature plays a role in both of these processes, there exists in standard MOCVD processes a growth regime, in which fluid dynamics and mass transport effects limit the growth rate.

Modeling of gas flow in an MOCVD reactor involves the solution of three partial differential equations. The first equation (4.6) describes conservation of mass:

$$\frac{\partial}{\partial t} \rho_i = -\nabla \cdot [\rho_i \mathbf{v} + \mathbf{j}_i] = -\nabla \cdot \mathbf{n}_i \quad \text{Equation (4.6)}$$

where  $\rho$  is mass density,

$\mathbf{v}$  is average velocity,

$\mathbf{n}_i$  is the total mass flux of component  $i$ ,

and  $\mathbf{j}_i$  is the diffusive flux with respect to  $\mathbf{v}$ .

The second equation (4.7) is known as the Navier-Stokes equation, which describes conservation of momentum:

$$\frac{\partial}{\partial t} \rho \mathbf{v} = -[\nabla \cdot \{\rho \mathbf{v} \mathbf{v} + \Pi\}] + \sum_i \rho_i \mathbf{g}_i \quad \text{Equation (4.7)}$$

where  $\rho$  is total mass density,

$\mathbf{v} \mathbf{v}$  is a second-order tensor,

$\Pi$  is the pressure tensor,

and  $\mathbf{g}_i$  is the sum of the external forces per unit mass on component  $i$ .

The third equation (4.8) describes conservation of energy:

$$\frac{\partial}{\partial t} \rho \left( E + \frac{1}{2} v^2 \right) = -\nabla \cdot \left\{ \rho \left( E + \frac{1}{2} v^2 \right) \mathbf{v} + \mathbf{q} + [\Pi \cdot \mathbf{v}] \right\} + \sum_i n_i \mathbf{g}_i \quad \text{Equation (4.8)}$$

where  $E$  is the internal energy per unit mass,

and  $\mathbf{q}$  is the conductive heat flux

The equations (4.6 – 4.8) are solved by imposing boundary conditions, e.g. velocity perpendicular to the surface is zero. Computer modeling software is often used to generate the solution of these modeling equations.

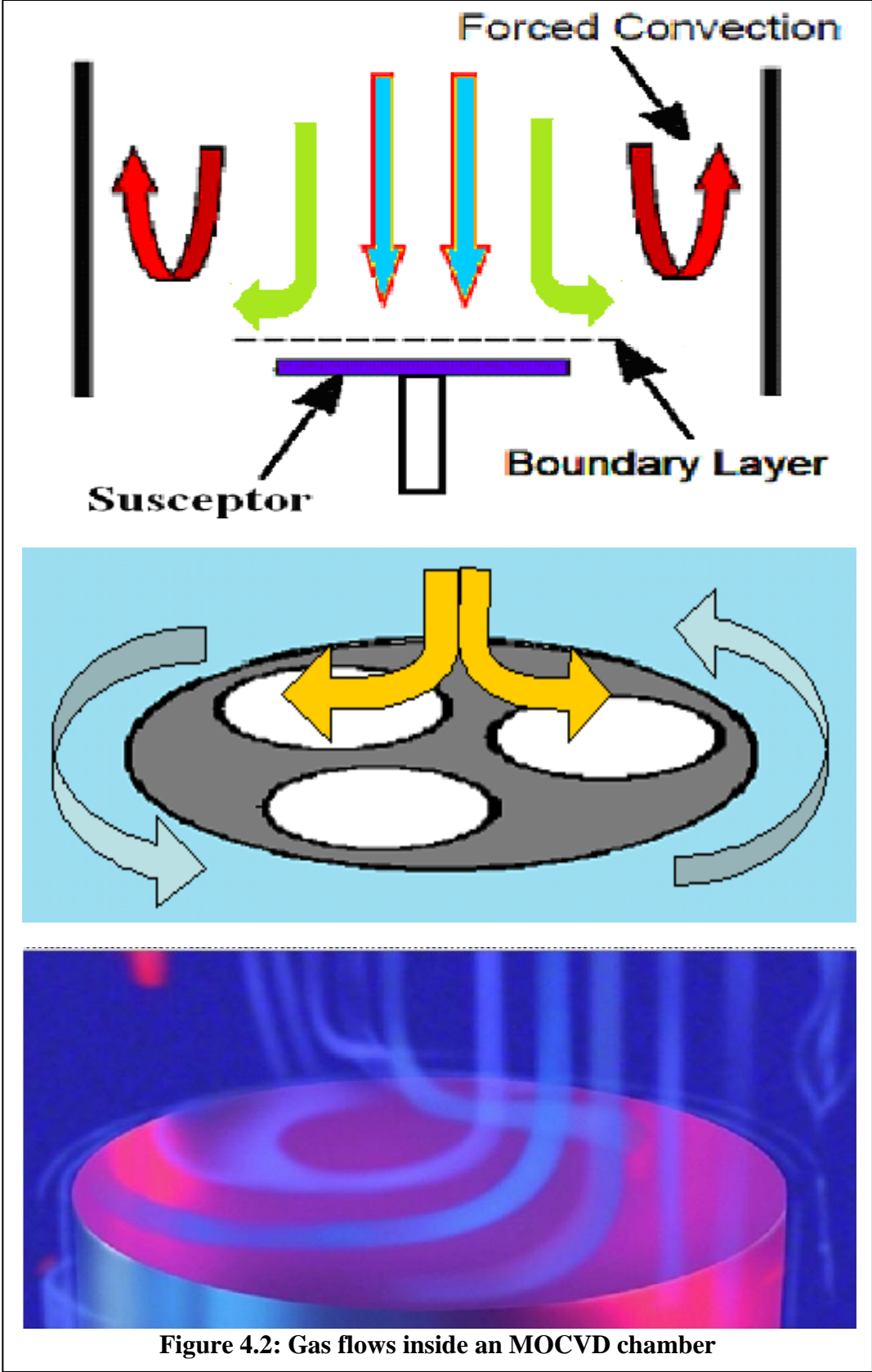
The velocity parallel to the surface decreases as the surface is approached, leading to the formation of a boundary layer, across which precursor atoms diffuse to adsorb onto the surface of the growing film (Figure 4.2). In vertical injection onto rotating disk reactors, the boundary layer thickness ( $\delta$ ) is given by:

$$\delta_0 \cong 4 \left( \frac{\nu}{\omega} \right)^{\frac{1}{2}} \quad \text{Equation (4.9)}$$

where  $\nu$  is the kinematics viscosity;

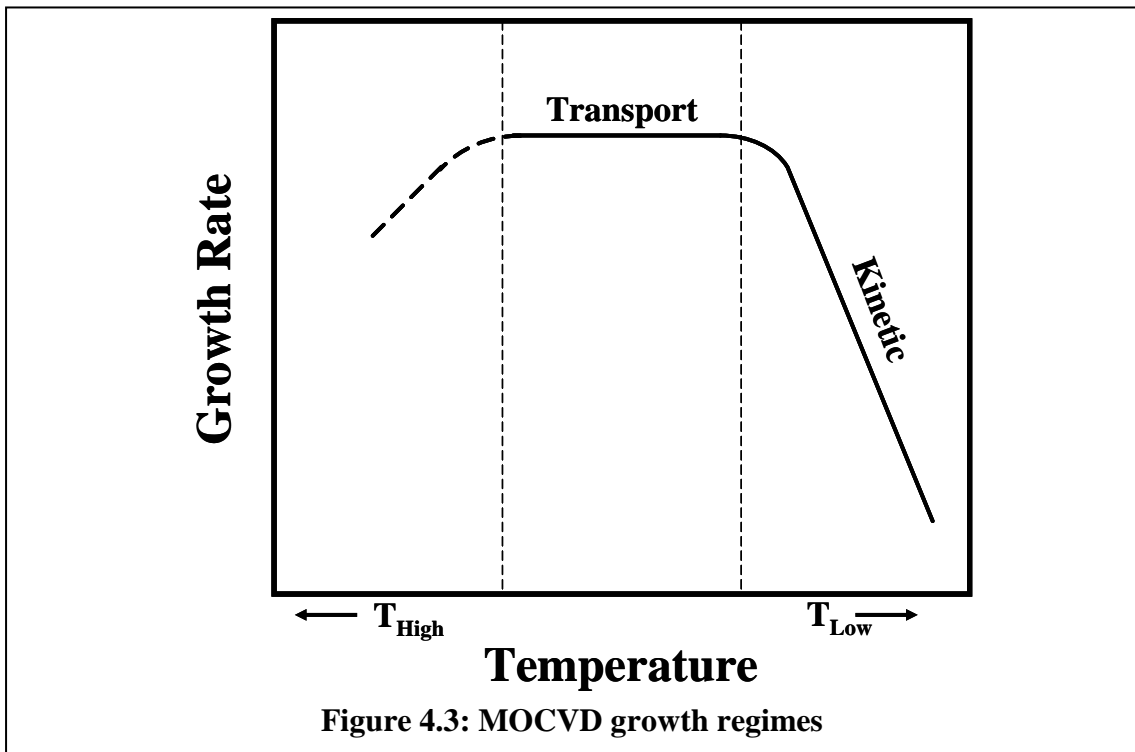
and  $\omega$  is the rotation speed of the disk.

It can be seen that the boundary layer thickness decreases with an increase in rotation speed. Fluid dynamics, along with thermodynamics and kinetics, can be used to paint a reasonably clear picture of the MOCVD process.



### 4.3 Growth Rate Regimes

The growth rate of the films in a MOCVD reactor depends on the temperature and the supply of precursors. Three growth rate regimes can be identified according to the temperature inside the reactor. The first regime is at low temperatures, where the growth rate increases exponentially with temperature, and is known as the kinetic regime. The second regime is at intermediate temperatures where the growth rate remains constant, i.e. it does not change with temperature, and is known as the mass transport regime. The third regime is at high temperatures where a roll off in growth rate is observed with increasing temperature due to desorption and depletion. Figure 4.3 depicts these regimes.



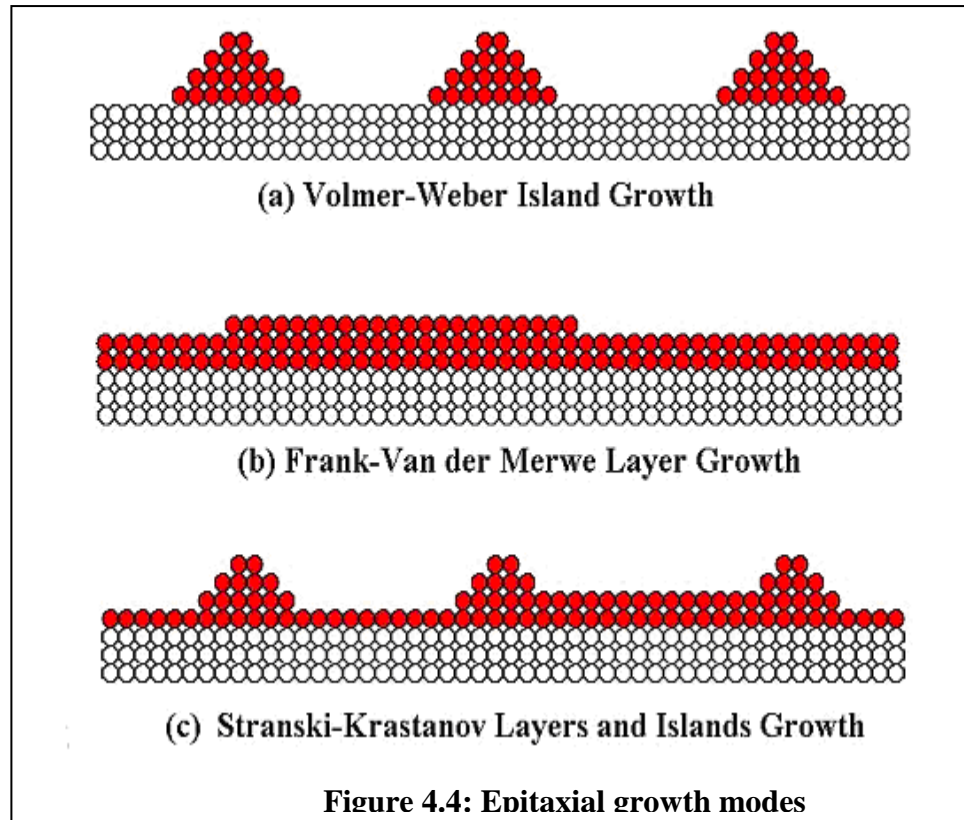
#### 4.4 Modes of Thin Film Growth

The three epitaxial growth modes of thin films on a substrate by MOCVD are Volmer-Weber (VW) growth, Frank-van der Merwe (FM) growth, and Stranski-Krastanov (SK) growth (Figure 4.4). The mode of growth that results during MOCVD depends on the interaction strength between the adatoms and the surface.

In Volmer-Weber (VW) growth, adatom-adatom interactions are stronger than those of the adatom with the surface, leading to the formation of 3-D adatom clusters or islands. This growth mode results in the formation of clusters and coarse or rough multi-layer film growth on the substrate surface.

During Frank-van der Merwe (FM) growth, adatoms attach preferentially to surface sites resulting in atomically smooth, fully formed layers. This growth mode is 2-D where a complete film forms prior to the growth of subsequent layers.[101, 102]

In a Stranski-Krastanov (SK) growth mode both 2D layer and 3D island growth are present. Transition from the layer-by-layer to island-based growth occurs at a critical layer thickness that depends on the chemical and physical properties, such as surface energies and lattice parameters of the substrate and film.[101-103]



#### 4.5 MOCVD Gas Delivery System

The gas delivery system of MOCVD tool for III-V semiconductor growth is composed of two separate gas streams: the metal-organics (MO) stream and the precursor gas stream. The metal-organic stream caters to the supply of MO sources (e.g. TMGa). It comprises a bank of manifolds that accommodate metal-organic source bubblers immersed in constant temperature baths. Nitrogen and/or hydrogen gas is passed through these bubblers as a push or carrier gas and is saturated with the MO vapor. The precursor gas stream supplies the gases (e.g.  $\text{NH}_3$ ), which flow through a separate run/vent manifold. The run/vent manifold allows rapid gas switching needed for the growth of multi-layered heterostructures (i.e. superlattice structures) and devices. A series of valves diverts the gas either to the growth chamber or to the vent line going to the scrubber.

The precursor gases and MOs are kept separate till they are injected in the growth chamber to avoid any premature reactions. The bubbler is always kept at a constant temperature and pressure ensuring constant flow of MO vapors out of it. The run and vent lines are also kept at the same pressure to ensure that the bubbler do not experience any pressure difference while switching from vent to run.

The feed rate of the bubbler depends on the following:

- Flow rate of the carrier gas
- Pressure of the bubbler
- Vapor pressure of the MO source in the bubbler.

The bubbler can be attached in one of two configurations: the direct connection as shown in Figure 4.5(a), and the double dilution configuration shown in Figure 4.5(b).

The MO flow rate for a direct connected bubbler is given by:

$$F_{MO} = F_{Raw} \frac{P_{MO}}{P_{Bubbler} - P_{MO}} \quad \text{Equation (4.10)}$$

Where  $F_{MO}$  is the MO flow rate;

$F_{Raw}$  is the raw flow through MFC;

$P_{MO}$  is the vapor pressure of the precursor;

and  $P_{Bubbler}$  is the bubbler pressure.

In the double dilution configuration, the MO flow is given by:

$$F_{MO} = F_{DD} \left( \frac{F_{Raw}}{F_{Raw} + F_{Push}} \right) \left( \frac{P_{MO}}{P_{Bubbler} - P_{MO}} \right) \quad \text{Equation (4.11)}$$

where  $F_{DD}$  is the flow through the double dilution (DD) MFC;

$F_{Push}$  is the flow through the push MFC.

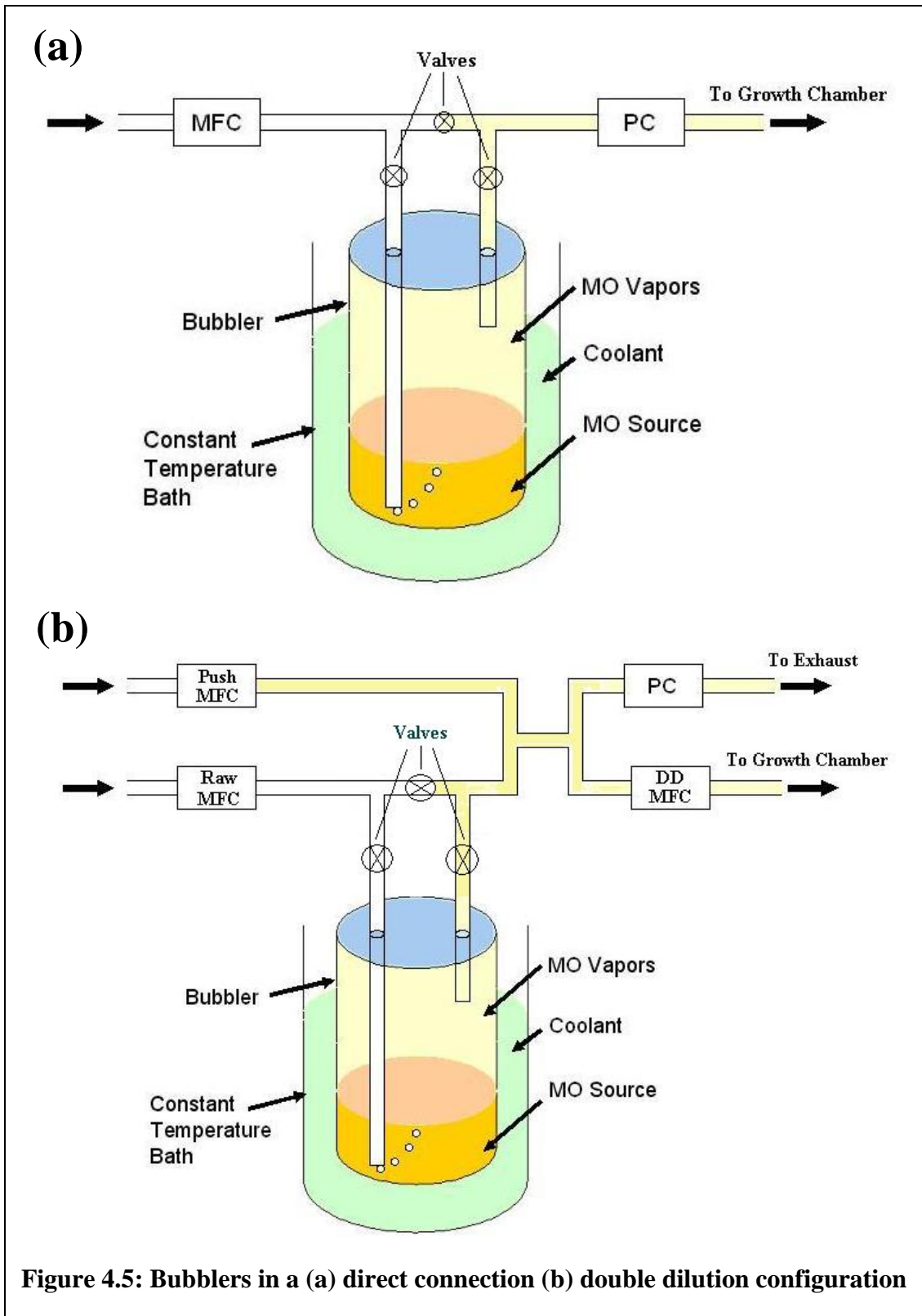
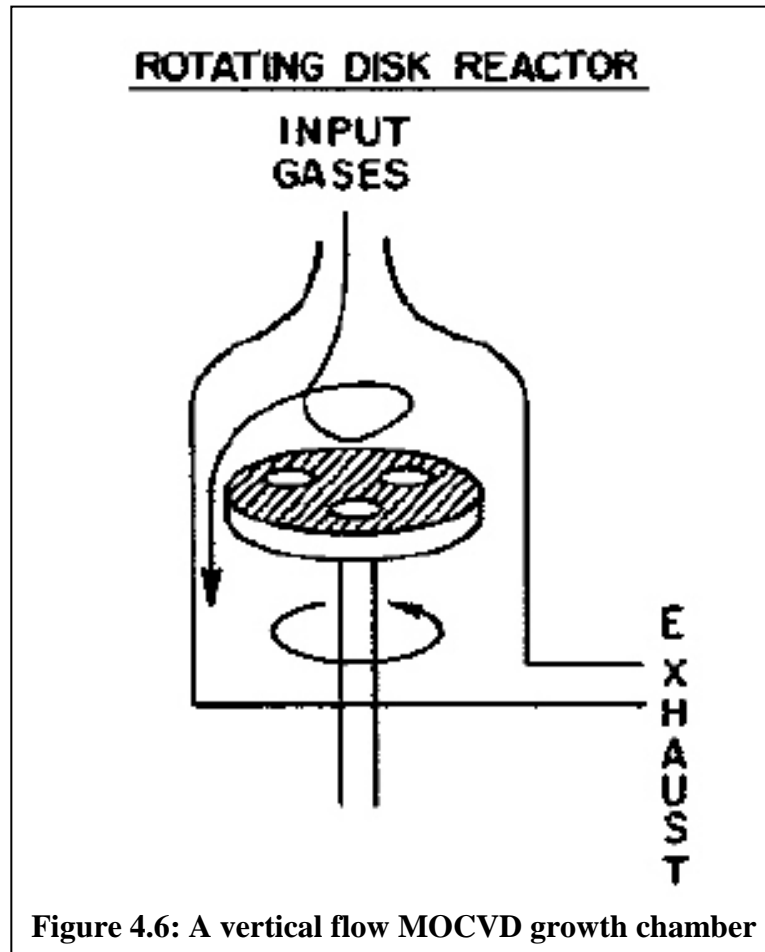


**Figure 4.5: Bubblers in a (a) direct connection (b) double dilution configuration**

## 4.6 MOCVD Reaction Chamber

The MOCVD growth tool used for all the depositions in this work is a modified Emcore/Veeco D125 system with a load lock. This tool has a vertical flow showerhead designed as depicted in Figure 4.6. The chamber head and spindle assembly are water-cooled by a closed loop chilled water supply system of the lab. The susceptor is rotated by a stepper motor located at the base of the ferro-fluidic spindle assembly.



The susceptors used were machined out of high purity graphite, and are coated with tantalum carbide (TaC). The delivered gases flow through a region called the forced convection region above the wafer (Figure 4.2). A boundary layer separates the forced

convection region from the wafer surface, where some gases flow through this layer and are deposited on the surface. Upon reaching the hot substrate surface, several reaction processes occur, as shown in Figure 4.1 above.

#### 4.7 Exhaust Handling System

The exhaust system for the gases of our MOCVD system is composed of an Ebara vacuum pump, a throttle valve, and a pressure transducer for measuring the chamber pressure. All of these components are connected to the scrubber, which is kept at 800°C to burn away the toxic exhaust gases into the atmosphere.

#### 4.8 Precursors for MOCVD Growth of GaN

High purity metal-organic precursors are used in MOCVD growth. The desirable properties of these precursors include high volatility (high vapor pressures), a minimal number of impurities (especially silicon and oxygen as they make GaN n-type), and complete pyrolyzation at low temperatures. The vapor pressure of the precursor determines the concentration of the source flowing inside the growth chamber and hence the growth rate. The vapor pressure of a metal-organic precursor used in MOCVD is generally given by:

$$\log_{10}(P) = A - \frac{B}{T} \quad \text{Equation (4.9)}$$

where **P** is the vapor pressure in Torr;

**T** is the absolute temperature in degrees Kelvin;

**A** and **B** are the vapor pressure coefficients.

Trimethylgallium (TMGa) is the commonly used gallium (Ga) MO precursor in MOCVD of GaN. TMGa completely pyrolyzes at 550°C in either an H<sub>2</sub> or N<sub>2</sub> ambient environment. Triethylgallium (TEGa) is the other Ga MO precursor, which is often used during growth at lower temperatures. TEGa pyrolyzes completely at 400°C. This is similar to the decomposition temperature of trimethylindium (TMIn), which makes it useful in growing In<sub>x</sub>Ga<sub>1-x</sub>N/GaN quantum well structures.

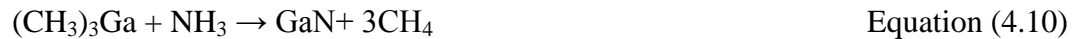
The nitrogen precursor used for GaN MOCVD is ammonia (NH<sub>3</sub>). NH<sub>3</sub> decomposes at much higher temperatures than the metal-organic precursors (600°C - 800°C at atmospheric pressure).

The n-type dopant commonly used for GaN is Si with Silane (SiH<sub>4</sub>) as the precursor. For p-type GaN, the most common dopant is Magnesium.

**Table 4.1: MO precursors used in MOCVD of GaN**

<b>Metal Organic</b>	<b>Chemical Formula</b>	<b>A</b>	<b>B</b>	<b>Vapor Pressure</b>
Trimethyl Gallium (TMGa)	(C <sub>3</sub> H <sub>3</sub> ) <sub>3</sub> Ga	8.495	1825	64.5 Torr @ 0 °C
Triethyl Gallium (TEGa)	(C <sub>2</sub> H <sub>5</sub> ) <sub>3</sub> Ga	9.165	2530	3.4 Torr @ 20 °C
Trimethyl Indium (TMIn)	(CH <sub>3</sub> ) <sub>3</sub> In	9.735	2830	1.2 Torr @ 20 °C
Bis(cyclopentadienyl) Magnesium (Cp <sub>2</sub> Mg)	(C <sub>5</sub> H <sub>5</sub> ) <sub>2</sub> Mg	10.56	3556	0.05 Torr @ 25 °C

The chemical reaction that occurs during GaN growth in the MOCVD chamber is as follows:



The MO precursors are kept in a thermal bath maintained at a particular temperature, and the gas lines connecting the precursors to the reactor chamber are heated. This ensures that the source enters the growth chamber in gaseous state instead of condensing and depositing in the gas lines. Table 4.1 shows the vapor pressure of the most commonly used MO precursors for MOCVD of GaN.

#### **4.9 Substrates for GaN Growth**

The production of bulk GaN is quite expensive due to large pressures and temperatures involved in the process. Consequently GaN is generally grown epitaxially on foreign substrates.

Ideally the substrate for GaN growth should have a lattice constant and thermal expansion coefficient close to GaN. Unfortunately, the two most common substrates used for GaN growth, sapphire and SiC, both have a large thermal and lattice mismatch with GaN. The growth processes on these substrates however have matured over the last decade since no other material has superseded them yet in large-scale industrial production of GaN- based devices.

Sapphire is most commonly used due to its low cost, good crystal quality, optical transparency, and chemical stability at high temperatures. GaN is usually grown on the sapphire c-plane (0001), and they have a lattice mismatch of ~15 % [104]. There is a 30° rotation of the (0001) III-Nitride plane with respect to the sapphire (0001) without which the lattice mismatch would be ~30 % [104]. In this work all growth is performed on sapphire substrates. Table 4.2 shows the lattice constants and parameters for GaN and sapphire [105].

**Table 4.2: Lattice constants and thermal expansion coefficients for GaN and sapphire [105].**

Material	Lattice Constant $a$ (Å)	Lattice parameter $c$ (Å)	Thermal Exp coefficients (K <sup>-1</sup> )
GaN	3.189	5.185	$\alpha_a = 5.59 \times 10^{-6}$ $\alpha_c = 3.17 \times 10^{-6}$
Al <sub>2</sub> O <sub>3</sub> c-plane	4.758	12.991	$\alpha_a = 7.5 \times 10^{-6}$ $\alpha_c = 8.5 \times 10^{-6}$

#### 4.10 MOCVD GaN Growth

MOCVD grown GaN-based device structures are presently employed in numerous optoelectronics devices such as blue LEDs, laser diodes, and UV-detectors [105]. The technique used for MOCVD of GaN on sapphire originates from Yoshida et. al. who in 1983 demonstrated enhanced GaN nucleation and improved film quality by incorporating an AlN buffer layer between the sapphire substrate and the GaN layer [106]. Amano et. al. reduced threading dislocations and improved electrical and optical properties of GaN films by using a two-step process, in which a low temperature AlN buffer layer was deposited on sapphire substrate and then crystallized prior to GaN growth [107]. Finally in 1991, Nakamura grew high quality GaN films and blue LED structures successfully, using a GaN buffer layer in the two-step process developed earlier [108, 109]. The entire growth process comprises of six steps as described below.

- Substrate Pre-Treatment. The sapphire substrate is heated to 1000 °C under hydrogen flow for about 5 minutes. This cleans and prepares the growth surface. The next step is the nitridation, where ammonia flows for approximately 3 minutes. This improves the surface quality for two-dimensional GaN growth [110, 111].

- GaN Buffer Growth. A low temperature GaN buffer layer is deposited at 500-550 °C for approximately 3 minutes. At this temperature a high density of nucleation centers (island formations) are obtained [112]. These islands expand and coalesce to form lateral growth.
- Buffer Recrystallization. The temperature is ramped up to 1000 °C under ammonia flow to convert the amorphous GaN to crystalline.
- Rough GaN Growth. The temperature is further ramped up to ~1015 °C. This results in the nucleation centers to increase in size and roughness.
- Recovery GaN Growth. The ripened nucleation centers coalesce and the growth transfers from a 3-D to a 2-D GaN film. The temperature during this phase is kept at ~1030 °C and the chamber pressure is maintained at 500 Torr. The increase in the in-situ reflectivity signal gives this stage the name “recovery stage”.
- Main GaN Growth. The growth chamber pressure is reduced to 200 Torr, the temperature is set at ~1050 °C, and the V/III ratio is kept in the range of 2000-3000. This layer is typically grown at a growth rate of ~2 μm/hr.

Figure 4.7 shows the temperature vs. time and reflectivity vs. time values during the six GaN growth steps. For the first five steps from substrate pre-treatment to recovery, the chamber pressure is maintained at 500 Torr. It is only reduced to 200 Torr in the final step of the main GaN growth.

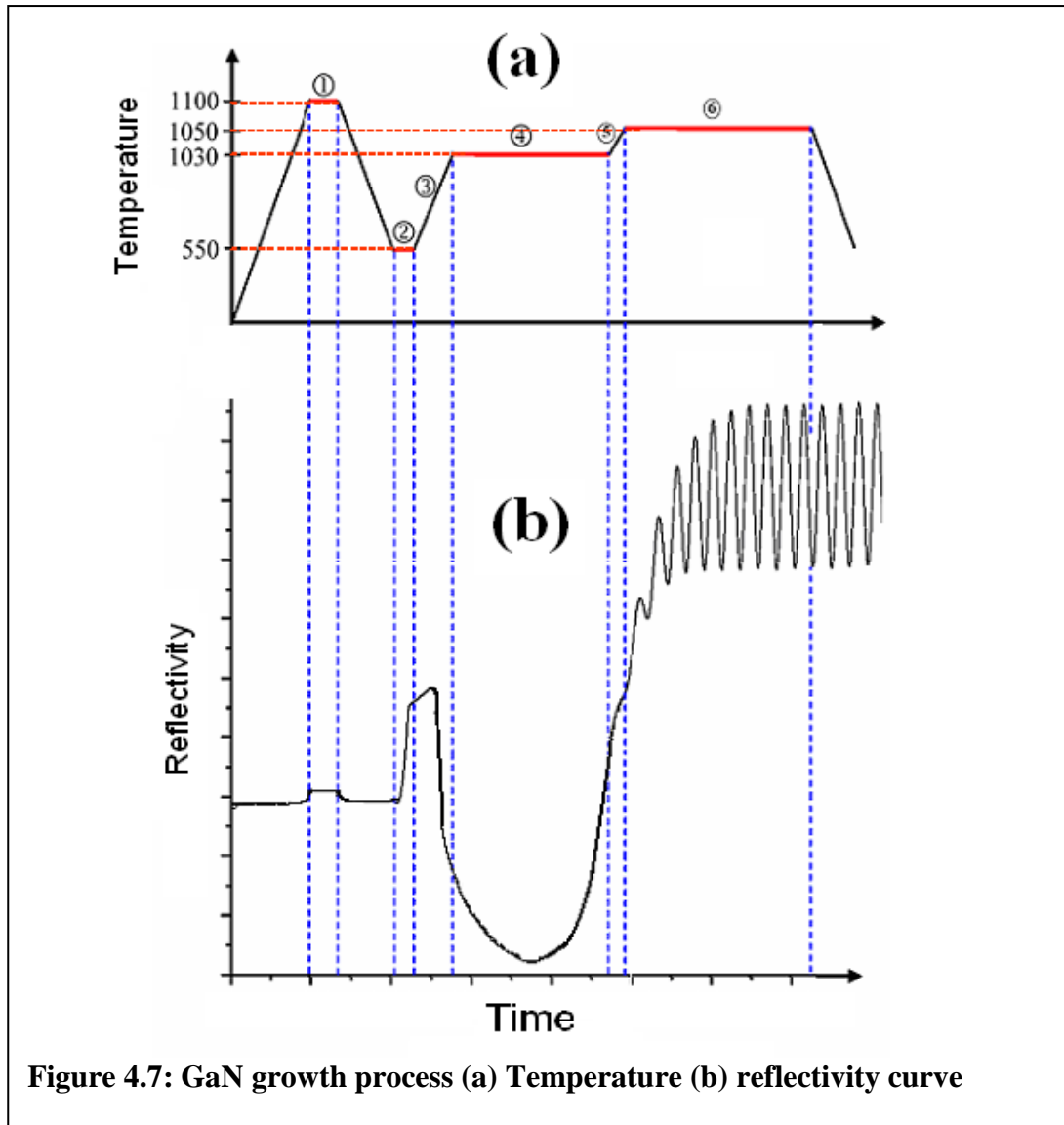


**Figure 4.7: GaN growth process (a) Temperature (b) reflectivity curve**

#### 4.11 Doping GaN Thin Films

The undoped GaN thin films grown on sapphire by the process mentioned above typically have an n-type free carrier concentration on the order of  $10^{16} \text{ cm}^{-3}$ . Intrinsic defects in GaN are donor-like defects ( $V_N$  and  $Ga_i$ ), which lead to an intrinsically n-type behavior when undoped. However, it is a widely accepted notion that unintentional incorporation of dopant impurities (oxygen and silicon) results in the observed n-type

conduction. [113, 114]. This background carrier concentration has to be accounted for while doping.

#### ***4.11.1 n-GaN Thin Films***

Si is the most widely used n-type dopant in GaN. Its properties include low activation energy (~12-17meV) [113, 115, 116] and ease of incorporation. Si substitutionally replaces Ga in the GaN lattice, as the nitrogen site and the interstitial configurations are energetically unfavorable [117]. This is a consequence of the similarity between the atomic radii of Ga and Si. Therefore, while Si sits readily at a Ga site, it induces strain if it replaces the smaller N atom or assumes an interstitial position in the lattice.

The source used for Si is silane (SiH<sub>4</sub>). The growth conditions for the growth of n-type material are identical to that of the undoped GaN described earlier, except for that SiH<sub>4</sub> is introduced into the gas mixture through the gas delivery manifold, as the final stage.

#### ***4.11.2 p-type GaN Thin Films***

Mg is the commonly used p-type dopant, with an activation energy of 170meV. The p-type doping of GaN using the activation of Mg acceptor via low energy electron beam irradiation was first reported in 1989 [118]. Later, Nakamura showed that Mg acceptor states also can be activated thermally by annealing the films at around 700°C in nitrogen ambient to break the Mg-H complexes [119]. Since then, hole concentrations exceeding  $3 \times 10^{18} \text{ cm}^{-3}$  have been demonstrated [120]. Still, p-type doping levels are not high enough to yield low resistance cladding layers and ohmic contacts. The materials used to form a good ohmic contact with p-type GaN are oxidized Ni and Au.

The temperature for MOCVD growth of p-GaN films is maintained around 900°C. This reduction in the growth temperature results in an increase in the native n-type defects due to non-optimal growth conditions. These defects increase the background carrier (electron) concentration that results in compensation of the holes in the layers. This compensation results in increased resistivity of the films.

#### **4.12 Characterizations**

Semiconductor thin films and substrates exhibit several types of properties that must be studied to gain a clear picture of material quality and functionality in optoelectronic devices. The major properties pertaining to this work are structural, surface, optical, and electrical properties. The characterization techniques used include XRD, AFM, SEM, PL, Hall Effect, VSM, SQUID, XPS, EPR, and EL. Details of these techniques are discussed in Appendix A.

#### **4.13 Summary**

A detailed discussion of the theoretical background of the MOCVD growth of thin films was presented in this chapter. This discussion included the thermodynamics, kinetic, fluid dynamics, mass transport, and different modes of epitaxial film growth that are experienced in MOCVD. The design of the major components of the MOCVD tool including the delivery system and the growth chamber were also briefly reviewed. Finally the steps involved in the MOCVD growth of GaN thin films on sapphire substrates were described in detail and followed by a discussion of Si and Mg-doping in order to obtain n- and p-type layers. The MOCVD growth technique and the GaN growth process covered in this chapter form the basis of all the work performed in this research.

## CHAPTER 5: MOCVD GROWTH OF $\text{Ga}_{1-x}\text{Gd}_x\text{N}$

### 5.1 Introduction

This chapter addresses the issues unique to the MOCVD growth and characterization of  $\text{Ga}_{1-x}\text{Gd}_x\text{N}$  thin films. The  $\text{Ga}_{1-x}\text{Gd}_x\text{N}$  thin films were typically grown on GaN template under standard GaN growth conditions using a modified delivery system with two different Gd precursors –  $(\text{Cp})_3\text{Gd}$  and  $\text{Gd}(\text{thd})_3$ . Co-doping of  $\text{Ga}_{1-x}\text{Gd}_x\text{N}$  films with Si and Mg was achieved to obtain n- and p-type films. These n- and p-type layers were subsequently used for the growth of a p-n diode structure. Finally a spin-LED was grown and fabricated.

The details of the experimental work completed for  $\text{Ga}_{1-x}\text{Gd}_x\text{N}$  films and their co-doping with Si and Mg forms part of this chapter. This is followed by the structural, magnetic, optical, and electrical characterization of these films. The chapter concludes with the analysis of the results. The experimental work and magneto-optical characterizations of the spin-LED are covered in Chapter 6.

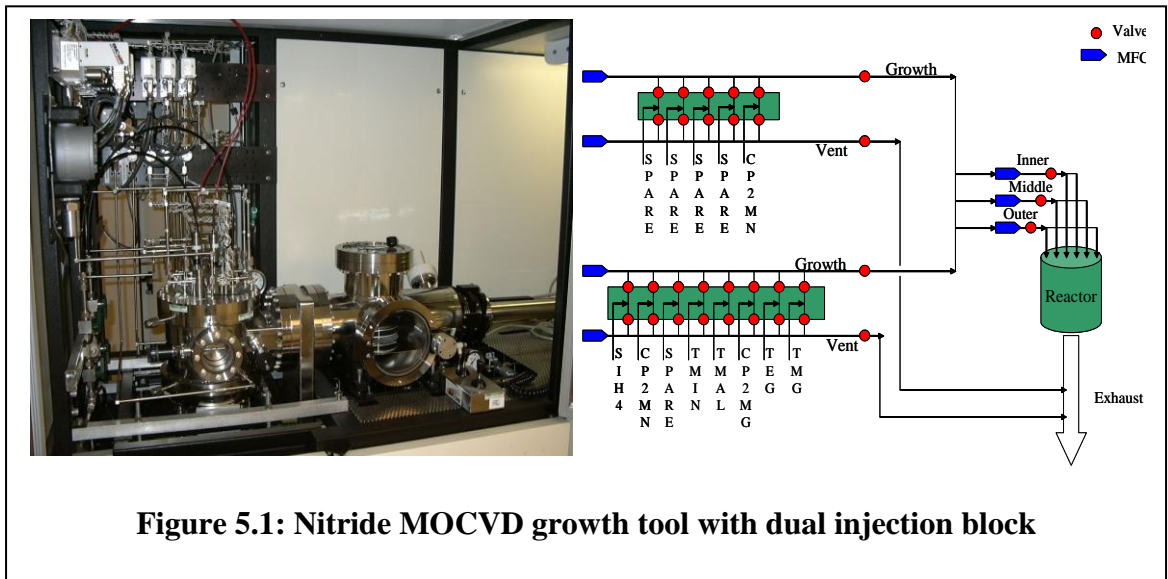
### 5.2 MOCVD Growth Tool

The highly modified MOCVD growth tool used in this research is shown in Figure 5.1. As discussed in Chapter 3, this tool is a vertical-injection commercial system with a rotating disk and short jar configuration. It has been modified by the addition of a second injector block to prevent cross-contamination between process gases and MO sources. This allows the use of a large number of unique MO sources not typically seen in other MOCVD systems. The gas panel of the tool has also been modified to permit the use of either hydrogen or nitrogen as a carrier gas. The electrical power system of the tool

allows for growth temperatures of up to 1200°C. The tool is equipped with a load-lock system for control of the reactor environment to ensure that no impurities enter the reactor from the atmosphere, thus preventing contamination of the growth chamber. The wafer carrier used in this tool can take up to three 2” substrates and was designed for commercial quality device growth.

The system capability is further enhanced by the modular design of the growth chamber with a duplicate backup chamber. The two growth chamber modules available for the system are labeled the materials chamber and the device chamber. The names correspond to the application of the chambers for materials research and device structure growths respectively.

The main disadvantage of growing Gd-doped GaN by MOCVD, the resulting system contamination, may have prevented other research groups from exploring this area. The modular design and redundancy of the growth chambers in our system helped to address this drawback.



### 5.3 Gd Precursors

The low vapor pressure of the commercially available Gd precursors is yet another major reason for hindering MOCVD growth of  $Ga_{1-x}Gd_xN$ . For this work the two commercially available Gd precursors selected were (1) Tris(2,2,6,6 tetramethyl 3,5 heptanedionato) gadolinium, commonly referred as  $Gd(thd)_3$ , and (2) Cyclopentine gadolinium, commonly referred as  $(Cp)_3Gd$ . The vapor pressure of  $Gd(thd)_3$  precursor is shown in Figure 5.2. It may be seen that even at 140°C, the maximum bubbler bath temperature possible, the vapor pressures of the precursor is very low.

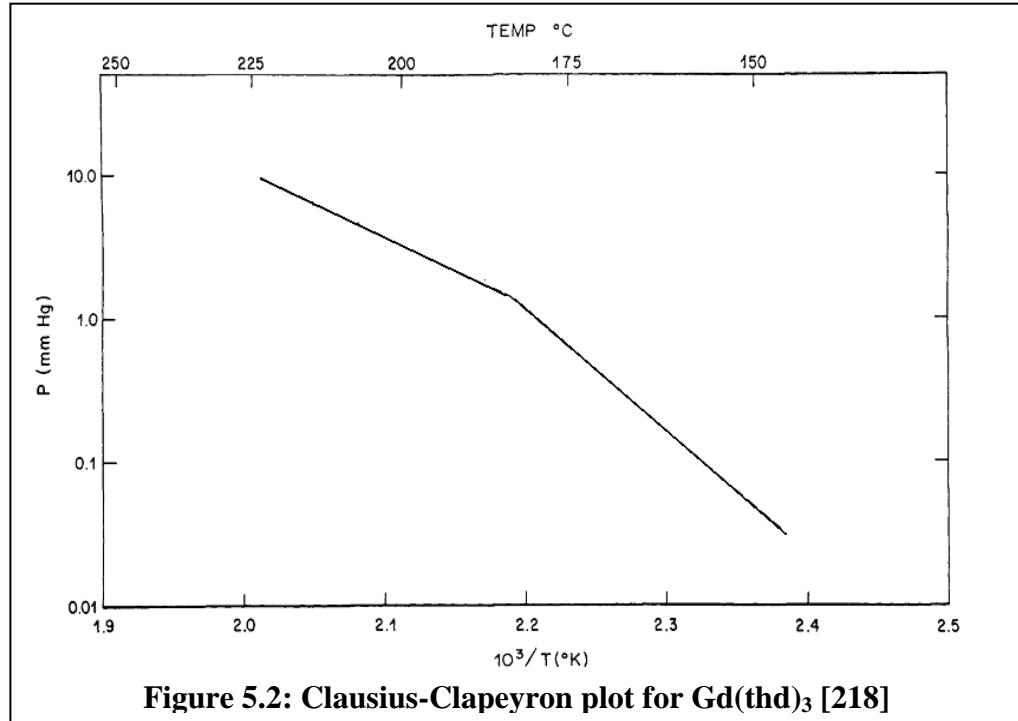


**Figure 5.2: Clausius-Clapeyron plot for  $Gd(thd)_3$  [218]**

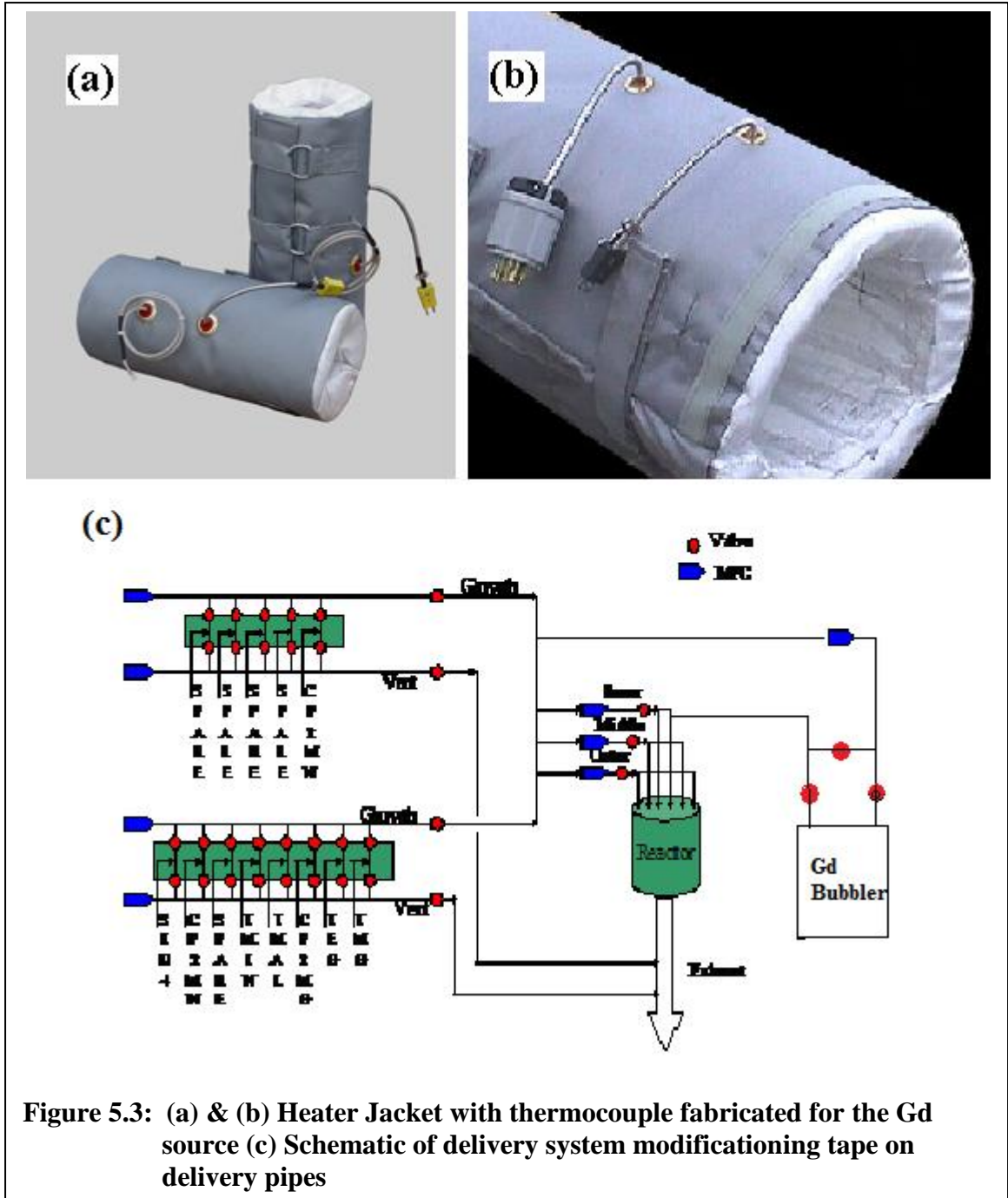
During the initial growth runs, the Gd bubblers were maintained at  $140^{\circ}C$ . Since the typical water or coolant mixture used in the baths would evaporate at this temperature, it was replaced with cooking oil. However, since the lines leading to the growth chamber were only heated to  $40^{\circ}C$ , it is very likely that most of the precursor was deposited to the interior of the delivery lines. At best, only a low doping concentration of Gd was

expected to reach the growth chamber. In addition to achieve reasonable Gd content, the H<sub>2</sub> carrier was pumped through the bubbler at a very high flow rate during these growth runs. These process conditions did not result in a reproducible, device-quality material.

In order to achieve device-quality Gd doped GaN, the vapor pressure of the Gd source must be sufficiently high. Consequently, the Gd source's temperature in the bubbler and in the lines to the chamber must be held between 150°C and 200°C (Figure 5.2). Since it was impossible to hold the Gd source at this temperature with the traditional baths, a more sophisticated arrangement was needed. For this reason, a special heating system was designed to ensure the delivery of Gd precursor at a suitable temperature range to the growth chamber, the details of which are disclosed in Section 5.4.

#### **5.4 Modified Precursor Delivery System**

The new precursor delivery system comprised a custom-designed electrical heater jacket for the source and the fabrication of a dedicated line for precursor delivery directly to the growth chamber, bypassing the existing MO delivery manifolds (Figure 5.3). This dedicated delivery line was wrapped with heavy-duty heater tape and insulation material capable of withstanding temperatures ranging from 20°C to 350°C. Figures 5.3a and b show the heater jacket that has heater tape along with embedded metallic bars for the distribution of heat and has the a thermocouple for temperature sensing. Figure 5.3c shows the schematic of the delivery system.



A molybdenum K-type thermocouple was embedded in both the heater jacket and the delivery line. A commercial temperature controller circuit board was procured and installed to control the temperature of the system. The delivery system was then integrated with the MOCVD growth tool.

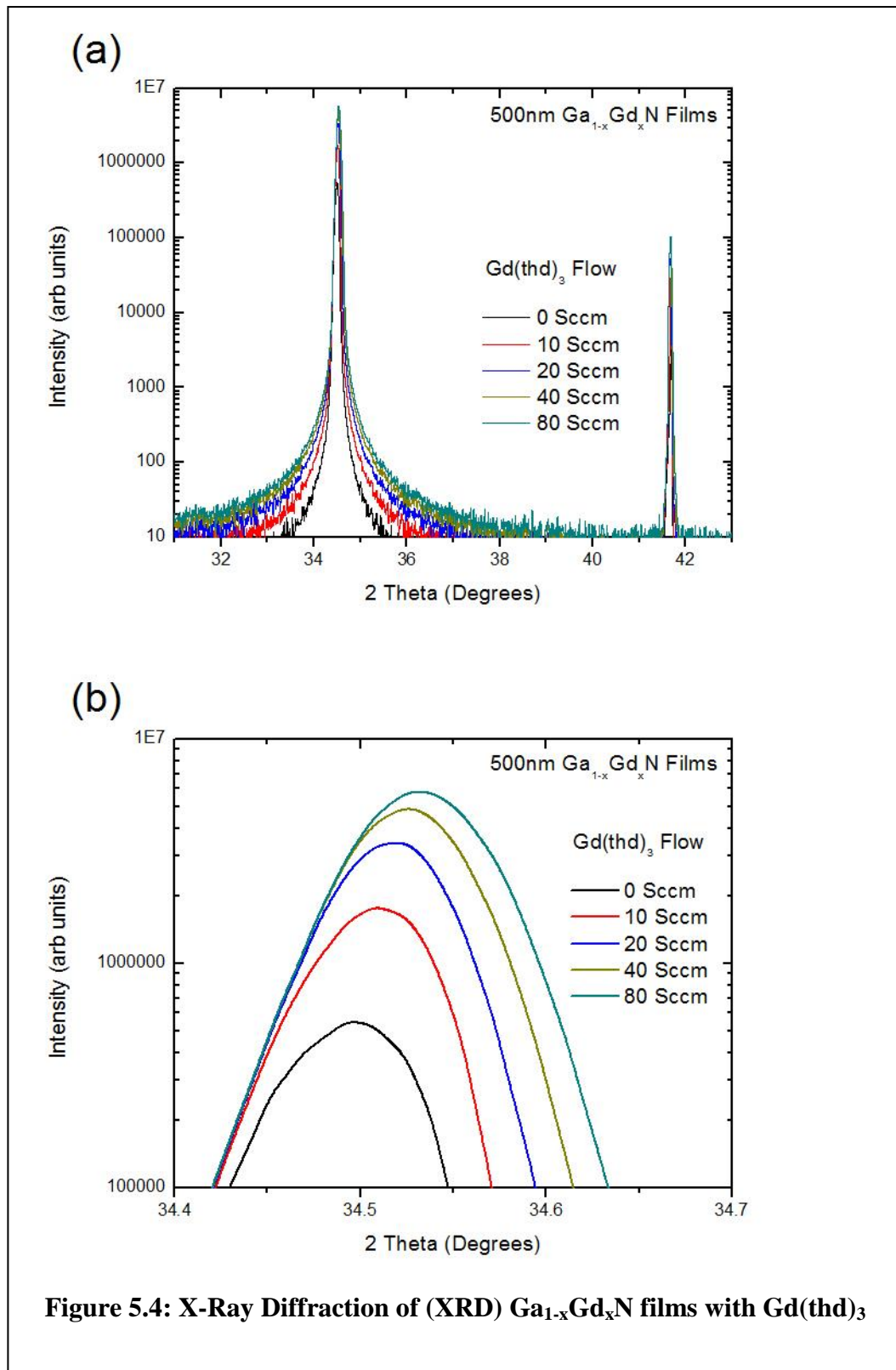
The novel control mechanism for the Gd source's temperature expanded the range and control of the Gd concentration in GaN, from the doping concentration to the lattice concentration. Moreover, since no large secondary flows, such as a push gas, are required, the quality of thin films and, consequently, device structure and performance improves.

## **5.5 Experimental Method**

In this work the  $\text{Ga}_{1-x}\text{Gd}_x\text{N}$  thin films and structures were typically grown on a  $2\mu\text{m}$  GaN template. The GaN templates were grown following the procedure outlined in Chapter 3 above. The  $\text{Ga}_{1-x}\text{Gd}_x\text{N}$  film thickness was kept at 500nm for better uniformity. In-situ monitoring of the film growth was performed by optical reflectometry, and no deterioration of crystal quality was observed in the reflectivity curves of the GaN films.

## **5.6 Structural Characterization**

Extensive on-axis and off-axis X-ray diffraction (XRD) scans of  $\text{Ga}_{1-x}\text{Gd}_x\text{N}$  films were performed. The results of these scans for  $\text{Ga}_{1-x}\text{Gd}_x\text{N}$  films with varying  $\text{Gd}(\text{thd})_3$  flow rate is shown in Figure 5.4. A deeper look at the GaN peak in these scans reveals a systematic shift to higher  $2\theta$  positions as the amount of Gd precursor delivered to the growth chamber increases (Figure 5.4b). The same scans for  $\text{Ga}_{1-x}\text{Gd}_x\text{N}$  films grown with  $(\text{Cp})_3\text{Gd}$  do not show this pattern, as seen from Figure 5.5.



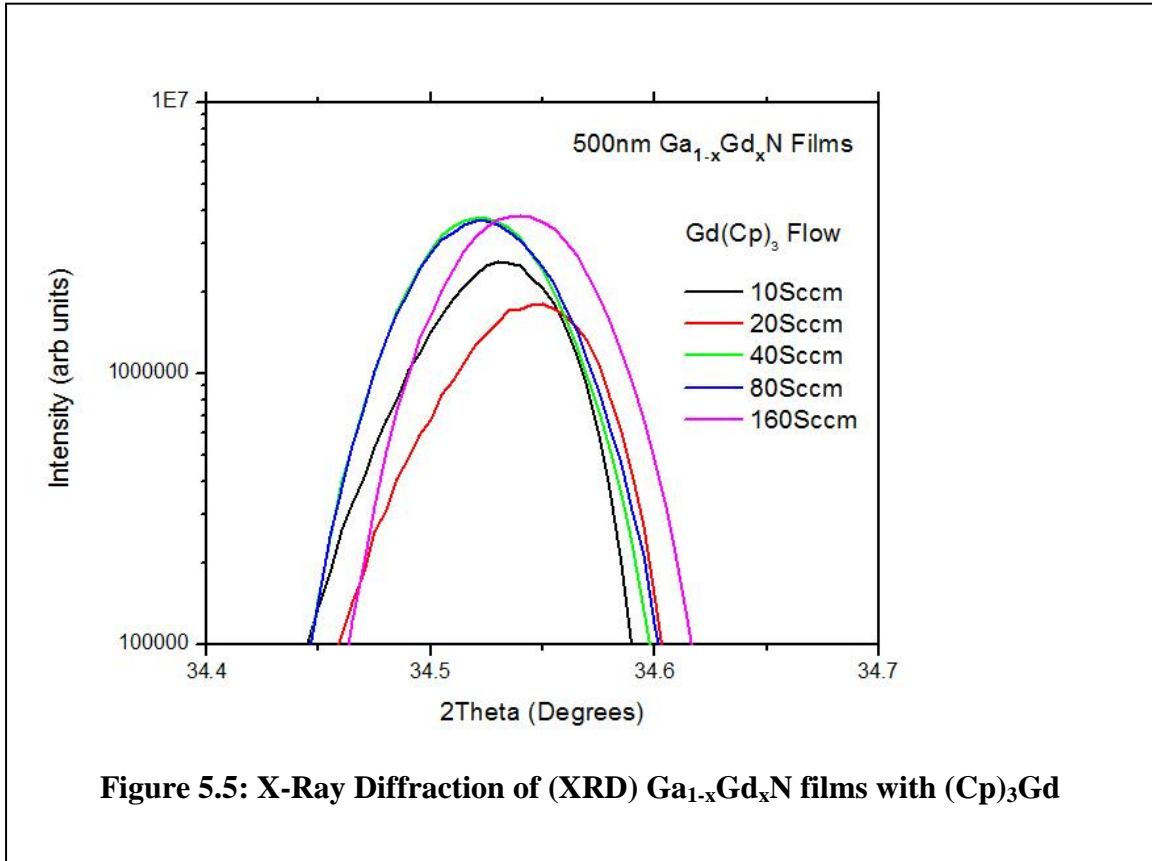
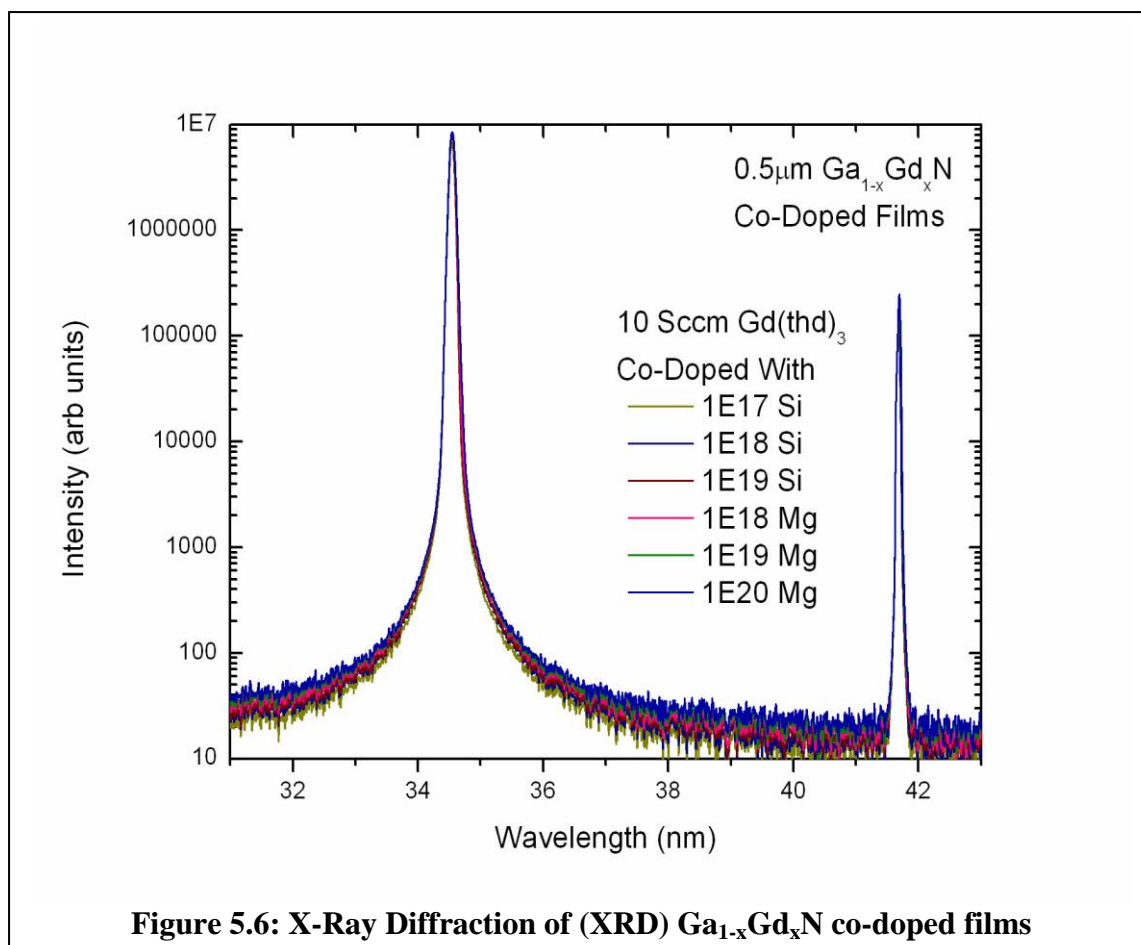


**Figure 5.5: X-Ray Diffraction of (XRD) Ga<sub>1-x</sub>Gd<sub>x</sub>N films with (Cp)<sub>3</sub>Gd**

In the case of Si and Mg co-doped Ga<sub>1-x</sub>Gd<sub>x</sub>N films, no major effect on the XRD was observed as a result of varying the Si doping level from  $1 \times 10^{17} \text{ cm}^{-3}$  to  $1 \times 10^{19} \text{ cm}^{-3}$  or varying the Mg doping level from  $1 \times 10^{18} \text{ cm}^{-3}$  to  $1 \times 10^{20} \text{ cm}^{-3}$ , as shown in Figure 5.6.



## 5.7 Optical Characterization

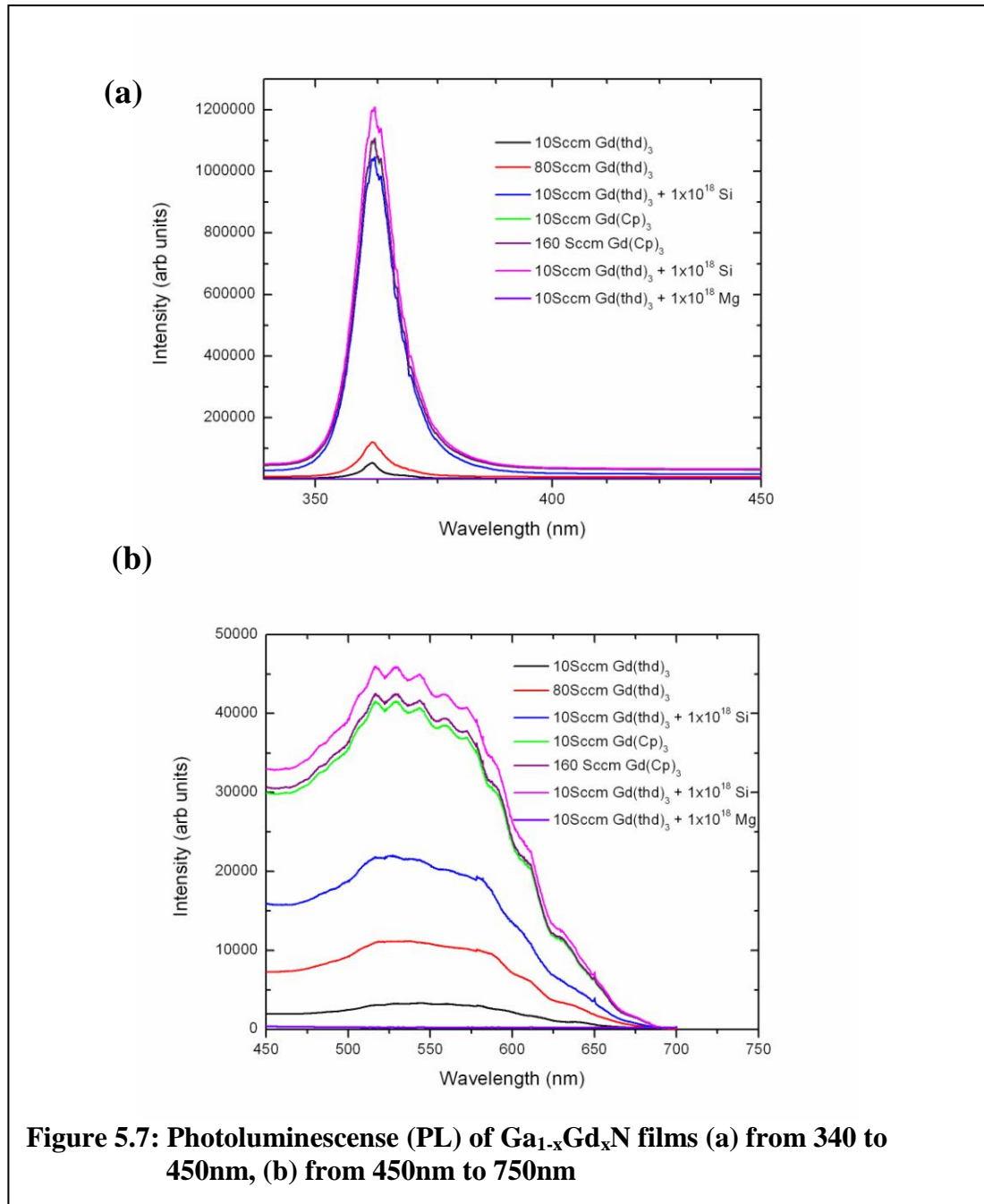
The PL spectra were observed for all undoped and doped Ga<sub>1-x</sub>Gd<sub>x</sub>N films. A continuous wave (CW) PL system with a HeCd 325nm wavelength laser as the pump source was used for these measurements.

The PL spectra of all the layers show the typical GaN band edge peak at 3.4eV except for the Mg co-doped samples, where it is absent (Figure 5.7a). The suppression of band edge emission is quite typical of a compensated sample, and such is the case with these Mg co-doped samples. The peaks of the PL spectra of the Ga<sub>1-x</sub>Gd<sub>x</sub>N films grown with the Gd(thd)<sub>3</sub> source are vastly diminished and are significantly enhanced with Si co-

doping. In contrast, the peaks of the films grown with the  $(\text{Cp})_3\text{Gd}$  source are of much higher intensity and do not change with Si co-doping.

The other prominent feature of the PL spectra of  $\text{Ga}_{1-x}\text{Gd}_x\text{N}$  films is the presence of a broad peak centered at 550nm for all the samples – again except for the Mg co-doped ones – as seen in Figure 5.7b. There are a number of different explanations in the literature for this typical feature present in GaN films. Most of the reports identify the Ga vacancies ( $V_{\text{Ga}}$ ) as its origin [121], however some reports ascribe it to a complex between  $V_{\text{Ga}}$  and Si or oxygen [122]. In either case the incorporation of Gd in the films causes this broad peak at 550nm to emerge more prominently than is typically observed in GaN films. Both the literature [123] and our experimental findings confirm this.

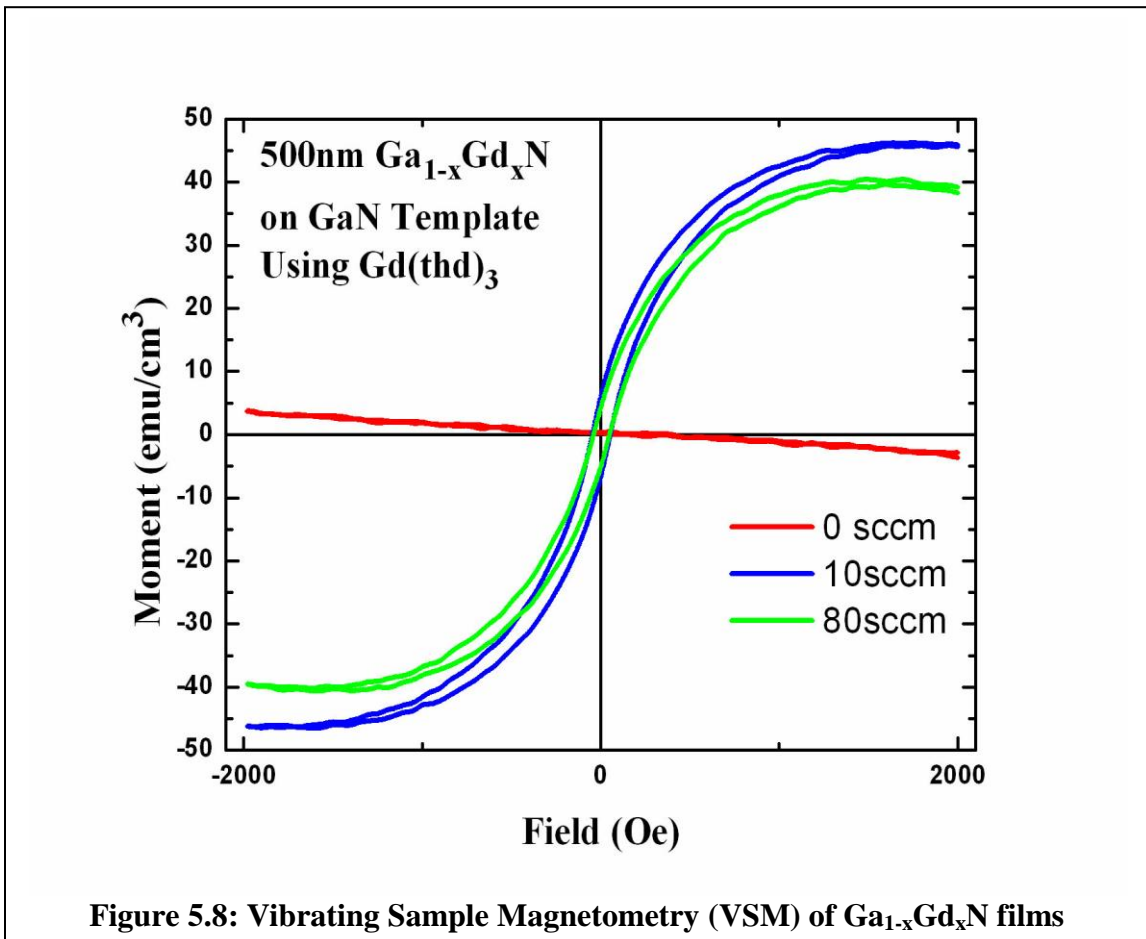
The intensity of the broad band seen in Figure 5.7b increases with increasing Gd incorporation, as observed in the EDS data – discussed later in Section 5.12 and tabulated in Table 5.2.



## 5.8 Magnetic Characterization

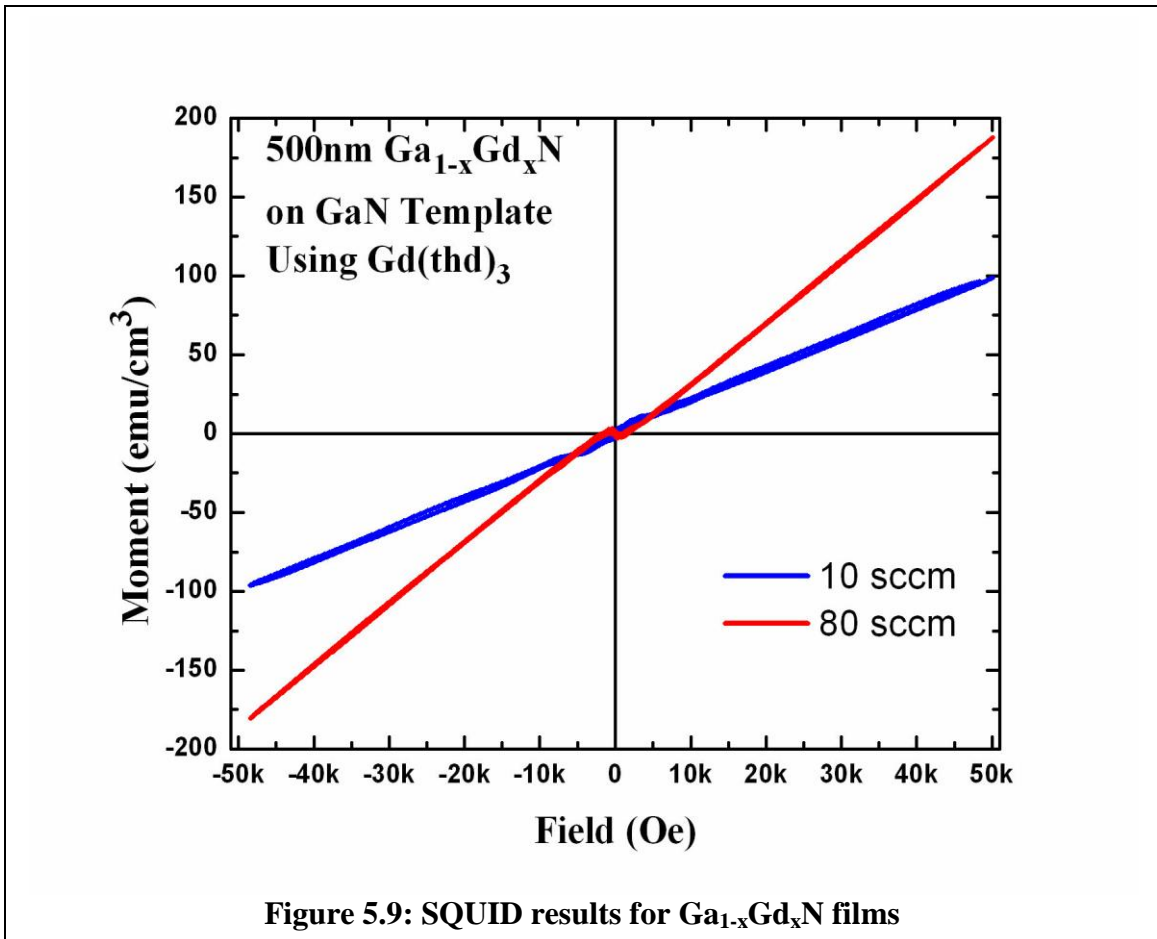
Two magnetic characterization techniques were used to analyze the samples: VSM and SQUID. A weak ferromagnetic behavior was observed for films grown with a

Gd(thd)<sub>3</sub> flow rate of 10sccm, and increasing the flow rate up to 80sccm did not significantly change the magnetic behavior, as seen in Figure 5.8. The coercive field for these films was approximately 50 Oe, and the saturation magnetization varied from 40 emu/cm<sup>3</sup> to 48 emu/cm<sup>3</sup>. The Ga<sub>1-x</sub>Gd<sub>x</sub>N films grown with the (Cp)<sub>3</sub>Gd precursor, however, did not show any significant ferromagnetic behavior. This leads to the conclusion that oxygen plays a major role in the ferromagnetic behavior of the Ga<sub>1-x</sub>Gd<sub>x</sub>N films grown in this work.

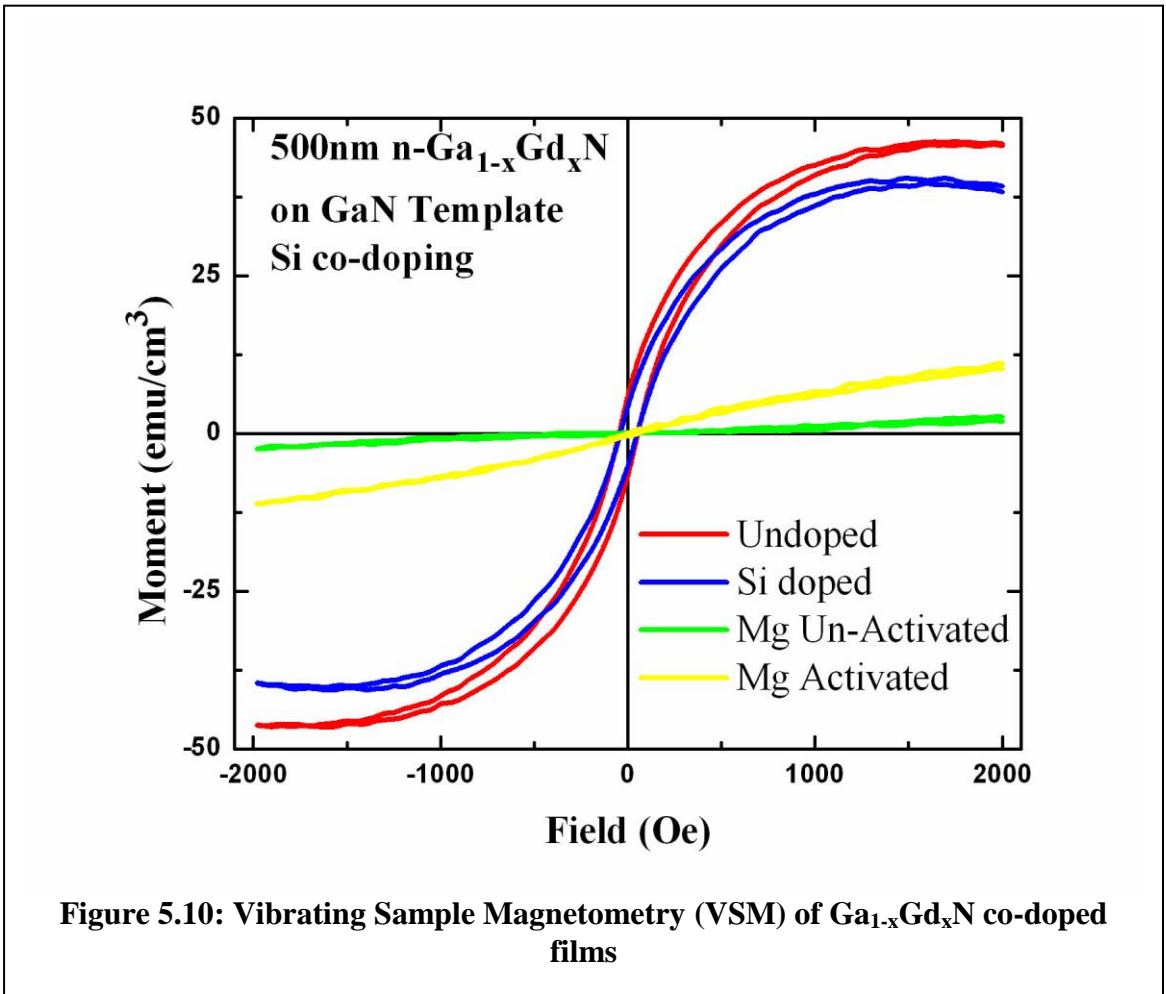


In order to observe the behavior of the films under high magnetic fields, measurements were made with SQUID. A salient paramagnetic signature was observed in the films under the influence of high magnetic fields (Figure 5.9). It can be concluded

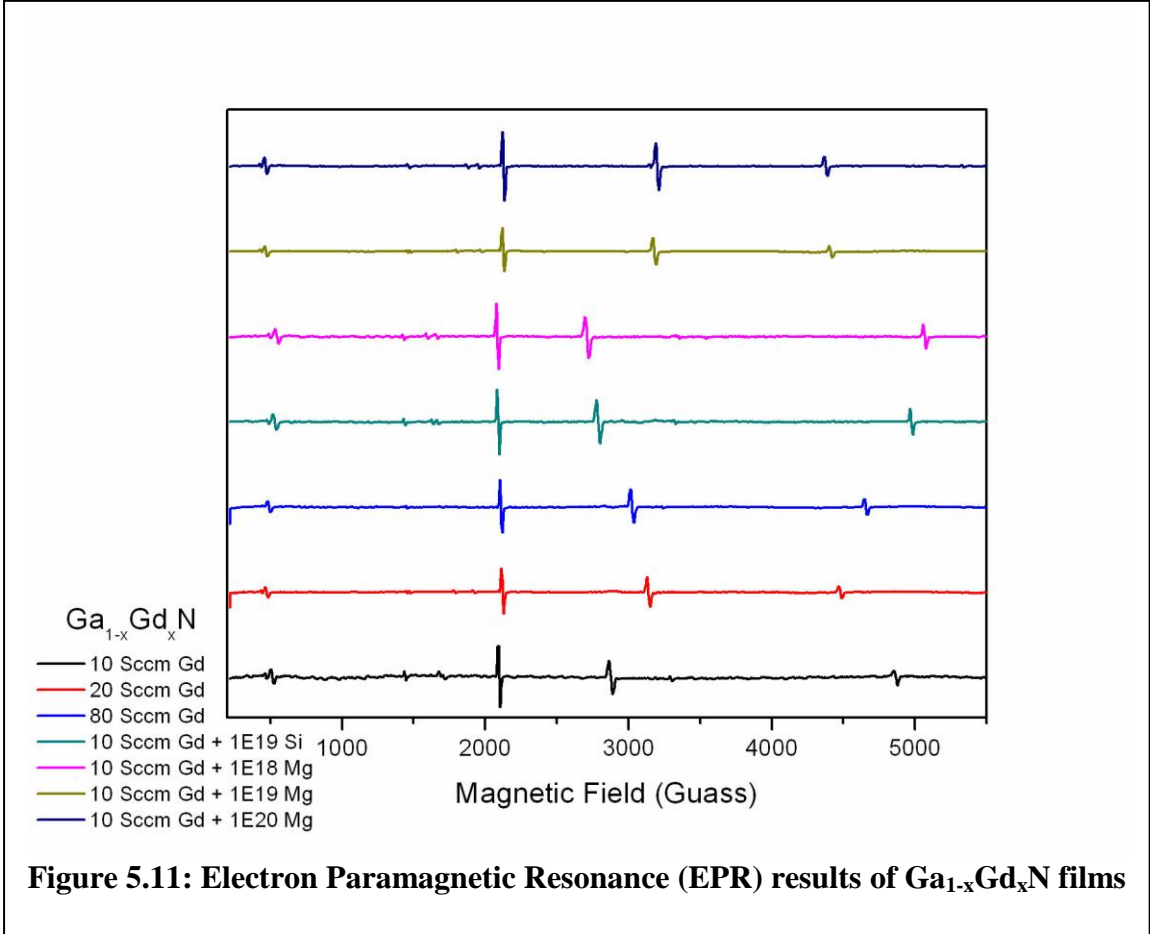
that these  $\text{Ga}_{1-x}\text{Gd}_x\text{N}$  films show dual magnetic behavior. Under weak magnet fields the weak ferromagnetic behavior observed can be attributed to the presence of oxygen in the films. The presence of nanoscale  $\text{Gd}_2\text{O}_3$  could provide a likely explanation, as it is known to display ferromagnetic behavior. The paramagnetic behavior observed scales with the Gd flow rate. Gd does show a paramagnetic behavior due to its  $4f^7$  electrons. The  $4f$  shell of rare earth elements is shielded by the outer  $5d$  and  $6s$  shells and is not quenched, as discussed earlier in Section 2.3. This type of dual magnetic behavior of the  $\text{Ga}_{1-x}\text{Gd}_x\text{N}$  films was reported by Hejtmánek et al. [124], and these experimental results confirm their findings.



As the  $\text{Ga}_{1-x}\text{Gd}_x\text{N}$  films grown with a 10sccm  $\text{Gd}(\text{thd})_3$  flow rate generated the best ferromagnetic signature, they were used as the reference to explore the ferromagnetic behavior as a function of co-doping with Si and Mg. The effect of co-doping  $\text{Ga}_{1-x}\text{Gd}_x\text{N}$  films with Si ( $10^{18}\text{cm}^{-3}$ ) and Mg ( $10^{19}\text{cm}^{-3}$ ) on their magnetic property is shown in Figure 5.10. It can be seen that co-doping with Si did not have any significant effect on the magnetic property, however co-doping with Mg decreased the ferromagnetic behavior. Upon activation of the Mg co-doped films by annealing in an  $\text{N}_2$  environment at  $800^\circ\text{C}$  for 10 minutes, a slight improvement in their ferromagnetic behavior was observed.



In order to determine the state of Gd within the  $\text{Ga}_{1-x}\text{Gd}_x\text{N}$  films, electron paramagnetic resonance studies were performed on all the samples. These samples were cleaved along the crystal axis, and the resulting spectra are shown in Figure 5.11.



EPR measurements were made at room temperature with a Bruker EleXsys E-500 spectrometer. The X-band spectrometer consists of an SHQE-W1 cavity, SuperX bridge, NMR Tesla meter, and field/frequency stabilizer. Data were acquired by taking the first derivative of the absorption curve with a field modulation of 100 kHz and amplitude of 0.5 mT. 5 mW of microwave power was applied to the sample. Single samples were placed on a specialized sample holder for samples with a known orientation and inserted

into the microwave cavity with a magnetic field oriented parallel to the plane of the sample.

Rotation studies were not performed, and this probably accounts for the varying field/g values at the larger fields. Future studies can utilize the oriented nature of the materials and examine the g value as a function of the magnetic field for the various samples. The sapphire substrate does not appear to generate a background signal. EPR signals due to Al in the substrate would give rise to a more complex pattern compared to the one observed, and the TM impurities likely to be present in it like  $\text{Cr}^{3+}$  would not generate the observed hyperfine pattern.

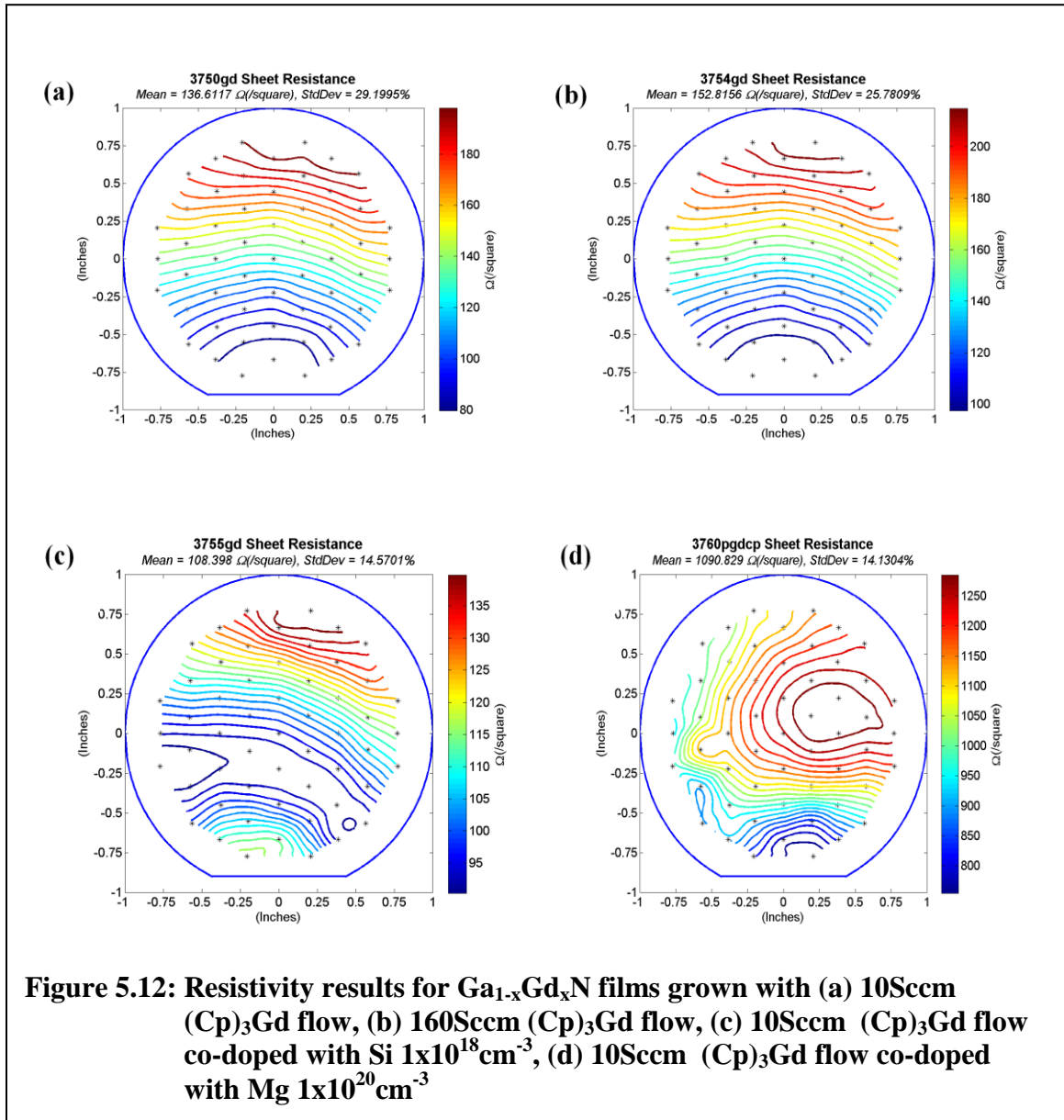
The dominant signals, with resonances near 500, 2000, ~3000, and ~4700 Gauss, are due to  $\text{Gd}^{3+}$ ; however an absolute confirmation would require rotational and temperature-dependent studies.

Judging from the asymmetry of the hyperfine pattern and the asymmetry of the individual resonances, the signal appears to have near-axial symmetry (in the g tensor,  $g_z = g_{\text{perpendicular}}$  and  $g_x = g_y = g_{\text{parallel}}$ ).

## 5.9 Electrical Characterization

Another unique characteristic of the  $\text{Ga}_{1-x}\text{Gd}_x\text{N}$  films grown by MOCVD was their low resistivity. This was confirmed by the measurements on these films with the Lakeshore resistivity mapper. The results of these measurements are shown in Figure 5.12. The resistivity of the films did not change significantly with an increase in the Gd precursor flow rate (Figure 5.12a and 5.12b). As expected, Si co-doping decreases the resistivity (Figure 5.12c) while Mg co-doping increases it (Figure 5.12d). The increase in

resistivity for Mg co-doping can be explained by the compensated nature of the films due to background carrier compensation by Mg doping.



Results of the Hall Effect measurements carried out on the  $\text{Ga}_{1-x}\text{Gd}_x\text{N}$  films are shown in Table 5.1.

**Table 5.1: Hall Data for  $\text{Ga}_{1-x}\text{Gd}_x\text{N}$  films**

Sample	Carriers ( $\text{cm}^{-3}$ )	Mobility ( $\text{cm}^2/\text{Vs}$ )
Undoped GaN	$-1.0 \times 10^{17}$	300
$\text{Ga}_{1-x}\text{Gd}_x\text{N}$ 10 Sccm Flow	$-1.3 \times 10^{18}$	418
$\text{Ga}_{1-x}\text{Gd}_x\text{N}$ 80 Sccm Flow	$-1.5 \times 10^{18}$	361
$\text{Ga}_{1-x}\text{Gd}_x\text{N}$ 10 Sccm Flow Si co-doped $1 \times 10^{18} \text{cm}^{-3}$	$-7.6 \times 10^{18}$	235
$\text{Ga}_{1-x}\text{Gd}_x\text{N}$ 10 Sccm Flow Mg co-doped $1 \times 10^{18} \text{cm}^{-3}$ to $1 \times 10^{20} \text{cm}^{-3}$ unactivated	$2.0 \times 10^{14}$ to $2.0 \times 10^{16}$	2.5 to 7.3

It was observed that Gd doping in GaN increased the background carrier concentration. This increase in carrier concentration should not result from Gd incorporation since Gd is expected to be isovalent in GaN, substitutionally replacing Ga in the lattice. The more likely reason for this increase in background carrier concentration might be as a consequence of an increased number of defects from either Gd incorporation or the oxygen (O) incorporation. Any large-scale increase in defects normally also results in an increase in the XRD FWHM, which was not observed for these films. As a donor impurity, oxygen could be responsible for this increase in background carriers. The increased oxygen incorporation will also result due to the affinity of Gd for oxygen, as described earlier, and EDS data for the films presented later in this chapter also confirms it.

An increase in resistivity of  $\text{Ga}_{1-x}\text{Gd}_x\text{N}$  films because of Mg co-doping was observed, as discussed earlier, and the Hall results confirm this. The Hall data for the Mg-doped films showed inconclusive evidence of p-type behavior of the films. The reason for this

observation is the passivated nature of the unactivated Mg due to Mg-H bonds. This makes the carrier concentration low, and, therefore, their detection through the Hall Effect is difficult. In addition, parallel conductivity of the Hall current through higher-conductivity lower layers in the  $\text{Ga}_{1-x}\text{Gd}_x\text{N}$  films also contributes to the inaccuracy of the Hall measurement. Finally the formation of ohmic contacts on a p-type GaN is a known problem. It is not possible to make a high-quality ohmic contacts by soldering Ga/In contacts in the lab. Typically, the best way to make an ohmic contact, is to deposit an oxidized Ni/Au contact onto the clean surface.

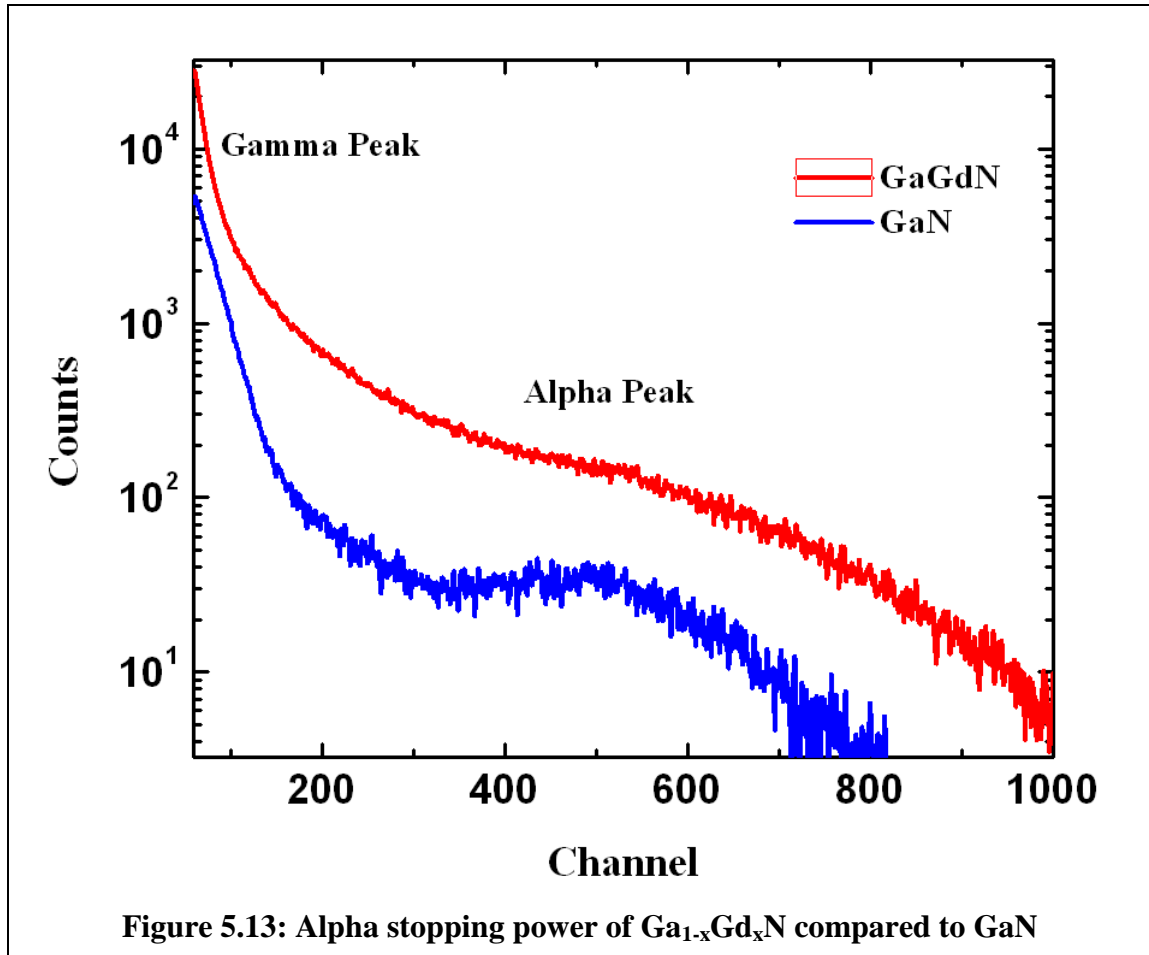
In order to establish the p-type behavior of the Mg co-doped  $\text{Ga}_{1-x}\text{Gd}_x\text{N}$  films, p-n diode structures were grown, comprising a  $1 \times 10^{18} \text{ cm}^{-3}$  Si co-doped  $\text{Ga}_{1-x}\text{Gd}_x\text{N}$  layer and a  $1 \times 10^{19} \text{ cm}^{-3}$  Mg co-doped layer. The Mg in the layer was activated in the growth reactor (in-situ) with a post-growth anneal at  $800^\circ\text{C}$  with an  $\text{N}_2$  environment. Subsequently, top and bottom ohmic contacts were deposited onto the diode structure. Finally, an LED structure using these n- and p-type layers was grown and fabricated. The I-V characteristic of the LED is shown in Figure 6.8.

### **5.10 Alpha Stopping Power of $\text{Ga}_{1-x}\text{Gd}_x\text{N}$ thin Films**

In order to detect the presence of Gd in the  $\text{Ga}_{1-x}\text{Gd}_x\text{N}$  thin films, one of the techniques employed, was to measure the alpha stopping power of the grown  $\text{Ga}_{1-x}\text{Gd}_x\text{N}$  thin films.

The theory that forms the basis for this technique is that the alpha particles can be more effectively stopped by the elements with a higher  $Z$  number (atomic number). So the higher the  $Z$  number of the elements in the target material's crystal structure, the more effectively it will stop the alpha particles.

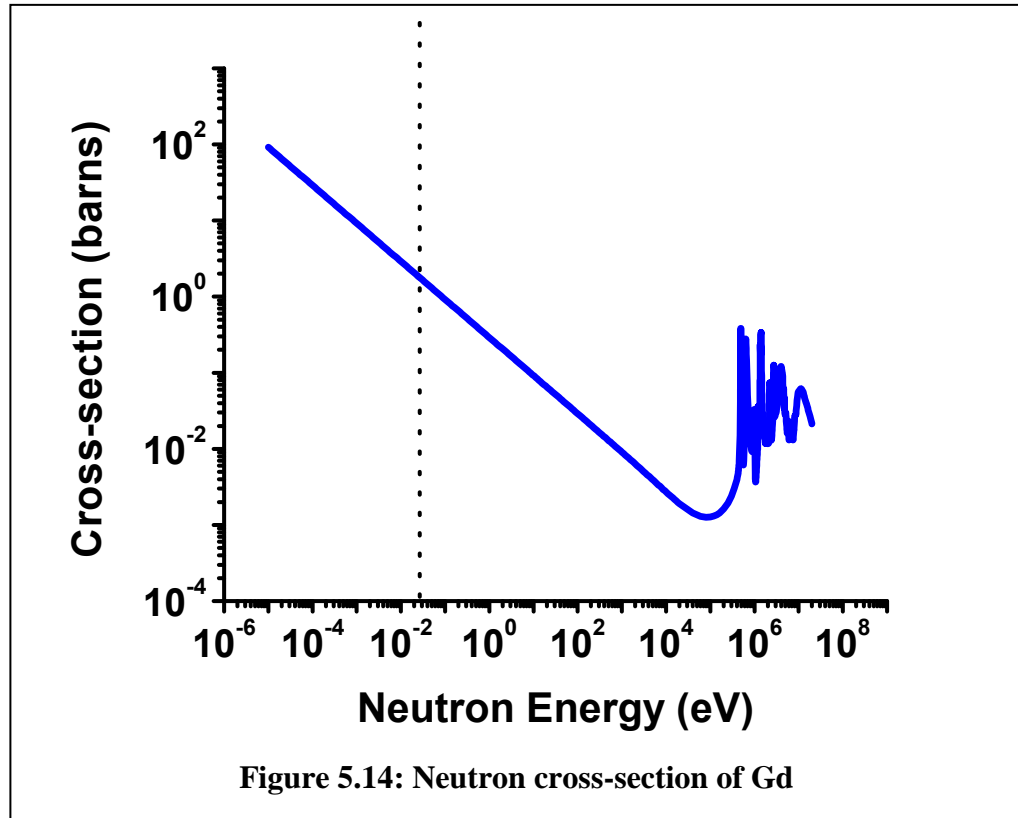
In this technique, alpha particles from a  $^{241}\text{Am}$  source bombarded a  $2.5\ \mu\text{m}$  GaN template and then an equally thick  $\text{Ga}_{1-x}\text{Gd}_x\text{N}$  film grown on GaN template. The results obtained from this technique are plotted in Figure 5.13. The increase in alpha stopping power clearly indicated a larger quantity of higher Z number particles in the  $\text{Ga}_{1-x}\text{Gd}_x\text{N}$  films.



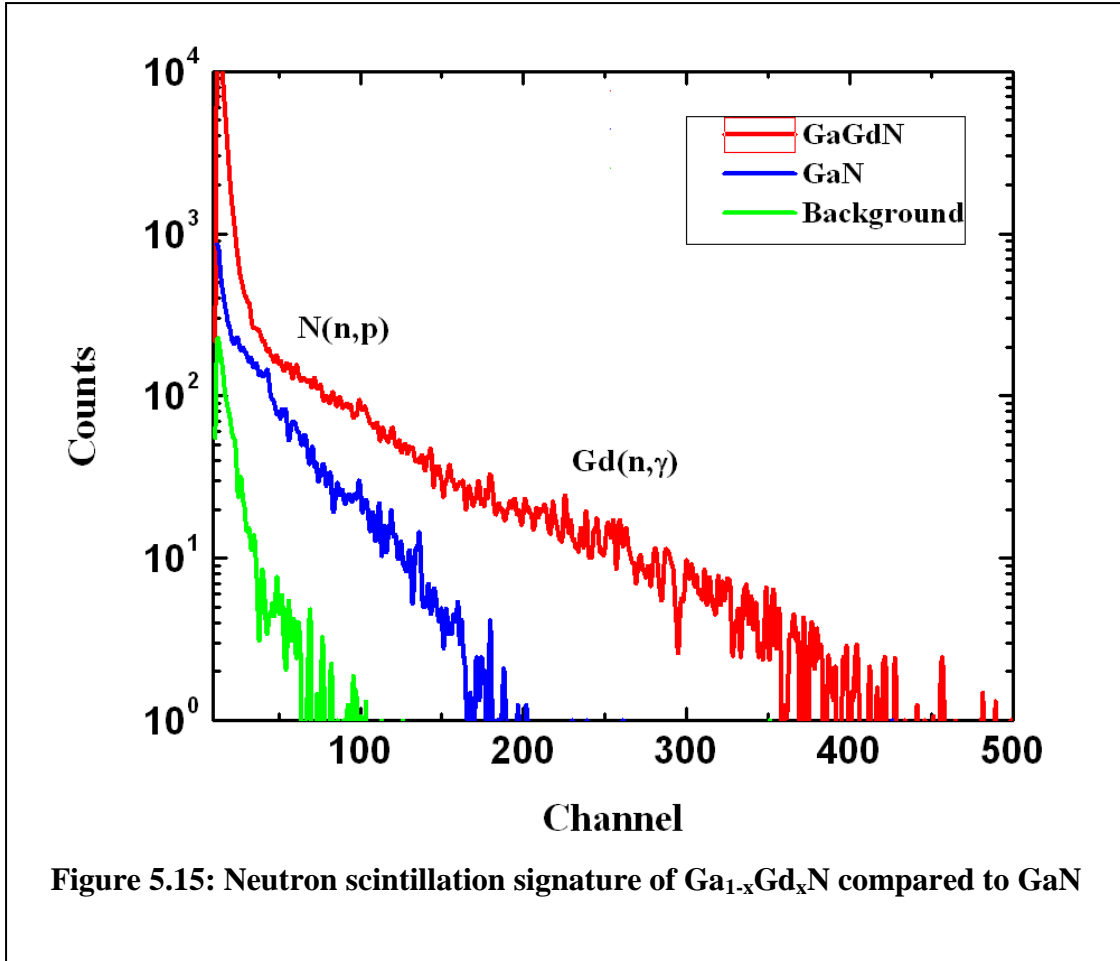
### 5.11 Neutron Scintillation Property of $\text{Ga}_{1-x}\text{Gd}_x\text{N}$ Thin Films

A very useful property of Gd element is its large neutron cross-section. The neutron cross-section  $\sigma$  is given in barns ( $10^{-28}\ \text{m}^2$ ). In the case of Gd, this neutron cross-section

for thermal neutrons (low energy neutrons) is 255,000 barns. Figure 5.14 shows how the neutron cross-section of Gd varies with the energy of the neutrons.



For this test, neutrons from a PuBe neutron source were first moderated to thermal energies using a graphite pile. These thermal neutrons were then used to bombard a 2.5  $\mu\text{m}$  GaN template and then an equally thick  $\text{Ga}_{1-x}\text{Gd}_x\text{N}$  film grown on a GaN template. The results are plotted in Figure 5.15. The increased tail clearly indicates a much larger neutron cross-section of the  $\text{Ga}_{1-x}\text{Gd}_x\text{N}$  films.



### 5.12 EDS Data for $\text{Ga}_{1-x}\text{Gd}_x\text{N}$ Thin Film Composition

EDS is a chemical microanalysis technique performed in conjunction with a scanning electron microscope (SEM). It identifies the elements in the sample by their characteristic X-ray energy. The spectrum of the energy versus the relative counts of the detected X-rays is obtained and evaluated for qualitative and quantitative determinations of the elements present in the sample. The EDS used in this study was attached to LEO 1530 SEM that had an operating voltage in the range of 200 V to 30 kV with a resolution of up to 1nm.

The Ga<sub>1-x</sub>Gd<sub>x</sub>N films were tested for Gd using EDS, and the results obtained are shown in Table 5.2. All the Ga<sub>1-x</sub>Gd<sub>x</sub>N films grown with the Gd(thd)<sub>3</sub> doping source show the presence of Oxygen in the films, while those with the (Cp)<sub>3</sub>Gd doping source do not show any significant amount of oxygen. The Gd presence was detected in all the Ga<sub>1-x</sub>Gd<sub>x</sub>N films. The amount of Gd varied from 0.01% to 0.06% with a Gd(thd)<sub>3</sub> gas phase flow rate of 10sccm to 80sccm. When the (Cp)<sub>3</sub>Gd doping source was applied, the amount of Gd varied from 0.35% to 0.53% for gas phase flow rate of 10sccm to 160sccm.

**Table 5.2: EDS for Ga<sub>1-x</sub>Gd<sub>x</sub>N films**

<b>Spectrum</b>	<b>C (%)</b>	<b>N (%)</b>	<b>O (%)</b>	<b>Ga (%)</b>	<b>Gd (%)</b>
3639ugd [10 Sccm Gd(thd) <sub>3</sub> ]	9.90	44.41	1.18	44.46	0.06
3641ugd [40 Sccm Gd(thd) <sub>3</sub> ]	3.55	48.46	0.88	49.07	0.01
3642ugd [80 Sccm Gd(thd) <sub>3</sub> ]	2.09	48.61	1.55	47.74	0.01
3750ugd [10 Sccm (Cp) <sub>3</sub> Gd]	8.83	47.03	-	46.51	0.35
3753ugd [80 Sccm(Cp) <sub>3</sub> Gd]	6.96	46.37	-	46.33	0.34
3754ugd [160 Sccm (Cp) <sub>3</sub> Gd]	2.31	49.67	-	47.48	0.53
3754ugd (1/2 etch) Etched to 250nm	5.89	46.34	-	47.45	0.31
3754ugd (Full etch) Etched to 750nm	1.66	48.10	-	50.36	-

In order to see if the Gd incorporation was deep inside the films, one of the samples (3754ugd) was etched and re-measured. This sample had a 500nm Ga<sub>1-x</sub>Gd<sub>x</sub>N film grown on a 2µm GaN template. The etch depth on the two pieces was set to a ½ etch (250nm depth) and full etch (750nm depth). The etching was done using inductively coupled plasma (ICP). The EDS results show Gd presence at ½ depths but did not detect Gd in full etch samples. The interesting thing to note is the detection of a lower percentage of

Gd at 1/2 depths in comparison to the amount detected on the surface for the same sample. This shows that the amount of Gd present on the surface is higher than within the films.

### 5.13 Analysis and Conclusions

The XRD data of the  $\text{Ga}_{1-x}\text{Gd}_x\text{N}$  films neither showed major signs of strain nor formation of any secondary phase. However, the films grown with  $\text{Gd}(\text{thd})_3$  did show a slight systematic shift to higher angles with increased gas phase flow rate. This systematic shift indicates a slight decrease in the 'c' lattice parameter. This runs contrary to the expectation of an increase in lattice parameter with Gd incorporation in the films, since the Gd atom is 28% larger in diameter in comparison to Ga atom that it is expected to substitutionally replace.

In the case of the films grown with the  $(\text{Cp})_3\text{Gd}$  source, this systematic shift of the peak is not seen and the behavior of these films is consistent with the reports in literature for  $\text{Ga}_{1-x}\text{Gd}_x\text{N}$  and points towards no secondary phase formation, no deterioration in crystal quality, and negligible stress in the films.

Formation of nanoscale secondary phase Gd complexes below the detection limit of XRD has been proposed by some and rejected by others; however none of our experimental results could either confirm or reject such a possibility.

According to the VSM measurements, all the  $\text{Ga}_{1-x}\text{Gd}_x\text{N}$  films grown using  $\text{Gd}(\text{thd})_3$  doping source show room temperature ferromagnetic behavior. Mg doping is seen to significantly reduce this saturation magnetization. The films grown using  $(\text{Cp})_3\text{Gd}$  doping source show negligible ferromagnetic behavior. This leads to the conclusion that oxygen plays a major role in magnetism in the  $\text{Ga}_{1-x}\text{Gd}_x\text{N}$  films grown in this work. EDS data of the films confirms a large oxygen presence in the films grown using the  $\text{Gd}(\text{thd})_3$  source.

All the  $\text{Ga}_{1-x}\text{Gd}_x\text{N}$  films were found to be conductive. Doping with Si increased the conductivity of the films, while doping with Mg increased their resistivity. The increased resistivity by Mg doping can be explained by the compensation of the background carriers. The Hall Effect data shows the increase in background carrier concentration with Gd incorporation. The interesting aspect is that the increased carrier concentration does not scale with the amount of Gd incorporated into the films and remains constant around  $1 \times 10^{18} \text{ cm}^{-3}$ . The reason for the increased background carrier concentration could be a result of increased Oxygen in the films. The increased Oxygen in the films in the case of films grown with  $\text{Gd}(\text{thd})_3$  precursor is confirmed by the EDS data. The increased conductivity in the film grown with the  $(\text{Cp})_3\text{Gd}$  precursor also raises the question, whether Oxygen is actually the cause, since this precursor does not have any Oxygen in it, unlike  $\text{Gd}(\text{thd})_3$  that has six Oxygen atoms with each Gd atom in its chemical structure. The likely cause of increased background carrier concentration and conductivity for the  $(\text{Cp})_3\text{Gd}$  films can still be the oxygen present, finding its way in the films as Gd has a strong affinity for Oxygen and is a known “Oxygen getter.” The other possible cause could be the defects resulting from the Gd incorporation.

The p-type behavior of Mg-doped  $\text{Ga}_{1-x}\text{Gd}_x\text{N}$  films could not be conclusively determined on the basis of Hall measurements. Hall carrier type does point towards p-type material; however the carrier concentrations shown were too low and varied with each measurement in the range of  $2 \times 10^{14} \text{ cm}^{-3}$  to  $2 \times 10^{16} \text{ cm}^{-3}$ . The reasons for this are discussed in detail in section 5.9 above. In order to conclusively determine the p-type behavior of the films p-n diode, LED structures were grown and Ohmic p and n contacts

were deposited onto the corresponding layer types. The I-V characteristics of the LED are shown in Figure 6.8. This established the p-type behavior of the Mg co-doped films.

The presence of Gd in the films was tested with the alpha stopping power and the neutron cross-section increase. These two techniques were borrowed from the nuclear science and engineering department of Georgia Tech. Both these techniques conclusively show the presence of Gd in the films. The magnitude of the increase in alpha stopping power and neutron cross-section increase can be calculated and used for determination of the amount of Gd in the films. These calculations, however, do not give the depth profile of the Gd in the films.

The most interesting characterization data came from the electron paramagnetic resonance (EPR) studies. The EPR results confirmed the 3+ charge state of the Gd atom. The hyperfine pattern of  $Gd^{3+}$  was seen in all the films with resonances near 500, 2000, 3000 and 4700 Gauss. The asymmetry of the hyperfine pattern points to a near-axial symmetry of Gd in the films. The EPR also confirms the highly oriented state of Gd that points towards a strong possibility of its substitutional placement inside the crystal structure.

#### **5.14 Summary**

The issues related to Gd-doping of GaN were discussed in detail in this chapter. Areas covered included Gd precursor selection, delivery system modification, optimum growth conditions for  $Ga_{1-x}Gd_xN$  films, n-type films with Si co-doping, p-type films with Mg co-doping, and growth of  $Ga_{1-x}Gd_xN$  pn diode structure. Finally, a p-n diode structure with  $Ga_{1-x}Gd_xN$  films was successfully grown and its I-V curve shown.

No change in structural property of the  $\text{Ga}_{1-x}\text{Gd}_x\text{N}$  films related to Gd doping was observed by XRD. The presence of Gd in the  $\text{Ga}_{1-x}\text{Gd}_x\text{N}$  films was detected using EDS, alpha stopping power increase, and neutron cross-section increase. All grown  $\text{Ga}_{1-x}\text{Gd}_x\text{N}$  films show conductive nature. The films grown using the  $\text{Gd}(\text{thd})_3$  doping source show significant room temperature ferromagnetic behavior.

This work highlighted in this chapter lays the foundation for the growth of a spin-polarized LED structure that is discussed in the next chapter.

## CHAPTER 6: SPIN-POLARIZED LIGHT EMITTING DIODE

### 6.1 Introduction

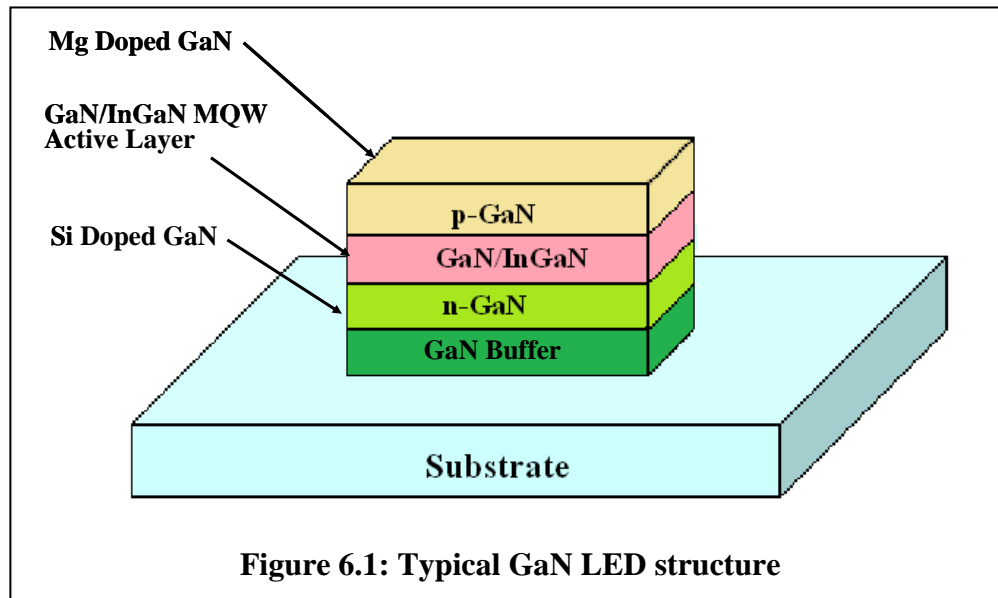
So far in this dissertation, the theoretical background, experimental work, characterization, and analysis of MOCVD-grown  $\text{Ga}_{1-x}\text{Gd}_x\text{N}$  thin films has been addressed. This chapter focuses on the development of a spintronic and optoelectronic device that, in essence, was the main driver for this research. The work presented thus far laid the foundation for a spin polarized LED – its material structure was grown by MOCVD, fabricated into a device, and, finally, tested for its performance characteristics.

### 6.2 Light Emitting Diode - Historical Background

Electroluminescence was discovered in 1907 by H. J. Round, using a crystal of silicon carbide and a cat's-whisker detector [125]. Oleg Vladimirovich Losev created the first LED in the mid 1920s by expanding on the work done by Round [126]. In 1955 Rubin reported infrared emission from Gallium Arsenide (GaAs) at 808nm (1.42eV) and other semiconductor alloys [127]. Braunstein observed infrared emission generated by simple diode structures using Gallium Antimonide (GaSb), GaAs, Indium Phosphide (InP), and Silicon-Germanium (SiGe) alloys at room temperature and at 77 K. In 1961, Robert Biard and Gary Pittman patented an infrared room temperature LED based on GaAs. Soon after this in 1962, the first practical, visible-spectrum red LED was developed by Nick Holonyak Jr. The first yellow LED was invented by M. George Craford [128], who also improved the brightness of red and red-orange LEDs by a factor

of ten in 1972. In 1976, T.P. Pearsall created the first high-brightness, high-efficiency LEDs for optical fiber telecommunications. [129]

The first blue LEDs were made in 1971 by Jacques Pankove. However, these devices had too little light output to be of much practical use. In the late 1980s, Isamu Akasaki and Hiroshi Amano achieved key breakthroughs in GaN epitaxial growth and p-type doping, ushering in the modern era of GaN-based optoelectronic devices [130-134]. The first high-brightness blue LED was developed by Shuji Nakamura based on InGaN, exploiting critical developments in GaN nucleation on sapphire substrates, and the p-type doping of GaN developed by Akasaki and Amano [135, 136].



By the late 1990s, blue LEDs had become widely available. The typical device structure includes an active region that consists of 3 to 5 InGaN quantum wells, sandwiched between thicker layers of GaN, called cladding layers. The light emission from these LEDs can be varied from violet to amber by varying the relative InN-GaN

fraction in the InGaN quantum wells. A typical schematic of a GaN LED structure is shown in Figure 6.1. The active region may comprise a single or multiple quantum wells (QW), or quantum dots (QD). The most common GaN LED structure has a Si-doped GaN for the n-type layer, GaN/InGaN MQWs with 3 to 5nm thickness, and Mg-doped GaN as the top p-type layer. This research group has extensive experience with the growth of GaN LED structures. This work builds from that expertise.

### 6.3 Spin-Polarized Light Emitting Diode

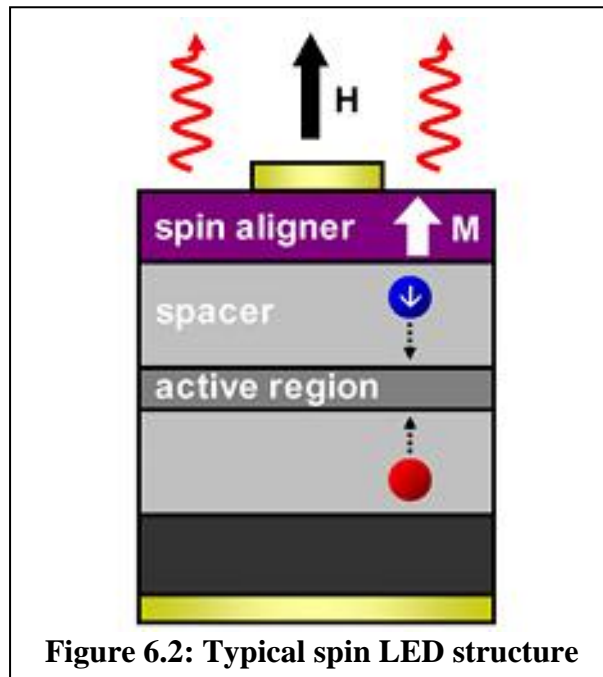


**Figure 6.2: Typical spin LED structure**

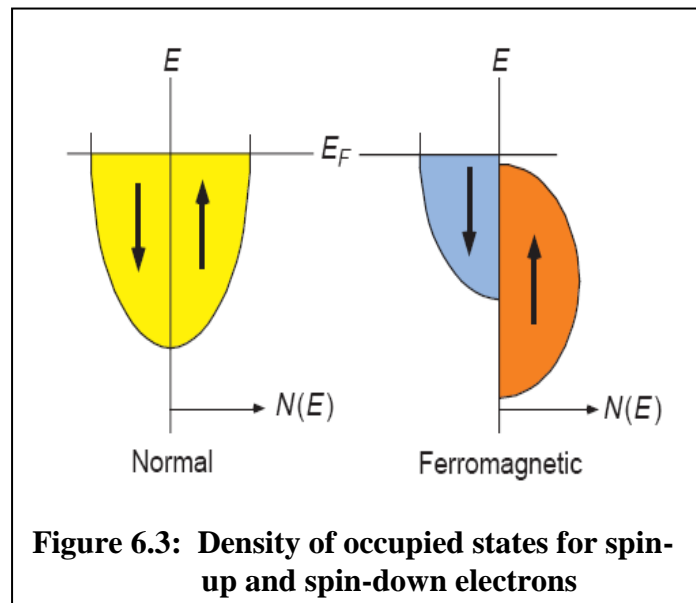
A spin-polarized LED has traditionally been implemented by transferring a non-equilibrium spin population from a ferromagnetic to a forward-biased p-i-n diode, consisting of non-magnetic semiconductors. The injected spins travel from the magnetic contact across a spacer layer and then reach the device's active region. Typically the active region comprises a single or multiple quantum well (QW), or quantum dot (QD) layers. The spin-polarized carriers recombine radiatively with unpolarized carriers

injected from a non-magnetic contact, and the resulting electroluminescence exhibits a net circular polarization. The schematic of a typical spin-LED structure is shown in Figure 6.2.

Implementation of a spin-LED includes two essential requirements: spin-injection, and spin transport. They are discussed in Section 6.3.1 and 6.3.3.

### 6.3.1 Spin-injection

The two primary means of generating spin-polarized carrier populations in semiconductor structures are optical pumping with circularly polarized light (optical orientation) and electrical pumping with a spin-polarized current. Apart from these two commonly implemented techniques, there have been several isolated reports of alternative methods for generating spin currents in literature [137 - 140].



In optical orientation, spin injection is achieved by illuminating a semiconductor with circularly polarized light. Upon absorption of a circularly polarized photon, an electron jumps from the valence band to the conduction band. Just as the energy difference

between the initial and final states must equal the energy of the absorbed photon (energy is conserved), the total spin of the electron-hole pair must equal the angular momentum of the absorbed photon (angular momentum is conserved) [141].

Electrical spin-injection into non-magnetic semiconductors may be achieved via direct injection from a ferromagnetic contact or via injection of current through a spin-aligning layer [142]. In ferromagnetic materials there is a difference in the density of occupied states for spin-up and spin-down electrons (Figure 6.3). When a current is passed from the ferromagnetic material into a non-magnetic semiconductor, the current will be mediated primarily by either majority or minority spins and the current is said to be spin-polarized. The spin asymmetry of the current is a direct consequence of the density of states and mobility asymmetries.

The spin-injection efficiency is limited by several factors including the interface quality, defect/impurity densities, and the band structure [143]. Rashba proposed the use of tunnel contacts as a solution to the conductivity mismatch problem [144], and both magnetic tunnel junctions [145] as well as tunneling through reverse-biased Schottky diodes [146] formed with ferromagnetic metals have been experimentally proven to result in high spin-injection efficiencies.

Another promising approach for efficient electrical spin-injection is through the use of a dilute magnetic semiconductor (DMS) spin aligner in which the conductivity mismatch can be greatly reduced. When an unpolarized current supplied from a non-magnetic metal contact is driven through the DMS layer, the injected electrons quickly scatter into the energetically lower spin sub-band and become spin-polarized within a

picosecond along the magnetic field direction. These spin-polarized carriers may then travel through drift or diffusion into an adjacent, non-magnetic semiconductor.

### 6.3.2 *Spin transport*

A spin-polarized light source can function, only if the injected spins in spin-polarized carriers can retain their orientation from the time they are injected to the time they recombine radiatively and contribute to the circularly polarized emission. Three spin-relaxation mechanisms—namely, the Elliott-Yafet (EY), D'yakonov-Perel (DP) and Bir-Aronov-Pikus (BAP) mechanisms—work to equilibrate asymmetric spin populations.

The EY process arises from spin-orbit coupling induced by host lattice ions, which creates an admixture of opposite spin states for electron wave functions. Whenever an electron is scattered and changes its orbital momentum, the possibility of spin-flip exists even when the scattering interaction is spin-independent. Impurities, boundaries and phonons can all induce transitions between spin-up and spin-down states through the spin-orbit interaction, resulting in spin degradation [147].

The DP spin-relaxation process manifests itself in semiconductors lacking inversion symmetry, e.g. GaAs, for which the spin degeneracy of the conduction band is lifted [148–150]. Mobile electrons experience an effective magnetic field whose magnitude and orientation depend on the electron momentum. Spin precession around this magnetic field gives rise to spin relaxation. The DP spin-relaxation rate is therefore inversely proportional to the electron momentum-scattering rate [151].

Lastly, the BAP process results from electron-hole exchange interactions and is an important relaxation mechanism for electrons in p-doped semiconductors [152]. The electron-hole exchange interaction depends on the spins of the interacting electrons and

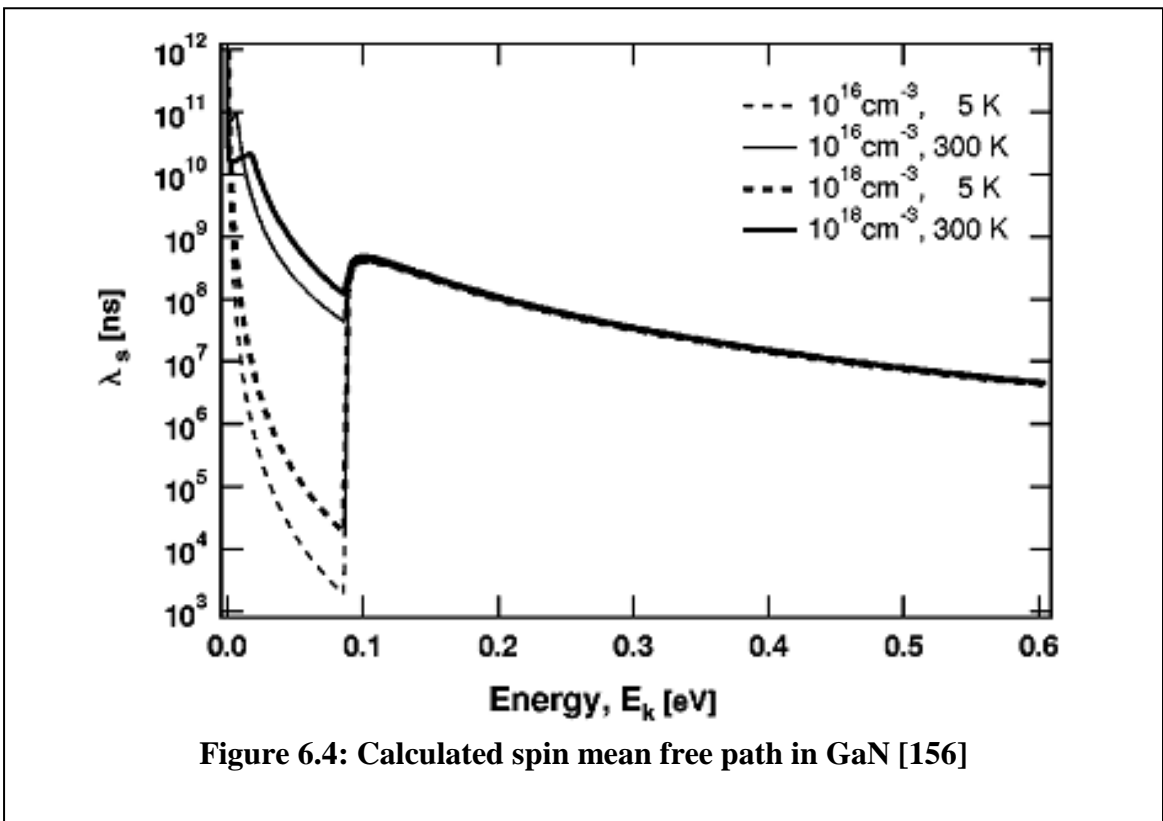
holes and acts upon the electrons as an effective magnetic field. Electron spin precession along this effective magnetic field results in spin relaxation. The BAP relaxation rate increases with the degree of electron and hole spatial overlap, which increases at lower temperatures and for larger confining potentials in the case of QWs and QDs. The relative severity of the three processes depends on the heterostructure design (e.g. the chosen semiconductor(s), dimensionality, doping profile, and epitaxial strain) and the experimental conditions (e.g. temperature, external magnetic/ electric field).

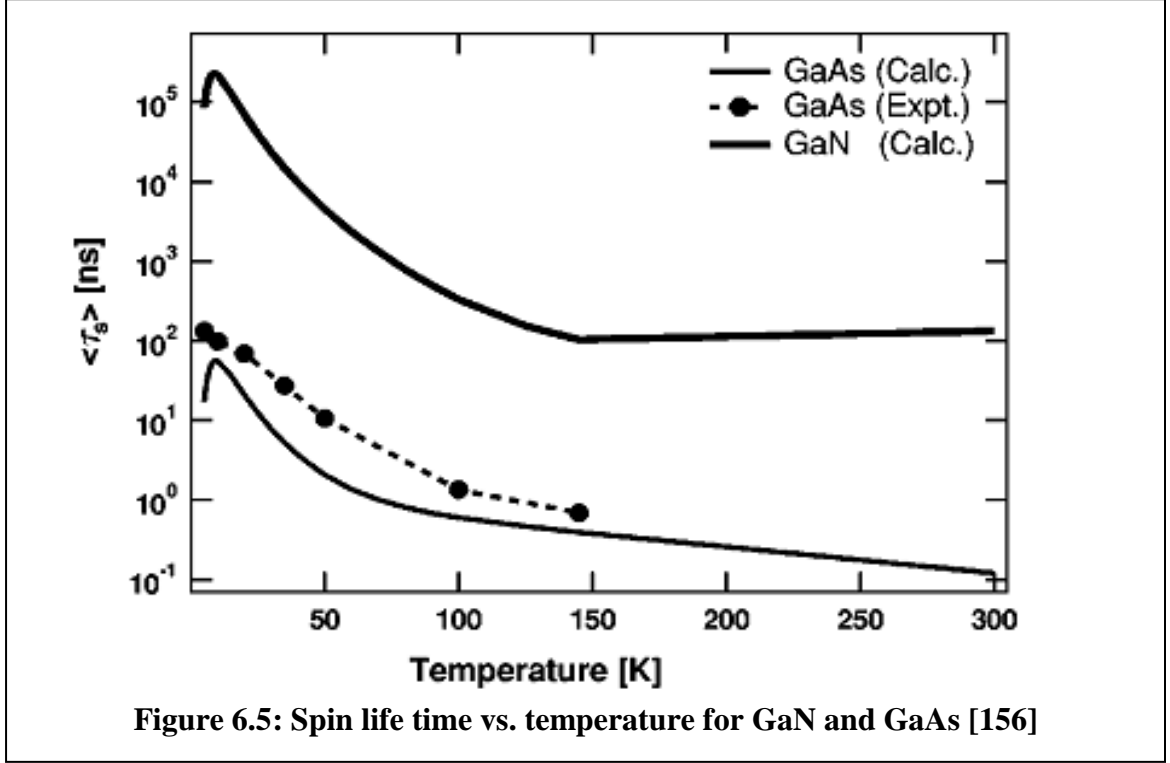
The EY mechanism dominates in small-gap and large-spin-orbit coupling semiconductors, while the DP process dominates in middle-gap materials and at high temperatures for systems with sufficiently low hole densities. In p+-doped semiconductors, the BAP mechanism dominates at lower temperatures, while the DP mechanism dominates at higher temperatures. Spin relaxation of holes is primarily due to EY processes. Spin dynamics differ dramatically in quantum-confined structures when compared with bulk material since the three spin-relaxation mechanisms are influenced by factors such as mobility, charge localization and band structure [154, 155].

The calculated spin mean-free path as a function of injection energy is shown for two donor doping concentrations and temperatures in Figure 6.3 for GaN [156]. For all energies above 10 meV, the DP mechanism is dominant, and, consequently, the spin scattering lifetimes are longer at higher temperatures and higher doping density, where momentum scattering lifetimes are shorter.

The mean-free path of electrons with one LO energy is about 1  $\mu\text{m}$  in GaN, which is much longer than the mean free path of electrons in GaAs (about 0.1  $\mu\text{m}$  for one LO energy). The longer mean-free path of the injected electrons in GaN is primarily

attributed to the small SO splitting (12 meV in GaN and 341 meV in GaAs), large band gap (of 3.4 eV in GaN and 1.5 eV in GaAs), and large DOS (effective mass of  $0.2 m_0$  in GaN and  $0.067 m_0$  in GaAs). At higher energies, the mean-free path continues to decrease in spite of the increase in group velocity. Figure 6.4 shows the averaged spin lifetimes for GaAs and GaN [156, 157]. At very low temperatures, the predicted lifetime decreases with temperature, whereas the measured lifetime appears to reach a plateau.





### 6.3.3 Spin Injection Detection

If the recombination time of the photo-excited spin-polarized electrons and holes is greater than the spin relaxation time in semiconductors then the luminescence will be polarized. If spin-polarized current is injected into an LED and the polarization efficiency of the emitted light is measured, it is possible to determine the spin injection efficiency.

The degree of circular polarization ( $P_{circ}$ ) is given by

$$P_{circ} = \frac{\sigma^+ - \sigma^-}{\sigma^+ + \sigma^-} = \frac{(3n_{\uparrow} + n_{\downarrow}) - (3n_{\downarrow} - n_{\uparrow})}{(3n_{\uparrow} + n_{\downarrow}) + (3n_{\downarrow} - n_{\uparrow})} = \frac{1}{2} \frac{n_{\uparrow} - n_{\downarrow}}{n_{\uparrow} + n_{\downarrow}} = \frac{1}{2} P_{spin} \quad \text{Equation (6.1)}$$

where  $\sigma^+$  is a heavy hole transition,

$\sigma^-$  is a light hole transition,

$n_{\uparrow}$  and  $n_{\downarrow}$  are the occupation of the spin levels, and

$P_{\text{spin}}$  is spin polarization.

Equation (6.1) connects the circular polarization of the emitted electroluminescence with the current density polarization degree, which is given by Equation (6.2):

$$P_j = \frac{j_{\uparrow} - j_{\downarrow}}{j_{\uparrow} + j_{\downarrow}} \quad \text{Equation (6.2)}$$

where  $j$  is the current density of the spin-polarized electrons.

In the case of non-degenerate light and heavy holes, the degree of optical polarization and spin polarization will be equal and has a maximum value of 0.5. In a quantum well the HH and LH bands are separated in energy by quantum confinement. The band splitting is typically several meV even in shallow QWs. Thus only the heavy holes participate in the recombination energy, yielding a maximum spin injection efficiency of 100 %.  $P_{\text{circ}}$  of 0.5 is used for 100 % spin injection efficiency. The degree of polarization of the light is proportional to the degree of polarization of the injected carriers. Spin scattering at the interface and during the diffusion into the QW, however, causes a reduction in this efficiency.

#### **6.3.4 Spin-polarized LED in Literature**

In a spin-polarized light source efficient injection and collection of spin-polarized carriers is critical. Several structures have been proposed and demonstrated experimentally to inject spin-polarized electrons and holes. A comparative summary of spin-injection efficiencies achieved in state-of-the-art spin-LEDs is given in Table 6.1.

**Table 6.1: Spin polarization percentages reported in emissions from spin LEDs.**

Spin injector	Active region	Spin polarization	Temperature	Reference
GaMnAs (holes)	InGaAs QW	7%	5°K	[158]
	InAs QD	1.00%	4.5°K	[159]
GaMnAs Zener	GaAs bulk	82%	4.6°K	[160]
	InGaAs QW	0.82%	5°K	[161]
	InAs QD	1.2% / 0.2%	5°K / 60°K	[162]
ZnMnSe	GaAs bulk	86% / 24%	1.5°K / 33°K	[163]
	InGaAs QD	21%	5°K	[164]
	CdSe QD	70%	2°K	[165]
CdCr <sub>2</sub> Se <sub>4</sub>	GaAs QW	4–6%	5°K	[166]

For efficient spin collection, oriented spins should traverse a minimal distance between the spin injector and the active region, preferably in a semiconductor with a long spin relaxation time. In order to minimize the spin transport length the spin aligner layer should be as close to the active region as possible. However, inter-diffusion of magnetic impurities into the active region could result in unwanted parasitic polarization masking evidence of spin-injection or short out the intrinsic region completely.

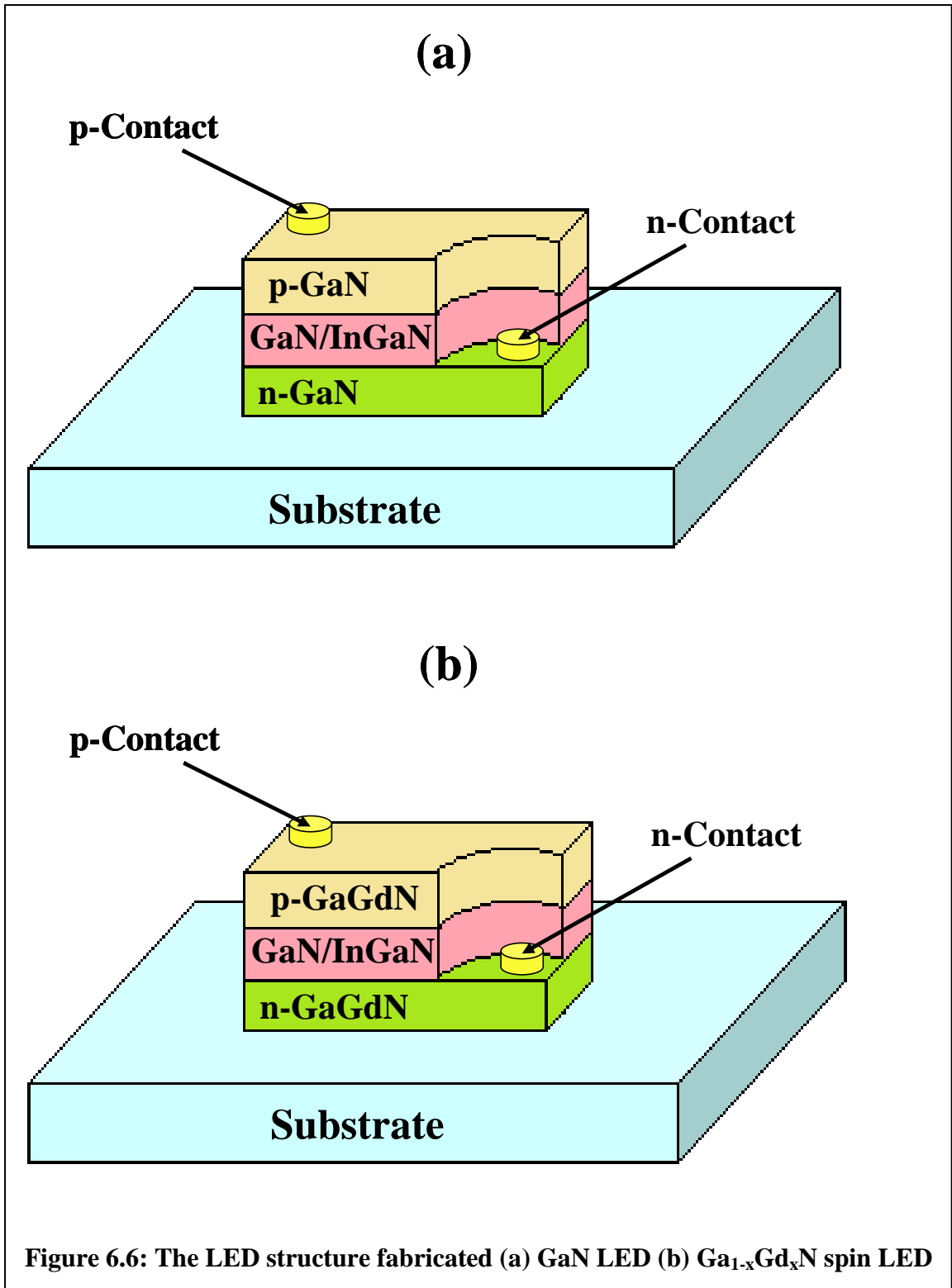
Investigation of anisotropic spin-injection in a (Ga,Mn)As QW spin-LED has shown the EL polarization decrease from 7% to 0.5%, as the thickness of the spacer layer separating the spin aligner and active region was increased from 20nm to 420 nm [158]. It is evident from this result that the spacer layer thickness should be kept to a minimum, while remaining large enough to prevent inter-diffusion of the magnetic dopant into the QWs.

There is still no unambiguous report of a GaN-based spin-polarized LED, inspite of a large spin relaxation time of GaN. This again is primarily due to lack of suitable GaN-based DMS prior to this work. In the previous work done in this lab and others, using magnetic TM impurities has shown these layers to be highly resistive and non-functional

for device structures. This work is aimed at the growth of a  $\text{Ga}_{1-x}\text{Gd}_x\text{N}$  thin film to act as the spin-aligner layer for spin-injection in a GaN-based spin-polarized LED.

#### **6.4 $\text{Ga}_{1-x}\text{Gd}_x\text{N}$ LED by MOCVD**

In the Chapter 5 growth primarily that of  $\text{Ga}_{1-x}\text{Gd}_x\text{N}$  thin films and their doping to get an n-type and p-type material were addressed. Here only the material properties important for and related to the LED structure will be covered. Figure 6.5a shows the schematic structures of a standard and an optimized GaN LED.



A schematic of the modified GaN LED structure used for the growth of a spin-polarized LED based on  $\text{Ga}_{1-x}\text{Gd}_x\text{N}$  is shown in Figure 6.6b. The schematic does not show the spacer layer used before and after the active region.

The baseline GaN LED is an optimized design typically grown in this lab. The design is modification of a commercially grown LED structure. This LED structure design has been successfully used for growth on sapphire, ZnO, Si, and ALD  $\text{Al}_2\text{O}_3$  in other work. The basic design parameters for the baseline GaN LED are shown in Table 6.2.

**Table 6.2: Design structure of the baseline GaN LED**

Layer		Thick	Press.	Temperature (Pyro temp.)	Growth rate	Carrier gas	Doping
<b>p-GaN capping</b>		10-15nm	200torr	U-GaN - 80C	0.2-0.5um/hr	H <sub>2</sub> (or N <sub>2</sub> mix)	same with P-GaN
<b>p-GaN</b>		120 - 150nm	200torr	U-GaN - 80C	1um/hr	H <sub>2</sub> (or N <sub>2</sub> mix)	Cp <sub>2</sub> Mg > 3x10 <sup>19</sup> /c m <sup>-3</sup>
<b>Barrier</b>	x5	12-15nm	100torr	Well + (100~120C)	0.5A/sec	N <sub>2</sub> (or H <sub>2</sub> mix)	No
<b>Well protection layer</b>		1-1.5nm	100torr	740C	0.5A/sec	N <sub>2</sub> only	No
<b>Well</b>		1.5 - 2nm	100torr	740C(470nm)	0.5A/sec	N <sub>2</sub> only	No
<b>Barrier</b>		12-15nm	100torr	Well + (100~120C)	0.5A/sec	N <sub>2</sub> (or H <sub>2</sub> mix)	No
<b>N-GaN</b>		1500-2000nm	200torr	1010-1020C	2um/hr	H <sub>2</sub> (or N <sub>2</sub> mix)	3x10 <sup>18</sup> /c m <sup>-3</sup>
<b>U-GaN</b>		1000-1500nm	200torr	1010-1020C	2um/hr	H <sub>2</sub> (or N <sub>2</sub> mix)	No
<b>High pressure U-GaN (roughing layer)</b>		300-500nm	500torr	990 –1000C	0.5um/hr	H <sub>2</sub> (or N <sub>2</sub> mix)	No
<b>Buffer</b>		25-30nm	500torr	520 – 540C		H <sub>2</sub> (or N <sub>2</sub> mix)	No
<b>Sapphire</b>		320-420um					

#### **6.4.1 Structural Characterization of Ga<sub>1-x</sub>Gd<sub>x</sub>N LED**

XRD of the Ga<sub>1-x</sub>Gd<sub>x</sub>N LED shows the GaN GaN/InGaN QW peaks next to the typical GaN peak (Figure 6.6a). The results of XRD for a standard GaN LED grown with the same GaN/InGaN QW structure is shown in Figure 6.6b.

XRD data of standard GaN LED and Ga<sub>1-x</sub>Gd<sub>x</sub>N LED shown in Figures 6.6(a and b) shows the structural properties of the wells to be the same. The Gd incorporation, however, is seen to cause slight deterioration. Comparison of the two results shows that the QW peaks in the case of the Ga<sub>1-x</sub>Gd<sub>x</sub>N spin LED are suppressed. The cause for this is the Gd diffusion inside the active region affecting the QW boundaries.

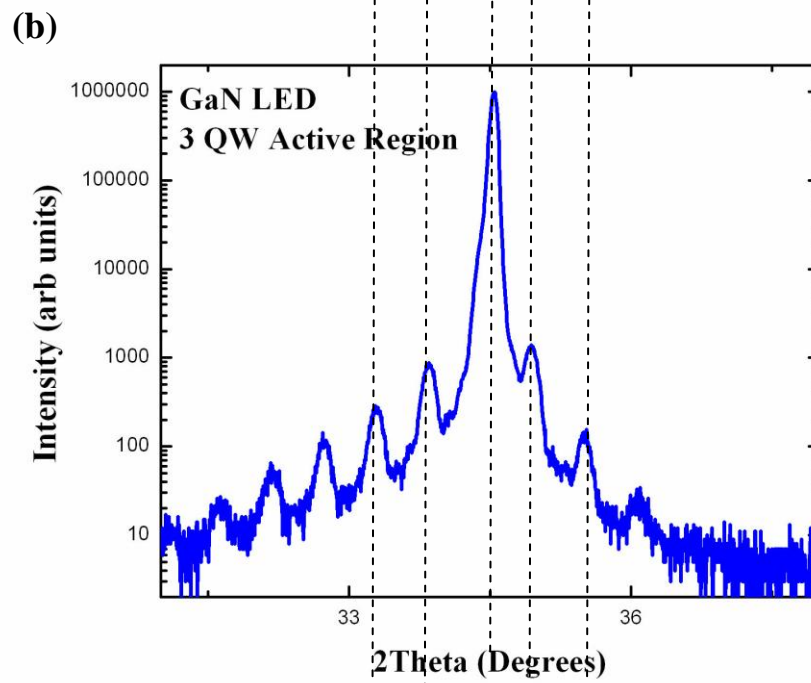
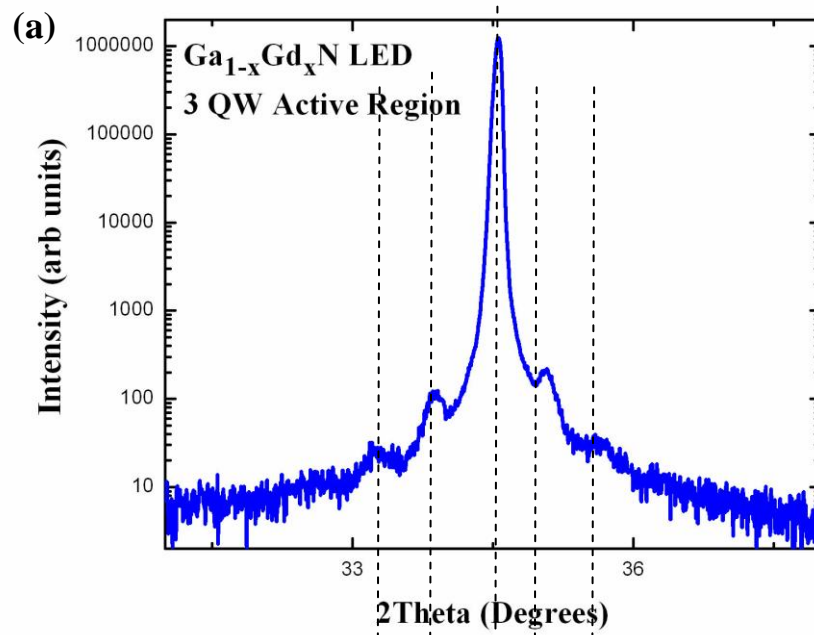
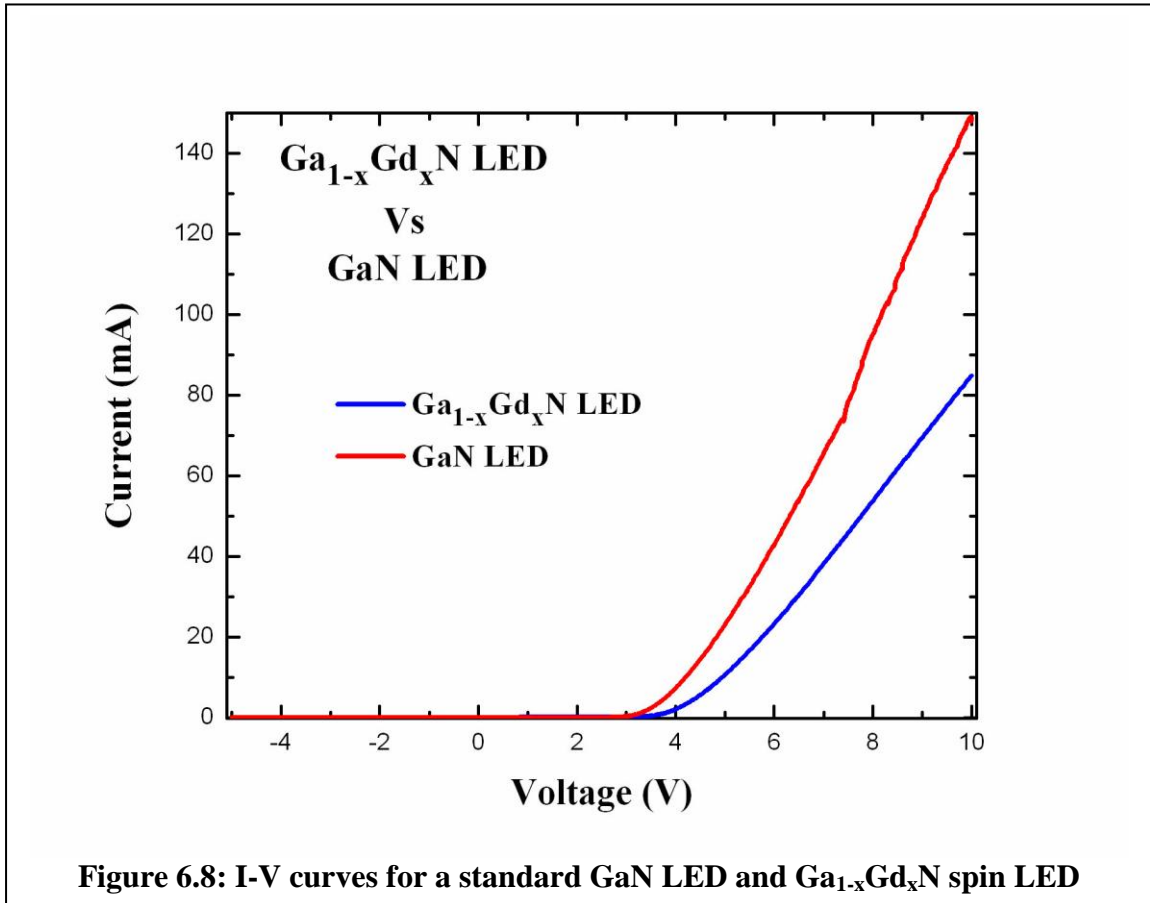


Figure 6.7: (a) XRD of Ga<sub>1-x</sub>Gd<sub>x</sub>N LED (b) XRD of standard GaN LED

### 6.4.2 Electrical Characterization

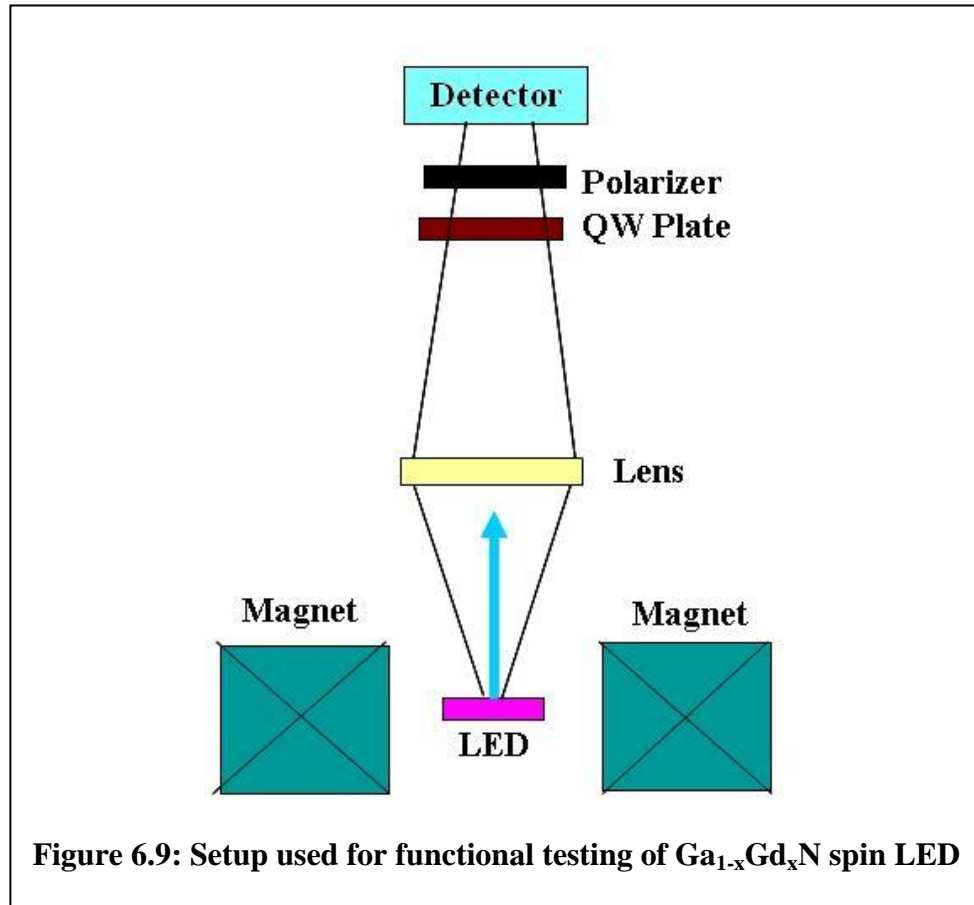
I-V curves for a standard GaN LED and a spin LED are shown in Figure 6.7. It can be seen that the spin LED has a larger series resistance and a slightly higher turn on voltage. This was expected in light of the higher resistance of the p-type  $\text{Ga}_{1-x}\text{Gd}_x\text{N}$ .



### 6.4.3 Magnetic and Spin Characterization

The  $\text{Ga}_{1-x}\text{Gd}_x\text{N}$  LED and the reference standard GaN LEDs were both mounted on a non-magnetic DIP package for functional testing under magnetic field. The Faraday setup used for this test is shown in Figure 6.8. In this technique, the LED is placed inside the poles of an electromagnet capable of generating up to 5KGauss magnetic field (the VSM data shown previously in Figures 5.8 and 5.10 saturates before 2KGauss). The light

emission from the LED is focused through the optical lens on to a CCD camera detector. The light passes through a quarter wave (QW) plate and a linear polarizer combination that is set to ensure that only the desired left or right circularly polarized light passes through before entering the detector.



The results of the circularly polarized light measurements for a standard GaN and  $\text{Ga}_{1-x}\text{Gd}_x\text{N}$  LEDs are shown in Figures 6.10 and 6.11. No noticeable variation in left or right circularly polarized light with the application of external magnetic field was seen for a standard GaN LED (Figure 6.11). The same set of measurements done on the  $\text{Ga}_{1-x}\text{Gd}_x\text{N}$  LED shows a clear difference in the intensities of left and right circularly polarized light (Figure 6.10). The important thing to note in Figure 6.10 is the variation of intensities of both left and right circularly polarized light with the external magnetic field.

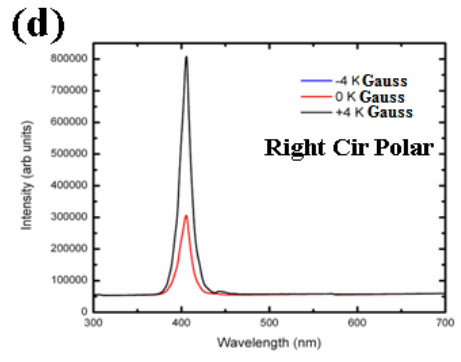
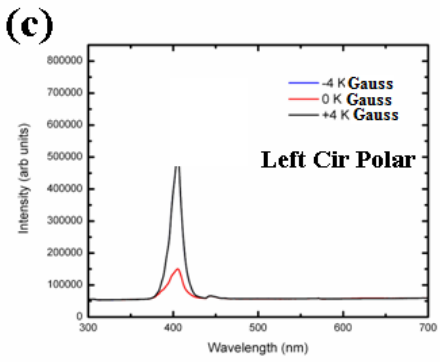
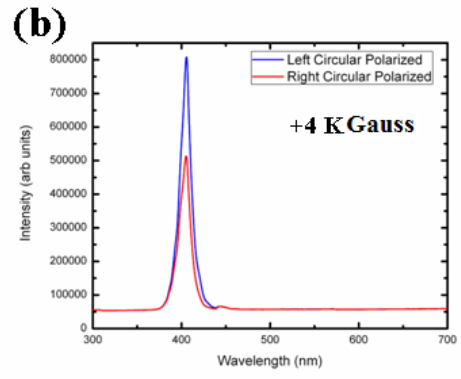
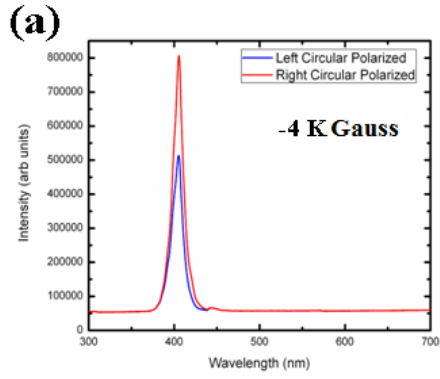


**Figure 6.10: Circularly polarized light measurements for  $\text{Ga}_{1-x}\text{Gd}_x\text{N}$  spin LED**

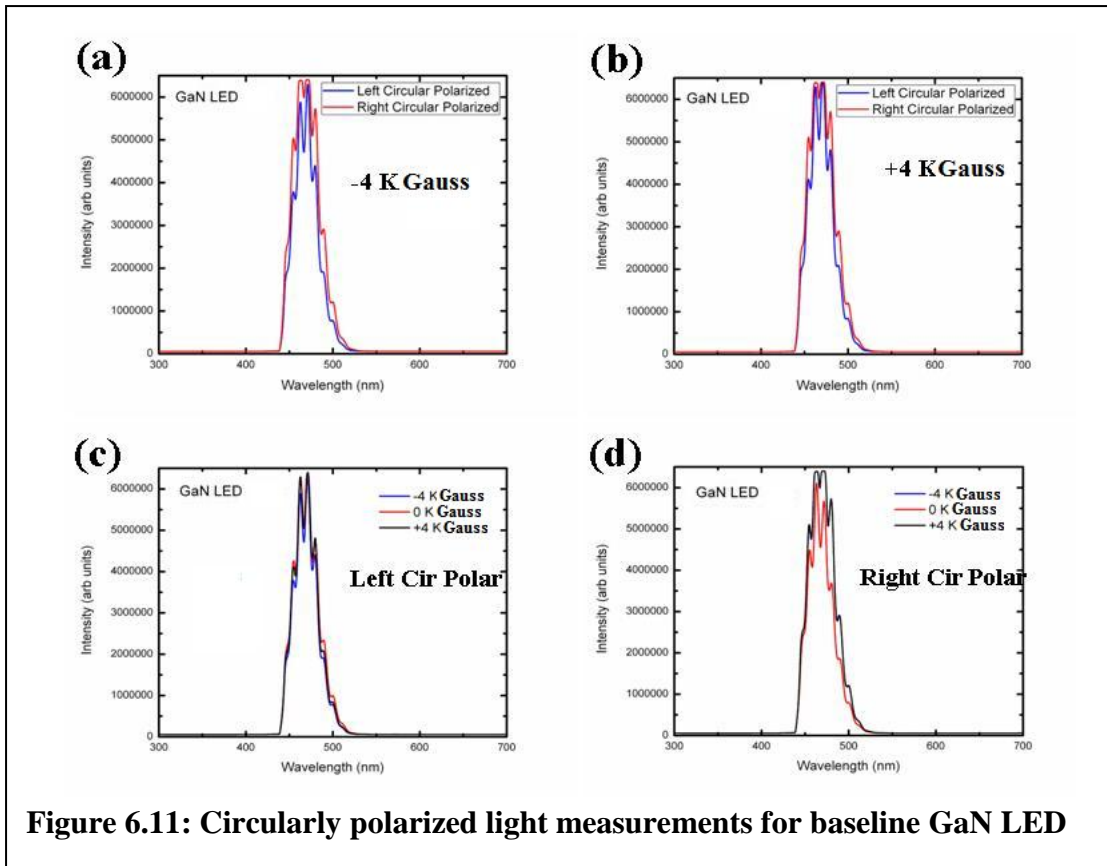


**Figure 6.11: Circularly polarized light measurements for baseline GaN LED**

An important aspect to consider in case of a spin LED is whether there is any change in spin polarization ( $P_{\text{spin}}$ ), given by the ratio of left and the right circularly polarized light, with the application of an external magnetic field: For this, both left and right circularly polarized EL measurements were compared using the test setup shown earlier in Figure 6.9. The results are shown in Figure 6.12.

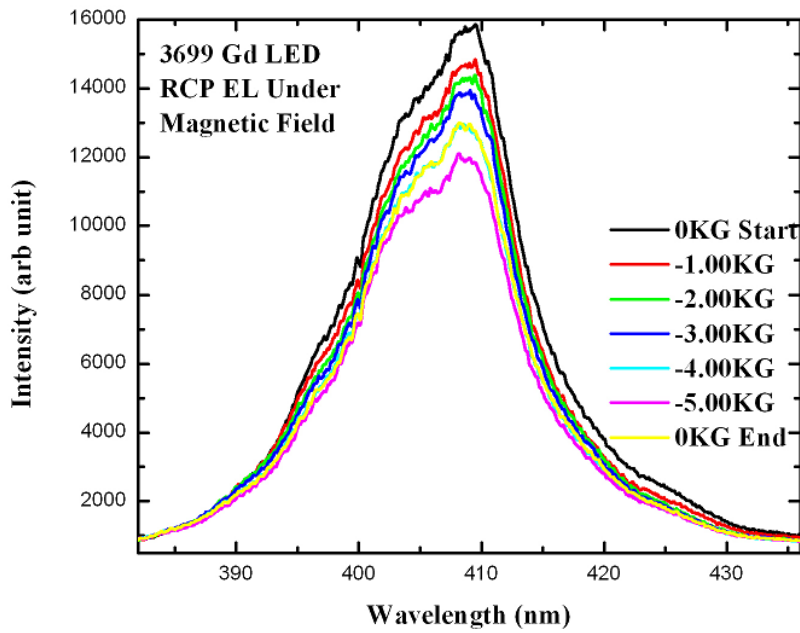
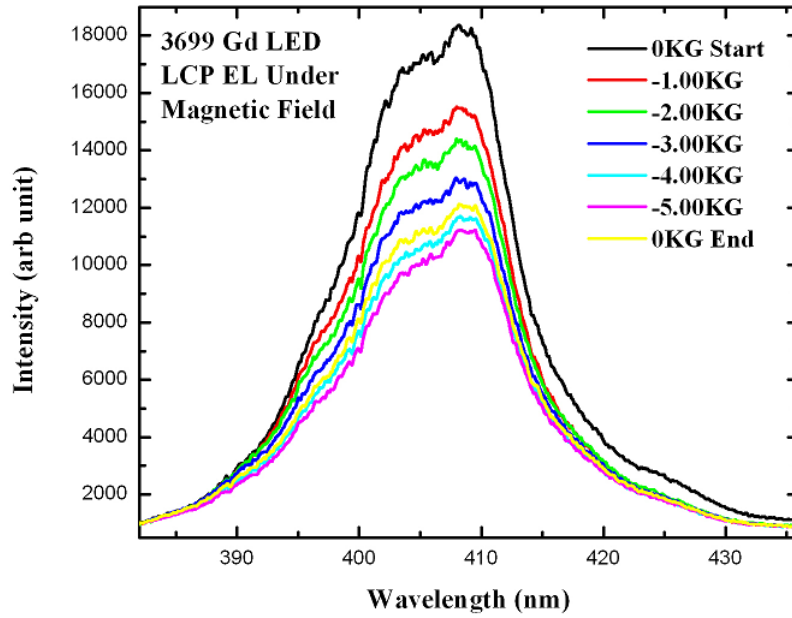


**Figure 6.12: Circularly polarized light measurements for  $Ga_{1-x}Gd_xN$  spin LED under external magnetic field**

The spin-polarization ( $P_{\text{spin}}$ ) for the  $\text{Ga}_{1-x}\text{Gd}_x\text{N}$  spin LED calculated from the LCP and RCP values from Figure 6.12 are plotted in Figure 6.13.

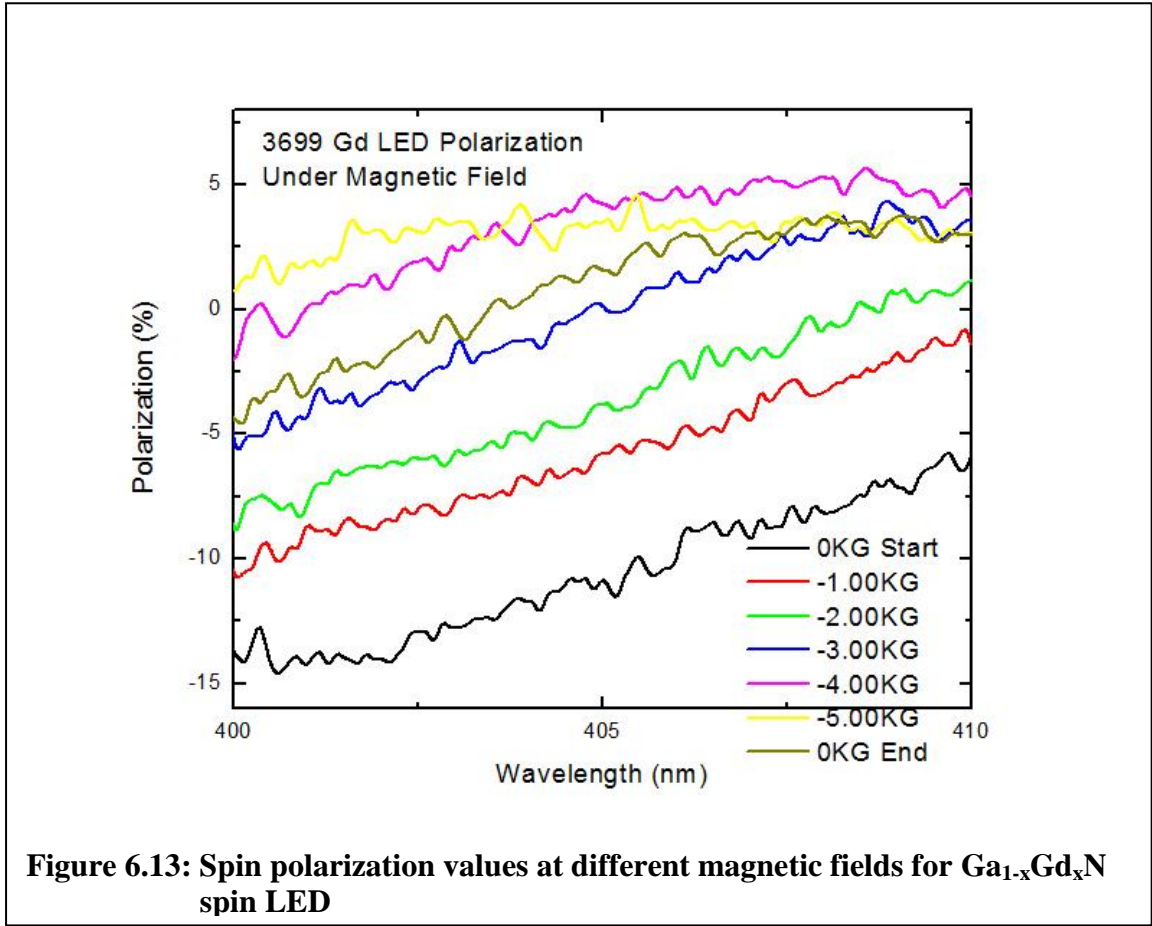
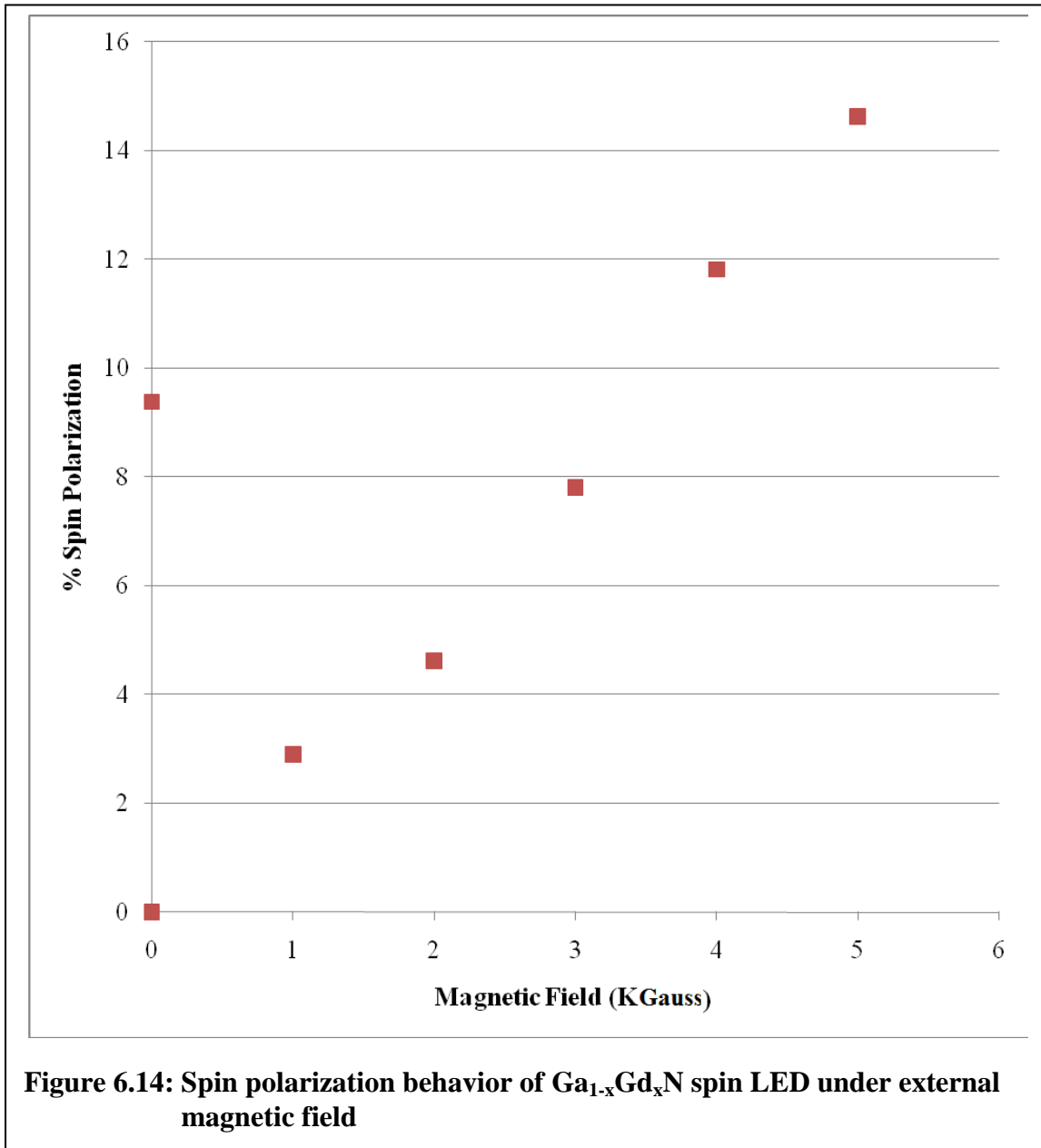


**Table 6.3:  $P_{\text{spin}}$  for  $\text{Ga}_{1-x}\text{Gd}_x\text{N}$  LED Vs Magnetic field**

Wavelength	0KG Start	1KG	2KG	3KG	4KG	5KG	0KG End
400.00	-13.89	-10.99	-9.27	-6.08	-2.08	0.73	-4.51
402.50	-13.02	-7.86	-6.02	-2.73	1.88	3.12	-0.64
405.00	-10.71	-5.70	-3.89	0.26	4.27	3.32	1.51
407.50	-8.94	-3.06	-1.82	3.23	5.24	3.74	2.88
410.00	-5.84	-1.42	1.20	3.53	4.56	3.06	3.03

Table 6.3 shows the  $P_{\text{spin}}$  values for five different emission frequencies. The measured spin-polarization at 400nm (Table 6.3) is scaled taking the value at 0KGauss as the

reference. These scaled values of the polarization percentage are plotted against the applied magnetic field in Figure 6.14. This gives us one quadrant of the measured percentage of spin polarization and shows a clear hysteresis with sweep of magnetic field from 0 to 5 KGauss. The dotted line shows the direction of the field.



## 6.5 Summary

A  $\text{Ga}_{1-x}\text{Gd}_x\text{N}$  spin LED was designed, grown and fabricated. Structural and functional characterization of this  $\text{Ga}_{1-x}\text{Gd}_x\text{N}$  spin LED was performed, and the results were compared with a standard GaN LED grown using the same recipe without the Gd doping.

The  $\text{Ga}_{1-x}\text{Gd}_x\text{N}$  layer selected for incorporation into the spin LED was the one doped with 10sccm flow of  $\text{Gd}(\text{thd})_3$  source. This selection was done based on the ferromagnetic properties of all the films grown, as discussed in Chapter 5.

The results shown in this chapter presents the first room temperature  $\text{Ga}_{1-x}\text{Gd}_x\text{N}$ -based spin LED whose circularly polarized light emission is successfully manipulated by an external magnetic field.

## CHAPTER 7: CONCLUSION AND FUTURE WORK

### 7.1 Introduction

Spintronics is currently an emerging research field that aims at attaining added functionality in microelectronic devices through the utilization of carrier spin as an extra degree of freedom in electronic device design. This dissertation evaluated  $\text{Ga}_{1-x}\text{Gd}_x\text{N}$  thin films as a candidate wide bandgap dilute magnetic semiconductor material for use in spintronics and optoelectronics devices.

In this work  $\text{Ga}_{1-x}\text{Gd}_x\text{N}$  thin films were grown on  $2\mu\text{m}$  GaN templates by MOCVD. These thin films were successfully co-doped with Si and Mg to achieve n-type and p-type materials. With these materials a pn diode structure was successfully grown and characterized. This was followed by growth of spin-polarized LED based on a GaN LED structure with a Si-doped  $\text{Ga}_{1-x}\text{Gd}_x\text{N}$  n-layer, an active region composed of three GaN/InGaN MQWs, and a Mg-doped  $\text{Ga}_{1-x}\text{Gd}_x\text{N}$  p-layer. This spin LED was shown not only to emit spin-polarized light, but also a change in polarization resulting from the application of an external magnetic field.

### 7.2 Conclusions

The structural properties of  $\text{Ga}_{1-x}\text{Gd}_x\text{N}$  films grown in this work were investigated by X-ray diffraction (XRD). The films did not show major strain or secondary phase formation, however the  $\omega$ - $2\theta$  scans of  $\text{Ga}_{1-x}\text{Gd}_x\text{N}$  films grown with the  $\text{Gd}(\text{thd})_3$  doping source did show a slight shift in peaks to higher angles with increasing Gd precursor in the gas phase. This behavior was not observed in  $\text{Ga}_{1-x}\text{Gd}_x\text{N}$  films grown using the

(Cp)<sub>3</sub>Gd doping source. The Gd atom is known to substitutionally occupy Ga site in the GaN crystal structure. The XRD results point to the Gd incorporation causing negligible change in the lattice parameter of GaN. The presence of nanoscale secondary phase formation not traceable by XRD is possible; however there is no evidence to support it. The slight systematic shift of the XRD peak with the use of the Gd(thd)<sub>3</sub> precursor can be attributed to the oxygen. The Gd(thd)<sub>3</sub> precursor in the the gas phase inside the growth chamber will result in the formation of Gd<sub>2</sub>O<sub>3</sub> that may find its way to the resulting films. Gd itself has a known strong affinity for Oxygen, and, even when it takes place of Ga inside GaN matrix, it has been reported to form a complex with O<sub>i</sub>. So a combination of oxide and an oxy-nitride complex is expected to form, both of which are reported to show magnetic behavior. EDS data of the films also shows the presence of oxygen in the films.

The Gd incorporation inside GaN was detected with a number different techniques including EDS, the alpha stopping power increase of the films, and increased neutron cross-section.

Ga<sub>1-x</sub>Gd<sub>x</sub>N films grown with Gd(thd)<sub>3</sub> were observed to be ferromagnetic at room temperature under the influence of a weak magnetic field; however, under the coercion of a strong magnetic field, it exhibits a paramagnetic behavior. The behavior of the films points to carrier-mediated magnetism, since a decrease in carriers with Mg doping is seen to reduce it. No significant ferromagnetic behavior was observed in case of Ga<sub>1-x</sub>Gd<sub>x</sub>N films grown using (Cp)<sub>3</sub>Gd source. This source does not have any oxygen in it, and the resulting Ga<sub>1-x</sub>Gd<sub>x</sub>N films do not show the presence of any significant amount of oxygen by the EDS. This again confirms the role played by oxygen in the ferromagnetic behavior of Ga<sub>1-x</sub>Gd<sub>x</sub>N films. No colossal magnetic moment was observed in the Ga<sub>1-x</sub>Gd<sub>x</sub>N

grown during this work. The increase in the paramagnetic behavior of the films with increased Gd can be attributed to the 4f electrons of Gd which are not quenched, as they are shielded by the outer 5d and 6s orbitals.

The as-grown  $\text{Ga}_{1-x}\text{Gd}_x\text{N}$  films were seen to have improved conductivity over undoped GaN films. This results from an increase in background carrier concentration with Gd incorporation. This increase was seen both when the  $\text{Gd}(\text{thd})_3$  and the  $(\text{Cp})_3\text{Gd}$  precursor were used, so the primary cause of the increase cannot be ascribed to the presence of oxygen.

Doping of the films with Si gave rise to an n-type material, improving further the resistivity of the films. Doping with Mg produced a p-type material; however the resistivity of the material was seen to increase. In order to confirm p-type behavior, p-n diodes were fabricated, followed by the fabrication of an LED using the  $\text{Ga}_{1-x}\text{Gd}_x\text{N}$  films. I-V curves of these structures confirm the p-type behavior of the films. An increase in series resistance was observed in these devices due to increased compensation in the Mg-doped  $\text{Ga}_{1-x}\text{Gd}_x\text{N}$  layers. However, successful growth and fabrication of LEDs using  $\text{Ga}_{1-x}\text{Gd}_x\text{N}$  films and their subsequent characterization confirms the device quality of the p-type films.

The EPR tests performed on the samples show a 3+ state of the Gd atom inside the samples and also show a high spin orientation state. A near-axial symmetry was shown in the EPR signature.

$\text{Ga}_{1-x}\text{Gd}_x\text{N}$ -based LEDs were fabricated and characterized. For the sake of comparison a baseline standard GaN LED was also fabricated with the same QW structure in the active region. It was observed that increasing the Gd flow rate in gas

phase resulted in suppression of the typical QW-related XRD peaks. This is attributed to diffusion of Gd inside the active region. This diffusion also results in a blue shift of the LED EL emission spectra.

The successful manipulation of the spin polarization of emitted light from the  $\text{Ga}_{1-x}\text{Gd}_x\text{N}$  based LEDs by an external magnetic field justifies their classification as a room temperature spin polarized LEDs. A number of  $\text{Ga}_{1-x}\text{Gd}_x\text{N}$  LEDs were fabricated and successfully tested. This confirmed their reproducibility and behavioral consistency.

An important contribution of this work is showing that, in a particular window of Gd concentration,  $\text{Ga}_{1-x}\text{Gd}_x\text{N}$  films can be successfully used for the growth of a spin-polarized LED. Too much Gd causes diffusion in the active region, which, in turn, causes a blue shift of EL emission and adversely affects the QWs. Too little Gd will not show the spin polarization.

The most useful quality of these  $\text{Ga}_{1-x}\text{Gd}_x\text{N}$  LEDs is their ability to operate at room temperature, which makes them suitable for application in future commercial devices. Another important aspect of these LEDs is the ability to grow them by the MOCVD technique, which is a standard industrial growth technique.

### **7.3 Achievements**

The achievements of this work are listed below:

- Successful growth of  $\text{Ga}_{1-x}\text{Gd}_x\text{N}$  by MOCVD
- Room temperature ferromagnetism observed in  $\text{Ga}_{1-x}\text{Gd}_x\text{N}$  layers
- Successful n-type and p-type ferromagnetic layers of  $\text{Ga}_{1-x}\text{Gd}_x\text{N}$  by MOCVD by Si and Mg co-doping respectively

- Observation of reduction in FM in  $\text{Ga}_{1-x}\text{Gd}_x\text{N}$  layers with Mg co-doping and an improvement by Mg activation
- Design and successful implementation of a new Gd source delivery system that caters for its low vapor pressures
- Design, growth and fabrication of  $\text{Ga}_{1-x}\text{Gd}_x\text{N}$  LED
- Observation of spin polarized emission from  $\text{Ga}_{1-x}\text{Gd}_x\text{N}$  and manipulation of spin polarization at room temperature with an external magnetic field
- 13 papers and 10 conference presentations

#### **7.4 Future Work**

The present work was aimed at the development of a suitable material system for use in spintronics and optoelectronic devices. In this respect  $\text{Ga}_{1-x}\text{Gd}_x\text{N}$  thin films were investigated and their use in a practical device demonstrated in the shape of a room temperature spin LED.

The same work can be extended to develop spin photo-detectors, which would have a similar structure to the LEDs grown in this work (Figure 6.5). These photo-detectors can then be used in conjunction with the spin polarized LED for the evaluation of optical polarization modulation techniques. The area of polarization modulation holds great promise in multiple domains, including the increase in the capacity of the installed optical communication bandwidth with minimal modification and secure communication.

This work used two techniques from the nuclear science field for the characterization of films. These characterizations can work as a proof of concept for development of neutron detectors based on  $\text{Ga}_{1-x}\text{Gd}_x\text{N}$  films. These detectors will utilize the large neutron

cross-section of Gd incorporated in the films for neutron detection using appropriate device structures.

## **7.5 Summary**

MOCVD growth of  $\text{Ga}_{1-x}\text{Gd}_x\text{N}$  thin films and their suitability for use in spintronics and optoelectronics was investigated in this work. The modifications carried out to the growth tool delivery system and the techniques developed in this work resulted in the growth of device-quality  $\text{Ga}_{1-x}\text{Gd}_x\text{N}$  thin films and structures culminating in growth and fabrication of a room temperature spin LED. This research provides a valuable contribution to the current knowledge base of the MOCVD growth of  $\text{Ga}_{1-x}\text{Gd}_x\text{N}$  thin films and lays the foundation for the future growth of spin-polarized LEDs for multiple applications.

## CHAPTER 8: ADDITIONAL WORK

### 8.1 Introduction

For this research a new gas panel and control system has been developed for a MOCVD tool devoted to oxide growth. This modification has enhanced the tool's capabilities by enabling management of four metal organic (MO) and two liquid injection sources. The modified tool can now select Ar or N<sub>2</sub> as the carrier gas and O<sub>2</sub>, N<sub>2</sub>O, NH<sub>3</sub>, PH<sub>4</sub> and SiH<sub>4</sub> as the process gases. A new control system and software have also been added to the tool to allow fine control over the precursors and process gases. An image of the recently updated liquid delivery MOCVD system is given in Figure 8.1. This tool successfully produced N-doped ZnO films that had room temperature ferromagnetic behavior.

The same oxide MOCVD tool was used for growth of bismuth ferrite (BiFeO<sub>3</sub>) thin films on a variety of substrates including sapphire, GaN template, and Si. BiFeO<sub>3</sub> (BFO) is a known multiferroic material and all the films grown in this work showed room temperature ferroelectric and ferromagnetic behavior. The growth of these films were done using direct liquid injection (DLI) of Bi(thd)<sub>3</sub> dissolved in THF.

Although the ZnO and BFO films grown did show room temperature ferromagnetic behavior their crystal qualities were not of device standard and so their use in device structure was not pursued. However the experience gained by this work helped in the growth of Ga<sub>1-x</sub>Gd<sub>x</sub>N thin films and device structures as described in previous chapters.

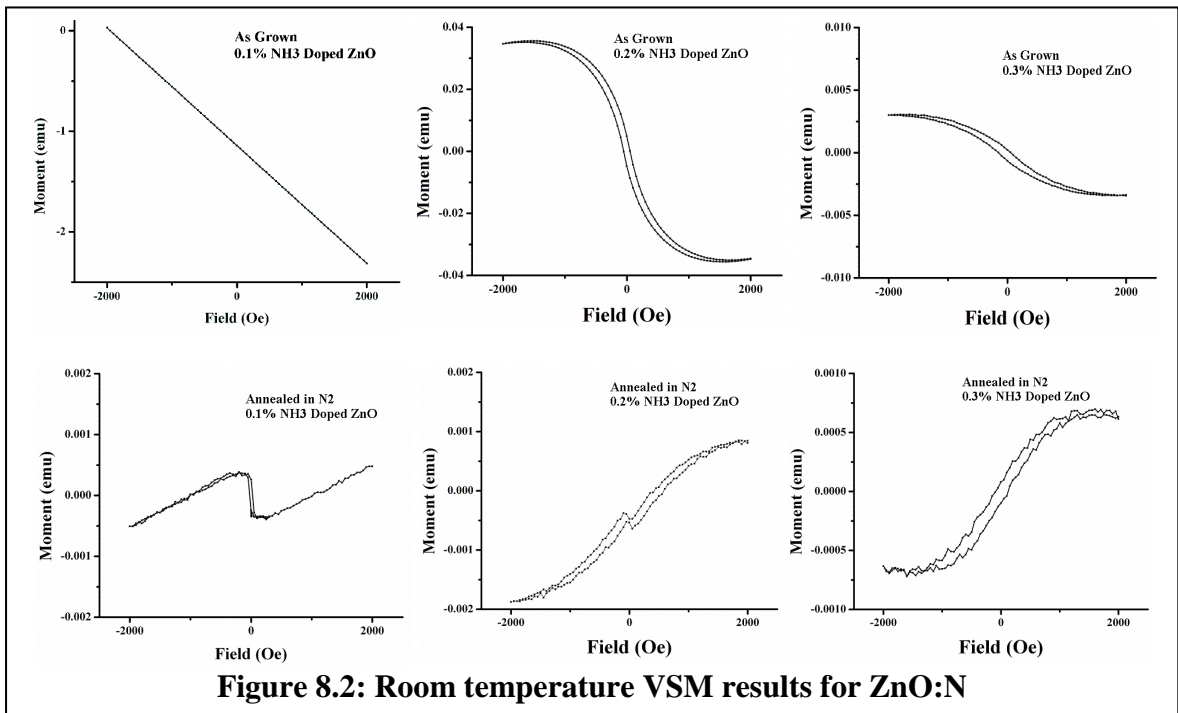


**Figure 8.1: Updated liquid delivery MOCVD system**

The sources used for epitaxial growth of Bi based multiferroic materials have very low vapor pressure, so best results are obtained by direct liquid injection into the MOCVD chamber.

## 8.2 N-Doped ZnO

ZnO:N thin films have been successfully grown on c-plane sapphire using diethyl zinc (DEZn) and O<sub>2</sub> precursors and NH<sub>3</sub> as the doping source. The ideal growth window for these films was found to be at 500°C with VI-II ratio above 500. The maximum practical doping level was determined to be 1% NH<sub>3</sub> beyond which the crystal quality degraded appreciably, turning almost amorphous for 4% NH<sub>3</sub> flow. The as grown films were found to be highly resistive however annealing in N<sub>2</sub> ambient at 800°C turned these films into highly conducting n-type with carrier concentration on the order of  $8.39 \times 10^{18} \text{ cm}^{-3}$ , mobility on the order of  $11.81 \text{ cm}^2/\text{Vs}$  and resistivity of  $0.063 \text{ } \Omega \text{ cm}$ .



These annealed ZnO:N films showed room temperature ferromagnetism as shown in Figure 8.2. Increased N doping was seen to increase the ferromagnetic behavior of these films.

X-ray diffraction (XRD)  $\omega$ -  $2\theta$  scans of ZnO:N films show a single (002) ZnO peak, suggesting a high (002) preferential orientation. With increased NH<sub>3</sub> flow the FWHM of ZnO (002) peak increases and its position shifts (Figure 8.3a). The shift in peak position was seen to be fairly linear as NH<sub>3</sub> flow was increased from 0.1% to 4% (Figure 8.3b).

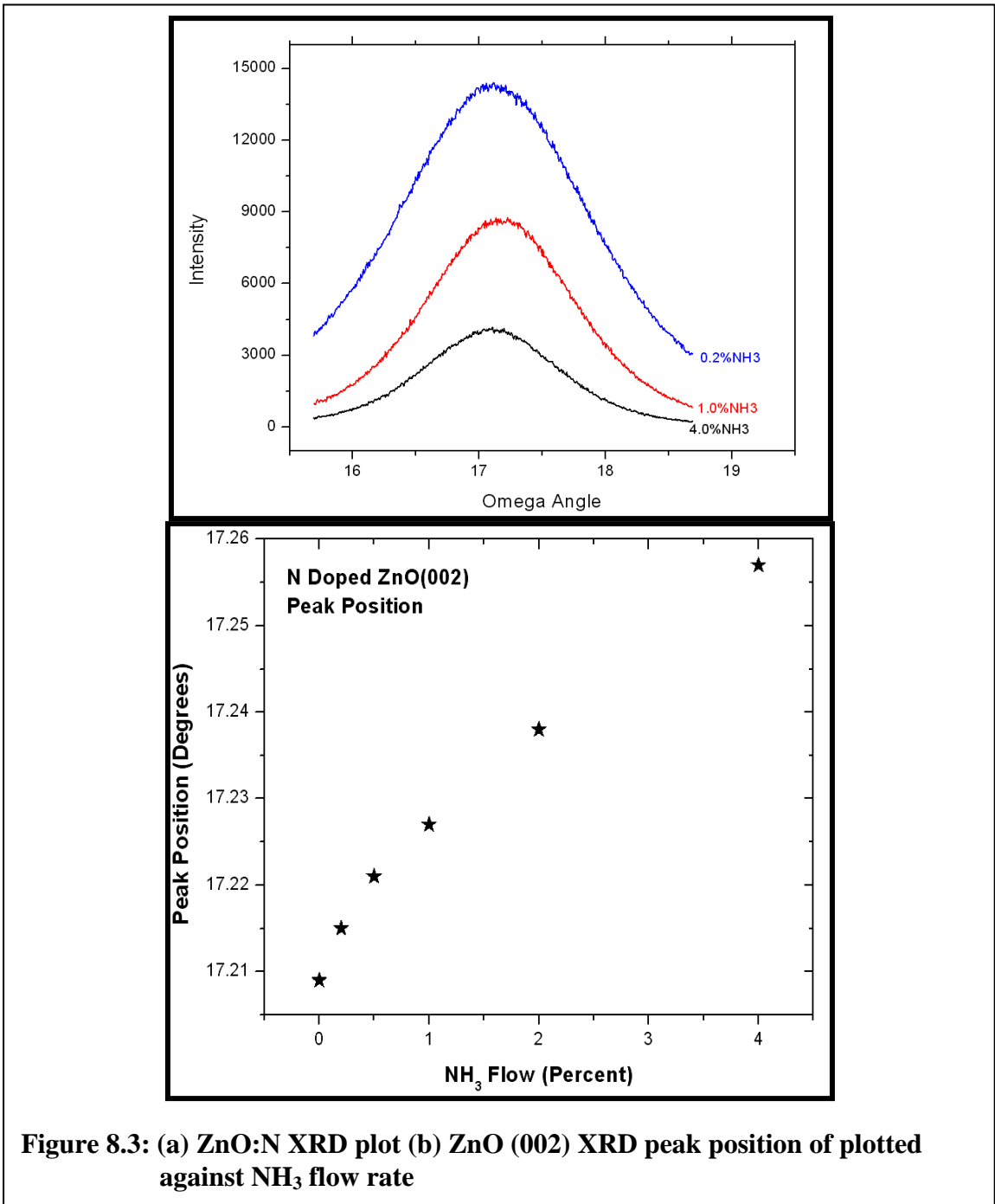
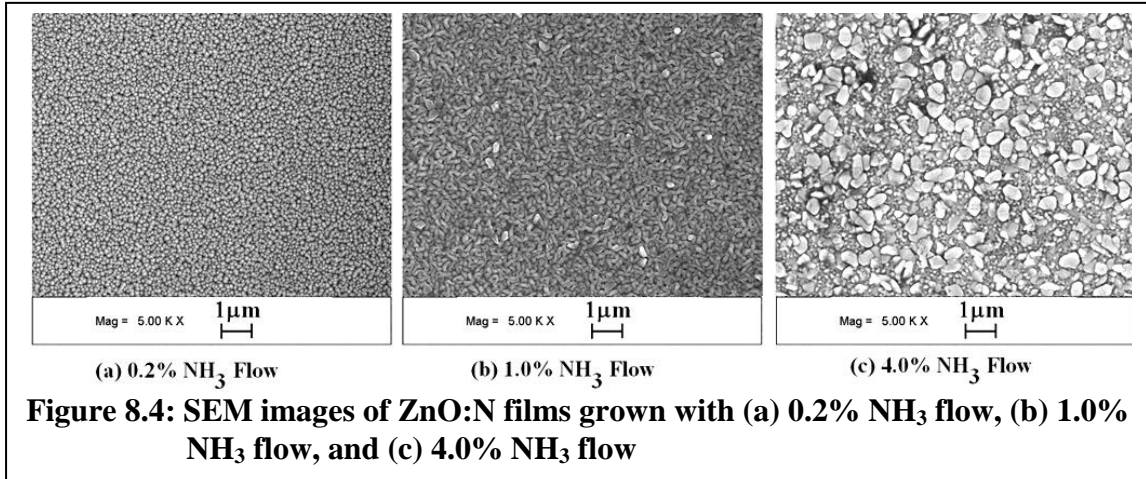


**Figure 8.3: (a) ZnO:N XRD plot (b) ZnO (002) XRD peak position of plotted against NH<sub>3</sub> flow rate**

Figure 8.4 shows the SEM images of 0.2-4% N doped ZnO film. It can be seen that the surface roughness and grain size both increase with increased  $\text{NH}_3$  flow during growth.



Raman spectroscopy for  $\text{NH}_3$  flows from 0.1% to 4% is shown in Figure 8.5. ZnO:N modes at  $275\text{cm}^{-1}$ ,  $510\text{cm}^{-1}$ ,  $575\text{cm}^{-1}$  and  $645\text{cm}^{-1}$  are clearly visible. Increased  $\text{NH}_3$  flow results in enhanced ZnO:N modes while suppressing the native ZnO modes of  $437\text{cm}^{-1}$ ,  $380\text{cm}^{-1}$ , and  $332\text{cm}^{-1}$ . This points towards deteriorating crystal quality with increased N incorporation.

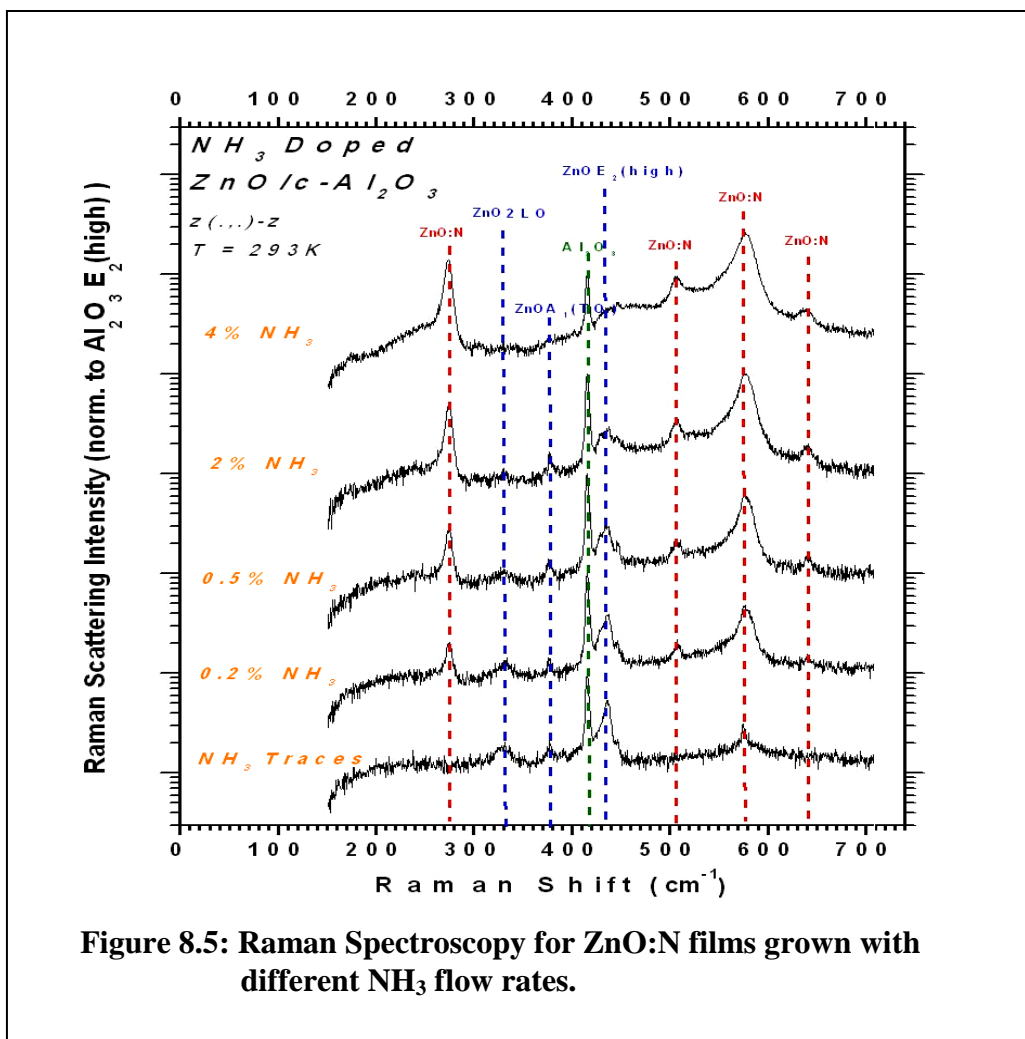
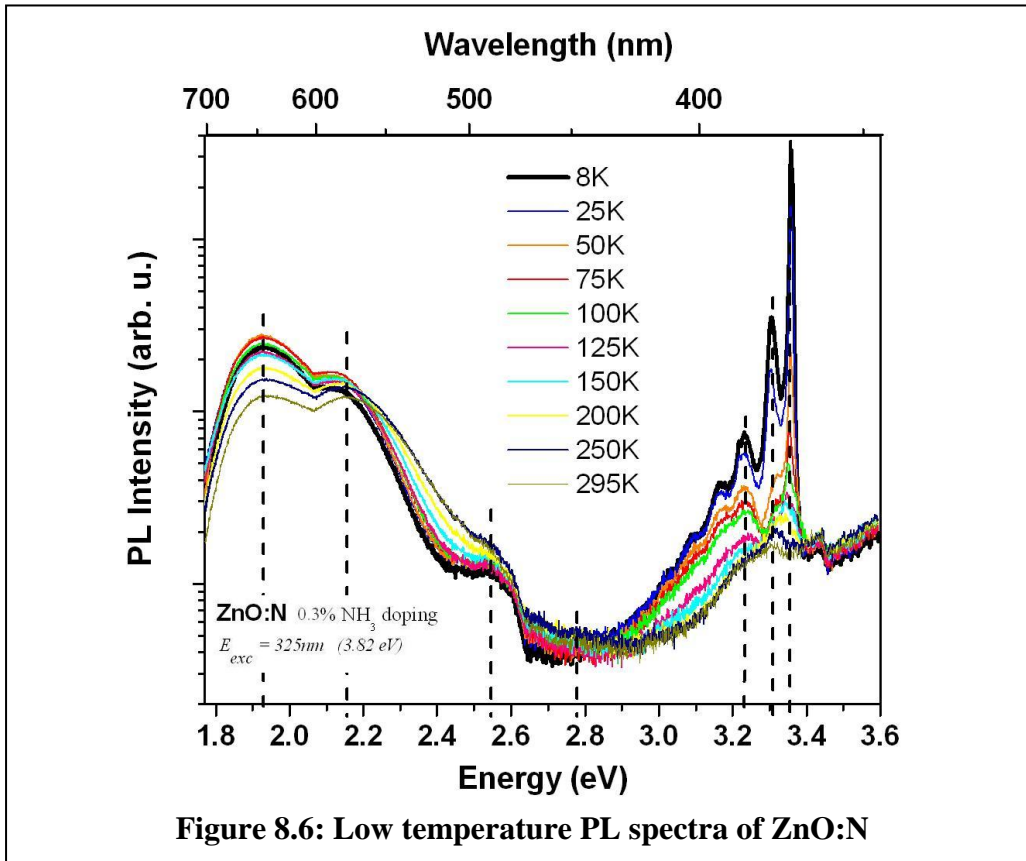


**Table 8.1: Hall effect data for samples annealed in N<sub>2</sub> ambient at 800°C for 60 min**

NH <sub>3</sub> Flow	Type	Carrier (cm <sup>-3</sup> )	μ (cm <sup>2</sup> /Vs)	ρ (Ω cm)
0.1%	n	-6.43 e 18	19.23	0.049
0.2%	n	-8.39 e 18	11.81	0.063
0.3%	n	-7.87 e 18	15.33	0.051

Table 8.2 gives Hall data for ZnO:N films after N<sub>2</sub> ambient annealing at 800°C for 60 minutes. It can be seen that all the films show highly conducting n-type behavior.

Figure 8.6 shows the low temperature PL spectra of a ZnO:N film after annealing in N<sub>2</sub> at 800°C for 60 minutes.



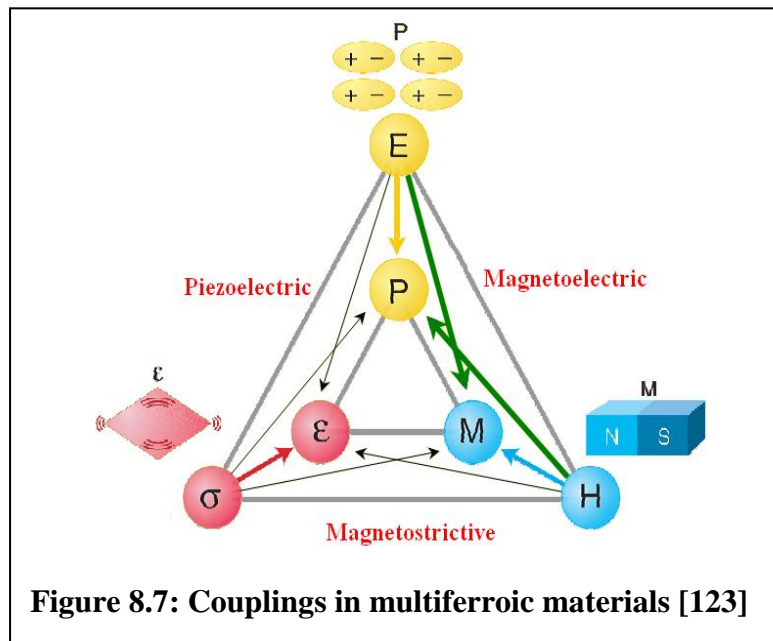
In MOCVD low growth temperatures drastically reduce crystal quality of ZnO films. Furthermore, below 500°C excessive carbon in the films readily formed (NC) complexes with NH<sub>3</sub> giving a pinkish-brown tint to the films. For high NH<sub>3</sub> flow rates the end result was an opaque brownish film. Thus there are two competing effects. While high temperature growth of ZnO thin films by MOCVD improves crystal quality and reduces the “hole killer” defects it also results in very low N incorporation. But if an attempt is

made to increase the nitrogen concentration by increased dopant ( $\text{NH}_3$ ) flow, the crystal quality deteriorates.

### 8.2.1 Pulsed MOCVD growth of N-Doped ZnO

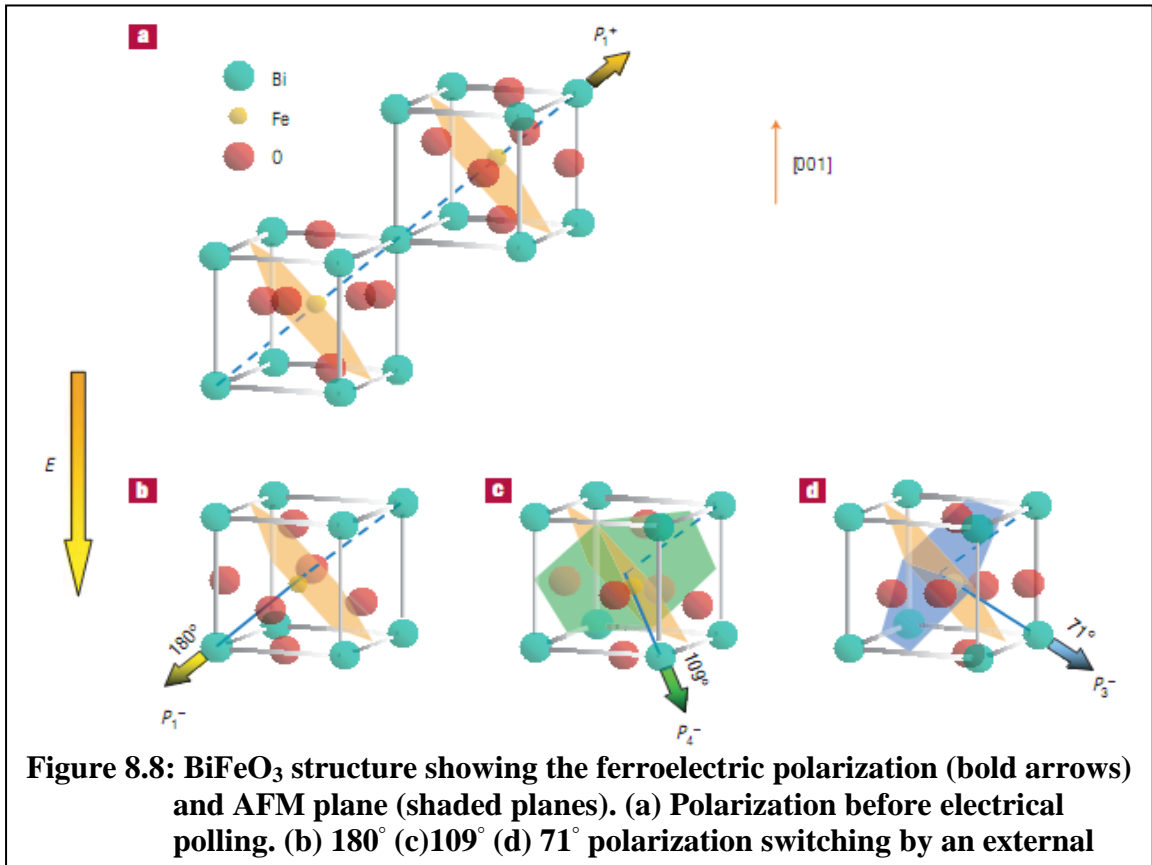
To increase the N incorporation a “pulsed MOCVD” technique was developed. This technique enabled growth of films with  $\text{NH}_3$  flow rate of up to 20% without appreciable loss of crystal quality. In this technique the precursors were pulsed alternately between ( $\text{DEZn} + \text{NH}_3$ ) and  $\text{O}_2$ . This was to allow  $\text{NH}_3$  to react with  $\text{DEZn}$  and form a layer of different (N-H) and (N-C) complexes with Zn before introducing  $\text{O}_2$  to react with these complexes. The cycle of the pulses was kept at 40sec ( $\text{DEZn} + \text{NH}_3$ ) and 20sec ( $\text{O}_2$ ).

### 8.3 Multiferroic Bismuth Ferrite



Multiferroics are a class of materials that have coupled magnetic, electric and structural order parameters [166]. This magneto-electric coupling enables the manipulation of the ferroelectric polarization by an applied magnetic field [167, 168] or

the control of the antiferromagnetic (AFM) vector orientation by an electric field [169]. A schematic illustrating different types of possible couplings in a multiferroic material is shown in Figure 8.7. Multiferroic materials have attracted considerable interest due to their potential usage in information storage, spintronics and sensors.



BiFeO<sub>3</sub> (BFO) is one of the most studied multiferroic materials and was first synthesized in the late 1950s [170]. BFO has a non-centrosymmetric rhombohedral perovskite structure that crystallizes in the space group R3c with  $a = 5.58\text{\AA}$  and  $c = 13.88\text{\AA}$  [171] as shown in Figure 8.8a. The larger Bi cations occupy the ‘A’ site while the smaller Fe atoms occupy the ‘B’ site.

The polarization  $\mathbf{P}$ , which is the ferroelectric order parameter, points along any one of the four body diagonals, or  $|111|$  directions of the cube. As  $\mathbf{P}$  can be either parallel or

antiparallel with  $[111]$ , there are 8 possible directions or variants of  $\mathbf{P}$ , as shown in Figure 8.8. BFO is reported to exhibit eight structural transitions, a canted spin ordering and ferroelectric ordering [172-175]. The anti-ferromagnetic order parameter is the staggered magnetization or  $\mathbf{L}$ , which is defined as the vector difference between nearest neighbor  $\text{Fe}^{3+}$  spins along the  $[111]$  direction.  $\mathbf{L}$  lies in the plane perpendicular to  $[111]$  and can be oriented along any one of the six preferred directions (Figure 8.8).

The values reported for the optical band gap of BFO range from 2.4eV-2.81eV and it is widely expected that strain plays an important role in shifting of the optical bandgap [176-179].

In contrast to its ferromagnetic properties, the ferroelectric character of BFO took longer to be firmly established because of the difficulty in preparing highly resistive samples [180]. The first ferroelectric polarization of BFO was reported in 1970 with a magnitude of about  $6\mu\text{C}/\text{cm}^2$  [181], however more recently ferroelectric polarization of up to  $100\mu\text{C}/\text{cm}^2$  has been observed in high-quality single crystals [182]. BFO films have been prepared by a number of groups [183-187] both in polycrystalline and epitaxial form. The electric control of different magnetic properties in BFO single crystals and thin films has been investigated by many authors [169, 188-191]. By now the change in ferroelectric polarization by application of external electric field and the consequent change in AFM plane is well established (Figure 8.8).

X-ray magnetic circular dichroism (XMCD) studies of BFO has revealed the intensity dependence on the angle of sample rotation (Figure 8.9). This observation is similar to the one reported by Alders for AFM NiO films [192]. Alders showed that the intensity at the absorption edge of an AFM depends on the sample rotation angle by a

cosine squared function. Like NiO, BFO also picks a preferred axis [193]. This observation coupled with the ability to electrically control the polarization direction and “easy axis” opens up exciting opportunities for future electro-magneto-optical devices.

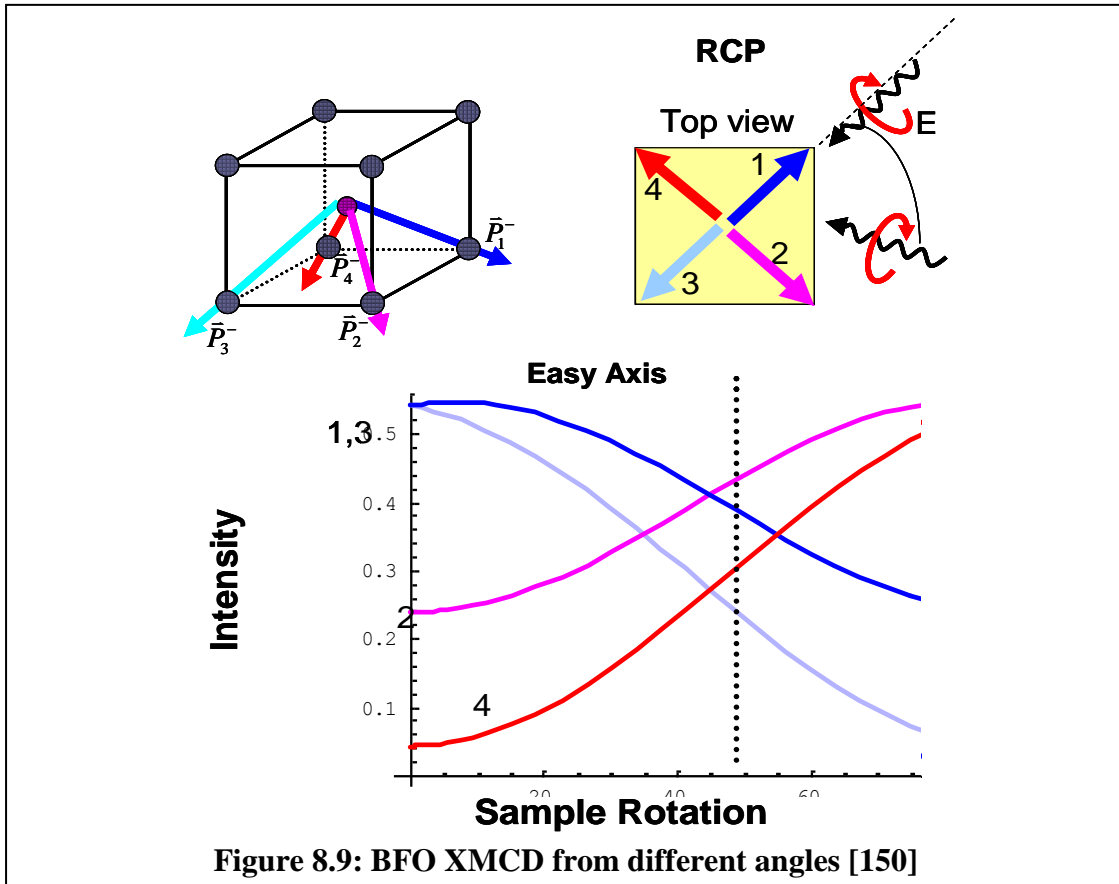


Figure 8.9: BFO XMCD from different angles [150]

The dichroism in a multiferroic is not very well understood. Study of multiferroic with PEEM technique has only recently been utilized. Multiferroic perovskites like BFO provide opportunity to study several unique physical phenomena such as the influence of strain on the magnetic and ferroelectric properties [194], the ferroelectric/antiferromagnetic domain structure [195-197], and coupling of multiferroic or finite size effects [197, 198] in systems with two or more order parameters. The real drivers behind most of the applied research on BFO are magneto-electric and spintronic applications.

### 8.3.1 BFO MOCVD Growth

MOCVD is the most suitable technique for creating precisely defined device structures at a commercially viable scale. It offers many advantages including good composition control, high uniformity, and deposition over large areas.

BFO thin films have been deposited using a number of different techniques. The two most common reported techniques are pulsed laser deposition (PLD) and chemical solution deposition (CSD). Very few reports of metal organic chemical vapor deposition (MOCVD) of BFO films exist in literature [199-202]. The main reason for this is the non availability of suitable precursors. [203,204]. Most of these MOCVD grown films focused on the ferroelectric properties for nonvolatile ferroelectric random access memory applications [204].

The two most common classes of precursors used (both Bi and Fe) for MOCVD growth of BFO are the  $\beta$ -diketonate complexes – also known as dipivaloylmethane or DPM complexes – and the mixed alkoxide/ $\beta$ -diketonates. The  $\beta$ -diketonates complexes with ligands such as tris(2,2,6,6-tetramethyl-3,5- heptanedionate) – simply referred to as tmhd or thd – exhibit high thermal stability, and require high temperatures for vaporization and decomposition. DPMs being more stable and harmless are preferred over alkoxides which are toxic and thus require special care in handling. Another advantage of DPM precursors is their almost equal reaction speed and diffusion coefficients which is ideal for producing stoichiometrically uniform compounds.

The commercially available precursors that have been most commonly used for the MOCVD growth of BFO are:  $\text{Fe}(\text{thd})_3$ ,  $\text{Fe}(\text{DIBM})_3$ , and  $\text{Bi}(\text{thd})_3$ . These precursors are solids at room temperature and so require delivery setups such as liquid-injection [204].

A list of earlier reports on MOCVD growth of BFO is given in Table 8.2

**Table 8.2: Reports of MOCVD growth of BFO thin films.**

Research Group	Year	Precursors	Ref
Ueno et al.	2005	Bi(CH <sub>3</sub> ) <sub>2</sub> 2-(CH <sub>3</sub> ) <sub>2</sub> NCH <sub>2</sub> C <sub>6</sub> H <sub>4</sub> Fe(C <sub>2</sub> H <sub>5</sub> C <sub>5</sub> H <sub>4</sub> ) <sub>2</sub>	[200]
Yang et al	2005	Bi(thd) <sub>3</sub> Fe(thd) <sub>3</sub>	[199]
Tasaki et al	2006	Bi(p-Tol) <sub>3</sub> Fe(DIBM) <sub>3</sub>	[202]
Kartavtseva et al	2007	Bi(C <sub>6</sub> H <sub>5</sub> ) <sub>3</sub> Fe(thd) <sub>3</sub>	[203]
They et al	2007	Bi(mmp) <sub>3</sub> Fe(thd) <sub>3</sub>	[201]
M Singh et al	2009	Bi(C <sub>6</sub> H <sub>5</sub> ) <sub>3</sub> Fe(N-butylferrocene)	[204]

The precursors used by Ueno et. al. [200] are not available commercially. They did not observe ferroelectric behavior at room temperature due to large leakage currents, and no data on magnetization was reported. Yang et al. [199] reported switched polarization values of 110–120 and 85–90 $\mu\text{C}/\text{cm}^2$  for BFO films on STO and STO/Si substrates, respectively. However, Tasaki et al. [202] reported a small remnant polarization value 2 $\mu\text{C}/\text{cm}^2$  measured at an unspecified temperature. Again, no magnetization data were reported in either of these studies. More recently, Kartavtseva et al. [203] reported a saturation magnetization value of 9 $\text{emu}/\text{cm}^3$  at 10 K. They et al. [201] reported a high saturation magnetization (70 $\text{emu}/\text{cm}^3$ ) attributed to the presence of impurity phases. However, no direct data on ferroelectric properties was mentioned in either of these reports.

### 8.3.2 BFO Spintronics Applications

A great deal of research effort in BFO spintronics applications has been directed towards memories that can be written using a voltage and read using a magnetic field.

The advantages of such a memory would be: solid-state circuitry without any mobile parts, low-energy requirement, and the ability to scale down voltage levels with decreasing thickness. Reading the memory magnetically, on the other hand, has the advantage of being a non-destructive process.

For such memories to actually work, the magnetic state therefore must be a) electrically switchable and b) magnetically readable. The first condition is met by BiFeO<sub>3</sub>, because the easy plane of its antiferromagnetic domains rotates with the ferroelectric polarization as discussed in the previous section [205-207]. The second condition is not directly met, because weakly canted antiferromagnetic BFO domains cannot be easily read. An indirect solution to this problem would be to use an exchange bias mechanism. Exchange bias is the magnetic interaction between the spins of an AFM and a thin FM layer attached to it [208]. The voltage-induced changes to the underlying AFM layer results in changes to the ferromagnetic hysteresis of the upper layer, which can then be read by conventional mechanisms. This concept has been successfully implemented for Cr<sub>2</sub>O<sub>3</sub> [165] and YMnO<sub>3</sub> [210]. The efforts to implement this idea using BFO has resulted in several important milestones, such as the observation of exchange bias in thin ferromagnetic layers grown on BFO [211,212], the correlation between exchange bias and ferroelectric domains [205], the observation that the antiferromagnetic domains can be switched by a voltage [207], and proof- of-concept that the exchange-biased ferromagnetic layer can indeed be switched by a voltage [213].

BFO has also been found useful for TMR applications [211, 214]. The fact that it retains switchable ferroelectric property down to a thickness of 2 nm [215] makes it feasible for use in an electrically switchable tunnel junction, whereby the ferroelectric

state controls the magnetic state of the thin ferromagnetic electrodes, thus modifying the tunneling magneto-resistance. A similar concept is used in the tunneling resistivity control both by electric and magnetic fields, giving rise to a four-state memory device [216].

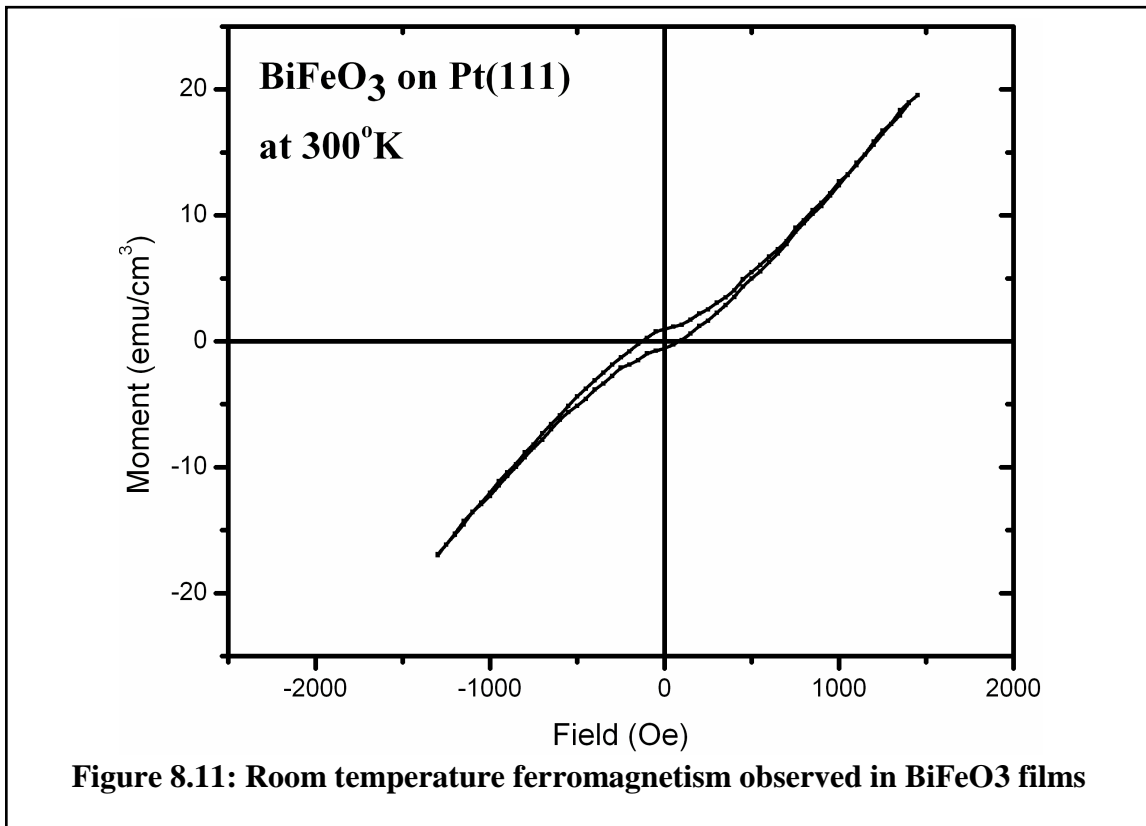
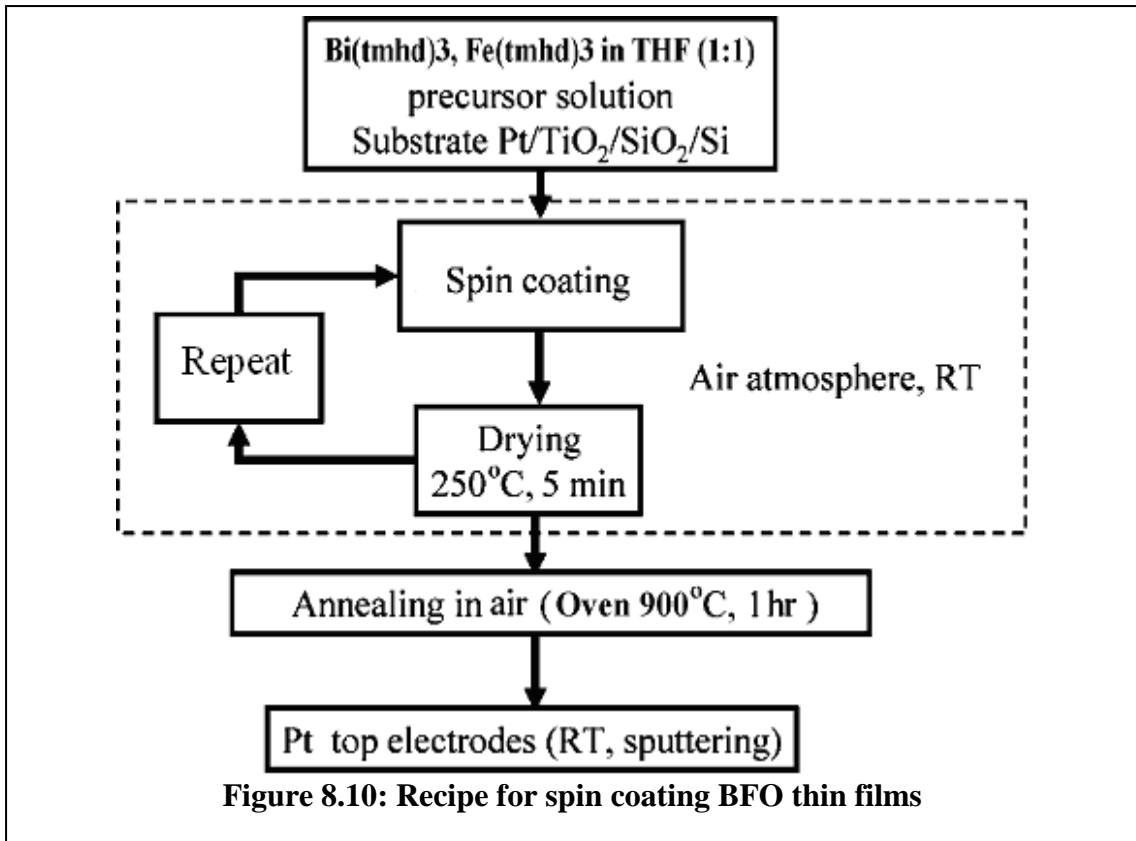
While the voltage-dependent barrier characteristics of BFO have not yet been established the above developments show that in principle it is possible to develop an MERAM (Magneto-electric Random Access Memory) based on BFO [217]

The optical response of BFO films is also an area of interest where its magneto-optic Kerr effect (MOKE), Verdet constant and dichroic properties are being explored at different frequency spectrums. In case effective manipulation of these properties is obtained by the application of electric/magnetic field, a whole range of new devices will be made possible.

### ***8.3.3 Growth and Characterization of BFO***

BiFeO<sub>3</sub> thin film growth has been performed by spin coating using two different sets of precursors. The first set of layers were grown using Bi(thd)<sub>3</sub> and Fe(thd)<sub>3</sub> dissolved in THF. The other set used BiNO<sub>3</sub>.5H<sub>2</sub>O and FeNO<sub>3</sub>.9H<sub>2</sub>O. The ratio of Bi:Fe in the precursor solution was kept at 1:1.

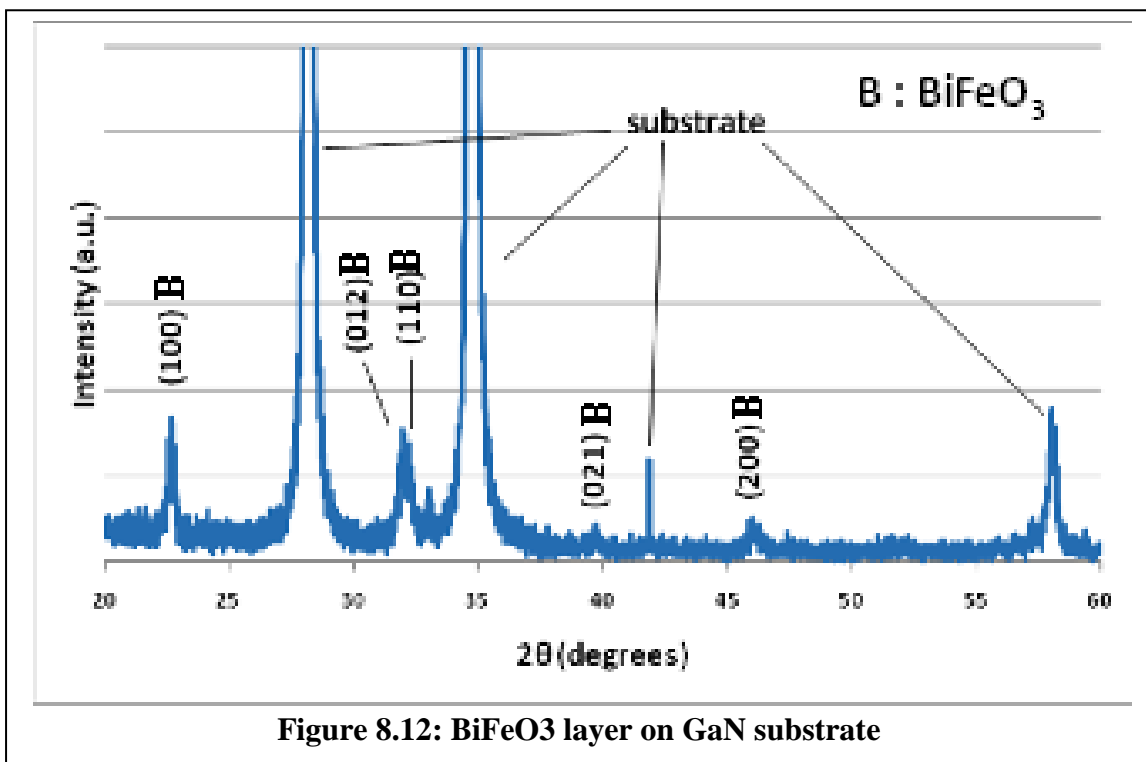
The recipe used for spinner system comprised of 800RPM spin for 10 seconds and then 3000RPM spin for 15 seconds. After each spin coating the sample was dried at 250°C for five minutes in air. This spin coating and drying cycle was repeated 10 times after which the sample was annealed in air at 900°C for one hour. The whole procedure is shown diagrammatically in Figure 8.10.



The spin-coated BFO layers were successfully deposited using the above mentioned procedure on different substrates including Pt(111)/TiO<sub>2</sub>/SiO<sub>2</sub>/Si, Pt(111)/TiO<sub>2</sub>/Al<sub>2</sub>O<sub>3</sub>, SiO<sub>2</sub>/Al<sub>2</sub>O<sub>3</sub>, and GaN templates.

The resulting layers were characterized for their structural and magnetic properties. Figure 8.11 shows room temperature ferromagnetic behavior observed by VSM.

XRD measurement of the films grown on undoped GaN template is shown in Figure 8.12. Prominent peaks for BFO(100) and BFO (012) are visible.

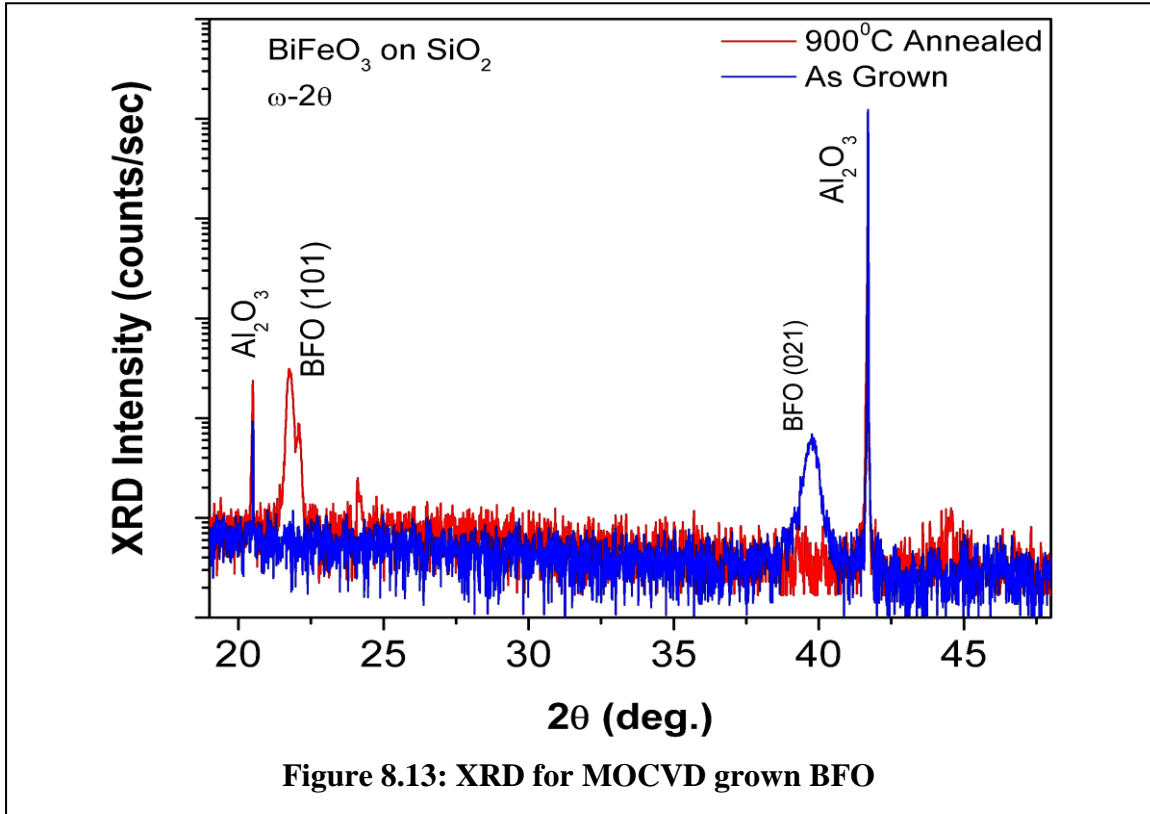


The films grown by spin coating were found to be highly conducting and so no ferroelectric behavior could be established for them.

### 8.3.4 MOCVD Growth of BFO

After successfully using the newly developed oxide tool for growth of N-doped ZnO films that helped baseline its performance liquid injection capability was added to it. The

very low vapor pressure of the selected BFO precursors necessitated use of liquid-injection capability of the tool.



The precursors used for liquid-injection were Bi(thd)<sub>3</sub> and Fe(thd)<sub>3</sub> dissolved in THF. 0.01M precursor solution was prepared with the ratio of Bi:Fe kept at 1.1:1. Growths were carried out at 700°C using O<sub>2</sub> as reactive gas and N<sub>2</sub> as process gas. The flow of liquid precursor was stabilized at 1g/hr. Post growth annealing at 800°C was done in air to achieve poly-crystalline BiFeO<sub>3</sub> thin films. Both the as grown and annealed films were highly resistive. The resulting films were characterized for their structural, optical, magnetic and electrical properties by X-ray diffraction (XRD), photoluminescence (PL), Optical Transmission, Vibrating sample microscopy (VSM) and Hall Effect measurements. Figure 8.13 shows the XRD of the films and Figure 8.14 shows the transmission data.

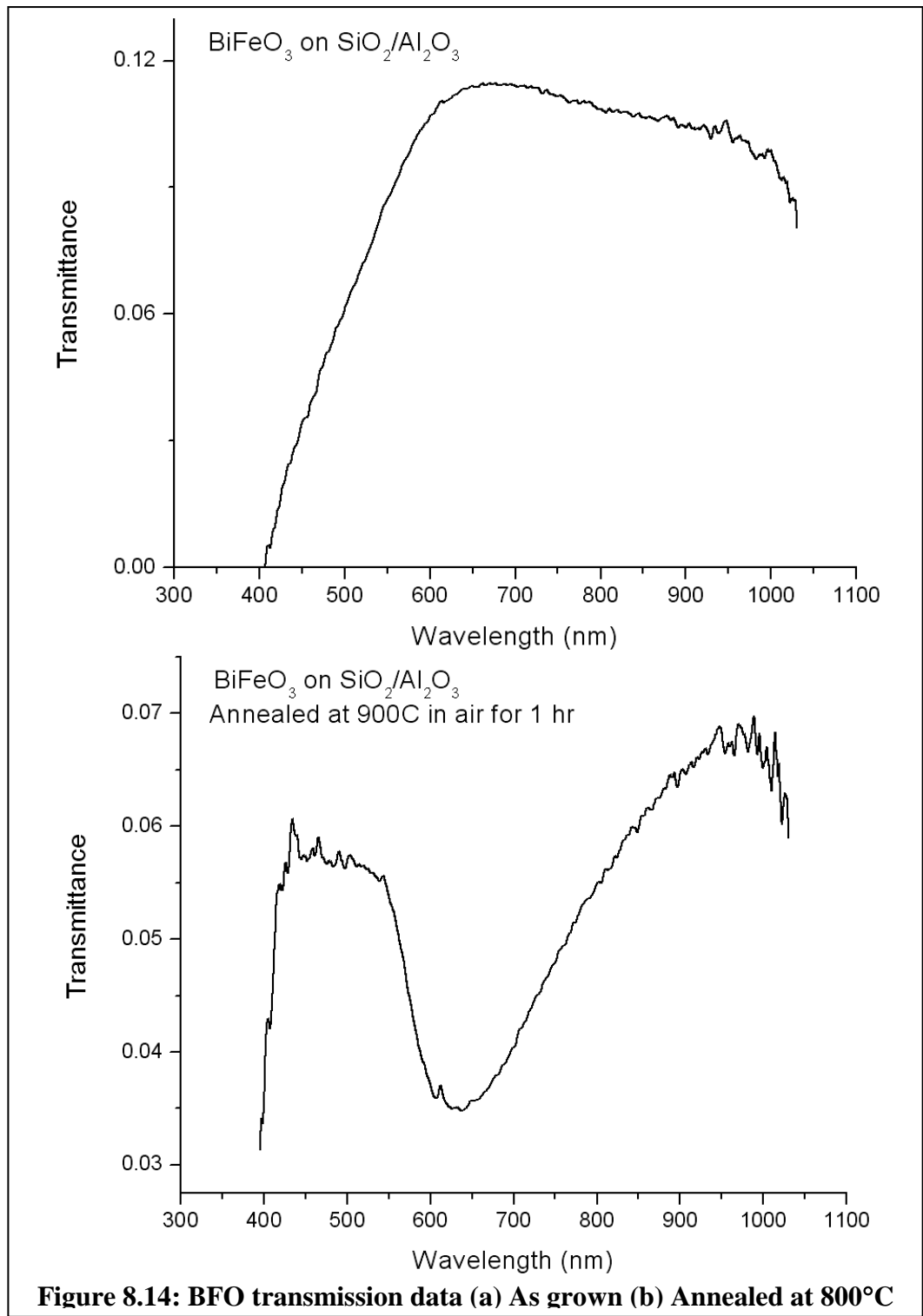


**Figure 8.14: BFO transmission data (a) As grown (b) Annealed at 800°C**

## 8.4 Summary

The work presented in this chapter under the head of additional work lists all the research activities done prior to undertaking this research. The main focus during all these activities was to develop a material system that can be used for spintronics and optoelectronics devices. The lessons learnt during the fabrication of the new gas panel and liquid injection capability helped in the present research work for the modification of the delivery system.

The ZnO films and the BFO layers grown in this work were both shown to have a ferromagnetic behavior at room temperature. However, both the material systems had their limitations making them less ideal for development of spintronics and layer.

## **APPENDIX A: CHARACTERIZATION**

### **A.1 Introduction**

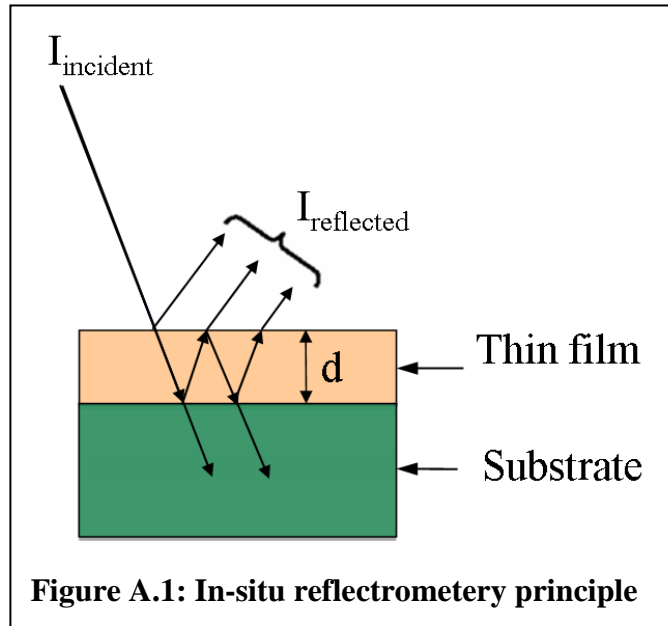
There are a number of properties exhibited by semiconductor thin films. These properties determine the material quality of these films and their functionality in optoelectronic devices. In order to get the desired property of material, and consequently the desired functionality of devices, various characterization techniques are employed to study the material to get a clear picture. The growth parameters during an epitaxial growth of the films can be then be tweaked to enhance or suppress a particular property. The major properties pertaining to this work are structural, magnetic, optical, and electrical properties. This section describes the equipment and techniques used to study these properties.

### **A.2 In-situ Characterization**

The growth parameters during epitaxial growth establish the properties of a semiconductor material. In order to ensure desired quality/property of materials it is critical to have the capability to monitor and control the growth process in real time. In an MOCVD growth tool in-situ optical reflectometry plays an important role in real time monitoring of the films. This technique helps in significantly improving the productivity of MOCVD systems. The real time information that is given by the in-situ optical reflectometry includes the growth rate, layer thickness, and surface roughness.

### A.2.1 Optical reflectometry

Optical reflectometry is based on shining light on to the substrate where epitaxial growth is occurring and monitoring of the reflected light in real time (Figure A.1). The fraction of the incident light that is reflected is called reflectance( $R$ ),



The reflectance depends on the wavelength of the incoming light, the composition of the layers, and the actual temperature of the substrate. During the epitaxial growth, the intensity of light reflected (reflectance) at the substrate-film interface changes and is measured as a function of time. As there is a phase difference between the beams reflected off the surface and interface, constructive or destructive interference will occur, leading to an intensity modulation of the reflected light. The period of these modulations give us a measure of the thickness and growth rate of the films.

Reflectance is given by the following equation

$$R = \frac{I_{\text{reflected}}}{I_{\text{incident}}} = (n - 1)^2 + \frac{k^2}{(n + 1)^2} + k^2 \quad \text{Equation (A.1)}$$

where I = light intensity,

n = refractive index of the material, and

k is the extinction index.

The phase difference and the intensity of the reflected light depend on the thickness of the growing layer as well as on the optical constants of the materials and the wavelength of the light. For normal incidence, constructive interference and maximum reflectance occur if the path difference between two beams is equal to an even integer multiple of the half wavelength

$$2nd = m\lambda \quad \text{Equation (A.2)}$$

where n = refractive index,

d = thickness of the layer,

m = even number, and

$\lambda$  = wavelength.

For destructive interference and minimum reflectance the path difference is equal to an odd integer multiple of the half wavelength

$$2nd = \left(m + \frac{1}{2}\right)\lambda \quad \text{Equation (A.3)}$$

The layer thickness (d) ideally increases continuously during epitaxy with respect to time (t). The growth rate (G.R.) can in turn be determined by taking the ratio of the thickness and the growth time. High growth rates results in a short period in intensity-

modulation and slower rates gives a longer period. The equation below gives us the growth rate of the films

$$G.R. = \frac{d}{t} \quad \text{Equation (A.4)}$$

For maximum reflectance:

$$(G.R) * t = \frac{m\lambda}{2n} \quad \text{Equation (A.5)}$$

and for minimum reflectance:

$$(G.R) * t = \left(m + \frac{1}{2}\right) \frac{\lambda}{2n} \quad \text{Equation (A.6)}$$

The surface roughness and optical waviness (fluctuation caused due to strain or composition of the material) of the layer being grown is indicated by the shape of the reflectance-transient curve. An improvement in surface roughness is indicated by the increase in the mean of the oscillations while a decrease in mean points towards an increase in roughness. Ideally the interest during growth is to have a constant mean indicating uniform quality of the films.

The reflectometry equipment installed in our MOCVD growth tool is made by Filmetrics Corporation. It uses a broadband light source that is filtered through a narrow bandpass filter to select a particular wavelength. This filtered light is then carried through an optical fiber and focused on the substrate in the reactor. The intensity of the light reflected by the substrate (reflectance) is detected by a photo diode. The wavelength of the light in this study was set at 600 nm.

### A.3 Structural Characterization

The arrangement of atoms in a material is described by its crystal structure (hexagonal, zinc-blende, etc.) and the lattice constant, which is the spacing between atoms. The regular ordering of atoms (crystal lattice) in semiconductor materials is investigated using various characterization techniques that are based on radiation of incident beam on the surface. The major technique employed for structural characterization is the X-ray diffraction (XRD).

#### A.3.1 X-ray Diffraction (XRD)

In XRD short-wavelength radiation (X-rays) are used to probe the structural properties of a material. It measures the diffraction of X-rays from a crystal. This diffraction is given by Bragg's law:

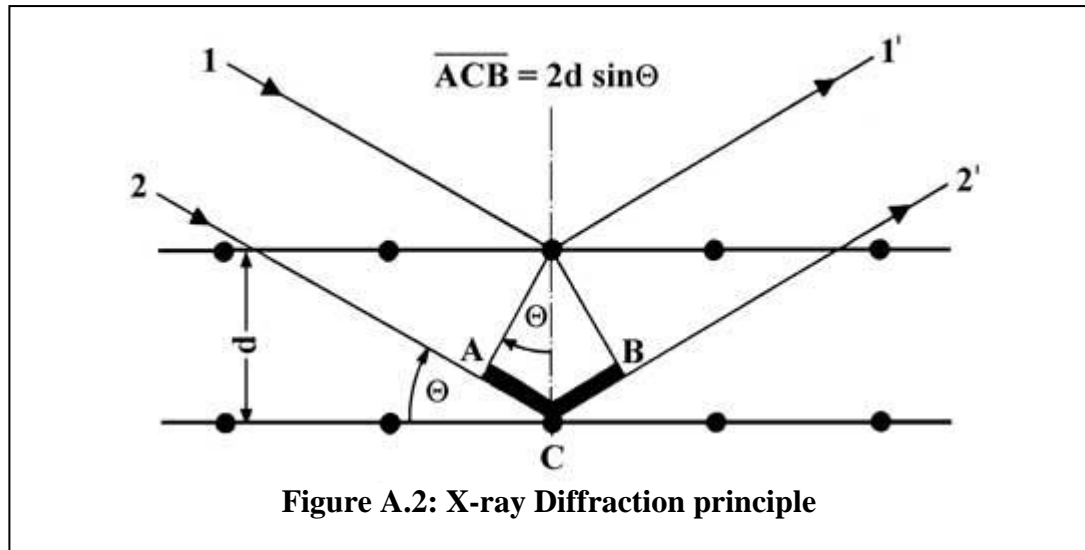
$$n\lambda = 2d \cdot \sin \theta \quad \text{Equation (A.7)}$$

where  $n$  is an integer,

$\lambda$  is the X-ray wavelength,

and  $d$  is the spacing between atoms.

The relationship between the X-ray wavelength ( $\lambda$ ), the diffraction angle ( $\Theta$ ), and the atomic spacing ( $d$ ) is illustrated in Figure A.2.



When the extra distance traveled by the beam '2' in Figure A.2 (ACB) equals an integral multiple of the wavelength ( $n \lambda$ ) of the incident X-ray we get a constructive interference. These constructive interferences are seen as a peak in intensity detected by the detector.

Since the atomic spacing is unique to the crystal structure of the material, XRD can be used to identify materials by comparing the spectrum of the samples with the known standard. XRD can also be used to extract such information as strain, grain size, and defect density.

The (002) reflection is commonly taken as a measure of crystal quality in c-plane GaN, as the (002) reflection plane is perpendicular to the growth axis, allowing probing of the 'c' lattice constant and providing a good gauge of crystal orientation and quality. Determination of the 'a' lattice constant in hexagonal materials must be done using an off-axis reflection such as the (102) reflection.

The line width of the diffraction peak can be taken as a measure of overall crystal quality. The broadening of the diffraction peak points towards a whole range of possible

contributions. The main reason for this broadening is the decrease in crystal quality caused by an increase in defects like dislocation density.

In this work, XRD was performed with a Philips X'Pert Pro MRD diffractometer using a  $\frac{1}{4}$ " slit on both the incident and diffracted beam optics.

## **A.4 Magnetic Characterization**

As this study is focused on developing a RT ferromagnetic semiconductor, it is essential to perform magnetization studies on the TM and RE doped GaN films. The magnetic characterization techniques used in this study are described below.

### ***A.4.1 Vibrating Sample Magnetometry***

The most common measurement method employed for the measurement of the magnetic behavior of magnetic materials at ambient temperature is the Vibrating Sample Magnetometer (VSM). VSM was invented by Simon Foner in 1956 it is based on Faraday's law of induction, which states that an electromotive force (e.m.f) is induced in an inductor by a changing magnetic field. This electric field can be measured and provides information on the changing magnetic field.

In this measurement technique the sample to be measured is mounted on a rod and placed in between the coils of an electromagnet (Figure A.3).The sample is made to undergo sinusoidal motion, i.e., mechanically vibrated, a magnetic moment  $m$  will be induced in the sample. The resulting magnetic flux changes induce a voltage in the suitably placed sensing coils that is proportional to the magnetic moment induced in the sample.

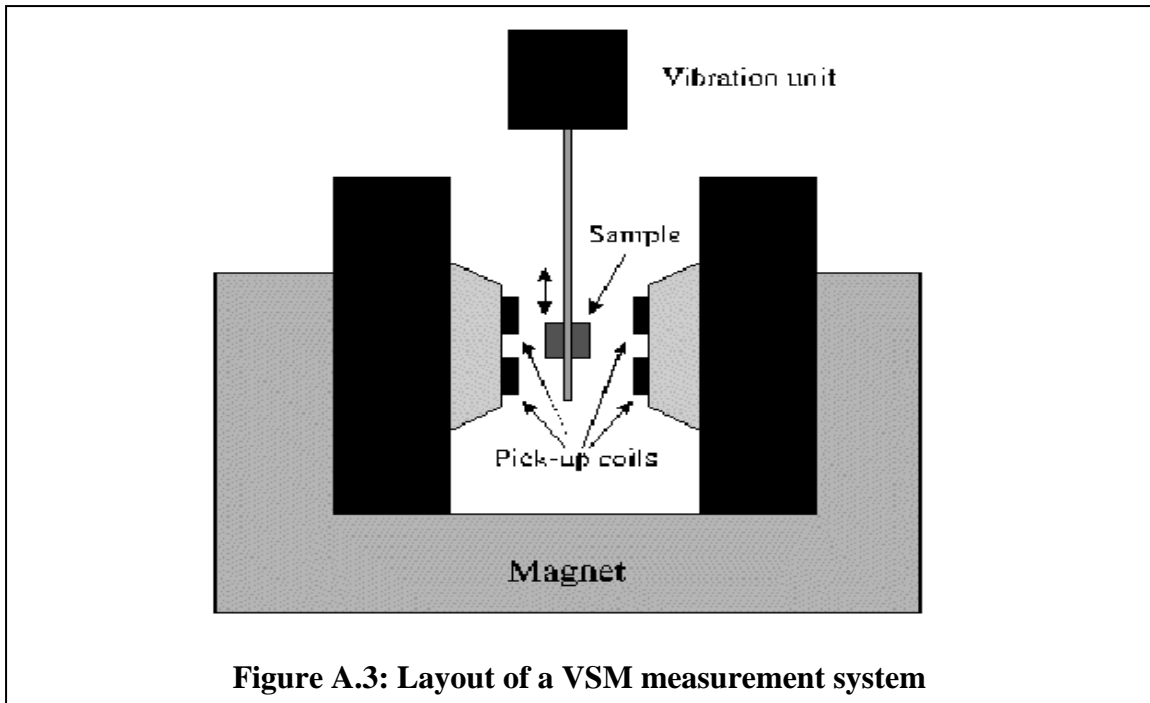


**Figure A.3: Layout of a VSM measurement system**

If the sample is magnetic, the magnetic domains will be aligned to the applied magnetic field. The low frequency vibration of the sample causes the magnetic field to alternate with respect to the sample, resulting in an electric field in the pick-up coils. The resulting current will be directly proportional to the magnetization of the sample, and the greater the magnetization, the greater is the induced current. For this work Lakeshore 7404 Vibrating Sample Magnetometer was used.

#### ***A.4.2 SQUID***

A superconducting quantum interference device (SQUID) is the most sensitive device used for detecting magnetic flux. This device can also be used to detect small magnetic fields, current, voltage, inductance, and magnetic susceptibility. The DC SQUID is commonly used and consists of two superconductors separated by thin insulating layers to form two parallel Josephson junctions. The central element of a SQUID is a ring of superconducting material through which a constant biasing current is fed.

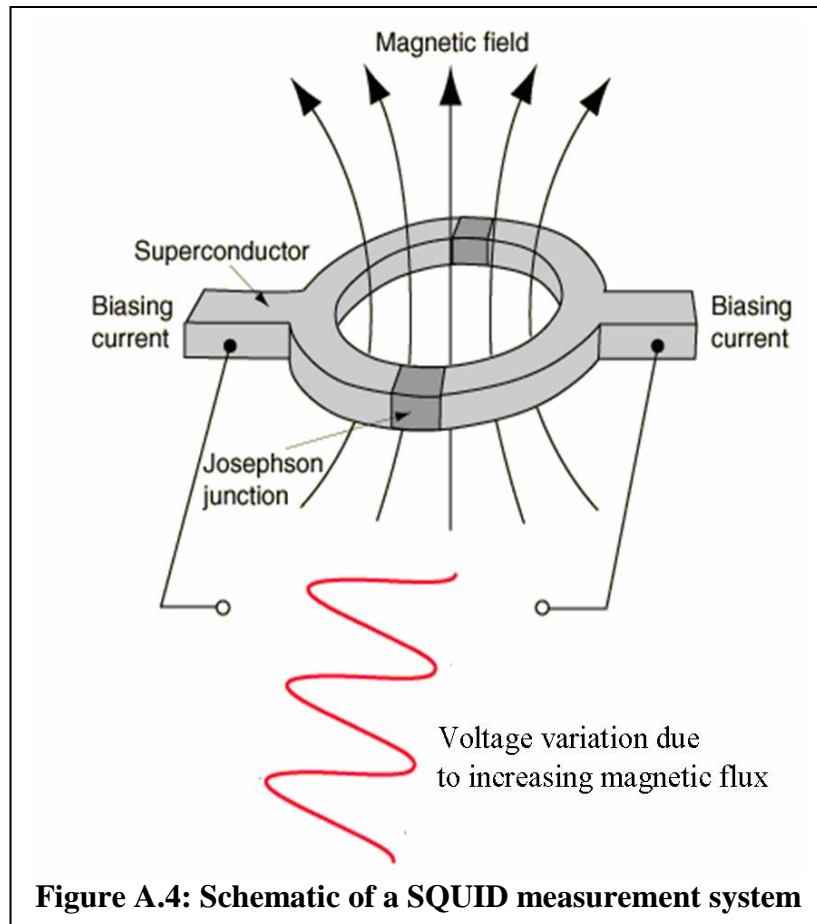


**Figure A.4: Schematic of a SQUID measurement system**

The sample under test is placed on a rod and moved using a step motor through a pair of induction coils in the presence of a superconducting magnet. As the sample passes through, the magnetic moment of the sample induces an electric current in the coils. These current changes are indicative of the changes in the magnetic flux. The SQUID functions as a linear current-voltage converter, thus the variations in the current result in corresponding variations of the SQUID voltage, which is proportional to the change in magnetic flux (Figure A.4). The SQUID response is the voltage plotted as a function of the sample position and is fitted to yield the sample magnetization.

In addition to measuring the magnetization as a function of the applied field at a constant temperature, the magnetization of the sample can also be measured as a function

of temperature under a constant applied field. The commonly used temperature measurements are the zero-field cooled (ZFC) and the field cooled (FC) measurements. ZFC measurements are done by cooling the sample from RT to a low temperature (LT) with the magnetic field set to zero. A magnetic field is applied and the magnetic moment is measured as the temperature is increased to desired level.

In the FC measurements the sample is cooled to the lowest point in the presence of a magnetic field and the magnetic moment is measured as the temperature is increased. ZFC/FC measurements are good to determine the Curie temperature of the sample and to determine the temperature range over which the magnetization is reversible.

A Quantum Design MPMS-5S SQUID magnetometer was used for these measurements. The magnetization measurements were conducted by varying the applied field from -5 T to +5 T. The ZFC/FC measurements were conducted from 5 K to 400 K under an applied field of 100 G.

## **A.5 Optical Characterization**

Careful examination of the optical properties of semiconductors can yield a wealth of information about overall material quality, strain, impurities, and native defects. The temperature dependence of these properties can also yield information about the energy level of impurities. One of the most common methods of investigating optical properties in semiconductors is photoluminescence (PL) spectroscopy. PL was employed in this work, along with optical transmission, to study the optical properties of the GaN layers on both ZnO and silicon.

### ***A.5.1 Photoluminescence Spectroscopy (PL)***

The photoluminescence spectroscopy is based on the property of materials to absorb photons of one wavelength and emits photons of another wavelength. The light source used for illumination of the material with photons is generally a high energy laser. The photons from the laser photo-excite the electrons in the sample to a higher energy state. These electrons then return to their ground state via a radiative recombination mechanism, emitting a photon in the process.

In semiconductor materials, PL spectroscopy is used to study many properties including the bandgap energy, electronic defects, strain, and general optical quality of the material. The near-bandgap emission is often the most prominent feature in the PL spectrum of a semiconductor material taken with above bandgap excitation. However, PL also shows radiative transitions involving impurities and electronic defects in the material.

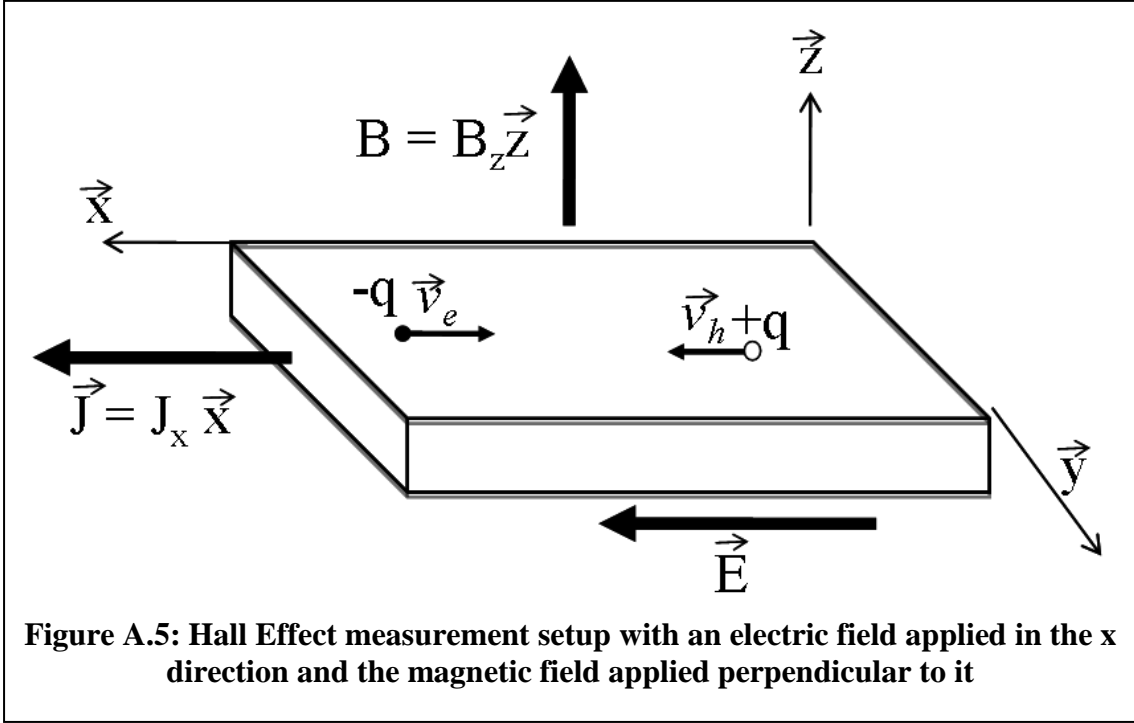
In this work PL measurements were done using two different setups. One setup comprised of a 325nm Melles-Griot HeCd laser with an Acton Spectra Pro 2300i monochromator and PIXIS 100 CCD camera. The other setup had a 238 nm pulsed NeCu laser with a CVI monochromator and a Hamamatsu photomultiplier tube (PMT).

### **A.6 Electrical Characterization**

Electrical characterization techniques yield information about the free carrier concentration as well as conductivity and resistivity of the material. This information is useful in determining impurity levels and overall material quality, as some key impurities in GaN, such as oxygen (a shallow donor), contribute to conduction. Thus, in addition to providing crucial electrical information, electrical characterization techniques, when

properly interpreted, also provide information regarding impurity levels and overall material quality.

### A.6.1 Hall Effect Measurement



The Hall Effect is observable when a magnetic field is applied perpendicular to the flow of current in a semiconductor bar, deflecting the path of the carriers (Figure A.5). In a right-handed coordinate system, if the magnetic field is applied in the  $z$  direction, and current flows in the  $x$  direction, then the force experienced by the carriers is given as

$$F_y = q(\mathcal{E}_y - v_x \mathcal{B}_z) \quad \text{Equation (A.10)}$$

where  $\mathcal{E}_y$  is the electric field in the  $y$  direction,

$v_x$  is carrier velocity in the  $x$  direction,

and  $\mathcal{B}_z$  is the magnetic field applied in the  $z$  direction.

The result of Equation A.10 is that carriers will experience a net force in the  $-y$  direction unless an electric field equal in magnitude to  $v_x B_z$  is created to compensate. The shift of the carriers along the  $y$ -axis, however, creates this compensating electric field and allows the carriers to maintain the  $x$ -axis as their overall direction.

The compensating electric field that is generated by the Hall effect is proportional to the product of magnetic flux density and current density. The proportionality constant is known as the Hall coefficient:

$$R_H = \frac{1}{qp_0} \quad \text{Equation (A.11)}$$

where  $p_0$  is the carrier density.

Thus, for a known current and magnetic field, the free carrier concentration can be calculated by measuring the induced voltage across the sample. Other information, including the resistivity, conductivity, and carrier mobility, can be determined using the Hall effect as well.

The Hall effect was measured in this work using a Lakeshore HMS3000 Hall effect measurement system with a 0.51 T applied field. Samples were cut to 1 cm x 1 cm for the measurements.

## **A.7 Device Characterization**

There are two main aspects to the characterization of LEDs. The first aspect is the electrical properties of the device. This includes measurement of I-V curves and series resistance. The second aspect is the measurement of optical properties, i.e. spectrum, polarization, and the total output power. Device efficiency can be determined by

correlating electrical and optical properties of LEDs. This section describes the details of these measurements as well as the information that can be obtained from them.

### ***A.7.1 Current-Voltage (I-V) Measurement***

The most fundamental property of a diode is its I-V characteristics. The I-V curve is what identifies the device as a diode. A semiconductor diode consists of a p-n junction, and current flow through the device is controlled by the voltage across the junction.

There are two types of current in a p-n junction: drift and diffusion. Electrons and holes diffuse across the junction due to the steep concentration gradients at the junction. This diffusion of carriers, however, leads to the formation of a space-charge region consisting of uncompensated donors and acceptors. The uncompensated charge near the interface leads to an electric field pointing from the n-region toward the p-region. This electric field induces a drift current that, at equilibrium, exactly cancels the diffusion current.

Applying a voltage so that the p-region is at a positive potential with respect to the n-region reduces the electric field across the junction. This reduction in electric field makes the diffusion of carriers across the junction more likely by an exponential factor that is dependent on the forward voltage. Thus, the total current through the junction with forward bias applied is the total diffusion current minus the total drift current. This relationship can be expressed as

$$I = I_0 \left( e^{qV/kT} - 1 \right) \quad \text{Equation (A.12)}$$

where  $I_0$  is the absolute value of the drift current,

$q$  is electronic charge,

$V$  is the voltage across the junction,

and  $k$  is Boltzmann's constant

The series resistance – a measure of the on resistance of the device – can also be calculated from the I-V curve.

The current-voltage characteristics of a device are the key to understanding the mechanisms at work in the device as well as determining its usefulness in a given application. A Keithley 2420 sourcemeter was used in this work to evaluate the I-V characteristics of the devices.

### ***A.7.2 Electroluminescence (EL)***

Light is generated in an LED by recombination of carriers in the active region of the device. The color of light is determined by the bandgap energy,  $E_g$ , of the semiconductor material. More precisely, when an electron is excited into the conduction band and then recombines with a hole in the valence, it loses the energy difference,  $E_g$ , in the form of a photon.

Electrons in the conduction band follow a Boltzmann distribution with an average kinetic energy of  $kT$ . Near the conduction band edge, the density of electrons per unit energy is also limited by the electron density of states. This energy distribution also holds true for holes in the valence band. Recombination of these electrons and holes leads to an emission spectrum that follows the relationship

$$I(E) = \sqrt{E - E_g} e^{-E/kT} \quad \text{Equation (A.12)}$$

where  $I(E)$  is the emission intensity as a function of energy.

A homojunction LED in which the emitted light is equal to or slightly above the bandgap of the material, however, suffers from reabsorption in the bulk, degrading

efficiency. One solution to this problem is the use of quantum wells in the active region, as in  $\text{In}_x\text{Ga}_{1-x}\text{N}/\text{GaN}$  multiple quantum well LEDs. Quantum well structures in the active region of LEDs typically emit light at energy lower than the bandgap of the surrounding material, suppressing reabsorption in the surrounding layers and increasing the amount of light extracted from the device.

$\text{In}_x\text{Ga}_{1-x}\text{N}/\text{GaN}$  multiple quantum well LEDs were grown in this work. The EL properties were measured using a Keithley 2420 sourcemeter, OL-770 spectrometer, and IS-670 integrating sphere from Optronic Laboratories.

### ***A.7.3 Optical Power Measurements***

Total light output from an LED is of great importance in solid state lighting applications. The ratio of optical power emitted from an LED to electrical power consumed by the LED is known as the external quantum efficiency (EQE). EQE is the product of the light extraction efficiency and internal quantum efficiency (IQE), which is the ratio of photons generated in the active region of the LED to electrons injected into the active region. These quantities – optical power, EQE, and IQE – are used to describe the efficiency of an LED. The measurements in this work were taken using the Keithley sourcemeter and Optronic Laboratories equipment described above.

## **APPENDIX B: DEVICE FABRICATION**

### **B.1 Introduction**

A standard process for fabrication of GaN-based LEDs was used in this work. The end result of the process is a wafer with vertically-emitting devices that are 350 $\mu$ m on each side, Figure B.1. The exact steps of the process are as follows:

- 1) Annealing for p-GaN activation
- 2) Metal deposition for current spreading layer
- 3) Annealing current spreading layer
- 4) Photolithography for mesa pattern
- 5) Etch – removal of current spreading layer
- 6) Hard bake to cure photoresist
- 7) Dry etch to define mesa
- 8) Removal of baked photoresist
- 9) Transfer of p-type contact pattern
- 10) Deposition of p-type contact metal
- 11) Lift-off of p-type contact metal
- 12) Transfer of n-type contact pattern
- 13) Deposition of n-type contact metal
- 14) Lift-off of n-type contact metal

The major steps involved in this process are annealing, photolithography, etching, and metal deposition. Each of these steps will be discussed in more detail in the following sections.

## **B.2 Annealing**

Activation of the Mg acceptors in GaN is required for reliable p-type material. This is due to the formation of Mg-H donor complexes during growth. Annealing in a nitrogen atmosphere drives out the hydrogen and activates the Mg as an acceptor in GaN. In this work, p-GaN activation was done in an RTA system at 800 °C for 4 minutes under N<sub>2</sub> ambient. The current spreading layer was also annealed at 500 °C for 2 minutes in an RTA under atmospheric ambient. The presence of oxygen allows for oxidation of the Ni-Au layer, forming NiO, which provides a better ohmic contact to p-type GaN.

## **B.3 Photolithography**

Photolithography is the process of transferring a pattern from a mask onto a wafer. The photolithography process relevant to this study is described below.

## **B.4 Wafer Cleaning**

After the MOCVD growth of a GaN based LED the wafer is cleaned with organic solvents to remove any surface impurities. This consists of rinsing the sample with acetone followed by a methanol and then by DI water. The wafer is then dried using a nitrogen gun leaving it ready for photoresist coating.

## **B.5 Metal Deposition – Current Spreading Contact**

The p-GaN resistance is a few orders of magnitude higher than the n-GaN layer, so a current spreading layer is deposited on top of the p-GaN layer to ensure that current spreads to regions not covered by the top electrode. This current spreading layer acts as an Ohmic contact and should be transparent to the emitted light so as not to negatively impact efficiency. An electron beam evaporator is used to deposit this current spreading

layer which consists of 5 nm of Ni (adhesion layer) followed by 5 nm of Au. In this research a CVC e-beam evaporator was used for metal deposition. In this deposition technique a high energy electron beam is focused on the center of a crucible that contains the metal to be evaporated. This energy causes the metal to melt and evaporate onto the sample which is placed face down above the crucible. The chamber is pumped down to a pressure of  $5 \times 10^{-7}$  Torr to increase the mean free path of the evaporated particles. The deposition rates range from 2 to 5 Å/second.

### **B.6 Current Spreading Contact Annealing**

The current spreading contact is annealed in an RTA at 500 °C in atmosphere for 2 minutes. This causes the formation of a NiO layer at the inference and facilitates an Ohmic contact to the p-GaN surface.

### **B.7 Mesa Pattern Transfer**

Next photolithography is used to transfer the mesa pattern onto the wafer, which defines the outline for each LED. Two coats of the positive photoresist AZ5214 are spun onto the sample at 2500 RPM for 30 seconds. The wafer then undergoes a soft bake which entails heating a wafer on a hotplate at 100 °C for 1.5 minutes. The soft bake drives away the solvent from the resist and makes it more photosensitive. A mask aligner is used to align the mesa mask with the wafer being patterned. Ultraviolet light having energy of  $60\text{mJ}/\text{cm}^2$  is exposed through the mask pattern onto the photoresist on the sample. The exposed areas of the resist undergo a chemical change when exposed to light. The sample then undergoes a post-exposure bake at 115 °C for 2.5 minutes; this causes cross linkage of the PR in the exposed regions. This is followed by a flood exposure of

UV light (no mask is used) at  $180 \text{ mJ/cm}^2$  which causes the unexposed photoresist area to undergo a chemical reaction which makes it more soluble in the developer. Finally the pattern is obtained by placing it in a developer solution of 5:1  $\text{H}_2\text{O}:\text{AZ 400 K}$  for 1 minute.

## **B.8 Mesa Etch**

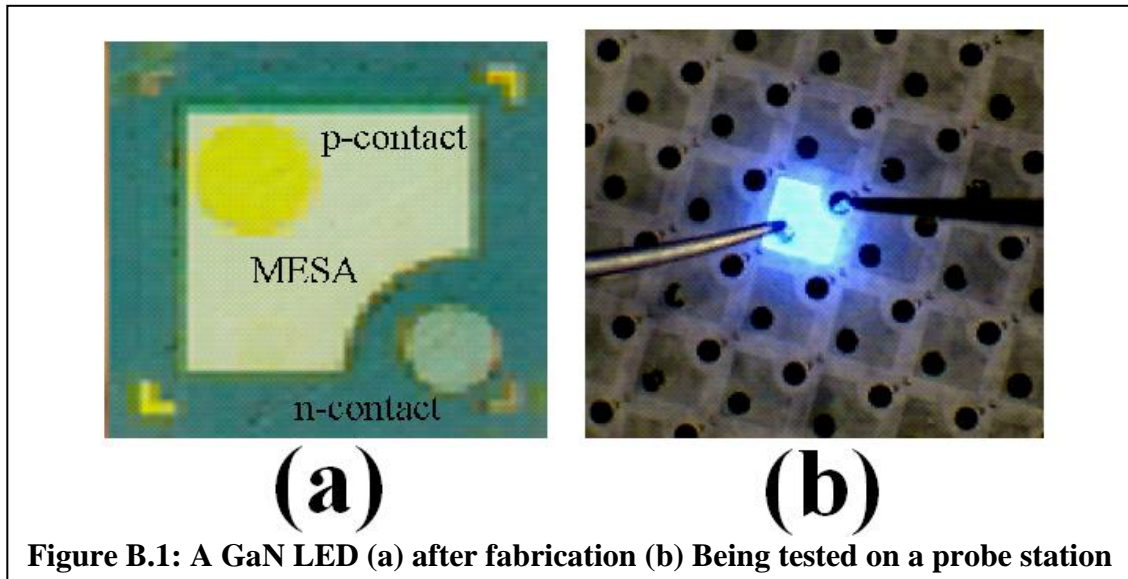
Before the LED mesas can be defined by etching, the devices are dipped in potassium iodide to etch away any metal that is not covered by the photoresist. The sample is then cured by baking in an oven for 30 minutes at  $120 \text{ }^\circ\text{C}$ . A Plasma-Therm inductively coupled plasma (ICP) etcher is used to etch the GaN films. ICP etching uses radio frequency induced plasma consisting of  $\text{Cl}_2\text{-Ar}$  gas to generate free ions which are accelerated towards the surface to be etched. Chemical reactions occur between chlorine and gallium, and the surface is etched away. The sample is removed from the chamber, and its depth profile is measured to confirm the etch depth. After this, it is cleaned and is ready for the next processing step.

## **B.9 n-GaN Contact**

The pattern transfer for the n-GaN bonding pad is performed next. This procedure begins with the same photolithography step mentioned prior to the mesa etch, except only a single coat of photoresist is used, and the spin speed is increased to 3500 rpm. The metal deposition begins with 10 nm of titanium acting as an adhesion layer, followed by 50 nm of aluminum, 10 nm of titanium, and finally 200 nm of gold. A thick layer of gold is deposited so that the sample can be wire bonded if needed. After metal deposition, a

lift off process is performed by dipping the wafer in acetone to remove the metal from the regions that were covered by the photoresist.

### B.10 p-GaN Contact



Finally, the p-contact is deposited. This procedure is similar to the n-GaN contact, except the layers used are 50 nm of nickel and 200 nm of gold. A GaN LED after fabrication is shown in Figure B.1.

### B.11 Packaging

Patterns are transferred to the wafer using photolithography. A thin layer of photoresist is applied to the wafer by spinning at 2500 rpm for 30 seconds. Two layers of photoresist are typically used in this process. The photoresist is then cured by baking it at 100 °C for one and a half minutes. Next, a mask is used to expose the photoresist with the desired pattern, and another bake is performed. Finally, the photoresist is developed in AZ-400K developer, leaving the desired pattern on the wafer.

## REFERENCES

- [1] S. A. Wolf, A. Y. Chtchelkanova, and D. M. Treger, *IBM Journal of Research and Development* 50, 101 (2006)
- [2] S. A. Wolf, D. D. Awschalom, R. A. Buhrman, J. M. Daughton, S. von Molnar, M. L. Roukes, A. Y. Chtchelkanova, and D. Treger, *Science* 294, 1488 (2001)
- [3] Prinz, *Science* 282, 1660 (1998)
- [4] G. Schmidt, D. Ferrand, L. W. Molenkamp, A. T. Filip, and B. J. van Wees, *Physical Review B (Condensed Matter and Materials Physics)* 62, R4790 (2000)
- [5] H. Ohno, *Science* 281, 951 (1998)
- [6] T. Dietl, *Journal of Applied Physics* 103, 07D111 (2008)
- [7] J. S. Moodera, X. Hao, G. A. Gibson, and R. Meservey, *Physical Review Letters* 61v 637 (1988)
- [8] U. Luders, M. Bibes, K. Bouzehouane, E. Jacquet, J. P. Contour, S. Fusil, J. F. Bobo, J. Fontcuberta, A. Barthlmy, and A. Fert, *Applied Physics Letters* 88, 082505 (2006)
- [9] R. Fiederling, M. Keim, G. Reuscher, W. Ossau, G. Schmidt, A. Waag, and L. W. Molenkamp, *Nature* 402, 787 (1999)
- [10] B. T. Jonker, Y. D. Park, and B. R. Bennett, *Physical Review B* 62, 8180 (2000)
- [11] H. Ohno, *Journal of Magnetism and Magnetic Materials* 200, 110 (1999)
- [12] T. Dietl, H. Ohno, F. Matsukura, J. Cibert, and D. Ferrand, *Science* 287, 1019 (2000)

- [13] G. Schmidt, D. Ferrand, L. W. Molenkamp, A. T. Filip, and B. J. van Wees, *Physical Review B (Condensed Matter and Materials Physics)* 62, R4790 (2000)
- [14] C. Liu, F. Yun, and H. Morkoc, *Journal of Materials Science-Materials in Electronics* 16, 555 (2005)
- [15] K. Sato and H. Katayama-Yoshida *Semicond. Sci. Technol.* 17 377 (2002)
- [16] T. Dietl *Nat. Mat.* 2 646 (2003)
- [17] G. Das, B. Rao and P. Jena *Phys. Rev. B* 69 214422 (2004)
- [18] Theodoropoulou N, Hebard A, Overberg M, Abernathy C, Pearton S, Chu S and Wilson R *Appl. Phys. Lett.* 78 3475 (2001)
- [19] Thaler G et al *Appl. Phys. Lett.* 80 3964 (2002)
- [20] Park M, Kuh K, Myoung J, Lee J, Chang J, Lee K, Han S and Lee W, *Solid State Commun.* 124 11 (2002)
- [21] Kim K, Lee K, Kim D, Kim H, Ihm Y, Djayaprawira D, Takahashi M, Kim C, Kim C and Yoo S, *Appl. Phys. Lett.* 82 1775 (2003)
- [22] Sonoda S, Shimizu S, Sasaki T, Yamamoto Y and Hori H, *J. Cryst. Growth* 237 1358 (2002)
- [23] Sarigiannidou E, Wilhelm F, Monroy E, Galera R, Bellet-Amalric E, Rogalev A, Goulon J, Cibert J and Mariette H *Phys. Rev. B* 74 041306 (2006)
- [24] Reed M, El-Masry N, Stadelmaier H, Ritmus M, Reed M, Parker C, Roberts J and Bedair S *Appl. Phys. Lett.* 79 3473 (2001)
- [25] Graf T, Goennenwein S T B and Brandt M S *Phys. Status Solidi b* 239 277 (2003)
- [26] S. J. Pearton, C. R. Abernathy, M. E. Overberg, G. T. Thaler, D. P. Norton, N. Theodoropoulou, A. F. Hebard, Y. D. Park, F. Ren, J. Kim and L. A. Boatner, *J. Appl. Phys.* 93 1 (2003)

- [27] Dietl T Materials Research Society Fall Meeting: MRS Proceedings (Boston, USA, November 2004) vol 831, ed C Wetzel, B Gil, M Kuzuhara and M Manfra (2004)
- [28] Liu C, Yun F and Morkoc , H J. Mater. Sci.: Mater. Electron. 16 555 (2005)
- [29] Frazier R, Thaler G, Overberg M, Gila B, Abernathy C and Pearton S Appl. Phys. Lett. 83 1758 (2003)
- [30] Liu H, Wu S, Singh R, Gu L, Smith D, Newman N, Dilley M, Montes L and Simmonds M Appl. Phys. Lett. 85 4076 (2004)
- [31] Hashimoto M, Zhou Y K, Kanakura M and Ashai H Solid State Commun. 122 37 (2002)
- [32] Wu S, Liu H, Gu L, Singh R, van Schilfgaarde M, Smith D, Dilley M, Montes L and Simmonds M Mat. Res. Soc. Symp. Proc. 798 Y1057 (2004)
- [33] Lee J, Lim J, Khim Z, Park Y, Pearton S and Chu S J. Appl. Phys. 93 4512 (2003)
- [34] Shon Y et al J. Appl. Phys. 95 761 (2004)
- [35] Heikman S, Keller S, Mates T, DenBaars S and Mishra U J. Cryst. Growth 248 513 (2003)
- [36] Akinaga H, Nemeth S, Boeck J D, Nistor L, Bender H, Borghs G, Ofuchi H and Oshima M Appl. Phys. Lett. 26 4377 (2000)
- [37] Kane M, Gupta S, Fenwick W, Li N, Park E H, Strassburg M and Ferguson I Phys. Status Solidi a 204 61 (2007)
- [38] Talut G, Reuther H, Mcklich A, Eichhorn F and Potzger K Appl. Phys. Lett. 89 161909 (2006)
- [39] Bonanni A et al Phys. Rev. B 75 125210 (2007)
- [40] Lee J H et al Appl. Phys. Lett. 90 032504 (2007)

- [41] Schulthness T, Temmerman W, Szotek Z, Butler W and Stocks G, Nat. Mat. 4 838 (2005)
- [42] Keavney D, Cheung S, King S, Weinert M and Li L, Phys. Rev. Lett. 95 257201 (2005)
- [43] Graf T, Gjukic M, Brandt M, Stutzmann M and Ambacher oxygen Appl. Phys. Lett. 81 5159 (2002)
- [44] Pacuski W, Ferrand D, Cibert J, Gaj J, Golnik A, Kossacki P, Marcet S, Sarigiannidou E and Mariette H Preprint cond-mat/0703041 (2007)
- [45] Zajac M, Gosk J, Kaminska M, Twardowski A, Szyszko T and Podsiadlo S Appl. Phys. Lett. 79 2432 (2001)
- [46] A. Y. Polyakov, N. B. Smirnov, A. V. Govorkov, N. V. Pashkova, A. A. Shlensky, S. J. Pearton, M. E. Overberg, C. R. Abernathy, J. M. Zavada, and R. G. Wilson, Journal of Applied Physics 93, 5388 (2003)
- [47] S. Kuroda, E. Bellet-Amalric, X. Biquard, J. Cibert, R. Giraud, S. Marcet, and H. Mariette, Physica Status Solidi B-Basic Research 240, 443 (2003)
- [48] Byuanova I A et al, Appl. Phys. Lett.84, 2599 (2004)
- [49] BuyanovaIA, Chen W M, Ivill M P, Pate R, Norton D P, Pearton S J, Dong J W, Osinsky A, Bertog B, Dabiran A M and Chow P P, J. Vac. Sci. Technol. B 24, 259 (2006)
- [50] T. Graf, M. Gjukic, M. S. Brandt, M. Stutzmann, and O. Ambacher, Applied Physics Letters 81, 5159 (2002)
- [51] P. Mahadevan and A. Zunger, Applied Physics Letters 85, 2860 (2004)
- [52] G. H. Zhong, J. Lwang, and Z. Zeng, Journal of Physics-Condensed Matter 20, 295221 (2008)

- [53] N. Teraguchi, A. Suzuki, Y. Nanishi, Y. K. Zhou, M. Hashimoto, and H. Asahi, Solid State Communications 122, 651 (2002)
- [54] S. Dhar, L. Perez, O. Brandt, A. Trampert, K. H. Ploog, J. Keller, and B. Beschoten, Physical Review B (Condensed Matter and Materials Physics) 72, 245203 (2005)
- [55] Wang Y and Steckl A 2003 Appl. Phys. Lett. 82 402
- [56] Teraguchi N, Suzuki A, Nanishi Y, Zhou Y K, Hashimoto M and Asahi H 2002 Solid State Commun. 122 651
- [57] Choi S, Zhou Y, Emura S, Teraguchi N, Suzuki A and Asahi H 2002 Phys. Status Solidi c 3 2250
- [58] Dhar S, Kammermeier T, Ney A, P´erez L, Ploog K, Melnikov A and Wieck A D 2006 Appl. Phys. Lett. 89 062503
- [59] Han S Y et al 2006 Appl. Phys. Lett. 80 042102
- [60] P´erez L, Lau G, Dhar S, Brandt oxygen and Ploog K 2006 Phys. Rev. B 74 195207
- [61] Overberg M, Lee K, Abernathy C, Pearton S, Hobson W, Wilson R and Zavada J 2001 Mat. Sci. Eng. B 81 150
- [62] Zhou Y, Kim M, Teraguchi N, Hashimoto M, Tanaka H, Suzuki A, Nanishi Y and Asahi H 2003 Phys. Status Solidi b 240 440
- [63] Bang H, Sawahata J, Piao G, Tsunemi Y, Yanagihara H, Kita E and Akimoto K 2003 Phys. Status Solidi c 0 2874
- [64] Ugolini C, Nepal N, Lin J, Jianga H and Zavada J 2006 Appl. Phys. Lett. 89 151903
- [65] P. Mahadevan and S. Mahalakshmi, Physical Review B 73, 4 (2006)

- [66] P. Larson and S. Satpathy, *Physical Review B* 76, 8 (2007)
- [67] J. K. Hite, R. M. Frazier, R. P. Davies, T. Thaler, C. R. Abernathy, S. J. Pearton, J. M. Zavada, E. Brown, and U. Hommerich, *Journal of Electronic Materials* 36, 391 (2007)
- [68] Y. K. Zhou, S. W. Choi, S. Emura, S. Hasegawa, and H. Asahi, *Applied Physics Letters* 92 (2008).
- [69] H. Asahi, Y. K. Zhou, M. Hashimoto, M. S. Kim, X. J. Li, S. Emura, and S. Hasegawa, S5555 (2004)
- [70] S. Dhar, O. Brandt, A. Trampert, L. Daweritz, K. J. Friedland, K. H. Ploog, J. Keller, B. Beschoten, and G. Guntherodt, *Applied Physics Letters* 82, 2077 (2003)
- [71] Y. K. Zhou, S. W. Choi, S. Kimura, S. Emura, S. Hasegawa, and H. Asahi, p. 429 (2007)
- [72] H. J. Round. *Electrical World* 19, 309 (1907)
- [73] Zheludev, N. *Nature Photonics* 1 (4), 189 (2007)
- [74] M Holub, P Bhattacharya, *J. Phys. D: Appl. Phys.* 40, 179 (2007)
- [75] D. Jiles, *Introduction to Magnetism and Magnetic Materials*, Chapman & Hall, New York, 1991
- [76] M. A. Ruderman and C. Kittel, *Physical Review* 96, 99 (1954)
- [77] T. Kasuya, *Progress of Theoretical Physics* 16, 45 (1956)
- [78] K. Yosida, *Physical Review* 1, 893 (1957)
- [79] H. Ohno, A. Shen, F. Matsukura, A. Oiwa, A. Endo, S. Katsumoto, and Y. Iye, *Applied Physics Letters* 69, 363 (1996)
- [80] H. Ohno and F. Matsukura, *Solid State Communications* 117, 179 (2001)

- [81] C. Zener, *Physical Review* 82, 403 (1951)
- [82] H. Akai, *Physical Review Letters* 81, 3002 (1998)
- [83] H. A. Kramers, *Physica* 1, 182, (1934)
- [84] P. W. Anderson, *Physical Review* 79, 350 (1950)
- [85] M. Zajac, J. Gosk, M. Kaminska, A. Twardowski, T. Szyszko, and S. Podsiadlo, *Applied Physics Letters* 79, 2432 (2001)
- [86] S. Nakamura and S. F. Chichibu, “Introduction to Nitride Semiconductor Blue Lasers and Light Emitting Diodes”, Taylor & Francis 2000.
- [87] O. Ambacher, *Journal of Physics D-Applied Physics* 31 (1998) 2653
- [88] R. Stepniewski, M. Potemski, W. Wismolek, K. Pakula, J. M. Baranowski, J. Lusakowski, I. Grzegory, S. Porowski, G. Martinez, and P. Wyder, *Physical Review B (Condensed Matter)* 60 (1999) 4438.
- [89] “Interactive Periodic Table”, Infoplease. © 2000–2007 Pearson Education, publishing as Infoplease. 03 May. 2010  
<http://www.infoplease.com/ipa/A0765967.html>
- [90] Patnaik, Pradyot (2003). *Handbook of Inorganic Chemical Compounds*, McGraw-Hill, pp. 302–306
- [91] A. Ney, T. Kammermeier, E. Manuel, V. Ney, S. Dhar, K. H. Ploog, F. Wilhelm, A. Rogalev: *Applied Physics Letters* 90 (2007) 252515
- [92] A. Ney, T. Kammermeier, V. Ney, S. Ye, K. Ollefs, E. Manuel, S. Dhar, K. H. Ploog, E. Arenholz, F. Wilhelm, A. Rogalev: *Physical Review B (Condensed Matter and Materials Physics)* 77 (2008) 233308
- [93] G. M. Dalpian and S. H. Wei, *Physica Status Solidi B-Basic Solid State Physics* 243 (2006) 2170

- [94] Chandrima Mitra and Walter R. L. Lambrecht, *Physical Review B (Condensed Matter and Materials Physics)* 80, 081202R (2009)
- [95] L. Liu, P. Y. Yu, Z. Ma, S. S. Mao: *Physical Review Letters* 100 (2008) 127203 68, 76, 80
- [96] Y. Gohda, A. Oshiyama: *Physical Review B (Condensed Matter and Materials Physics)* 78 (2008) 161201 68, 76
- [97] P. Dev, Y. Xue, P. Zhang: *Physical Review Letters* 100 (2008) 117204 55, 69, 81
- [98] G. M. Dalpian, S.-H. Wei: *Phys. Rev. B* 72 (2005) 115201 67, 69, 70, 74, 75
- [99] W. R. L. Lambrecht, P. Larson: *Materials Research Society* (2006) 67, 70
- [100] S. Limpijumnong, C. G. V. de Walle: *Physical Review B (Condensed Matter and Materials Physics)* 69 (2004) 035207 viii, 78, 79
- [101] Venables, John, *Introduction to Surface and Thin Film Processes*, Cambridge: Cambridge University Press. (2000)
- [102] Pimpinelli, Alberto; Jacques Villain, *Physics of Crystal Growth*, Cambridge: Cambridge University Press, (1998)
- [103] Oura, K.; V.G. Lifshits, A.A. Saranin, A.V. Zotov, and M. Katayama, "Surface Science: An Introduction", Berlin: Springer, (2003)
- [104] L. Liu and J. H. Edgar, *Materials Science & Engineering R-Reports* 37 (2002)
- [105] B. Gil, *Group III Nitride Semiconductor Compounds*, Oxford University Press, England, 1998
- [106] S. Yoshida, S. Misawa, and S. Gonda, *Applied Physics Letters* 42 (1983) 427.
- [107] H. Amano, N. Sawaki, I. Akasaki, and Y. Toyoda, *Applied Physics Letters* 48 (1986) 353

- [108] S. Nakamura, Japanese Journal of Applied Physics Part 2-Letters 30 (1991) L1705
- [109] S. Nakamura, M. Senoh, and T. Mukai, Japanese Journal of Applied Physics Part 2-Letters 32 (1993) L8
- [110] S. Keller, B. P. Keller, Y. F. Wu, B. Heying, D. Kapolnek, J. S. Speck, U. K. Mishra, and S. P. DenBaars, Applied Physics Letters 68 (1996) 1525
- [111] K. Uchida, A. Watanabe, F. Yano, M. Kouguchi, T. Tanaka, and S. Minagawa, Journal of Applied Physics 79 (1996) 3487
- [112] O. Briot, J. P. Alexis, M. Tchounkeu, and R. L. Aulombard, Elsevier Science Sa Lausanne, 1997, p. 147
- [113] W. Götz, N. M. Johnson, C. Chen, H. Liu, C. Kuo, W. Imler., Appl. Phys. Lett., 1996 (68): p. 3114.
- [114] Götz, J. Walker, L. T. Romano, and N. M. Johnson, Proc. Mater. Res. Soc. Symp., 1997 (449): p. 525.
- [115] Levinshtein, S. L. Rumyantsev, M. S. Shur, Editors, Properties of Advanced Semiconductor Materials: GaN, AlN, InN, BN, SiC, and SiGe, New York, John Wiley and Sons, (2001).
- [116] P. Hacke, A. Maekawa, N. Koide, K. Hiramatsu, N. Sawaki, Jpn. J. Appl. Phys., 1993(74): p. 5901
- [117] J. Neugebauer, C. G. Van de Walle, Festkörperprobleme / Advances in Solid State Physics, ed. R. Helbig, Vol. 35. 1996, Wiesbaden: Vieweg, Braunschweig. 25
- [118] H. Amano, M. Kito, K. Hiramatsu, and I. Akasaki., Jpn. J. Appl. Phys. Part 2, 1989(28): p. L2112.
- [119] S. Nakamura, N. Iwasa, M. Senoh, T. Mukai, Jpn. J. Appl. Phys. Part 1, 1992(31): p. 1258.

- [120] S. W. Kim, J. M. Lee, K. S. Ahn, R. M. Park, J. S. Jang, S. J. Park, Kwangju Institute of Science and Technology (2001) Method for Manufacturing p-type GaN, Based on Thin Film Using Nitridation, U.S. Pat. 6,294,016 B1.
- [121] Toshio Ogino and Masaharu Aoki, *Jpn. J. Appl. Phys.* 19 (1980) pp. 2395-2405
- [122] X. Li and P. W. Bohn, *Applied Physics Letters*, VOLUME, vol 75 (1999) n 26
- [123] S.W. Choi, S. Emura, S. Kimura, M.S. Kima, Y.K. Zhou, N. Teraguchi, A. Suzuki, A. Yanase, H. Asahi, *Journal of Alloys and Compounds* 408–412 (2006) 717–720
- [124] J. Hejtmánek, K. Knížek, M. Maryško, Z. Jiráček, D. Sedmidubský, Z. Sofer, V. Peřina, H. Hardtdegen, and C. Bucha, *J. Appl. Phys.* 103, 07D107 (2008)
- [125] H. J. Round, *Electrical World* 19, 309 (1907)
- [126] N. Zheludev, *Nature Photonics* 1 (4), 189 (2007)
- [127] Braunstein, Rubin, *Physical Review* 99, 1892 (1955)
- [128] Perry T.S., *Spectrum*, IEEE 32, Issue2, 52 (1995)
- [129] T.P. Pearsall, B.I. Miller, R.J. Capik, and K.J. Bachmann, *Appl. Phys. Lett.*, 28, 499-501 (1976)
- [130] Akasaki, I., Amano, H., Koide, Y., Hiramatsu, K., and Sawaki, N., *J. Crystal Growth* 98, 209 (1989)
- [131] Amano, H. and Akasaki, I., *Mat. Res. Soc.* 165 (1990)
- [132] Amano, H., Akasaki, I., Kozawa, T., Hiramatsu, K., Sawaki, N., Ikeda, K., and Ishii, Y., *J. Lumin.* 40&41, 121 (1988)
- [133] Amano, H., Kito, M., Hiramatsu, K., and Akasaki, I., *Jpn. J. Appl. Phys.* 28, L2112 (1989)

- [134] Amano, H., Asahi, T., and Akasaki, I., *Jpn. J. Appl. Phys.* 29, L205 (1990)
- [135] Nakamura, S. et al., *Appl. Phys. Lett.* 64, 1687 (1994)
- [136] Nakamura, S. et al., *Appl. Phys. Lett.* 67, 1868 (1995).
- [137] M Holub, P Bhattacharya, *J. Phys. D: Appl. Phys.* 40, 179 (2007)
- [138] Murakami S., *Adv. Solid State Phys.* 45, 197 (2005)
- [139] Sharma P., Brouwer P. W., *Phys. Rev. Lett.* 91, 166801 (2003)
- [140] Governale M, Taddei F., Fazio R., *Phys. Rev. B*, 68, 155324 (2003)
- [141] Mal'shukov A G, Tang C S, Chu C S, Chao K A, *Phys. Rev. B* 68, 233307 (2003)
- [142] Meier F and Zakharchenya B P, *Optical Orientation* (1984)
- [143] Oestreich M, Hübner J, Hägele D, Klar P J, Heimbrodt W, Rühle W W, Ashenford D E, Lunn B, *Spin* (1999)
- [144] Li C H, Kioseoglou G, van 't ErveOMJ, Hanbicki A T, Jonker B T, Mallory R, Yasar M and Petrou A., *Appl. Phys. Lett.* 85, 1544 (2004)
- [145] Rashba E I., *Phys. Rev. B* 62, R16267 (2000)
- [146] Motsnyi V F, De Boeck J, Das J, Van Roy W, Borghs G, Goovaerts E and Safarov V I., *Appl. Phys. Lett.* 81, 265 (2002)
- [147] Hanbicki A T, van 't ErveOMJ, Magno R, Kioseoglou G, Li C H, Itskos G, Mallory R, Yasar, M., Petrou A., *Appl. Phys. Lett.* 82, 4092 (2003)
- [148] Elliott R J., *Phys. Rev* 96, 266 (1954)
- [149] Dresselhaus G., *Phys. Rev.* 100, 580 (1955)
- [150] Winkler, Berlin: Springer, 190, 69 (2003)

- [151] Zawadzki W and Pfeffer P., *Semicond. Sci. Technol.* 19, R1–17 (2003)
- [152] D'yakonov M I and Perel' V I., *Sov. Phys. Solid State* 13, 3023 (1971)
- [153] Bir G L, Aronov A G and Pikus G E., *Sov. Phys.—JETP* 42 705–12 (1975)
- [154] Wagner J, Schneider H, Richards D, Fischer A and Ploog K., *Phys. Rev. B* 47, 4786 (1993)
- [155] Gotoh H, Ando H, Sogawa T, Kamada H, Kagawa T and Iwamura H., *J. Appl. Phys.* 87, 3394 (2000)
- [156] Srinivasan Krishnamurthy, Mark van Schilfgaarde and Nathan Newman, *Applied Physics Letters*, 83, 9 (2003)
- [157] J. M. Kikkawa and D. D. Awschalom, *Phys. Rev. Lett.* 80, 4313 (1998)
- [158] Young D K, Johnston-Halperin E, Awschalom D D, Ohno Y and Ohno H., *Appl. Phys. Lett.* 80, 1598 (2002)
- [159] Chye et al, *PRB* 66 201301R (2002)
- [160] Van Dorpe et al, *APL* 84 3495–7 (2004)
- [161] Johnston-Halperin et al, *PRB* 65 041306 (2002)
- [162] Fiederling et al, *Nature* 402 787–90 (1999)
- [163] Loffler et al, *APL* 88 062105 (2006)
- [164] Seufert et al, *PRB* 69 035311 (2004)
- [165] Kohda et al, *JJAP* 40 L1274–6 (2001)
- [166] L. W. Martin, S. P. Crane, Y. H. Chu, M. B. Holcomb, M. Gajek, M. Huijben, C. H. Yang, N. Balke and R. Ramesh, *J. Phys.: Condens. Matter* 20 434220 (13pp) (2008)

- [167] N. Hur, S. Park, P. A. Sharma, J. S. Ahn, S. Guha, and S.-W. Cheong, *Nature*, vol. 429, p. 393 (2004)
- [168] T. Kimura et al., *Nature*, vol. 426, p. 55, (2003)
- [169] T. Zhao, A. Scholl, F. Zavaliche, K. Lee, M. Barry, A. Doran, M.P. Cruz, V.H. Chu, C. Ederer, N.A. Spaldin, R.R. Das, D.M. Kim, S.H. Baek, C.B. Eom and R. Ramesh, *Nature Mater.* 5, 283 (2006)
- [170] Binek Ch and Doudin B., *J. Phys.: Condens. Matter* 17 L39 (2005)
- [171] P. Royen and K. Swars, *Angew. Chem.*, vol. 24, p. 779, 779.
- [172] Kumar M and Palkar V R, *Appl. Phys. Lett.* 76, 2764 (2000)
- [173] Sosnowska I, Peterlin-Neumaier T and Steichele E, *J. Phys. C: Solid State Phys.* 15, 4835 (1982)
- [174] Achenbach G D, James W J and Gerson R., *J. Am. Ceram. Soc.* 50, 437 (1967)
- [175] Teague J R, Gerson R and James W J., *Solid State Commun.* 8, 1073 (1970)
- [176] V. Fruth, E. Tenea, M. Gartner, A. Anastasescu, D. Berger, R. Ramer, and M. Zaharescu, *J. Eur. Ceram. Soc.* 27, 937 (2007)
- [177] T. P. Gujar, V. R. Shinde, and C. D. Lokhande, *Mater. Chem. Phys.* 103, 142 (2007)
- [178] T. Kanai, S. Ohkoshi, and K. Hashimoto, *J. Phys. Chem. Solids* 64,391 (2003)
- [179] J. F. Ihlefeld, N. J. Podraza, Z. K. Liu, R. C. Rai, X. Xu, T. Heeg, Y. B. Chen, J. Li, R. W. Collins, J. L. Musfeldt, X. Q. Pan, J. Schubert, R. Ramesh, and D. G. Schlom, *Applied Physics Letters* 92, 142908 (2008)
- [180] H el ene B ea, Manuel Bibes, Gervasi Herranz, Xiao-Hong Zhu, St ephane Fusil, Karim Bouzehouane, Eric Jacquet, Cyrille Deranlot, and Agn es Barth el emy, *IEEE transactions on magnetics*, vol. 44, no. 7 (2008)

- [181] J. R. Teague, R. Gerson, and W. J. James, *Solid State Commun.*, vol. 8, p. 1073, (1970)
- [182] D. Lebeugle, D. Colson, A. Forget, and M. Viret, *Appl. Phys. Lett.*, vol. 91, p. 022907 (2007)
- [183] J. Wang et al., *Science*, vol. 299, p. 1719 (2003)
- [184] K. Y. Yun, M. Noda, and M. Okuyama, *Appl. Phys. Lett.*, vol. 83, p. 3981 (2003)
- [185] X. Qi, M. Wei, Y. Lin, Q. Jia, D. Zhi, J. Dho, M. G. Blamire, and J. L. MacManus-Driscoll, *Appl. Phys. Lett.*, vol. 86, p. 071913 (2005)
- [186] S. K. Singh, R. Ueno, H. Funakubo, H. Uchida, S. Koda, and H. Ishiwara, *Jpn. J. Appl. Phys.*, vol. 44, p. 8525 (2005)
- [187] Y. B. Chen, M. B. Katz, X. Q. Pan, R. R. Das, D. M. Kim, S. H. Baek, and C. B. Eom, *Appl. Phys. Lett.*, vol. 90, p. 072907 (2007)
- [188] R. de Sousa and J.E. Moore, *Appl. Phys. Lett.* 92, 022514 (2008)
- [189] Y.-H. Chu, L.W. Martin, M.B. Holcomb, M. Gajek, S.-J. Han, Q. He, N. Balke, C.-H. Yang, D. Lee, W. Hu, Q. Zhan, P.-L. Yang, A. Fraile-Rodriguez, A. Scholl, S.X. Wang and R. Ramesh, *Nature Mater.* 7, 478 (2008)
- [190] S. Lee, W. Ratcliff, S.-W. Cheong and V. Kiryukin, *Appl. Phys. Lett.* 9, 192906 (2008)
- [191] V. Laukhin, V. Skumriev, X. Marti, D. Hrabovsky, F. Sanchez, M.V. Garcia-Cuenca, C. Ferrater, M. Varela, U. Luders, J.F. Bobo and J. Fontcuberta, *Phys. Rev. Lett.* 97, 227201 (2006)
- [192] D. Alders, L. H. Tjeng, F. C. Voogt, T. Hibma, G. A. Sawatzky, C. T. Chen, J. Vogel, M. Sacchi, and S. Iacobucci, *Phys. Rev. B* 57, 11623 (1998)

- [193] M. Barry, K. Lee, Y.H.Chu, P.L. Yang, L.W. Martin, C.A. Jenkins, R. Ramesh, A. Scholl, and A. Doran, APS, Mar (2007)
- [194] J. X. Zhang, Y. L. Li, Y. Wang, Z. K. Liu, L. Q. Chen, Y. H. Chu, F. Zavaliche, and R. Ramesh, J. Appl. Phys., vol. 101, p. 114105 (2007)
- [195] F. Zavaliche, S. Y. Yang, T. Zhao, Y. H. Chu, M. P. Cruz, C. B. Eom, and R. Ramesh, Phase Transit., vol. 79, p. 991 (2006)
- [196] G. Catalan et al., Phys. Rev. Lett., vol. 100, p. 027602 (2008)
- [197] H. Bea, S. Fusil, K. Bouzehouane, M. Bibes, M. Sirena, G. Herranz, E. Jacquet, J.-P. Contour, and A. Barthélémy, Jpn. J. Appl. Phys., vol. 45, p. L187 (2006)
- [198] Y. H. Chu, T. Zhao, M. P. Cruz, Q. Zhan, P. L. Yang, L. W. Martin, M. Huijben, C. H. Yang, F. Zavaliche, H. Zheng, and R. Ramesh, Appl. Phys. Lett., vol. 90, p. 252906 (2007)
- [199] S. Y. Yang, F. Zavaliche, L. Mohaddes-Ardabili, V. Vaithyanathan, D. G. Schlom, Y. J. Lee, Y. H. Chu, M. P. Cruz, Q. Zhan, et al., Appl. Phys. Lett., 87, 102903 (2005)
- [200] R. Ueno, S. Okaura, H. Funakubo, and K. Saito, Jpn. J. Appl. Phys., Part 2, 44, L1231 (2005)
- [201] J. Thery, C. Dubourdieu, T. Baron, C. TERNON, H. Roussel, and F. Pierre, Chem. Vap. Deposition, 13, 232 (2007)
- [202] Y. Tasaki, T. Kanoko, M. Kabeya, N. Chifu, and S. Yoshizawa, Integr. Ferroelectr., 81, 281 (2006)
- [203] M. S. Kartavtseva, O. Y. Gorbenko, A. R. Kaul, T. V. Murzina, S. A. Savinov, and A. Barthélémy, Thin Solid Films, 515, 6416 (2007)
- [204] M. Singh, Y. Yang, C. G. Takoudis, A. Tatarenko, G. Srinivasan, P. Kharel, and G. Lawes, Electrochemical and Solid-State Letters, 12 (5) H161 (2009)

- [205] D. Lebeugle, D. Colson, A. Forget, M. Viret, A. M. Bataille, A. Gukasov, *Phys. Rev. Lett.*, 100, 227602 (2008)
- [206] S. Lee, W. Ratcliff, S.-W. Cheong, V. Kiryukhin, *Appl. Phys. Lett.*, 92, 192 906 (2008)
- [207] T. Zhao, A. Scholl, F. Zavaliche, K. Lee, M. Barry, A. Doran, M. P. Cruz, Y. H. Chu, C. Ederer, N. A. Spaldin, R. R. Das, D.M. Kim, S. H. Baek, C. B. Eom, R. Ramesh, *Nat. Mater.* 2006, 5, 823.
- [208] J. Nogues, I. K. Schuller, *J. Magn. Magn. Mat.* 1999, 192,203.
- [209] P. Borisov, A. Hochstrat, X. Chen, W. Kleemann, C. H. Binek, *Phys. Rev. Lett.* 2005, 94, 117203.
- [210] V. Laukhin, V. Skumryev, X. Martí <sup>´</sup>, D. Hrabovsky, F. Sa <sup>´</sup>nchez, M. V. Garcí <sup>´</sup>a-Cuenca, C. Ferrater, M. Varela, U. Lü <sup>¨</sup>ders, J. F. Bobo, J. Fontcuberta, *Phys. Rev. Lett.* 2006, 97, 227201.
- [211] J. Dho, X. Qi, H. Kim, J. L. MacManus-Driscoll, M. G. Blamire, *Adv. Mater.* 2006, 18, 1445. [198] H. Be <sup>´</sup>a, M. Bibes, S. Cherifi, F. Nolting, B. Warot-Fonrose, S. Fusil, G. Herranz, C. Deranlot, E. Jacquet, K. Bouzehouane, A. Barthe <sup>´</sup>le <sup>´</sup>my, *Appl. Phys. Lett.*, 89, 242114 (2006)
- [212] H. Be <sup>´</sup>a, M. Bibes, F. Ott, B. Dupe <sup>´</sup>, X.-H. Zhu, S. Petit, S. Fusil, C. Deranlot, K. Bouzehouane, A. Barthe <sup>´</sup>le <sup>´</sup>my, *Phys. Rev. Lett.*, 100, 017204 (2008)
- [213] Y.-H. Chu, L. W. Martin, M. B. Holcomb, M. Gajek, S.-J. Han, Q. He, N. Balke, C.-H. Yang, D. Lee, W. Hu, Q. Zhan, P.-L. Yang, A. Fraile-Rodr <sup>´</sup>iguez, A. Scholl, S. X. Wang, R. Ramesh, *Nat. Mater.*, 7, 478 (2008)
- [214] H. Bea, M. Gajek, M. Bibes, A. Barthelemy, *J. Phys.: Cond. Mat.*, 20, 434231 (2008)

- [215] H. Bea, S. Fusil, K. Bouzehouane, M. Bibes, M. Sirena, G. Herranz, E. Jacquet, J.-P. Contour, A. Barthelemy, *Jpn. J. Appl. Phys.*, L187, 45 (2006)
- [216] M. Gajek, M. Bibes, S. Fusil, K. Bouzehouane, J. Fontcuberta, A. Barthelemy, A. Fert, *Nat. Mater.*, 6,296 (2007)
- [217] M. Bibes, A. Barthelemy, *Nat. Mater.*, 7, 425 (2008)
- [218] J. E. Sice, J. T. Dubois, K. J. Eisentraut, and R. E. Sievedd, *Journal of the American Chemical Society*, 91:13 June 18, pp3476 (1969)

## PUBLICATIONS

- [1] **T. Zaidi**, W. E. Fenwick, A. Melton, N. Li, S. Gupta, H. B. Yu, A. Ougazzaden, and I.T. Ferguson, “Effects of N doping on ZnO thin films grown by MOVPE”, *Journal of Crystal Growth*, vol. 310, pp. 5011-5015, 2008.
- [2] **T. Zaidi**, A. Melton, M. Jamil, W.E. Fenwick, I. T. Ferguson, “n-type, p-type and Semi-insulating ZnO:N thin films Growth by MOCVD with NH<sub>3</sub> Doping”, *Journal of Vacuum Science and Technology* June, 2009
- [3] **T. Zaidi**, M. Jamil, A. Melton, N. Li, W. E. Fenwick, I. T. Ferguson, “NH<sub>3</sub> Doping in MOCVD Growth of ZnO Thin Films”, *MRS Fall 2008*
- [4] S. Gupta, **T. Zaidi**, M. H. Kane, and I. T. Ferguson, “Topical Review: Transition metal and rare earth doping of GaN”, *Physica Status Solidi (B)*, 2008, in press, Invited paper.
- [5] W. E. Fenwick, **T. Zaidi**, S. Gupta, H. Yu, A. Melton, A. Ougazzaden, and I. T. Ferguson, “Effects of group V doping and III-N Co-Doping on ZnO thin films grown by MOVPE”, *Proc. IC MOVPE*, 2008, pp. 205.
- [6] W. E. Fenwick, S. Gupta, H. Yu, A. Melton, **T. Zaidi**, A. Ougazzaden, and I. Ferguson, “MOCVD growth of transition-metal doped GaN and ZnO for spintronic applications”, *IC MOVPE*, June 01-06, 2008.
- [7] S. Gupta, A. Melton, E. Malguth, W. E. Fenwick, **T. Zaidi**, H. Yu, and I. T. Ferguson, “Rare earth doping of GaN with gadolinium by MOCVD”, 2008, in press.
- [8] S. Gupta, W. E. Fenwick, A. Melton, **T. Zaidi**, H. Yu, V. Rengarajan, J. Nause, A. Ougazzaden, and I. T. Ferguson, “MOVPE growth of transition-metal doped GaN and ZnO for spintronic applications”, *Journal of Crystal Growth*, vol. 310, pp. 5032-5038, 2008, Invited paper.
- [9] S. Gupta, W. E. Fenwick, A. Melton, **T. Zaidi**, H. Yu, V. Rengarajan, J. Nause, A. Ougazzaden, I. T. Ferguson, “MOVPE growth of transition-metal-doped GaN and ZnO for spintronic applications”, *Journal of Crystal Growth*, v 310, n 23, p 5032-8, 15 Nov. 2008

- [10] W. E. Fenwick, M.H. Kane, R. Varatharajan, **T. Zaidi**, Z.Fang, B. Nemeth, D. J. Keeble, H. El-Mkami, G.M. Smith, J. Nause, C.J. Summers, I.T. Ferguson, “Transition metal- and rare earth-doped ZnO: a comparison of optical, magnetic, and structural behavior of bulk and thin films”, Proceedings of the SPIE - The International Society for Optical Engineering, v 6474, p 64741Q-1-8, 2007
- [11] W.E. Fenwick, M.H. Kane, Z.Fang; **T. Zaidi**, N. Li; V. Rengarajan, J. Nause, I.T. Ferguson, “Transition metal-doped ZnO: a comparison of optical, magnetic, and structural behavior of bulk and thin films”, Zinc Oxide and Related Materials Symposium, p 55-60, 2007
- [12] A. Melton, S. Gupta, E. Malguth, W.E. Fenwick, **T. Zaidi**, H. Yu, I. T. Ferguson, “Rare Earth Doping of GaN with Gadolinium by MOCVD”, MRS Proceedings Fall 2008
- [13] M. Jamil , T. Xu, **T. Zaidi**, A. Melton, B. Jampana, C.L. Tan, B.S. Ooi, I. T. Ferguson, “physica status solidi (a), online on 15 Apr 2010, Accepted for print

## CONFERENCE PRESENTATIONS

- [1] **T. Zaidi**, M. H. Kane, S. Gupta, N. Li, W. E. Fenwick, M. Han, Z. J. Zhang, C. Summers and I. T. Ferguson, “Magnetic and Optical properties of Ga(Cr, Mn, Fe)N grown by Metal Organic Chemical Vapor Deposition”, 52nd Magnetism and Magnetic Materials Conference, Tampa, FL, November 5-9, 2007
- [2] S. Gupta; H. Kang; M. Kane; E.H. Park; **T. Zaidi**; I.T. Ferguson, “Growth and Magnetization Study of Transition Metal Doped GaN Nanostructures”; 7th Int'l Conference of Nitride Semiconductors (ICNS-7) Las Vegas, NV, Sept. 16-21, 2007
- [3] S. Wang; N. Li; E.H. Park; Z. Feng; A. Valencia; J. Nause; M. Kane; **T. Zaidi**; I.T. Ferguson; “Metalorganic Chemical Vapor Deposition of InGaN Layers on ZnO Substrates”; 7th Int'l Conference of Nitride Semiconductors (ICNS-7) Las Vegas, NV, Sept. 16-21, 2007
- [4] M. Kane, S. Gupta, W. Fenwick; M. Han; Z. Zhang; **T. Zaidi**; I.T. Ferguson; “Comparison of Transition Metal Incorporation and Phase Segregation in MOCVD-Grown Ga(Fe,Mn)N”; 7th Int'l Conference of Nitride Semiconductors (ICNS-7) Las Vegas, NV, Sept. 16-21, 2007
- [5] M. Jamil, **T. Zaidi**, A. Melton, S. Gupta, W. Fenwick, E. Malguth, I. T. Ferguson, “MOCVD Growth of Ferromagnetic Ga Gd N and Effect of Co-Doping”, ICNS-8, Oct 2009
- [6] **T. Zaidi**, M. Jamil, A. Melton, and I. T. Ferguson, “Liquid injection MOCVD growth of BiFeO<sub>3</sub> thin films on GaN”, MRS Fall 2009
- [7] M. Jamil, T. Xu, **T. Zaidi**, A. Melton, I. T. Ferguson, C.L. Tan and B.S. Ooi, “Controlled Epitaxy and Characteristics of InN Nanopyramids by MOCVD”, MRS, Fall 2009
- [8] O. Hitzemann, M. Kaiser, E. Malguth, M. R. Wagner, J. H.. Schulze, A. Hoffmann, S. Gupta, **T. Zaidi**, I.T. Ferguson, M. Röver, D.D. Mai, J. Malindretos, and A. Rizzi, “Optical measurements on Gd doped GaN“, EMRS, Regensburg 2010
- [9] A. Melton, E. Burgett, M. Jamil, **T. Zaidi**, N. Hertel, I. T. Ferguson, “GaN As a Neutron Detection Material”, IEEE Southeastcon, Mar 2010

- [10] **T. Zaidi**, A. Melton, M. Jamil, B. Jampana, T. Xu, and I. T. Ferguson, "Spin polarized light emitting diode with  $\text{Ga}_{1-x}\text{Gd}_x\text{N}$  injection layer," Accepted, SPIE Tenth International Conference on Solid State Lighting, Aug 2010